Willi Michael Brandstädter

Partial Oxidation of Raffinate II and other Mixtures of n-Butane and n-Butenes to Maleic Anhydride in a Fixed-Bed Reactor

universitätsverlag karlsruhe

Willi Michael Brandstädter

Partial Oxidation of Raffinate II and other Mixtures of n-Butane and n-Butenes to Maleic Anhydride in a Fixed-Bed Reactor

Partial Oxidation of Raffinate II and other Mixtures of n-Butane and n-Butenes to Maleic Anhydride in a Fixed-Bed Reactor

von
Willi Michael Brandstädter

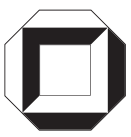

universitätsverlag karlsruhe

Dissertation, Universität Karlsruhe (TH)
Fakultät für Chemieingenieurwesen und Verfahrenstechnik, 2007
Referenten: Prof. Dr. Bettina Kraushaar-Czarnetzki
Prof. Dr.-Ing. Thomas Turek, Technische Universität Clausthal

Impressum

Universitätsverlag Karlsruhe
c/o Universitätsbibliothek
Straße am Forum 2
D-76131 Karlsruhe
www.uvka.de

Universitätsverlag Karlsruhe 2008
Print on Demand

ISBN: 978-3-86644-199-6

Partial Oxidation of Raffinate II and other Mixtures of *n*-Butane and *n*-Butenes to Maleic Anhydride in a Fixed-Bed Reactor

Zur Erlangung des akademischen Grades eines

DOKTORS DER INGENIEURWISSENSCHAFTEN (Dr.-Ing.)

von der Fakultät für Chemieingenieurwesen und Verfahrenstechnik
der Universität Fridericiana Karlsruhe (TH)
genehmigte

Dissertation

von

Dipl.-Ing. Willi Michael Brandstädter
aus Karlsruhe

Tag des Kolloquiums: 12. Oktober 2007
Referentin: Prof. Dr. Bettina Kraushaar-Czarnetzki
Korreferent: Prof. Dr.-Ing. Thomas Turek, Technische Universität Clausthal

Acknowledgements

This thesis evolved during my time at the Institute of Chemical Process Engineering (CVT) at the University of Karlsruhe (TH). I would like to thank everyone who contributed to this thesis.

Special thanks go to Prof. Dr. Bettina Kraushaar-Czarnetzki who made it possible for me to work on this very exciting topic.

I would also like to thank Prof. Dr.-Ing. Thomas Turek for his interest in my work, and his availability as co-referent of this thesis.

During their projects at the institute, Dipl.-Ing. Eberhard Burr, Dr. Mohamed Abd El-Wahab and Pablo Casaretto contributed significantly to this thesis. It would not have been possible to have such an amount of experimental data without their great help.

I am very thankful for the many fruitful discussions with Prof. Dr. Hans-Günther Lintz and Dr.-Ing. Andreas Reitzmann. Particulary joyful was the time with Dipl.-Ing. Matthias Pieper with whom I was allowed to share an office, his experience and myriads of different types of teas and chocolates.

I would like to thank Dr. Andreas Wurl and Andreas Hüther M.A. for the assistance in finding all odd english expressions in this thesis.

I also acknowledge the financial assistance provided for this project by the Max-Buchner-Forschungsstiftung.

Finally, my greatest thanks go to my wife Dipl.-Ing. Nicola Simon for her support, her love and her understanding for numerous week-ends where I was working on this thesis rather than spending time with her.

Contents

Chapter 1

Introduction

1.1 Motivation

Maleic anhydride is one of the intermediate products with the highest forecasted increase in demand in the near future [1]. Nowadays, it is predominantly produced by the partial selective oxidation of *n*-butane. *n*-Butane is not directly available at every chemical production site and has to be transported to the site if needed. Locally produced C_4 hydrocarbon mixtures[1] may become an economic alternative as raw materials in such cases [2]. Processes based on *n*-butane/*n*-butene mixtures have only minor importance in the present, since the yields of maleic anhydride achieved in the conversion of the mixtures are lower than the yields achieved in the conversion of pure *n*-butane [3].

The C_4 production capacities are directly coupled to the production capacities of ethylene and propylene, whose demands are steadily increasing. Therefore, the prices of C_4 hydrocarbon mixtures may decrease in the future. Ethylene and Propylene are mainly produced in steamcracker plants, which are often fed with liquid feedstocks like naphtha. The production of the C_2 and C_3 olefins leads to an inevitable co-production of C_4 streams. The components of such C_4 streams are difficult to separate. Some strategies have been developed to increase revenues by recovering certain components of the stream by physical or chemical means or recycle the stream to the feed of the cracking units to decrease the required amount of fresh feed [4].

The recovery of individual components automatically leads to complex processes. Processes that convert as many C_4 components as possible in one step are therefore favoured. One possible process could be the conversion of *n*-C_4 hydrocarbon mixtures to maleic anhydride. The successful implementation of such a process would cope with the growth of demand of maleic anhydride and would lead to a better valorisation of C_4 hydrocarbon streams.

The development of a production process based on mixed C_4 hydrocarbons has interesting scientific aspects that are worth investigating. The conversion behaviours of *n*-butenes and *n*-butane are different concerning reaction rates, intermediates and selectivities and therefore result in different overall reactor performances. The composition of C_4 mixtures may vary depending on the origin of the feedstock. It is necessary to consider the reactions of *n*-butane and *n*-butenes individually in an appropriate kinetic description

[1] C_4 mixtures contain hydrocarbons with four carbon atoms such as *n*-butane and the *n*-butene isomers. They can also contain isobutane, isobutene and butadiene.

in order to predict reactor performance. However, the quantitative description should be as simple as possible to be able to identify the necessary parameters by experiments in laboratory reactors under conditions resembling those of the industrial process.

Vanadium-phosphorous oxide (VPO) catalysts are typically used in the conversion of *n*-butenes and *n*-butane to maleic anhydride. In this work, an industrially developed VPO catalyst type was used. It was therefore possible to focus on the development of kinetic models without the need to develop and produce a VPO catalyst at the institute's laboratories.

The catalyst types used in this work consist of non-catalytic supports with the catalytic layer deposited on the surface. The thickness of this layer can be varied and therefore presents a parameter which has to be considered for the optimisation of the catalyst performance. The thickness influences the diffusional resistances of the reactants and products in the pores of the active layer. The resulting effects on the performance of the catalyst bodies are discussed in the present work.

Another challenge of the reaction system is the high exotherm of the individual reactions which leads inevitably to non-isothermal operation conditions of a potential industrial fixed-bed reactor. The effects of the non-isothermal operation on reactor performance have to be quantified. The quantification is achieved by coupling reaction kinetics with reaction thermodynamics and by choosing the appropriate mathematical reactor model for the simulation.

Only by considering all important non-idealities of the industrial reactor, mainly the non-isothermal operation, it is possible to determine suitable operation conditions for a production-scale reactor. The results of the reactor simulations can also be used to identify sensitive operation parameters. These are important steps towards the optimisation of the whole process since the reactor is the most crucial apparatus of the plant.

1.2 Outline

In chapter 2, state of the art industrial processes and possible raw materials for the production of maleic anhydride will be discussed. Additionally, it deals with the choice of different reactor and process options to convert mixed C_4 hydrocarbons to maleic anhydride. A literature survey is given for the VPO catalyst type that was used in this thesis.

The experimental and data analysis methods for functional characterisation of the catalysts are presented in chapter 3.

In chapter 4, the experimental results and the quantification of reaction kinetics for the oxidation of pure *n*-butane, pure *n*-butenes and mixtures thereof are presented. Influences of operational parameters such as feed composition and reaction temperature on the performance of an ideal fixed-bed reactor are discussed. Furthermore, the chapter presents first results concerning the ageing of the catalyst.

Transport resistances in the porous active material have a surprising effect on the performance of the catalyst. They are covered in chapter 5. Additionally, the effects of external mass transport resistances from the bulk gas phase to the catalyst surface on reactor performance are discussed.

In chapter 6, the simulation of a potential production-scale reactor is dealt with. The underlying reactor model is presented together with the discussion of the simulation

results. The discussion leads to the suggestion of suitable reactor conditions and provides the basis for pilot plant experiments which would be the next step in developing a process for the conversion of *n*-butane/*n*-butene mixtures to maleic anhydride.

A process overview is given in chapter 7. Energy balances for the process are presented and the effects of a recycle stream on the process performance are discussed.

The summary of the present work and the overall conclusions are found in chapter 8.

Chapter 2

Background

2.1 Economic Importance and Use of Maleic Anhydride

Maleic anhydride is one of the most important anhydrides that is industrially produced. Its structural formula is presented in Fig. 2.1. It is a dicarboxylic anhydride which can be used for both, polycondensation and polyaddition reactions. The most important technical end products are resins, plasticisers and lubricants. It can also be used for the copolymerisation with styrene, acrylic acid and other monomers because of the double bond [5]. Over half of the produced maleic anhydride is used for unsaturated polyester resins and it has a growth rate of about 2 – 3% per year in this sector of use. The main driving force for the overall increase in demand of maleic anhydride, however, is the production of 1,4-butanediol and tetrahydrofuran with a growth rate forecast of over 10% [6]. This process path to butanediol and tetrahydrofuran is an alternative way to the Reppe process where acetylene is used as the feedstock [7].

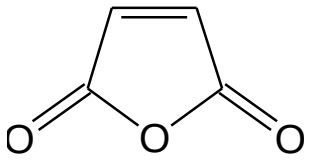

Fig. 2.1: *Structural formula of maleic anhydride. The main features are the double bond and the two carbonylic groups.*

The worldwide demand of maleic anhydride amounted to 775,000 t in 1995. A worldwide demand of 1,010,000 t with a market value of 900 million US $ was forecasted for the year 2000. The most important markets are in Western Europe, USA and Japan [8]. The price for maleic anhydride was about 1,600 DM/tonne in the year 2000 [6]. Biggest producers of maleic anhydride in the year 2000 were Sisas (225,000 t/year), Huntsman (110,000 t/year) and Ashland (63,000 t/year) [6].

2.2 Possible Raw Materials for the Production of Maleic Anhydride

There are several different ways to produce maleic anyhdride industrially. Apart from chemical conversion of suitable hydrocarbons, especially linear C_4 hydrocarbons and benzene, maleic anhydride can be obtained as a by-product of the phthalic anhydride production in quantities of about 5 – 6% in relation to the produced phtalic anhydride [9].

2.2.1 Benzene

The first industrial production of maleic anhydride was carried out by means of partial oxdiation of benzene:

$$C_6H_6 + \frac{9}{2}\,O_2 \longrightarrow C_4H_2O_3 + 2\,CO_2 + 2\,H_2O. \tag{2.1}$$

The disadvantage of this reaction is the difference in number of carbon atoms between benzene and maleic anhydride. Therefore, two of the carbon atoms of benzene have to be removed by formation of carbon dioxide. In 1962, Denka began to produce maleic anhydride by converting *n*-butenes and 1974 Monsanto began production by converting *n*-butane [3]. Since then, the amount of production plants with *n*-butane as a feedstock has increased steadily. In 1993, an amount of 38% of maleic anhydride was produced by oxidation of benzene [10].

2.2.2 *n*-Butane

The production of maleic anhydride by means of partial oxidation of a linear C_4 hydrocarbon can be generally expressed by the reaction equation

$$C_4H_y + \left(1 + \frac{y}{4}\right)\,O_2 \longrightarrow C_4H_2O_3 + \left(\frac{y}{2} - 1\right)\,H_2O, \tag{2.2}$$

where the amount of hydrogen in the hydrocarbon y equals 10 for *n*-butane and 8 for *n*-butene. A fraction of the oxygen atoms is incorporated in the hydrocarbon molecule. All but two of the hydrogen atoms in the hydrocarbon have to be removed. This is achieved by means of oxidative dehydrogenation resulting in the formation of water. Most of the provided oxygen atoms are used for this purpose.

Nowadays, the partial oxidation of *n*-butane is the predominant method for the production of maleic anhydride. *n*-Butane is present in some types of natural gas and in crude oil and can be recovered by distillation. It is also produced by a number of refinery cracking and reforming processes [11, 12].

Maleic anhydride, however, is needed and produced on sites of the chemical industry which are not necessarily in the vicinity of the sources of *n*-butane, such as refineries or natural gas processing plants. In those cases, the transport costs of *n*-butane can be a reason for turning to other feedstocks which are present at the chemical plants site [2]. Possible feedstocks could be the various components of C_4 streams obtained by steamcracking.

2.2.3 Typical C_4 Streams of Naphtha-Steamcrackers and their Uses

If liquid steamcracker feedstocks are used (e. g. naphtha), approximately 10% w/w of the liquid feedstock leaves the cracker as a C_4 stream. Since the demands and production capacities of both, ethylene and propylene increase steadily, more and more C_4 hydrocarbons are formed as by-products. There are two ways to add value to those C_4 streams:

- Recovery of some or all of the components which are contained in the stream for further uses.
- Recycling of the C_4 stream or part of it and co-cracking with the liquid feedstock to decrease the required amount of fresh feed.

The decision for one of the two possibilities depends strongly on local prices [4]. In industrial countries the recovery and usage of individual components of this stream is the predominant way. A typical example for the use of C_4-streams is given in Fig. 2.2. The

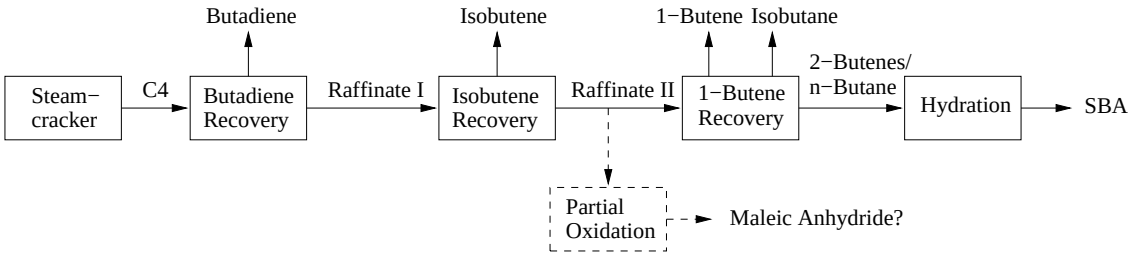

Fig. 2.2: *Typical use of a C_4 stream of a steamcracker [4].*

components of these streams are not economically separable by means of distillation, because of the close boiling points. Therefore some other physical or reactive separation methods have to be used. Over 40% w/w of the raw C_4 stream consists of butadiene which is typically isolated by extractive distillation. The remaining stream is called raffinate I and consists mainly of isobutene (≈50% w/w). Isobutene removal is carried out by means of selective reaction of the isobutene to methyl-tertiary-butyl-ether (MTBE) or other appropriate products which can be separated easily from the stream, and, if desired, converted back to isobutene. The remaining components are inert at those reaction conditions and leave the reactor as a mixture called raffinate II. Tab. 2.1 shows the composition of a typical raffinate II stream [3, 9, 13] and the boiling points of the individual species [14]. A further valorisation of raffinate II is typically achieved by the recovery of 1-butene. Because of the boiling points, the recovery has to be carried out in a two-stage super-fractionation unit. In the first stage, the isobutane content is removed. The subsequent main fractionation results in pure 1-butene and a mixture of 2-butenes and *n*-butane. A prerequisite of the super-fractionation method is the total absence of butadiene and isobutene. A preceding hydrogenation unit is necessary if the upstream butadiene and isobutene recovery sections are not fully efficient. The mixture of 2-butenes and *n*-butane can further be processed for the production of 2-butanol (SBA) by hydration [4]. Another possibility for the use of the 2-butene/*n*-butane mixture is the di- or trimerisation of the 2-butenes and the subsequent hydroformylation which leads to

plasticiser alcohols [13]. A special plasticiser alcohol is 2-propyl heptanol which can also be produced from raffinate II by means of a new process developed by UCC [15]. It is clear that the one-stage partial oxidation to maleic anhydride could be an alternative way for the valorisation of the raffinate II stream since this process does not require the complex recovery and further conversions of the individual components.

	isobutane	*n*-butane	1-butene	*cis*-2-butene	*trans*-2-butene	isobutene
% n/n	8	16	28	32	15	1
bpt (°C)	-11.7	-0.5	-6.5	3.73	0.96	6.6

Tab. 2.1: *Composition of a typical raffinate II mixture [3, 9, 13] and atmospheric boiling points of the individual species (from [14])*

The composition of the C_4 mixtures that are suitable for the conversion to maleic anhydride may change in the future. Forecasts show a decline of butadiene and an upcome of *n*-butenes. Therefore, the selective hydrogenation of butadiene to *n*-butenes may become an economic alternative [4]. The composition of the resulting streams of butenes and butanes would then be different to the present raffinate II streams. Higher relative amounts of *n*-butenes would be present. If 1-butene gained more importance as a pure component, raffinate II would clearly be fractionated to boost the 1-butene output. Another chance of production of maleic anhydride would then be the conversion of the remaining *n*-butane/2-butene mixture. This mixture has a higher fraction of *n*-butane than typical raffinate II mixtures. The investigations in this thesis focus on the conversion of raffinate II, but the results can also be used to show plant performance for the conversion of those alternative streams.

Typical prices of various raw materials concerning C_4 streams in the year 1997 (and price of maleic anhydride in the year 2000) are given in Tab. 2.2. The listed prices help to understand the economic driving forces behind the valorisation of the C_4 streams. Raffinate II has a lower value than naphtha and the C_4 stream directly leaving the steamcracker. This emphasises the problem concerning the valorisation of raffinate II.

	DM/t
naphtha	314
hydrogen	513
mixed C_4's	325
raffinate II	260
1-butene	975
steam	15
maleic anhydride	1600

Tab. 2.2: *Typical prices for raw materials in the year 1997 from [4] and price for maleic anhydride in the year 2000 from [6].*

2.3 Process Options for the Production of Maleic Anhydride

Many aspects have to be considered to develop a suitable process to convert a specific C_4 hydrocarbon feedstock to maleic anhydride. These aspects are the choice of catalyst, the process stages, the reactor type, the methods for recovery and purification, and the choice between recycling or disposal of unreacted hydrocarbons.

In [1], nine different industrial processes are listed for the oxidation of *n*-butane which differ in type of reactor, type of recovery of maleic anhydride and type of purification of the product. There are three different types of reactors which are used for the production of maleic anhydride: multi-tubular fixed-bed, fluidised-bed and transport-bed reactors. Four of the listed processes use a fixed-bed reactor (Lonza, Amoco, Denka – Scientific Design and Monsanto), four use a fluidised-bed reactor (ALMA, BP – UCB, Mitsubishi Kasei, Mitsui Toatsu) and the Du Pont process uses a transport-bed reactor. The main difference between the individual recovery sections is the choice of an aqueous or an organic solvent. The purification – if necessary – is carried out by means of batch distillation or continuous distillation. Unreacted *n*-butane is mostly burnt to carbon oxides. Only the Du Pont process uses recycling of part of the *n*-butane, because of the high *n*-butane concentrations in the product stream. The molar yields of the processes are in the range of 50 to 60%.

According to [3] some C_4 streams of steamcrackers after removal of butadiene are used as a feedstock for the production of maleic anhydride. Selectivities are reported to be 45 – 60%. Mitsubishi Chemical uses a fluidised-bed reactor for the production of maleic anhydride from such a C_4 stream. The plant has been extended to 21,000 tons per year in 1996. No references to detailed descriptions of these processes have been found. However, a detailed description of the Bayer process for the conversion of raffinate II is given in [9]. This process came into operation in 1969. The total capacity of maleic anhydride was 10,000 tons per year for captive use. The composition of their raffinate II feed is nearly identical to the composition that is assumed in the present work. Only the *n*-butenes were converted significantly in this process at a pressure of 2 bar. The hydrocarbon amount in the feed had a value slightly below the explosion limit. The reactor had 21,000 vertical tubes which were cooled by a mixture of molten sodium nitrite and potassium nitrate at 400 – 440 °C. The heat was removed by generation of high pressure steam. Organic by-products were acrylic and acetic acid as well as formaldehyde. The yield of maleic anhydride amounted to 60 – 62% w/w which corresponds to a molar yield of about 34%, which is much lower than the yields of the present *n*-butane processes. The lifetime of the catalyst was expected to be 4 – 5 years.

2.3.1 Choice of Catalyst

Vanadium-phosphorous oxide (VPO) catalysts are mainly used for the conversion of *n*-butane or *n*-butenes to maleic anhydride. Both, bulk catalysts and shell type catalysts are used in the individual processes. Typically, the conversion of hydrocarbons using a VPO catalyst is carried out at temperatures between 350 and 450 °C and pressures between 2 and 3 bar, irrespective of the use of *n*-butane, *n*-butenes or mixtures thereof. Because of the successful use of VPO catalysts in the oxidation of *n*-butane and *n*-butenes, the

focus of the present work was not the development of a new catalyst for the oxidation of raffinate II but the use of a modern industrial VPO catalyst to investigate and optimise reactor performance.

Pure 1,3-butadiene can be oxidised to maleic anhydride with a yield of 60% by use of a catalyst based on MoO_3 [16]. This catalyst type is not yet used in production plants but shows the feasibility of a two-stage process for the conversion of raffinate II.

2.3.2 Two-Stage Processes for the Conversion of Unsaturated C_4 Hydrocarbons

Industrial processes are preferably carried out in one stage since the investment and operation costs are lower compared to plants with multiple stages. Nevertheless, in patent literature also processes with two reaction stages are proposed.

A two–stage reactor to produce maleic anhydride from *n*-butene containing mixtures, especially raffinate II, is suggested in [2]. The yield of maleic anhydride from pure *n*-butenes was experimentally determined to be 62%. In the first stage the oxydehydrogenation of *n*-butenes to 1,3-butadiene is carried out by a Mo-Co-Fe-O-catalyst. 1,3-Butadiene is then oxidised to maleic anhydride in the second stage by a Sb-Mo-O-catalyst. Both stages are integrated into a single multi-tubular reactor with separate cooling systems for the two stages. In a typical raffinate II mixture, the fraction of *n*-butenes is 75% n/n. If the yield of maleic anhydride is related to both, *n*-butenes and *n*-butane in the feed and if *n*-butane is considered as inert, the yield amounts to 47%. A disadvantage of this process is the inflexibility to change operation conditions since both catalyst types are present in a single reactor equipped with two cooling zones. The amount of catalysts and the position of the boundary between both stages can only be altered by replacing the reactor.

Another option to produce maleic anhydride in a two–stage system is the hydrogenation of the unsaturated C_4 hydrocarbons to *n*-butane prior to the oxidation reactor. The hydrogenation could be carried out in a simple one-stage hydrogenation unit with selectivities above 98% [4]. The subsequent oxidation of *n*-butane results in higher yields of maleic anhydride than those of the oxidation of the *n*-butenes. However, the clear disadvantage of this process is the additional reactor stage and the continuous supply with hydrogen.

2.3.3 Choice of Reactor

The different industrial processes for the production of maleic anhydride differ in the type of reactor that is used for the oxidation. These reactor types are described briefly in this section and their properties are compared concerning different aspects like investment costs, overall yields of maleic anhydride and throughput. Three reactor types are used: multi-tubular fixed-bed, fluidised-bed and transport-bed reactors.

Multi-tubular Fixed-Bed Reactors

Like other highly exothermic oxidation reactions, the partial oxidation of hydrocarbons to maleic anhydride cannot be carried out in a simple fixed bed of catalyst pellets. The catalyst bed has to be cooled efficiently to prevent high temperatures which are detrimental to reactor performance or even can destroy the catalyst. Therefore, multi-tubular reactors

have to be used. Such reactors consist of some 30,000 individual tubes which are filled with the catalyst pellets. These tubes typically measure 3.5 to 6 metres in length and have inner diameters of about 20 to 35 mm. The tubes are cooled by a molten salt flowing through the shell side. The flow of the molten salt is directed perpendicular to the tubes by baffles for optimum heat transfer from the tube insides to the salt. The heat is removed from the circulating salt bath by generation of high pressure steam. The hydrocarbons usually enter the reactor from the top and are intensively mixed with a separate air stream by static mixers. The resulting mixture then enters the reactor tubes. Due to the separate feeding of hydrocarbons and oxygen, long residence times with conditions above the explosion limit are avoided. The products leave the reactor at the bottom. Because of this direction of flow, no fluidisation can occur and the catalyst pellets remain in their positions. The fixed-bed process is well known and can be scaled-up very easily. Typically, the reactions are carried out at temperatures between 350 and 450 °C and at slightly elevated pressures of 2 – 3 bar. Fractions of *n*-butane in the feed are 1 to 2.5% n/n.

Fluidised-Bed Reactors

In a fluidised-bed reactor, catalyst powder is used which is kept in suspension by the gas flowing from bottom to top with velocities high enough for fluidisation. Heat removal is achieved by cooling coils which are located inside the fluidised bed. Fluidised-bed reactors are used by BP, Mitsubishi, Mitsui Kasei and are also licensed by ABB Lummus/Lonza under the brand name ALMA [17]. The reaction is carried out at temperatures below 450 °C, the pressure ranges between 2 and 4 bar. The *n*-butane fractions in the feed are about 4 – 5% n/n. The hydrocarbon fractions in the feed are clearly higher than those used for fixed-bed reactors. Conversion levels above 80% are achieved. Molar yields of maleic anhydride range between 50% and 55%.

Transport-Bed Reactors

The VPO catalyst has the interesting feature that it uses lattice oxygen atoms for the selective oxidation of *n*-butane to maleic anhydride. Therefore, no gas phase oxygen is necessary for the desired reaction, provided the catalyst is in an oxidation state capable of transferring oxygen atoms to the hydrocarbon. With an oxygen free gas phase, the selectivity of maleic anhydride can be increased by values of about 7 to 10% compared to the conventional use of a hydrocarbon in air gas phase [18]. To make use of this feature, the hydrocarbon has to be brought into contact with an oxidised catalyst. The catalyst is then reduced during the formation of maleic anhydride and has to be reoxidised afterwards. Therefore, Du Pont has built a production plant comprising a transport-bed reactor for the *n*-butane oxidation and a fluidised-bed regenerator for the reoxidation of the VPO-catalyst. A transport-bed reactor can be regarded as a tube in which both, the gas phase and the catalyst enter and leave the reaction zone in co-current flow. The catalyst is circulated between the two reactors. Hydrocarbon fractions in the feed of up to 50% n/n of *n*-butane can be used.

Investment Costs and Scale-Up

The investment costs of tubular fixed-bed reactors are higher than those of fluidised-bed reactors, since the construction details of a fixed-bed reactor are more complicated. It is stated in [18] that the transport-bed reactor has the lowest investment costs.

The scale-up of fixed-bed reactors is easy and straightforward. The reactor concepts with moving catalyst fines are more difficult to scale up.

Ease of Operation

The fixed-bed reactor is the reactor type which is most easily operated, provided that it is operated away from temperature instabilities. In fluidised-bed and transport-bed reactors, the solids handling requires a careful and more difficult operation. The transport-bed reactor concept is clearly the most complicated system to handle, because of the coupled operation of the two reactors and the controlled transport of the circulating catalyst. Approximately 0.5 tonnes of catalyst fines have to be transported in one second between the transport-bed reactor and the regenerator.

Clear disadvantages of the fixed-bed reactor are the discharge and filling with the catalyst. The catalyst bodies have to be changed approximately every five years by opening the reactor by disassembling the top bonnet. The tubes have to be filled carefully to obtain the same pressure drop along all individual tubes, and to avoid bypasses which are detrimental to overall reactor performance. In fluidised-bed and transport-bed reactors, on the other hand, fresh catalyst can be added and spent catalyst can be removed continuously.

Heat Removal

Because of the high gas velocities and the ideal mixing of the catalyst fines in the fluidised systems, the heat transfer out of the reactor typically presents no problem in fluidised-bed and transport-bed reactors. In contrary to those reactor types, the heat removal in the fixed-bed reactor is more difficult. The heat transfer from the catalyst bed to the molten salt on the shell side is not sufficient to guarantee isothermal operation. There is a zone of higher temperatures in the vicinity of the gas inlet in every individual tube. The higher temperatures decrease the selectivity of maleic anhydride in case of the oxidation of pure n-butane.

Throughput

The reaction heat which has to be removed from the reactor depends strongly on the throughput. Because of the inefficient heat removal in a fixed-bed reactor, the temperature in the hot spot is increasing with increasing throughput. The temperature is limited to a value of about 450 °C to avoid damage to the catalyst. As a result, the inefficient heat removal in a fixed-bed reactor can be a limiting factor concerning throughput. Therefore, the fluidised-bed reactor and the transport-bed reactor have a clear advantage if higher production capacities are desired. The fractions of n-butane in the feed are approximately 2, 4 and 10% n/n for fixed-bed, fluidised-bed and transport-bed reactors, respectively. As a result, costs of air compression are highest for the fixed-bed reactor assuming identical

hydrocarbon throughputs. Additionally, the recovery section is less efficient and more costly for lower product concentrations as experienced in the fixed-bed reactor.

Aspects Concerning the Catalyst

For the Du Pont process the highest selectivities are claimed because of the absence of gas phase oxygen during the conversion of *n*-butane to maleic anhydride. The selectivity in a fixed-bed reactor is slightly higher than in a fluidised-bed system, because of the back-mixing effects in the fluidised bed and possible bypass flows resulting from the formation of gas bubbles.

In the Du Pont process, the transport-bed reactor and the regenerator are separate vessels. It is therefore possible to operate both reactors at different reaction conditions. Another advantage of the Du Pont process is the individual optimisation of both reaction steps, reduction and reoxidation. But, on the other hand, the variation of the residence times of the catalyst in the reactors is limited by construction details and *n*-butane throughput. The operation range of a transport-bed reactor – regenerator system might therefore be more limited compared to the other concepts. Additionally, there is the danger of irreversibly over-reducing the catalyst fines in the transport-bed reactor. The residence times of the catalyst fines have to be limited to avoid over-reduction [19].

In a fixed-bed reactor, catalyst bodies are used which have characteristic dimensions of above 2 mm which is one order of magnitude larger than the catalyst fines (50 – 200 μm) that are used in the fluidised systems. Therefore, the influence of pore diffusion resistances on catalyst performance may be higher in the fixed-bed process. Indeed, as it is shown in chapter 5, the selectivity and activity is decreased by transport resistances in the oxidation of *n*-butane.

Since the catalyst bodies in the fixed-bed reactor have a fixed position, a big advantage of this reactor type could be the application of different types of catalysts or different catalyst dilutions in well defined reactor zones. This feature is especially interesting if mixtures of *n*-butenes and *n*-butane have to be converted. The use of two different types of catalysts could possibly optimise the different reactions of the individual hydrocarbons.

In the fluidised-bed and the transport-bed reactors, attrition resistant catalysts have to be used. The catalyst preparation procedures which are needed to produce the desired attrition resistance may be detrimental to the catalyst performance. The abrasion of reactor walls has also to be taken into consideration.

2.3.4 Recovery and Purification of Maleic Anhydride

The different possibilities of recovery and purification of maleic anhydride are described in [5]. In an aqueous recovery method, a small amount of maleic anhydride is obtained directly by cooling of the product stream and partial condensation of part of the maleic anhydride. The larger amount is washed out with water as maleic acid in a subsequent absorption unit. Subsequently, the maleic acid has to be dehydrated with a high energy input. Because of the elevated temperatures which are needed for the dehydration, maleic acid isomeration to fumaric acid can occur which reduces the yield of maleic anhydride. This type of recovery is explained in detail in [9]. To overcome the disadvantages of high energy input and formation of fumaric acid, recovery methods using organic solvents have been developed. Typical solvents are tritolyl phosphate, dibutyl maleate, and dibutyl

phtalate [20]. No maleic acid is formed in such an absorption process and more than 98% of the maleic anhydride can be absorbed. Maleic anhydride is then obtained by fractional distillation and the organic solvent is purified and recycled. During operation of a raffinate II to maleic anhydride production plant at Bayer, formation of resinous products were experienced that tended to deposit on the column internals [9]. The resinuous products were presumably formed by unsaturated hydrocarbons, especially butenes and butadiene. Therefore, one aspect which has to be considered in the present work is the necessity of entirely converting the *n*-butenes and butadiene in the oxidation reactor.

Purification of the raw maleic anhydride is done either by batch distillation for smaller or by continuous distillation for higher production capacities.

2.3.5 Recycling of Unreacted Hydrocarbons

In the case of high concentrations of unreacted hydrocarbons in the product stream, a recycling of these hydrocarbons could be an economic option. For example, the Du Pont process recycles part of the off-gas of the recovery section to the transport-bed reactor. It is impossible to recycle the whole gas stream, since inert components like nitrogen would accumulate in the gas cycle. Therefore, the remaining part of the off-gas is purged. In processes where the fixed-bed reactor technology is used, typically no hydrocarbons are recycled. The remaining *n*-butane in the purge gas is burnt and the reaction heat of this total oxidation is used for steam generation.

2.4 The VPO Catalyst

The partial oxidation of *n*-butane and *n*-butenes to maleic anhydride is typically carried out by using a vanadium-phosphorous oxide catalyst. The most active and selective catalysts consist predominantly of vanadyl pyrophosphate $(VO)_2P_2O_7$ [21]. There are numerous reviews and articles dealing with the VPO catalyst system. A good review of preparation, characterisation and use of VPO catalysts is given by Hodnett in [21]. Often cited but somewhat older is an article by Centi and Trifirò [22].

2.4.1 Preparation of the Catalyst

In the present work, an industrial catalyst was used for the determination of reaction kinetics and reactor performance. No preparation of VPO catalysts was carried out in the present work. Therefore, only a brief description of the preparation of a typical VPO catalyst is given. According to [19, 21], the catalyst is prepared in an organic medium mostly consisting of two alcohols, e. g. isobutanol and benzyl alcohol. Benzyl alcohol is added to reduce V_2O_5 to a partially soluble V^{4+} complex or suspension. The reduction is accompanied by the oxidation of benzyl alcohol to benzaldehyde. Phosphoric acid and desired promoters (e. g. zirconium) are added. The precursor $(VO)_2H_4P_2O_9$ (also written as $VOHPO_4{\cdot}0.5H_2O$ and referred to as hemihydrate) is formed. The solids are obtained by filtration and are washed and dried. During the subsequent calcination process, the hemihydrate is converted to the active component vanadyl pyrophosphate $(VO)_2P_2O_7$. The catalyst is activated and equilibrated in an *n*-butane/air mixture.

2.4.2 Mechanistic Aspects of the Oxidation Reactions

Despite the vast research efforts carried out since 1970, the reaction mechanisms is not yet fully understood. It is clear, however, that the oxidation of the C_4 hydrocarbons to maleic anhydride is carried out by transfer of catalyst lattice oxygen species to the hydrocarbon. The lattice is then replenished by oxygen uptake from the gas phase. Earlier works postulated the presence of cyclic precursors of maleic anhydride such as furan [21, 22]. Recent studies propose a non-cyclic mechanism called the alkoxide route which is described in [23] and presented in Fig. 2.3. Both mechanistic models assume the activation and oxidative dehydrogenation of *n*-butane to *n*-butenes as the first and rate determining step. In the former cyclic route, the subsequent oxidative dehydrogenation to butadiene is proposed whereas the alkoxide route suggests the transfer of lattice oxygen to the butenes by formation of butanone or butanal. The precursors assumed in the cyclic route (butadiene, dihydrofuran and furan) are found in a side route in the newer model and are assumed to be unstable on the catalyst surface. Therefore, they desorb more readily and are detected in the gas phase during *n*-butene oxidation, whereas the alkoxic species remain on the surface and can only be detected by FTIR or similar techniques. Besides desorption, the cyclic species also can be reverted back to the corresponding alkoxide species by ring cleavage. The total oxidation of maleic anhydride involves the formation of carboxylic surface species.

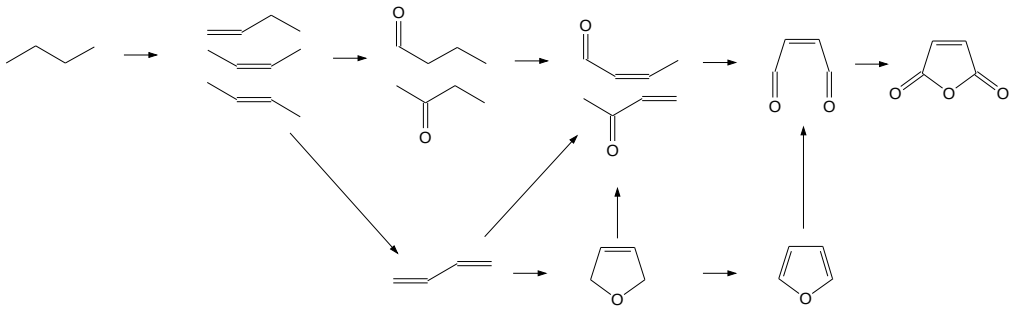

Fig. 2.3: *The mechanism of the partial oxidation of C_4 hydrocarbons on a VPO catalyst as proposed by Xue and Schrader [23].*

The proposed mechanism presumes that both, *n*-butane and *n*-butenes are converted to maleic anhydride via identical reaction routes. The only difference between both molecules is the additional step of the oxidative dehydrogenation of *n*-butane to *n*-butenes. Nevertheless, the analysis of the gas phase during reaction of the individual hydrocarbons shows great differences between the two hydrocarbon types. The conversion rate of *n*-butane is much smaller than the conversion rate of *n*-butenes. The rate constant of the *n*-butane conversion is a tenth of the rate constant of the conversion of *n*-butenes. This difference in reaction rates matches the presumption of the activation of *n*-butane as the rate determining step. The presence of gas phase intermediates such as butadiene and furan during the conversion of *n*-butenes is interesting since these intermediates are absent in case of the *n*-butane conversion. It is proposed that only small amounts of the intermediates like butadiene and furan are present on the surface during the *n*-butane conversion since the rate constant of the *n*-butane activation is much smaller than the rate constants of the consecutive reactions. Therefore, none of the intermediates are detected

in the gas phase during the *n*-butane oxidation. During the reaction of *n*-butenes, however, the correspondent rate constants are similar in their values and the concentrations of the adsorbed intermediates are higher, resulting in higher desorption probabilities and gas phase concentrations [22]. Experiments with selective poisoning of the catalyst showed that *n*-butenes adsorb more readily on non-selective sites. This leads to lower selectivities compared to the *n*-butane conversion.

2.4.3 Oxidation States of the Catalyst

The oxidation state of the vanadium atoms of the catalyst varies between +3 and +5, depending on the actual gas phase composition. About 95% of the vanadium in the catalyst is in the +4 oxidation state, but some +5 species are necessary to achieve high selectivities to maleic anhydride [21].

Poisoning experiments showed that different sites are responsible for selective and total oxidation of both, *n*-butane and maleic anhydride [24]. It is assumed that the selective oxidation takes place on the V^{+5} sites whereas the carbon oxides are produced on V^{+4} sites. Nevertheless, the V^{+4} sites are also responsible for *n*-butane activation and therefore are necessary for the partial oxidation.

Recent works showed that carbon dioxide is able to oxidise the catalyst surface. This leads to higher selectivity and lower activity. In [25] experiments are reported that were carried out in a membrane reactor with fractions of carbon dioxide of up to 45% n/n in the feed. A decrease in the conversion level of about 0.03 and an increase in selectivity of 0.05 compared to a carbon dioxide free feed were experienced.

The *n*-butenes have higher reducing potentials than *n*-butane. Therefore, *n*-butenes require a lower oxidation state of the catalyst surface for selective oxidation. Different reaction conditions and different ratios of hydrocarbon and oxygen concentrations are necessary for optimum performance. Additionally, it should be possible to improve the catalyst performance for *n*-butene conversion by considering the different nature of *n*-butenes [22].

2.4.4 A Macroscopic Point of View of the Catalytic Behaviour

Most of the species which are proposed to be present on the surface during the oxidation of *n*-butane and *n*-butenes cannot be detected in the gas phase. The development of a quantitative description of reaction kinetics that is based on the mechanism and that considers all intermediates on the surface is difficult, time-consuming and costly because of the experimental equipment that is needed to investigate the catalyst surface in-situ. A much more appropriate approach is to consider only the important reactions and species which are detectable in the gas phase.

The only carbon containing species in the oxidation of *n*-butane that are detected in the gas phase and that are significant for reaction kinetics are *n*-butane, maleic anhydride and carbon oxides. As in all partial oxidation reactions, the formation of carbon oxides is thermodynamically favoured over the formation of the desired product maleic anhydride. The parallel reaction of *n*-butane directly into carbon oxides and the consecutive reaction of maleic anhydride to carbon oxides are therefore considered in addition to the desired reaction. The description of the reaction kinetics is thus based on the widely used tri-

angular reaction network that is shown in Fig. 2.4. The network is shown in a distorted version of a triangle since it will be extended later in the thesis.

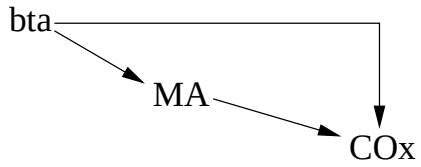

Fig. 2.4: *Reaction network for the oxidation of n-butane. The abbreviations bta, MA and COx refer to n-butane, maleic anhydride and carbon oxides, respectively.*

It is widely accepted that adding water to the feed causes a drop in the conversion rates while higher selectivities to maleic anhydride are achieved. But more significantly, the selectivities of the acid by-products, acetic and acrylic acid, are increased. The selectivities to those by-products are almost doubled at 10% n/n of water in the feed [17]. The yields of those by-products are typically below 2% and can be neglected for reactor design purposes. High amounts of these acids in the product stream, however, are detrimental for the efficiency of the recovery and purification units.

2.4.5 Reaction Kinetics of the Oxidation of *n*-Butane

In the present work, a kinetic model shall be developed which is able to quantify

- the conversion rates of our feed components n-butane and n-butenes,
- the formation rate of our desired product maleic anhydride, as well as
- the heat release rate

as a function of the gas phase composition as well as the temperature in the technically relevant range. The correlations between the rates and the composition/temperature are expressed by means of mathematical expressions with, ideally, a minimum of correlation parameters. Typically, rate equations are either chosen to be simple linear or power law equations, or they are postulated by assuming certain mechanistic aspects. This does not mean that the postulated mechanism indeed has a physical meaning. Mechanistic assumptions are a good base for finding new types of rate equations to be considered. A reaction kinetic model that is able to describe experimental observations cannot be seen as a proof of mechanistic models but shows that it can be used to quantify the key rates that were to be modelled. Physical interpretation of the rate equations is impossible.

This section shall give the reader a summary about what type of rate equations were used for the modelling of oxidation of n-butane.

The reaction rates $r_{i,j}$ for the reaction of species i to species j which are used throughout this thesis are defined in section 3.1.1. For the discussion of the individual approaches of the reaction rates in the subsequent literature survey, it should be sufficient to describe the general properties of the rate equations without the need to quantify the rates exactly.

Pseudo First Order Reaction Rates

The pseudo first order models assume rate equations of the type

$$r_{i,j} = k_{i,j} p_i, \tag{2.3}$$

where the reaction rate $r_{i,j}$ depends, apart from temperature, on the partial pressure p_i of the hydrocarbon species i which is converted. Since the amount of oxygen in the gas stream is high and only a small fraction of it is converted in the reactor, the exact oxygen dependence is assumed to be negligible resulting in a rate equation with an apparently constant parameter $k_{i,j}$. Quast used this type of approach on the partial oxidation of pure *n*-butane, *n*-butenes and 1,3-butadiene. The results are reported in [16]. The partial oxidation of *n*-butane by using the present catalyst was also studied and modelled with the assumption of first order reactions in [26]. Both investigations showed that this type of approach is sufficient to describe concentration profiles in an isothermal fixed-bed reactor for a fixed temperature and feed concentration only. This means that the parameter $k_{i,j}$ depends on the operation conditions of the reactor. For simulation of real reactors, this approach is not suitable.

Power Law Rate Equations

In general, power law rate equations can be written as

$$r_{i,j} = k_{i,j} \prod_{k}^{N_{\text{species}}} p_k^{n_{i,j,k}}. \tag{2.4}$$

They cover the special case of first order rate equations. For the partial oxidation of *n*-butane, Lerou and Mills tested the power law approach

$$r_{i,j} = k_{i,j} p_i^n p_{\text{O2}}^m, \tag{2.5}$$

but favoured other models described in the following with better agreement of experimental and calculated data [18].

Models based on Hyperbolic and Power Law Rate Equations

Sharma et al. use rate equations that were based on two different types of reaction mechanisms. The resulting rate equations are

$$r_{\text{bta,MA}} = \frac{k_{\text{bta,MA}} p_{\text{bta}}^{\alpha_{\text{bta,MA}}}}{1 + b_{\text{MA}} p_{\text{MA}}}, \tag{2.6}$$

$$r_{\text{MA,COx}} = \frac{k_{\text{MA,COx}} p_{\text{MA}}}{(1 + b_{\text{MA}} p_{\text{MA}})^2}, \tag{2.7}$$

$$r_{\text{bta,COx}} = k_{\text{bta,COx}} p_{\text{bta}}^{\alpha_{\text{bta,COx}}}. \tag{2.8}$$

The power of the *n*-butane partial pressure was determined to be $\alpha_{i,j} = 0.66$ [27]. Wellauer used an older version of the model of Sharma et al. [28]:

$$r_{\text{bta,MA}} = \frac{k_{\text{bta,MA}} p_{\text{bta}}^{\alpha}}{1 + b_{\text{MA}} p_{\text{MA}}}, \tag{2.9}$$

$$r_{\text{MA,COx}} = k_{\text{MA,COx}} p_{\text{MA}}, \tag{2.10}$$

$$r_{\text{bta,COx}} = \frac{k_{\text{bta,COx}} p_{\text{bta}}^{\alpha}}{1 + b_{\text{MA}} p_{\text{MA}}}, \tag{2.11}$$

for which the power of the n-butane partial pressure was determined to be $\alpha = 0.47$.

The experimental results showed that the oxygen content has no significant effect on reaction rates if oxygen fractions were above 15% and conversion levels were restricted to values below 70%. Therefore, no influences of the partial pressures of oxygen and water are considered in these models. The models suggest, however, a dependence of the reaction rates on the concentration of maleic anhydride: the reaction rates decrease with increasing amount of maleic anhydride in the gas phase. Uihlein carried out experiments where maleic anhydride was added to the feed. He showed, in contradiction to the model above, that the partial pressure of maleic anhydride has no influence on reaction rates [29]. However, Uihlein reports decreasing reaction rates by increasing the amount of water in the gas phase. Water is inevitably formed during the oxidation processes. Therefore, the formation of maleic anhydride also leads to the formation of water and the partial pressure of maleic anhydride increases by an approximately constant factor to the partial pressure of water. Presumably, the expression $b_{\mathrm{MA}}p_{\mathrm{MA}}$ should not be regarded as a dependence of the rate equation on the partial pressure of maleic anhydride, but on the partial pressure of water.

Langmuir-Hinshelwood and Eley-Rideal Approaches

The Langmuir-Hinshelwood approach is based on the assumption that the reaction of two species to a third must be preceded by adsorption of both reactants. Lerou and Mills used such an approach for the oxidation of n-butane:

$$r_{i,j} = \frac{k_{i,j}p_i\sqrt{p_{\mathrm{O2}}}}{1 + b_{\mathrm{bta}}p_{\mathrm{bta}} + b_{\mathrm{MA}}p_{\mathrm{MA}} + b_{\mathrm{H2O}}p_{\mathrm{H2O}}}. \tag{2.12}$$

They tested several other kinetic models and reported the results in [18]. A modified Sharma-model and the displayed Langmuir-Hinshelwood-model represent their experiments best. They claim that both models are equally suitable for the description of reaction kinetics.

In the Eley-Rideal approach, it is assumed that only one species has to be adsorbed on the catalyst surface for the reaction with a second species. Uihlein used the rate equations

$$r_{\mathrm{bta,MA}} = \frac{k_{\mathrm{bta,MA}}p_{\mathrm{bta}}\sqrt{p_{\mathrm{O2}}}}{1 + b_{\mathrm{bta}}p_{\mathrm{bta}} + b_{\mathrm{H2O}}p_{\mathrm{H2O}}}, \tag{2.13}$$

$$r_{\mathrm{bta,COx}} = \frac{k_{\mathrm{bta,COx}}p_{\mathrm{bta}}\sqrt{p_{\mathrm{O2}}}}{1 + b_{\mathrm{bta}}p_{\mathrm{bta}} + b_{\mathrm{H2O}}p_{\mathrm{H2O}}}, \tag{2.14}$$

$$r_{\mathrm{MA,COx}} = \frac{k_{\mathrm{MA,COx}}p_{\mathrm{MA}}\sqrt[4]{p_{\mathrm{O2}}}}{1 + b_{\mathrm{bta}}p_{\mathrm{bta}} + b_{\mathrm{H2O}}p_{\mathrm{H2O}}}, \tag{2.15}$$

$$\tag{2.16}$$

which were derived from the Eley-Rideal approach. He compared the suitability of these rate equations to that of a redox approach (see next paragraph) and found the Eley-Rideal approach more suitable. He changed the oxygen dependence of the rate equation for the oxidation of maleic anhydride to a power of 1/4, since the agreement between experimental data and calculated values was better than with a power of 1/2 that is normally expected in the Eley-Rideal approach [29]. Becker compared an Eley-Rideal approach, a redox approach and a Langmuir-Hinshelwood approach and favours the Eley-Rideal approach. He used the original power of 1/2 for the partial pressure of oxygen [8].

The Redox Mechanism

The redox mechanism, also known as Mars-/ van Krevelen-mechanism, is developed for the quantification of oxidation reactions where it is assumed that the oxidation of the hydrocarbon is accompanied by the reduction of the catalyst by transferring oxygen from the catalyst lattice to the hydrocarbon. The oxygen in the lattice is continuously replenished by molecular oxygen from the gas phase. Three adoptions of the redox mechanism for the partial oxidation of *n*-butane are presented in this section.

Bej and Rao found a simplified redox model to be the best choice to describe the conversion rate of *n*-butane:

$$R_{\mathrm{bta}} = -\frac{k_{\mathrm{bta}} p_{\mathrm{bta}}}{1 + b_{\mathrm{bta}} p_{\mathrm{bta}}}. \tag{2.17}$$

Their actual model considered an oxygen dependence, but it was simplified to equation (2.17) [30]. Varma and Saraf's version of a redox mechanism is reported in [31]. Their simplifications lead to

$$r_{i,j} = \frac{k_{i,j} p_i p_{\mathrm{O2}}}{b_i p_i + b_{\mathrm{O2}} p_{\mathrm{O2}}}. \tag{2.18}$$

Uihlein's redox approach is more complicated and results in

$$r_{i,j} = \frac{k_{i,j} p_i k_{\mathrm{ox}} \sqrt{P_{\mathrm{O2}}}}{k_{\mathrm{ox}} \sqrt{p_{\mathrm{O2}}} + [(k_{\mathrm{bta,MA}} + k_{\mathrm{bta,COx}}) p_{\mathrm{bta}} + k_{\mathrm{MA,COx}} p_{\mathrm{MA}}] \times [1 + b_{\mathrm{H2O}} p_{\mathrm{H2O}}]}. \tag{2.19}$$

Although the Mars-/ van Krevelen-mechanism seems to be the most appropriate model since it considers mechanistic aspects as well as reduction and reoxidation of the catalyst surface, the quantitative results regarding reaction rates are worse compared to other approaches [19]. Examples for the discrimination between the redox model and other models are presented in [8, 29]. The redox model was found to be less suitable than other models.

Models with Separate *n*-Butane Oxidation and Catalyst Reoxidation Equations

All models that have been presented so far are based on the assumption that the catalyst is in a steady state. Results show a better performance of the catalyst in the Du Pont process where *n*-butane reacts with an oxidised catalyst to maleic anhydride in the absence of gas phase oxygen. The reduced catalyst is reoxidised afterwards in a regeneration reactor. The development of this process led to the use of rate equations that describe the reaction kinetics of the *n*-butane oxidation as well as the oxidation and reoxidation kinetics of the catalyst. Because of the unsteady state of the catalyst in this process, the quantification of reaction rates requires models with separate rate equations for oxidation and reduction of the catalyst.

In the present work, the experimental investigations were carried out with the catalyst in steady state. The catalyst is also assumed to be in a steady state in the potential industrial fixed-bed process that is investigated in the present work. Therefore, the models with separate equations for the oxidation and reoxidation of the catalyst are not discussed here. An overview of the models and their uses is given in [19].

Chapter 3

Experimental Methods and Data Analysis

The present work aims at the description of the reactor performance in the partial oxidation of mixtures of *n*-butane and *n*-butenes to maleic anhydride at technically relevant operational conditions. The most important step for the quantification of the reactor behaviour is the determination of the reaction kinetics. Since the exotherm of the oxidation reactions is high and leads to a non-isothermal behaviour of a production-scale fixed-bed reactor, thermodynamic aspects have to be considered. This chapter describes the experimental reactor and the methods of data analysis to determine the reaction kinetics and energetics.

3.1 Properties Concerning Reactions and Ideal Fixed-Bed Reactors

3.1.1 Conventions Regarding Reaction Stoichiometry and Rates

There are different conventions regarding stoichiometry of reactions and the definition of reaction rates. It has been chosen for the present work to use reaction equations of the pattern

$$\nu_{\mathrm{R},j}\,\mathrm{HC} + \nu_{\mathrm{O2},j}\,\mathrm{O_2} \longrightarrow \nu_{\mathrm{P},j}\,\mathrm{P} + \nu_{\mathrm{H2O},j}\,\mathrm{H_2O} \tag{3.1}$$

with stoichiometric coefficients $\nu_{i,j}$ of species i in reaction j which are negative in the case of the reactants HC and oxygen and positive in case of the products P and water. By defining the extent of reaction j (ζ_j) as a measure of the progress of the reaction, the molar changes of all single species i by reaction j ($\mathrm{d}n_{i,j}$) are related to each other by

$$\mathrm{d}n_i = \nu_{i,j}\mathrm{d}\zeta_j. \tag{3.2}$$

The overall molar change of species i ($\mathrm{d}n_i$) amounts to

$$\mathrm{d}n_i = \sum_{j}^{N_{\mathrm{rcts}}} \nu_{i,j}\mathrm{d}\zeta_j. \tag{3.3}$$

The reaction rate r_j of a reaction j is defined as

$$r_j = \frac{1}{m_{\text{active}}} \times \frac{\mathrm{d}\zeta_j}{\mathrm{d}t}, \tag{3.4}$$

relating the change of extent of the reaction with time to the amount of catalytically active mass. The formation rate of a certain species results in

$$R_i = \sum_{j}^{N_{\text{rcts}}} \nu_{i,j} r_j. \tag{3.5}$$

Rates denoted by a small r_j are related to a certain reaction j and rates denoted by a capital R_i are related to a certain species i.

To explain the different approaches for the rate equations, the simple numbering of the reactions $j = 1, 2, \ldots, N_{\text{rcts}}$ was replaced by a more appropriate numbering with two indices. A reaction rate denoted as $r_{i,j}$ refers to the reaction of hydrocarbon i to hydrocarbon j.

3.1.2 The Ideal Fixed-Bed Reactor

In the present work, a fixed-bed laboratory reactor was used. It was assumed to behave ideally because of its construction design and its operation conditions. An ideal behaviour of a fixed-bed reactor means that non-isothermal effects, radial concentration and temperature gradients, axial mass and energy dispersion and deviation of local gas velocities from the mean velocity can be neglected. Because of the isothermal operation, no energy balance has to be taken into consideration and it is sufficient to consider the species balances. For an ideal fixed-bed reactor, the balance for species i can be written as

$$\frac{\mathrm{d}\dot{n}_i}{\mathrm{d}z} = \rho^{\text{active}} S R_i. \tag{3.6}$$

This represents the change of the molar flow of this species $\dot{n}_i$ along the axial position in the reactor z. This change is directly proportional to the mass density of the active material ρ^{active} at the axial position. It is defined as the mass of catalytically active material in a differential volumetric element $S\,\mathrm{d}z$. The cross sectional area of the reactor tube is denoted as S. R_i represents the formation rate of species i as defined in the previous section.

Since most of the gas phase consisted of inert nitrogen and the reactor was operated isothermally, the volumetric flow rate through the reactor remained constant. By definition of the modified residence time

$$t_{\text{mod}} = \frac{m_{\text{active}}}{\dot{V}}, \tag{3.7}$$

which relates the mass of active material from reactor inlet up to the present location to the volumetric flow rate through the reactor, the balance equations can be written as

$$\frac{\mathrm{d}c_i}{\mathrm{d}t_{\text{mod}}} = R_i. \tag{3.8}$$

By integration of the differential equations of all species with the boundary conditions that all concentrations at reactor inlet are equal to the feed concentrations $c_i(z = 0) = c_{i,0}$, the concentration profiles along the reactor are obtained:

$$\int_{c_{i,0}}^{c_i} \frac{\mathrm{d}c_i}{R_i} = t_{\mathrm{mod}}. \tag{3.9}$$

The concentration profiles depend on active catalyst mass and feed flow rate.

In the evaluation of the experiments, the amount of the individual carbon containing species in the gas phase was expressed in terms of normalised dimensionless molar fractions of species i according to

$$Y_i = \frac{\epsilon_{\mathrm{C},i}}{4} \times \frac{\dot{n}_i}{\dot{n}_{\mathrm{HC},0}}, \tag{3.10}$$

where the molar flow of species i is related to the molar flow of hydrocarbons at reactor inlet. By considering the amount of carbon atoms in each species i ($\epsilon_{\mathrm{C},i}$), the sum of all normalised dimensionless molar fractions at a certain position equals unity because of the element conservation of carbon. The values of the individual dimensionless fractions range between 0 and 1. In case of the reaction products, Y_i represents also the yield of this species, or more precisely, the amount of product that can be obtained with a certain amount of reactants in the feed. A second dimensionless molar fraction definition was used for the oxygen containing species

$$Z_i = \frac{\epsilon_{\mathrm{O},i}}{2} \times \frac{\dot{n}_i}{\dot{n}_{\mathrm{O2},0}} \tag{3.11}$$

with the same properties as Y_i, only related to oxygen. The conversion levels of n-butane, n-butenes and hydrocarbons can be expressed as

$$X_i = \frac{\dot{n}_{i,0} - \dot{n}_i}{\dot{n}_{i,0}} = 1 - \frac{Y_i}{Y_{i,0}}. \tag{3.12}$$

The dimensionless molar fraction of hydrocarbons equals the sum of the corresponding fractions of n-butane and n-butenes. 1,3-Butadiene is not regarded as a hydrocarbon reactant but as a product, since it is an intermediate which belongs to the pseudo-species IP that is introduced later. The conversion level of oxygen equals

$$X_{\mathrm{O2}} = 1 - Z_{\mathrm{O2}}. \tag{3.13}$$

Conversion levels refer to the behaviour of the reactants, or more precisely, they quantify the relative amount of a specific reactant that is converted to products.

By-products are formed during the oxidation of hydrocarbons. The product distribution can be quantified by defining a reactor selectivity of a specific species i

$${}^{\mathrm{R}}S_i = \frac{\epsilon_{\mathrm{C},i}}{4} \times \frac{\dot{n}_i}{\dot{n}_{\mathrm{HC},0} - \dot{n}_{\mathrm{HC}}} = \frac{Y_i}{X_{\mathrm{HC}}}. \tag{3.14}$$

A reactor selectivity related to oxygen is defined in the same way and results in

$${}^{\mathrm{R}}S_i^{\mathrm{O}} = \frac{Z_i}{X_{\mathrm{O2}}}. \tag{3.15}$$

The values of the reactor selectivities range between 0 and 1. The reactor selectivity of a specific product i quantifies the relative amount of the converted reactant that was used to form this product.

3.1.3 Control Volumes and their Properties

The yields, conversion levels and reactor selectivities are properties which can be calculated directly from the measured concentrations in the reactor and are therefore integral properties which are valid for a specific control volume of the reactor only. Such a control volume can contain gradients, and the integral properties depend on the reactor type that was chosen for the reaction. In order to predict the behaviour of different reactor types or at least to predict the behaviour for different operation conditions, it is necessary to determine properties which are independent of the laboratory reactor that was used to determine the properties.

To understand a system as complex as a reactor, it is necessary to divide it into control volumes and to describe the individual effects that are responsible for the behaviour of the whole system separately. Different encapsulated control volumes can be considered in a reactor system, starting with the smallest (macroscopic) volume including only a couple of active sites on the surface of the catalyst. Each volume with a larger extent includes the smaller one and additional effects are added.

Typical control volumes which are used for reactor and reaction analysis are shown in Fig. 3.1. The dashed lines represent the boundaries of the control volumes. Individual

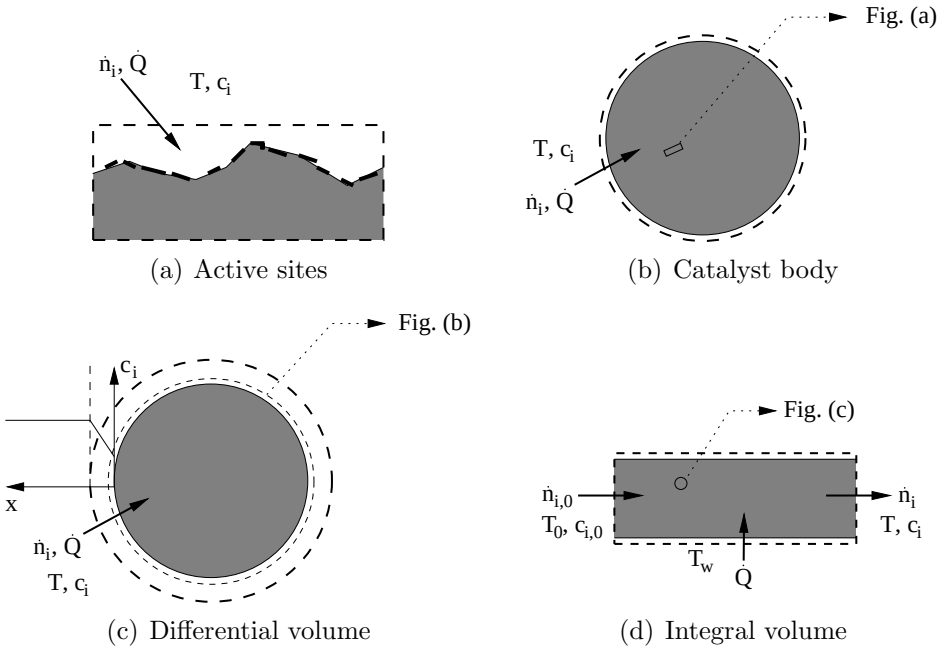

(a) Active sites (b) Catalyst body

(c) Differential volume (d) Integral volume

Fig. 3.1: *The individual control volumes which are used in reactor and reaction analysis. The dashed lines represent the boundaries of the control volumes. For better understanding, the catalyst bodies are presented as circular shapes despite being hollow cylinders in reality.*

molar fluxes and heat fluxes through the boundaries are displayed as well as the individual concentrations and temperatures directly at the boundary.

To present the properties of the individual control volumes more clearly, the partial oxidation of *n*-butane according to the reaction scheme in Fig. 2.4 is used as an example.

By assuming first order rate equations, isothermal conditions in the catalyst bodies and identical effective diffusivities of the individual species in the catalyst pores, properties can be defined which characterise the physical behaviour belonging to the individual control volumes and which are independent of reaction conditions except for the temperature. These properties have been introduced for a general triangular reaction scheme by Kotter and Riekert and are reported in [32, 33].

Intrinsic Properties

The smallest macroscopic control volume contains only a couple of active sites as displayed in Fig. 3.1(a). The properties belonging to this control volume are the intrinsic catalytical properties. These properties are, for example, reaction rates. The reaction rates ${}^{\mathrm{I}}\hat{r}_j$ and rate constants ${}^{\mathrm{I}}\hat{k}_j$ are related to the surface area of the active catalyst material. Some additional intrinsic properties can be defined which describe the behaviour for a given gas phase composition and temperature. The intrinsic selectivity ${}^{\mathrm{I}}S_i$ is defined in the same way as the reactor selectivity, except that the differences in molar flows are replaced by the intrinsic reaction rates, resulting in

$$ {}^{\mathrm{I}}S_i = \frac{\epsilon_{\mathrm{C},i}}{4} \times \frac{{}^{\mathrm{I}}\hat{R}_i}{-{}^{\mathrm{I}}\hat{R}_{\mathrm{HC}}}. \tag{3.16} $$

The formation rates are defined as

$$ {}^{\mathrm{I}}\hat{R}_i = \sum_{j}^{N_{\mathrm{rcts}}} \nu_{i,j}\, {}^{\mathrm{I}}\hat{r}_j. \tag{3.17} $$

The reaction and formation rates can also be related to the amount of active mass per volume of catalyst. The relation between the reaction rates can be expressed as

$$ {}^{\mathrm{I}}r_i = \frac{a_{\mathrm{i}}}{\rho^{\mathrm{body}}} {}^{\mathrm{I}}\hat{r}_i. \tag{3.18} $$

The relation contains the density of active material of the catalyst body and the inner surface of the body. The density of active material of the body equals the mass of active material in the body divided by the geometric volume of the body. The inner surface of the body is the catalytically active surface area in the body related to the geometric volume of the body.

For the partial oxidation of *n*-butane with first order rate equations assumed, the intrinsic selectivity of maleic anhydride equals

$$ {}^{\mathrm{I}}S_{\mathrm{MA}} = \frac{{}^{\mathrm{I}}\hat{k}_{\mathrm{bta,MA}}(T)}{{}^{\mathrm{I}}\hat{k}_{\mathrm{bta,MA}}(T) + {}^{\mathrm{I}}\hat{k}_{\mathrm{bta,COx}}(T)} \tag{3.19} $$

and depends solely on the reaction temperature. The intrinsic selectivity describes the behaviour of the parallel reactions of *n*-butane, since it quantifies the fraction of the momentarily converted *n*-butane that is used to form maleic anhydride.

An intrinsic stability of maleic anhydride

$$ {}^{\mathrm{I}}\lambda_{\mathrm{MA}} = \frac{{}^{\mathrm{I}}\hat{k}_{\mathrm{bta,MA}}(T)}{{}^{\mathrm{I}}\hat{k}_{\mathrm{MA,COx}}(T)} \tag{3.20} $$

can be introduced which quantifies the stability of maleic anhydride as an intermediate in the total oxidation of *n*-butane. It characterises the consecutive reaction. A higher value of ${}^{\mathrm{I}}\lambda_{\mathrm{MA}}$ denotes a faster formation of maleic anhydride compared to the decomposition of maleic anhydride.

A third parameter can be defined that quantifies the 'activity' of the catalyst, called the activity parameter. It is defined as

$$ {}^{\mathrm{I}}\hat{k}_{\mathrm{a}} = {}^{\mathrm{I}}\hat{k}_{\mathrm{bta,MA}}(T) + {}^{\mathrm{I}}\hat{k}_{\mathrm{bta,COx}}(T) \tag{3.21} $$

and is a measure of how fast *n*-butane is converted.

Properties of the Catalyst Body

A larger control volume than the previous is a porous catalyst body with boundaries directly enclosing the geometrical catalyst body surface. It is displayed in Fig. 3.1(b). In the control volume of the body, possible pore diffusional resistances and heat conductivity resistances can lead to concentration and temperature gradients. As stated before, it is impossible to obtain properties of smaller control volumes that contain only the active sites if the transport resistances are unknown. Nevertheless, the body can be regarded as a 'black box' and effective reaction rates ${}^{\mathrm{B}}r_j$ can be proposed which do not distinguish between true reactions and effects resulting from transport resistances. The corresponding selectivities can be defined as

$$ {}^{\mathrm{B}}S_i = \frac{\epsilon_{\mathrm{C},i}}{4} \times \frac{{}^{\mathrm{B}}R_i}{-{}^{\mathrm{B}}R_{\mathrm{HC}}}. \tag{3.22} $$

Negligible transport resistances result in the identity of the intrinsic properties and the catalyst body properties:

$$ {}^{\mathrm{B}}r_j = {}^{\mathrm{I}}r_j, \tag{3.23} $$

$$ {}^{\mathrm{B}}S_i = {}^{\mathrm{I}}S_i. \tag{3.24} $$

In case of our example, the oxidation of *n*-butane with first order rate equations and isothermal conditions in the catalyst bodies assumed, the catalyst body selectivity and the catalyst body stability of maleic anhydride as well as the catalyst body activity can be defined in a similar way as the corresponding intrinsic properties and depend solely on the reaction temperature for a given catalyst. In case of negligible transport resistances, the catalyst body selectivity and stability of maleic anhydride as well as the activity parameter equal the corresponding intrinsic properties.

Differential Properties

The next larger control volume adds the gas phase boundary layer surrounding the catalyst body. The control volume is displayed in Fig. 3.1(c). The corresponding concentrations at the catalyst body surface and in the bulk gas phase are different if there are significant external transport resistances. The external transport properties depend on the flow field surrounding the catalyst body and therefore depend on reactor type and reactor conditions. The differential properties are named 'differential' because they appear as source expressions in the differential balances of reactor models. If external transport

properties are negligible, the differential properties equal the catalyst body properties. An important feature of the laboratory reactor should therefore be negligible external transport resistances. It is then possible to determine the catalyst body properties.

Integral Properties

All control volumes larger than the previous one include changes in the bulk of the gas phase, and their properties are therefore integral properties of the reactor. If a control volume is chosen to extend from the reactor inlet to a certain position of the catalyst bed, its integral properties are also called reactor properties. Examples are conversion levels, reactor selectivities and yields.

Catalyst Body Properties in the Context of Plots of Reactor Selectivities

The reactor selectivities for conversion levels $X \to 0$ are independent of the reactor type and equal the differential selectivities for the gas composition and temperature of the reactor feed. If external transport resistances are negligible, these differential selectivities also equal the catalyst body selectivities:

$$^{\mathrm{B}}S_i(\mathbf{c}_0, T_0) = {}^{\mathrm{D}}S_i(\mathbf{c}_0, T_0) = \lim_{X_{\mathrm{HC}} \to 0} {}^{\mathrm{R}}S_i. \tag{3.25}$$

The catalyst body selectivities can be determined directly from plots of reactor selectivities against conversion levels as the extrapolation of the reactor selectivity to zero conversion levels. They are valuable information on parallel reactions of the hydrocarbon feedstock.

The activity parameter that was defined above for the example of first order rate equations depends solely on the temperature. The more exact reaction kinetics of the partial oxidation of hydrocarbons to maleic anhydride, however, consider the inhibition of reactions by hydrocarbons. An activity parameter should quantify the 'activity' of a catalyst for a given reaction temperature and feed composition. The activity parameter $^{\mathrm{B}}k_{\mathrm{a}}$ that is used in the present work considers the inhibition effects and is a direct measure for the initial conversion rate of the hydrocarbons. It is implicitly defined as

$$^{\mathrm{B}}R_{\mathrm{HC}}\big|_{\mathbf{p_0},T} = {}^{\mathrm{B}}k_{\mathrm{a}} \times p_{\mathrm{HC},0}. \tag{3.26}$$

In case of negligible external transport resistances, the activity parameter is proportional to the negative slope of the dimensionless fraction of the hydrocarbons for zero conversion levels:

$$\left.\frac{\mathrm{d}Y_{\mathrm{HC}}}{\mathrm{d}t_{\mathrm{mod}}}\right|_{X_{\mathrm{HC}=0}} = -RT \times {}^{\mathrm{B}}k_{\mathrm{a}}. \tag{3.27}$$

For first order rate equations, the activity parameter only depends on the temperature and equals the activity parameter as defined in the example above.

Proceedings in the Present Work

The difficulties in determining properties that are related to a certain control volume increase sharply with decreasing extension of the control volume. It is sufficient for reactor design to determine the catalyst body properties if a specific catalyst type has been chosen. The determination of the catalyst body properties belongs to the objectives of the present work.

3.1.4 Effects of Transport Resistances on Catalyst Performance

The effects of transport resistances on catalyst performance are discussed in detail in chapter 5. For discussion of the experimental results in the next chapter, however, it is necessary to understand some basic transport effects qualitatively. This section gives an overview mostly of the transport effects in catalyst bodies.

Because of the high thermal conductivity of the oxidic catalyst compared to the low thermal conductivity of the gas phase, the heat transport in the catalyst bodies is typically high enough to ensure an isothermal condition within the bodies [34]. Hein studied the total oxidation of ethane and propane in a fixed bed reactor at low gas velocities. These conditions led to high heat transport resistances in the boundary layer surrounding the catalyst bodies. The reaction heat of the total oxidation led to differences in temperatures of the catalyst bed of about 150 K. At the same time, however, the differences in temperatures between the catalyst bodies and the gas phase were only 8 K [35]. Since the reaction enthalpies are lower in the present work, it can be expected that this difference in temperature is much smaller and heat transport resistances from the gas phase to the catalyst bodies can therefore be neglected.

Fig. 3.2 shows the concentration profiles of the three important species in the partial oxidation of *n*-butane as a function of the position. The reactions take place in the porous layer of active material. The reactant *n*-butane has to be transported from the bulk gas phase through the boundary layer into the pores of the catalyst. The products maleic anhydride and carbon oxides have to be transported out of the pores of the catalyst through the boundary layer to the bulk gas phase. If transport resistances were small enough, the concentrations of each species on every location of this system would be equal. Transport resistances, however, lead to gradients in the boundary layer and in the porous layer. Concentration profiles as presented in Fig. 3.2 are typical result of transport resistances. If concentration and temperature profiles are known, the differential formation rates, the 'effective rates', can be calculated by integration. If the active layer can be assumed to be flat, equation

$$^{\mathrm{D}}R_i(\mathbf{c}^{\mathrm{bulk}}, T^{\mathrm{bulk}}) = \frac{1}{L} \times \int_0^L {}^{\mathrm{I}}R_i(\mathbf{c}, T)\mathrm{d}x \tag{3.28}$$

is obtained. Since our catalyst consists of a thin layer of active material coated onto an inert and non-porous support, the active layer can be assumed to be flat. If no transport resistances are present, the differential formation rates equal the intrinsic formation rates:

$$^{\mathrm{D}}R_i(\mathbf{c}^{\mathrm{bulk}}, T^{\mathrm{bulk}}) = {}^{\mathrm{I}}R_i(\mathbf{c}^{\mathrm{bulk}}, T^{\mathrm{bulk}}). \tag{3.29}$$

Some qualitative statements can be made concerning differential activity and selectivity if they are influenced by transport resistances. The mean concentration of *n*-butane in the catalyst body is then lower than the corresponding concentration in the bulk gas phase. The differential conversion rate[1] is smaller than the differential conversion rate that would be obtained without transport resistances. An effectiveness factor can be introduced:

$$^{\mathrm{D}}\eta_{\mathrm{bta}} = \frac{^{\mathrm{D}}R_i(\mathbf{c}^{\mathrm{bulk}}, T^{\mathrm{bulk}})}{^{\mathrm{I}}R_i(\mathbf{c}^{\mathrm{bulk}}, T^{\mathrm{bulk}})}. \tag{3.30}$$

[1] The conversion rate of a species can be considered as the negative formation rate of this species.

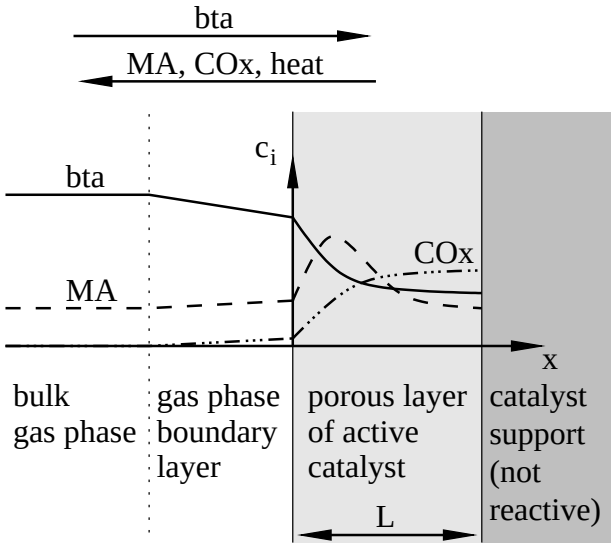

Fig. 3.2: *Schematic concentration profiles for a catalyst body with transport resistances in the gas phase and in the porous layer of the catalytically active material. The abbreviations bta, MA and COx denote n-butane, maleic anhydride and carbon oxides, respectively.*

In case of negligible transport resistances, this effectiveness factor equals 1.

The differential selectivity of maleic anhydride is also influenced by transport resistances. Typically, the differential selectivity of an intermediate such as maleic anhydride is smaller than the intrinsic selectivity since some of the intermediates which were formed in the catalyst body cannot leave the body fast enough to avoid further conversion.

If the reaction rates are assumed to be of first order and the external transport resistances are negligible, the effectiveness factor and the catalyst body selectivity can be explicitly calculated [32, 33]. For this calculation, a Thiele number ϕ can be introduced. For first order reactions, it is defined as

$$\phi = L \times \sqrt{\frac{RT a_{\mathrm{i}} \times {}^{\mathrm{I}}\hat{k}_{\mathrm{a}}}{D^{\mathrm{body}}}}. \tag{3.31}$$

The Thiele number relates the intrinsic activity parameter as a measure for the reaction rate to the effective diffusivity in the catalyst pores as a measure of the transport rate. The width of the active layer is denoted as L and a_{i} is the inner active surface related to the geometric volume of the catalyst body. In the case of the partial oxidation of n-butane with the assumption of first order rate equations, the effectiveness factor equals the ratio of the catalyst body activity parameter and the intrinsic activity parameter. The effectiveness factor, the catalyst body selectivity, as well as the catalyst body stability of

maleic anhydride can be calculated from the intrinsic properties:

$$ {}^{\mathrm{B}}\eta_{\mathrm{bta}}(\phi) = \frac{\tanh\phi}{\phi}, \tag{3.32} $$

$$ {}^{\mathrm{B}}S_{\mathrm{MA}}(\phi,T) = \frac{{}^{\mathrm{I}}S_{\mathrm{MA}}(T)}{1-\sigma(T)}\left(1-\frac{\sqrt{\sigma(T)}\tanh(\phi\sqrt{\sigma(T)})}{\tanh\phi}\right), \tag{3.33} $$

$$ {}^{\mathrm{B}}\lambda_{\mathrm{MA}}(\phi,T) = \frac{{}^{\mathrm{I}}S_{\mathrm{MA}}(T)}{1-\sigma(T)}\left(\frac{\tanh\phi}{\sqrt{\sigma(T)}\tanh(\phi\sqrt{\sigma(T)})}-1\right), \text{ with} \tag{3.34} $$

$$ \sigma(T) = \frac{{}^{\mathrm{I}}S_{\mathrm{MA}}(T)}{{}^{\mathrm{I}}\lambda_{\mathrm{MA}}(T)}. \tag{3.35} $$

In Fig. 3.3, the catalyst body parameters are plotted against the Thiele number for an intrinsic selectivity of ${}^{\mathrm{I}}S_{\mathrm{MA}} = 72\%$ and an intrinsic stability of ${}^{\mathrm{I}}\lambda_{\mathrm{MA}} = 13$. For $\phi = 0$, the catalyst body stability and catalyst body selectivity equals the corresponding intrinsic properties. The effectiveness factor equals 1. For increasing Thiele numbers, all parameters are decreasing. For $\phi \to \infty$, the effectiveness factor equals 0. The selectivity and stability curves, however, lead to asymptotical values. For high values of the Thiele number, only the inert carbon oxides are present in the centre of the catalyst body since n-butane and maleic anhydride are converted before they reach the centre. Therefore, no reaction progress is achieved in the centre. The catalyst can be divided in a stagnation zone in the centre and a reaction zone in the outer perimeters of the catalyst body. At larger Thiele numbers, only the extent of the stagnation zone is increased while the reaction zone remains unchanged.

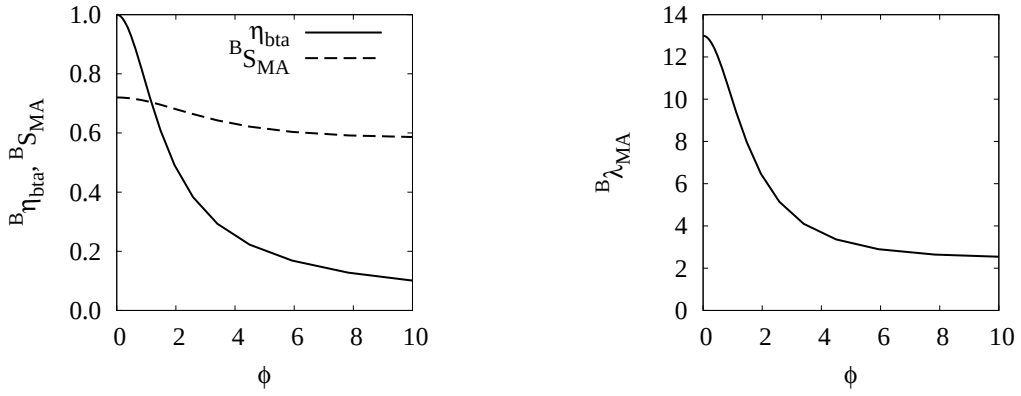

(a) Catalyst body activity and catalyst body selectivity

(b) Catalyst body stability

Fig. 3.3: *Catalyst body parameters as functions of the Thiele number for the simplified description of the partial oxidation of n-butane.*

The temperature dependences of the effective catalyst body diffusivities are weak compared to the temperature dependence of the activity parameter. Therefore, for a given catalyst, the Thiele modulus is increasing with increasing temperature. The temperature dependences of the catalyst body properties differ from the temperature dependences of

the intrinsic properties if transport resistances have to be considered. The resulting effective or apparent activation energies of a first order reaction can be approximated as half of the intrinsic activation energies for Thiele numbers $\phi > 2$.

The presence of external transport resistances complicates the system and the differential properties differ from the catalyst body properties. In general, the qualitative statements that are given for pore transport resistances are also valid for the external transport resistances. The mass transport resistances in the pores are generally much higher than the external resistances. In the present work, the estimated effective diffusivities in the catalyst bodies are about an order of magnitude lower than the corresponding diffusivities in the gas phase. The external transport resistances are therefore neglected in the present work and signs of transport resistances in the experimental results are attributed to catalyst body transport properties. Estimations about external transport resistances in the laboratory reactor are presented in section 5.4.2.

3.2 Experimental

3.2.1 The Catalyst Types VPO-50 and VPO-14

Two different catalyst types were used in the present work. Both types were egg-shell catalysts with the catalytically active and porous VPO material deposited on a non-porous steatite support. The catalyst types differ in the amount of active material and thus in the thickness of the active layer as well. The catalyst type that was mainly used in this thesis had a weight fraction of active material of 50% and is called VPO-50 throughout this thesis. The second catalyst type consisted of 14% w/w of active material and is named VPO-14. By comparing the behaviour of both catalyst types in the oxidation experiments, it was possible to detect possible influences of pore transport properties on the catalyst performance. The catalyst performance can deviate from the behaviour of an ideal catalyst where the surface can be accessed without transport resistances. Possible pore transport effects on the performance are more likely for the VPO-50 catalyst, since the thicker active layer increases the probability of significant pore diffusional resistances from the catalyst body surface to the innermost active sites.

The steatite supports had the shape of hollow cylinders and were inert. The catalyst bodies had a height of 4 mm and an outer diameter of 5 mm. The inner diameter amounted to slightly above 1 mm.

3.2.2 A Synthetic Mixture as a Substitute for Raffinate II

Preliminary studies were carried out by Quast with a raffinate II mixture and a mixture of *trans*-2-butene and *n*-butane with the same ratios of butane and butene concentrations. No significant differences were observed between the two mixtures. Other experiments showed no difference between the conversion behaviours of the individual *n*-butene isomers [16]. The flexibility of feeding *n*-butane and *n*-butenes separately was used in the present work. It was therefore possible to vary the relative amounts of both hydrocarbons. A composition of raffinate II was assumed as presented in Tab. 2.1. This composition was approximated by using 16% n/n of *n*-butane, 75% n/n of 1-butene and 9% of nitrogen

as the replacement for isobutane and isobutene. Isobutane was fed individually to the reactor in two experiments. The results of these experiments are presented in section 4.6.

3.2.3 The Laboratory Reactor and Methods of Gas Analysis

The determination of the reaction kinetics is based on experiments of the partial oxidation of C_4 hydrocarbons in a laboratory tubular fixed-bed reactor. Fig. 3.4 shows a schematic representation of the experimental reactor setup.

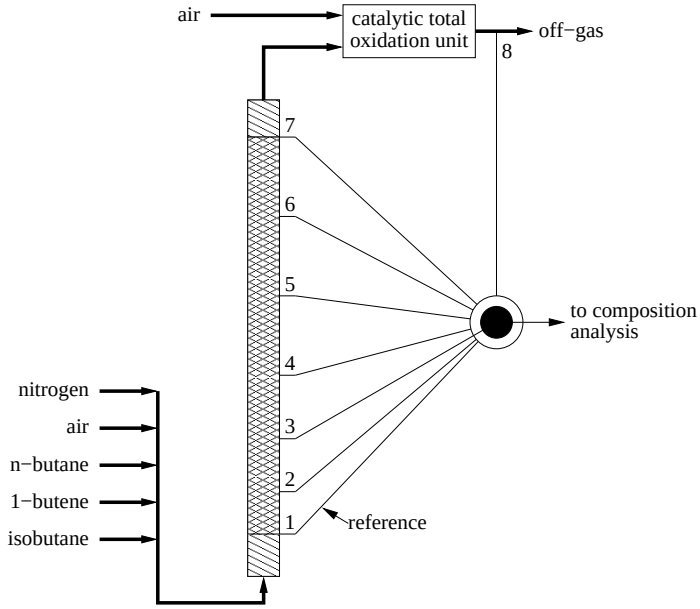

Fig. 3.4: *Scheme of the reactor setup. The catalyst bed is located between sampling ports 1 and 7. Below sampling port 1 and above sampling port 7, the reactor is charged with inert spheres of steatite.*

By using mass flow controllers, some of the gases nitrogen, air, *n*-butane, 1-butene and isobutane were fed individually to the reactor with well defined flow rates. The streams were mixed and preheated in a tube filled with spheres of steatite to ensure perfect mixing and to avoid spontaneous explosions of the hydrocarbon/air mixture by shortening the collision distances of the free radicals. This precaution was necessary since some of the experiments were carried out above the lower explosion limit. A rupture disc was installed at the reactor inlet. In case of pressure buildups exceeding 2.5 bar, the reaction gases would be vented to avoid damage of the laboratory equipment. No explosions have been experienced in the present work. The total flow rate through the reactor was varied in the range of 10 to 30 ml/s related to standard temperature and pressure (0 °C, 1.013 bar). The pressure in the reactor had a constant value of 1.3 bar.

Downflow to the mixing and preheating zone, the gas flow entered the reaction zone consisting of a fixed bed of catalyst bodies mixed with inert spheres with a height of 1.5 m and a diameter of 15 mm.

The temperature in the catalyst bed was controlled by six independent heating zones along the reactor and was monitored by 13 axially distributed thermocouples. The thermocouples reached into the fixed bed and were used to measure the temperature in the

reactor at the specific axial positions. By using different set points for the six heating zones, it was possible to operate the reactor in a well defined non-isothermal mode where a temperature profile could be forced onto the catalyst bed. Experiments that were carried out non-isothermally and their results are reported in [36].

Seven sampling ports were distributed along the reactor to determine the concentration profiles in the reactor tube. Sampling port number 1 was located directly at the beginning of the catalyst bed where the gas composition equalled the feed composition. Sampling port number 7 was located directly at the end of the bed.

The fixed bed was diluted with spheres of steatite with a diameter of 2 – 3 mm. The dilution had multiple beneficial effects: first of all, it was possible to vary the amount of active material in the reactor without the need to use other catalyst types with a different amount of active mass. The dilution also reduced the amount of reaction heat which had to be removed from the reactor. Additionally, it was possible to adapt the 'resolution' of the concentration profiles in the reactor. This was especially helpful for the conversion of mixtures of *n*-butenes and *n*-butane since the rates of the individual conversion reactions were different. With higher catalyst dilution in the first zone of the reactor, the conversion progress of the *n*-butenes were observable in the same quality as the conversion of the *n*-butane in the second reactor zone, where a higher density of active mass compensated the lower reaction rates connected to the *n*-butane conversion.

The mixing of solid particles with different dimensions like the catalyst bodies and the inert spheres led to a more even radial porosity distribution and therefore evened out the radial velocity distribution.

The dimensions of the reactor were large compared to typical laboratory reactors which resulted in clear advantages. For example, axial mixing effects caused by mass dispersion were negligible in this reactor, because the characteristic mixing lengths were much smaller than the height of the reactor. Negligible axial mixing effects are a second prerequisite for the assumption of plug flow, one important aspect of an ideal reactor behaviour. Another advantage of the height of the reactor was the better temperature control, since the temperatures in the six independent heating zones along the reactor were controlled individually.

The choice of the reactor diameter of 15 mm resulted from a compromise between two reactor properties which are necessary for ideal behaviour. Larger diameters are better suited for the exclusion of wall effects. On the other hand, removal of reaction heat and isothermal conditions are better achieved with slower diameters. Since the oxidation reactions investigated in the present work are highly exothermic, the removal of the reaction heat had a higher priority.

The gas flow leaving the reactor was mixed with preheated air. Subsequently, all carbon containing species were oxidised to carbon dioxide in a catalytic total oxidation reactor which contained a perovskite catalyst. The total oxidation reactor was operated at a temperature of about 350 °C. A further sampling port was located downstream of the combustion unit which enabled the monitoring of the carbon mass balance. This helped to identify malfunctions of mass flow controllers or gas analysis devices.

A continuous gas stream with a flow rate of about 2% of the flow rate through the reactor left the sampling port which had been selected by the multi-position valve and entered the analysis section displayed in Fig. 3.5. The gas samples that were taken from the ports flowed through small heated pipes (220 °C) to avoid condensing of the organic

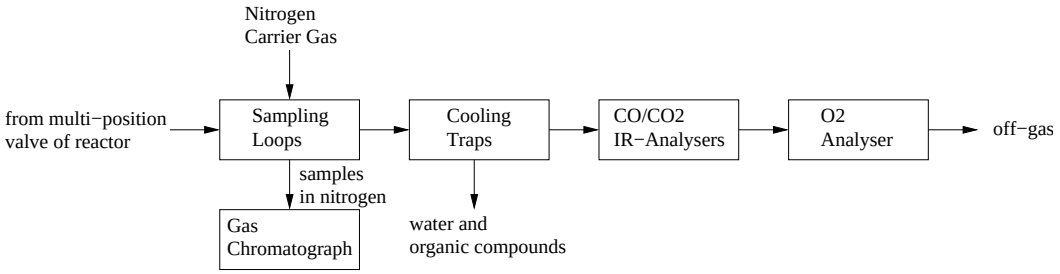

Fig. 3.5: *Gas analysis setup. The gas stream from the selected sampling port could be analysed by means of gas chromatography, non-dispersive infrared analysers and an oxygen analyser.*

species and water and were passing through one of two sampling loops before entering four cooling traps which were connected in series. The first one was cooling down the stream to ambient temperature, in which most of the maleic anhydride was separated by crystallisation. The subsequent traps were cooled by solid carbon dioxide resulting in removal of water and all organic species. The species that remained in the gas stream were carbon oxides, oxygen and nitrogen. The concentrations of both carbon oxides were determined by means of non-dispersive infrared analysers. A third analyser determined the concentration of oxygen by means of the paramagnetic properties of oxygen.

A nitrogen carrier stream was used in order to inject the contents of the sampling loop into the gas chromatograph for the detection of organic species and the quantification of their concentrations. The gas chromatograph was calibrated for all important reactants, namely *n*-butane, isobutane and all individual *n*-butene isomers, and the products 1,3-butadiene, furan and maleic anhydride. It was also calibrated for many side products like acrylic acid, acetic acid and crotonaldehyde. One difficulty of the gas analysis was the simultaneous detection of *n*-butane and 1,3-butadiene since their retention times were equal. 1,3-Butadiene was formed only during the conversion of *n*-butenes. Therefore, the presence of both species in the gas phase occurred only if mixtures of *n*-butane and *n*-butene were used as a feedstock. For the oxidation of those mixtures, like raffinate II, an assumption was made concerning the concentrations of *n*-butane and 1,3-butadiene which was based on experimental observation of the conversions of the pure components and the conversion of the mixture. The conversion of *n*-butane was strongly inhibited by the presence of *n*-butenes and 1,3-butadiene. It was therefore assumed that *n*-butane had not been converted until no 1,3-butadiene was present in the gas phase. If the measured sum concentration of both species was greater than the concentration of *n*-butane in the feed, the concentration of *n*-butane was assumed to be the same as in the feed and the difference to the sum concentration was ascribed to 1,3-butadiene. Sum concentrations lower than the feed concentration of *n*-butane were fully ascribed to *n*-butane and no 1,3-butadiene was expected to be in the gas phase. This assumption is justified by comparison of the conversion of raffinate II to the conversion of pure *n*-butenes with the same amount as it was present in the experiment with raffinate II. The justification is presented in appendix A. The concentration of water was calculated from the oxygen balance and was cross checked by solving the hydrogen balance.

The experimental setup was controlled by a computer which waited for steady state of the concentrations measured by the gas analysers and injected the contents of the

sampling loop into the gas chromatograph after steady state had been achieved. Two samples were taken at each port, one sample with each sampling loop. After that, the computer switched to the subsequent port in axial direction and stored the results of the analysis devices and all measured temperatures in a data file. During one night of operation, four measurements were carried out at each of the seven sampling ports.

3.3 Quantification of Reaction Kinetics

3.3.1 Reaction Networks, Stoichiometry and Rate Equations

The widely used triangular reaction network for the oxidation of *n*-butane to maleic anhydride is presented in section 2.4.4. The oxidation of *n*-butenes is more complicated since more intermediate species are formed, mostly butadiene and furan. It is not necessary to quantify the concentrations of all the individual intermediates. Instead, it is possible to lump the species together to a pseudo-species which is called IP throughout the thesis. Quast investigated the conversion of pure *n*-butenes and proposed the reaction network displayed in Fig. 3.6 [16]. Experimental results in the present work verified this network and it is therefore used throughout this thesis. The network consists of the triangular subnetwork of the species *n*-butenes (bte), maleic anhydride (MA) and carbon oxides (COx) that resembles the network of the *n*-butane oxidation. Additionally, a reaction path for the formation of the pseudo-species IP from *n*-butenes is considered. The species IP, maleic anhydride (MA) and carbon oxides (COx) also form a triangular subnetwork.

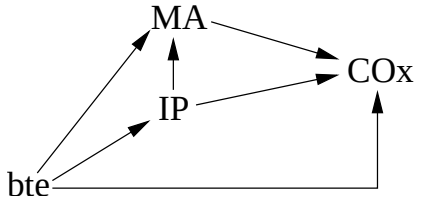

Fig. 3.6: *Reaction network for the oxidation of n-butenes. The abbreviations bte, IP, MA and COx denote n-butenes, lumped together intermediates, maleic anhydride and carbon oxides, respectively.*

Quast also carried out experiments with raffinate II and proposed the merging of the two networks for the oxidation of *n*-butane and *n*-butenes as displayed in Fig. 3.7.

The total oxidation of a hydrocarbon is thermodynamically much more favoured than the desired partial oxidation. The strict definition of total oxidation of a hydrocarbon states that only carbon dioxide and water and no other products are formed. In the present thesis, the total oxidation is conveniently defined as the formation of both, carbon monoxide and carbon dioxide, since the conversion of carbon monoxide to carbon dioxide can be neglected at the typical reaction conditions in the presence of VPO catalysts [17]. Therefore, the 'total' oxidation reaction of an arbitrary C_4 hydrocarbon with y hydrogen atoms and z oxygen atoms results in

$$C_4H_yO_z + \left(4 - 2s + \frac{y}{4} - \frac{z}{2}\right) O_2 \longrightarrow 4s\,CO + 4(1-s)\,CO_2 + \frac{y}{2}\,H_2O. \qquad (3.36)$$

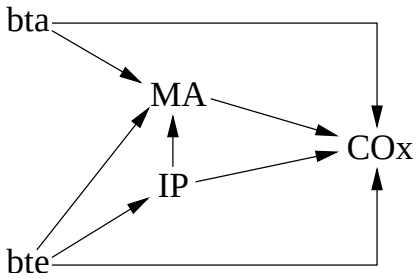

Fig. 3.7: *Reaction network of the oxidation of mixtures of n-butane and n-butene.*

The stoichiometric parameter s represents the amount of formed carbon monoxide. A constant of $s = 1$ means that only carbon monoxide is formed whereas $s = 0$ represents the classical definition of total oxidation by forming carbon dioxide as the only carbon containing species. An individual stoichiometric parameter s_j is defined for each total oxidation reaction in the networks.

In Tab. 3.1 all crucial reaction equations for the oxidation of n-butane and n-butenes are summarised. Since the pseudo-species IP consists of several intermediate products, the amounts of carbon, hydrogen and oxygen atoms in one pseudo-molecule had to be quantified. The quantification is presented in section 4.3.5. Here, the general formula for IP, $C_xH_yO_z$, is used. In each reaction, the number of carbon atoms on each side equals 4.

Different approaches were tested in the present work to quantify the reaction rates of the individual reactions. For the partial oxidation of n-butane to maleic anhydride, first order, power law and hyperbolic rate equations were tested. The hyperbolic rate equation type used was

$$r_{i,j} = \frac{k_{i,j} p_i}{1 + b_{\mathrm{bta}} p_{\mathrm{bta}}}. \tag{3.37}$$

For the partial oxidation of mixtures of n-butane and n-butenes, the inhibiting effect of n-butenes and IP on the conversion of n-butane required the partial pressure of n-butenes and IP to be present in the rate equation of n-butane, resulting in the approach

$$r_{\mathrm{bta},j} = \frac{k_{\mathrm{bta},j} p_{\mathrm{bta}}}{1 + b_{\mathrm{bta}} p_{\mathrm{bta}} + b_{\mathrm{IP}} p_{\mathrm{IP}}}. \tag{3.38}$$

This equation resembles the Eley-Rideal approach which was successfully applied for the oxidation of n-butane and is discussed in section 2.4.5. The agreement between experiments and calculation were improved by merging the Eley-Rideal approach and the approach in equation (3.38), resulting in rate equations of the type

$$r_{i,j} = \frac{k_{i,j} p_i \sqrt{p_{\mathrm{O2}}/p^+}}{1 + b_{\mathrm{bta}} p_{\mathrm{bta}} + b_{\mathrm{bte}} p_{\mathrm{bte}} + b_{\mathrm{IP}} p_{\mathrm{IP}} + b_{\mathrm{H2O}} p_{\mathrm{H2O}}}. \tag{3.39}$$

The reference pressure $p^+ = 26\,\mathrm{kPa}$ has been introduced so that the rate constants $k_{i,j}$ are independent of the power of the partial pressure of oxygen and the root amounts to values around unity. The rate constants were assumed to obey Arrhenius' law

$$k_{i,j} = k_{i,j}^{\infty} \exp\left(-\frac{E_{\mathrm{A},i,j}}{RT}\right). \tag{3.40}$$

Oxidation of n-butane to maleic anhydride:

$$C_4H_{10} + 3.5\,O_2 \longrightarrow C_4H_2O_3 + 4\,H_2O$$

Total oxidation of n-butane:

$$C_4H_{10} + (6.5 - 2s_{\mathrm{bta}})\,O_2 \longrightarrow 4s_{\mathrm{bta}}\,CO + 4\,(1 - s_{\mathrm{bta}})\,CO_2 + 5\,H_2O$$

Oxidation of n-butenes to IP:

$$C_4H_8 + \left(2 + \frac{2z - y}{x}\right) O_2 \longrightarrow \frac{4}{x}\,C_xH_yO_z + \left(4 - \frac{2y}{x}\right) H_2O$$

Oxidation of n-butenes to maleic anhydride:

$$C_4H_8 + 3\,O_2 \longrightarrow C_4H_2O_3 + 3\,H_2O$$

Total oxidation of n-butenes:

$$C_4H_8 + (6 - 2s_{\mathrm{bte}})\,O_2 \longrightarrow 4\,s_{\mathrm{bte}}\,CO + 4\,(1 - s_{\mathrm{bte}})\,CO_2 + 4\,H_2O$$

Oxidation of IP to maleic anhydride:

$$\frac{4}{x}\,C_xH_yO_z + \left(1 + \frac{y}{x} - 2\frac{z}{x}\right) O_2 \longrightarrow C_4H_2O_3 + \left(2\frac{y}{x} - 1\right) H_2O$$

Total oxidation of IP:

$$\frac{4}{x}\,C_xH_yO_z + \left(4 + \frac{y}{x} - \frac{2z}{x} - 2s_{\mathrm{IP}}\right) O_2 \longrightarrow 4\,s_{\mathrm{IP}}\,CO + 4\,(1 - s_{\mathrm{IP}})\,CO_2 + \frac{2y}{x}\,H_2O$$

Total oxidation of maleic anhydride:

$$C_4H_2O_3 + (3 - 2s_{\mathrm{MA}})\,O_2 \longrightarrow 4s_{\mathrm{MA}}\,CO + 4\,(1 - s_{\mathrm{MA}})\,CO_2 + H_2O$$

Tab. 3.1: *The individual reaction equations of the partial oxidation of mixtures of n-butane and n-butenes. In each reaction, the number of carbon atoms on each side equals 4.*

The inhibition constants b_i and the stoichiometric parameters which represent the amount of carbon monoxide formed (s_i) were found to be independent of the temperature.

The chosen approach is based on kinetic models for the oxidation of pure n-butane. The expressions considering n-butenes and IP as inhibiting species were added. As will be shown in part 4.7, the measured reaction kinetics in the present work are affected by pore diffusion resistances.

Three different sets of reaction kinetics were determined in the present thesis: one for the partial oxidation of n-butane on VPO-50, one for the partial oxidation of mixtures on VPO-50 and one for the partial oxidation of mixtures on VPO-14.

3.3.2 Determination of Kinetic and Stoichiometric Parameters

If the kinetic and stoichiometric parameters are known, the concentration profiles along an ideal fixed-bed reactor can be calculated as shown in section 3.1.2. These parameters have to be determined from experimental data. No explicit calculation of the parameters is possible. The determination of the parameters was carried out by means of non-linear regression where the parameters are found by a least-squares minimisation of the deviation between the model and the experiments. The approach results in the task to minimise

$$\chi^2 = \sum_{i=1}^{N_{\text{samples}}} \sum_{j=1}^{N_{\text{species}}} \left(\frac{x_j^{\text{calc}}({}^i z, {}^i\mathbf{s}, \mathbf{a}) - {}^i x_j^{\text{exp}}}{{}^i\sigma_j} \right)^2 . \tag{3.41}$$

The expression $x_j^{\text{calc}}({}^i z, {}^i\mathbf{s}, \mathbf{a}) - {}^i x_j^{\text{exp}}$ represents the deviation between measured and calculated values. The value ${}^i x_j^{\text{exp}}$ denotes the measured molar fraction of species j in sample i. The sample was obtained at reactor position ${}^i z$ during an experiment with operation conditions compiled in ${}^i\mathbf{s}$. This vector of operation conditions contains information about the temperature profile in the reactor, the profile of the density of catalytically active mass in the reactor, pressure, volumetric flow rate and feed concentrations. The estimated kinetic and stoichiometric parameters are represented by the vector $\mathbf{a}$. The calculated molar fraction of a species j is represented by $x_j^{\text{calc}}({}^i z, {}^i\mathbf{s}, \mathbf{a})$. To determine the standard deviation ${}^i\sigma_j$ of the measured molar fraction of species j in sample i, many repeated experiments would be necessary. This is impractical considering the complexity of the experiments. Therefore, the standard deviations were approximated by an error estimation

$${}^i\sigma_j = \sigma_{\text{abs}} + \sigma_{\text{rel}}\, {}^i x_j^{\text{exp}} \tag{3.42}$$

consisting of a fixed and a relative amount. The fixed amount σ_{abs} represents the detection limit and was chosen to be 0.01%. Therefore, the detection limit corresponded to 1% of a typical molar fraction of hydrocarbons in the feed. The relative amount σ_{rel} is the relative error of the measured molar fractions and was assumed to be 5%.

The parameter estimations were carried out with the optimisation toolbox of Matlab. The built-in Levenberg-Marquard and Newton methods vary the model parameters to minimise χ^2. These methods cannot distinguish between local and global minima. Minimisers which are based on statistical approaches and can give estimates for the probability of the global minimum to be found, simulated annealing for example, cannot be used in the present problem, since they cannot cope with the number of necessary integrations of the reactor equations in an acceptable time. Instead, the test for identification of the

global minimum was carried out by varying the initial guesses of the model parameters in ranges with physically meaningful values and estimate the parameters. Most of the estimations led to the same model parameters, only some of them were significantly different but resulted in much higher values of χ^2 and were rejected. It was therefore assumed that the global minima were found. The value of χ^2 after the minimisation should equal, for a 'moderately' good fit, roughly the number of data points[2] minus the number of parameters [37].

Subsequently, the linear approximations of the confidence limits of the individual model parameter and of the cross correlation coefficients were calculated by methods presented in [37]. A probability of 95% was chosen for the confidence limits. This means that the probabilities of the true model parameters to be in the confidence limits are 95%.

Cross correlation coefficients $\gamma_{i,j}$ are a measure for the extent of correlation between parameters a_i and a_j. A value of $\gamma_{i,j} = 1$ means that a change in a_i can be fully compensated by a change in a_j without altering the quality of the fit. Therefore the individual parameters cannot be determined individually. No correlation was found for $\gamma_{i,j} = 0$. Practically, a value of $\gamma_{i,j} < 0.9$ can be considered as the absence of a significant correlation. 'Strong' correlations result in values above 0.95. Values in-between denote a 'weak' correlation [38]. A correlation between parameters has no effect on the suitability of a model for the description of the experimental data. Parameters which correlate, however, cannot be interpreted individually. For example, if a rate constant correlates with an inhibition constant, no statement can be given concerning the inhibiting effect.

The model parameters were transformed prior to the minimisation to avoid intrinsic cross correlations between the pre-exponential factors and the activation energies in the Arrhenius equations by following suggestions made in [39]. The parameter transformation is described in appendix C.1.

3.4 Thermodynamic Aspects

The prediction of the non-isothermal behaviour of a potential production-scale reactor can only be carried out if all important enthalpies of reaction are known or can at least be approximated. This thermodynamic aspect is covered in sections 3.4.1 and 3.4.2.

Another thermodynamic aspect is covered in section 3.4.3. There, the calculation of the molar fractions of the individual *n*-butenes, namely 1-butene, *cis*-2-butene and *trans*-2-butene, in their isomerisation equilibrium is presented. These fractions are interesting in the discussion of isomerisation reactions during the oxidation of the *n*-butenes which is presented in section 4.3.4.

3.4.1 Enthalpies and Gibbs Energies of Formation

The calculation of the enthalpies and Gibbs energies of reaction are based on the standard enthalpies and Gibbs energies of formation, respectively. For the standard enthalpies of formation $\Delta_\mathrm{F} H_i(T^\ominus, p^\ominus)$ and the standard Gibbs energies of formation $\Delta_\mathrm{F} G_i(T^\ominus, p^\ominus)$, values listed in [40] were used, if available. The corresponding values for maleic anhydride were taken from [41]. For some of the intermediates, no values could be found in the

[2]The number of data points equals the number of species multiplied by the number of samples.

literature and estimations based on group contribution methods taken from [40] were used. Since ideal gas state can be assumed, the enthalpies and energies are independent of the pressure. The entropies of formation were calculated with the relation

$$\Delta_{\mathrm{F}} S_i(T^{\ominus}, p^{\ominus}) = \frac{\Delta_{\mathrm{F}} H_i(T^{\ominus}, p^{\ominus}) - \Delta_{\mathrm{F}} G_i(T^{\ominus}, p^{\ominus})}{T^{\ominus}}. \tag{3.43}$$

The calculation of the entropy of formation was a necessary intermediate step in the calculation of the enthalpies and energies of formation at a specific temperature which result in

$$\Delta_{\mathrm{F}} H_i(T) = \Delta_{\mathrm{F}} H_i(T^{\ominus}) + \int_{T^{\ominus}}^{T} C_{\mathrm{p},i}(T)\mathrm{d}T \text{ and} \tag{3.44}$$

$$\Delta_{\mathrm{F}} S_i(T) = \Delta_{\mathrm{F}} S_i(T^{\ominus}) + \int_{T^{\ominus}}^{T} \frac{C_{\mathrm{p},i}(T)}{T}\mathrm{d}T. \tag{3.45}$$

The heat capacities $C_{\mathrm{p},i}(T)$ were calculated either by correlations from [40], or, if no values were given, estimated by methods presented in [42]. The Gibbs energies of formation at reaction temperature were calculated according to

$$\Delta_{\mathrm{F}} G_i(T) = \Delta_{\mathrm{F}} H_i(T) - T\Delta_{\mathrm{F}} S_i(T). \tag{3.46}$$

The enthalpies and Gibbs energies of a specific reaction j amount to

$$\Delta_{\mathrm{R}} H_j(T) = \sum_{i}^{N_{\mathrm{species}}} \nu_{i,j} \Delta_{\mathrm{F}} H_i(T) \text{ and} \tag{3.47}$$

$$\Delta_{\mathrm{R}} G_j(T) = \sum_{i}^{N_{\mathrm{species}}} \nu_{i,j} \Delta_{\mathrm{F}} G_i(T), \tag{3.48}$$

respectively. The reaction enthalpies turned out to be temperature independent in the range of 300 to 500 °C. The variations of the values were below 1%. This was not the case for the Gibbs energies of reaction.

3.4.2 Thermodynamic States

By considering all detected species, it was possible to calculate the heat which was removed from the reactor to keep it isothermal. The reaction kinetics, however, were based only on the important reaction species. The composition of the lumped species IP changes during reaction progress and no exact enthalpy of formation can be ascribed to this pseudo-species. The problem concerning the calculation of reaction thermodynamics from the kinetic model is, therefore, to elaborate suitable estimations or simplifications. These estimations are presented in this section. The justification is presented in chapter 4, where the more exactly calculated reaction heats by considering the detailed knowledge of all species of the experimental data were compared to the simplified calculations considering only the crucial reaction and rate equations.

The formation of maleic anhydride can be regarded as the formation of an intermediate in the total oxidation of *n*-butane. This point of view can be applied to every intermediate which is detected in the gas phase. The reaction of *n*-butane to carbon dioxide

$$\mathrm{C_4H_{10}} + 6.5\,\mathrm{O_2} \longrightarrow 4\,\mathrm{CO_2} + 5\,\mathrm{H_2O} \tag{3.49}$$

can therefore be split up into two reactions: the formation of a specific intermediate and the consecutive total oxidation of the intermediate. The explicit reaction equations for maleic anhydride as the specific intermediate are

$$C_4H_{10} + 6.5\,O_2 \longrightarrow C_4H_2O_3 + 2.5\,O_2 + 4\,H_2O \longrightarrow 4\,CO_2 + 5\,H_2O. \tag{3.50}$$

The mixture of maleic anhydride, water and oxygen can be regarded as an intermediate state of the total oxidation. In Tab. 3.2, several of such states of the *n*-butane to carbon dioxide system are listed together with the respective enthalpy which is defined as the enthalpy of reaction of the oxidation of *n*-butane to the specific state. All other enthalpies of reaction are obtained by subtracting the corresponding enthalpies of state. The reaction

substance	reacting species						$\frac{\Delta_S H_i}{\text{kJ/mol}}$
n-butane		C_4H_{10}	+ 6.5	O_2			0
1-butene		C_4H_8	+ 6	O_2	+	H_2O	-117
1,3-butadiene		C_4H_6	+ 5.5	O_2	+ 2	H_2O	-244
furan		C_4H_4O	+ 4.5	O_2	+ 3	H_2O	-634
maleic anhydride		$C_4H_2O_3$	+ 2.5	O_2	+ 4	H_2O	-1266
carbon monoxide	4	CO	+ 2	O_2	+ 5	H_2O	-1523
carbon dioxide	4	CO_2			+ 5	H_2O	-2658

Tab. 3.2: *Thermodynamic reaction states in the oxidation of n-butane to intermediates and carbon dioxide.*

enthalpy of the conversion of *n*-butane to maleic anhydride is −1266 kJ/mol, roughly half of the value of the total oxidation of *n*-butane which amounts to −2658 kJ/mol. The reaction enthalpy of the total oxidation of 1-butene is only slightly lower and amounts to −2541 kJ/mol. The oxidative dehydrogenation of *n*-butane to 1-butene amounts to −117 kJ/mol. The differences in the enthalpies of the *n*-butene isomers are about 10 kJ/mol. These differences are small compared to all other reaction enthalpies and were therefore neglected.

The enthalpy of reaction for the oxidation of a hydrocarbon or intermediate i to carbon oxides $\Delta_R H_{i,COx}$ can be calculated by weighting the corresponding enthalpies of reaction of this species to carbon monoxide and carbon dioxide by the stoichiometric parameter s_i and equals

$$\Delta_R H_{i,COx} = s_i \Delta_R H_{i,CO} + (1 - s_i)\Delta_R H_{i,CO2}. \tag{3.51}$$

Hence, the value of the enthalpy of reaction lies in-between the values of the oxidation of species i to carbon monoxide and carbon dioxide.

Experimental results showed that the lumped species IP consists mainly of 1,3-butadiene and furan, as it is shown in section 4.3.5. By assuming that IP consists solely of 1,3-butadiene and furan and the molar fraction of 1,3-butadiene in IP equals 70%, the enthalpy of state of IP amounts to

$$\Delta_S H_{IP} = 0.7\Delta_S H_{btd} + 0.3\Delta_S H_{fur} = -361\frac{\text{kJ}}{\text{mol}}. \tag{3.52}$$

There was a good agreement between the more exact calculations of reaction heat by considering all experimentally detected species and the calculation based on the pseudo-species IP and the reaction kinetics. No variability of the enthalpy of state of IP had to be considered.

3.4.3 Thermodynamic Equilibrium of the Isomerisation of *n*-Butenes

Quast investigated the conversion of different *n*-butene isomers to maleic anhydride at 340 °C. He found that the use of different *n*-butenes resulted in only negligible differences in the reactor performance [16]. The *n*-butenes did undergo isomerisation reactions and reached the isomerisation equilibrium at a conversion level of about 20%. In the present work, temperatures up to 450 °C were used. To validate the assumption of equilibrium for higher temperatures, the molar fractions of the three isomers were calculated for the temperature range from 300 to 500 °C. The following isomerisation reactions

$$\text{1-butene} \xrightarrow{1} \textit{cis}\text{-2-butene}, \tag{3.53}$$

$$\text{1-butene} \xrightarrow{2} \textit{trans}\text{-2-butene} \tag{3.54}$$

were used to calculate the equilibrium fractions. In thermodynamic equilibrium, the relations

$$\left(\frac{p^{\ominus}}{p}\right)^{\Delta\nu_1} \exp\left(\frac{-\Delta_{\mathrm{R}}G_1(T,p^{\ominus})}{RT}\right) = K_{\mathrm{x},1}(T,p) = \frac{x_{\mathrm{c2}}}{x_1}, \tag{3.55}$$

$$\left(\frac{p^{\ominus}}{p}\right)^{\Delta\nu_2} \exp\left(\frac{-\Delta_{\mathrm{R}}G_2(T,p^{\ominus})}{RT}\right) = K_{\mathrm{x},2}(T,p) = \frac{x_{\mathrm{t2}}}{x_1} \tag{3.56}$$

between the Gibbs energies of reaction and the molar fractions x_1, x_{c2}, x_{t2} of the isomers 1-butene, *cis*-2-butene and *trans*-2-butene, respectively, must be fulfilled. Since there is no change in number of moles during the reaction progress ($\Delta\nu_1 = \Delta\nu_2 = 0$), the equilibrium constants $K_{\mathrm{x},i}$ and therefore also the molar fractions of the isomers in equilibrium are independent of pressure. By rearrangement of equations (3.55) and (3.56) and considering $\sum_i x_i = 1$, the molar fractions of the isomers

$$x_1 = \frac{1}{1 + K_{\mathrm{x},1} + K_{\mathrm{x},2}}, \tag{3.57}$$

$$x_{\mathrm{c2}} = \frac{K_{\mathrm{x},1}}{1 + K_{\mathrm{x},1} + K_{\mathrm{x},2}}, \tag{3.58}$$

$$x_{\mathrm{t2}} = \frac{K_{\mathrm{x},2}}{1 + K_{\mathrm{x},1} + K_{\mathrm{x},2}} \tag{3.59}$$

are obtained. The molar fractions are displayed in Fig. 3.8 as a function of temperature. The molar fraction of 1-butene increases with increasing temperature from about 20% at 300 °C to about 30% at 500 °C, whereas the fractions of both 2-butene isomers each decrease to about half of the amount.

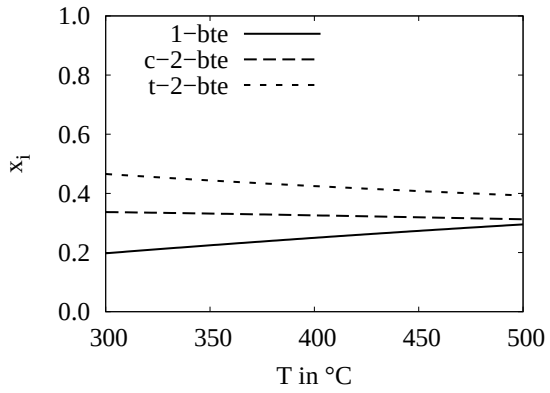

Fig. 3.8: *Molar fractions x_i of the n-butene isomers 1-butene (1-bte), cis-2-butene (c-2-bte) and trans-2-butene (t-2-bte) in the isomerisation equilibrium as a function of temperature.*

Chapter 4

Effective Reaction Kinetics

In this chapter, experimental results are reported, and the effective reaction rates for the catalyst types VPO-50 and VPO-14 are quantified. Influences of reaction conditions on the conversion levels, selectivities and yields are discussed.

The first section presents the results concerning the conversion of pure n-butane, followed by sections discussing the conversion of pure n-butenes and raffinate II. Each of these sections consists of at least three parts. In the first part, the results of the parameter estimation are reported. The subsequent parts show the influence of the most important operation parameters, namely the temperature and the hydrocarbon fraction in the feed, on the catalyst performance.

In sections 4.5 and 4.6, effects of varying ratios of concentrations of n-butane and n-butenes on the reactor performance, and the oxidation of isobutane are discussed.

Most of the experiments were carried out with the VPO-50 catalyst. The VPO-50 catalyst has a thicker layer of active material than the VPO-14 catalyst. In section 4.7, the oxidation of raffinate II on VPO-14 is presented and compared to the corresponding oxidation on VPO-50. The chapter ends with section 4.8.1 where irreversible changes of the catalyst during reaction, e. g. ageing, are reported.

4.1 Blank Run Without Catalyst

A blank run was carried out with a mixture of n-butane and air as reactor feed. The reactor was filled with steatite spheres and no catalyst was present. No significant conversion of n-butane was experienced. The steatite spheres and the stainless steal reactor wall could, therefore, be regarded as inert in the oxidation of n-butane. Dente et al. carried out two experiments to investigate the 'blind' conversion of n-butane [17]. In the first experiment, the tube reactor was filled with inert material; in the second, the reactor was empty. The conversion level of n-butane was insignificantly small in the filled reactor, confirming the observations in the present work. In the empty reactor, however, n-butane was converted. They concluded, that n-butane can be converted by a homogeneous reaction at the typical reaction conditions of the partial oxidation with VPO catalysts, but the gas phase volume necessary for a significant homogeneous conversion is too small in a filled reactor tube.

4.2 Oxidation of *n*-Butane over VPO-50

The oxidation of *n*-butane over VPO catalysts is reported in numerous articles and reviews. The reaction network for this oxidation has already been discussed in section 2.4.4 and is presented in Fig. 2.4. In the present section, the progress of the *n*-butane conversion is explained in more detail, and conversion rates and selectivities are quantified.

The experiments with pure *n*-butane as a feedstock were carried out isothermally at temperatures between 360 and 420 °C. Feed fractions were varied between 1.0 and 2.5% n/n of *n*-butane in air.

The results of the partial oxidation of *n*-butane at a temperature of 400 °C are presented in four plots in Fig. 4.1. The symbols represent experimentally determined values whereas the lines represent the calculations that are based on the rate laws which are quantified in the next section. A molar fraction of *n*-butane of 1% in air was fed to the reactor that contained the VPO-50 catalyst. The pressure was 1.3 bar.

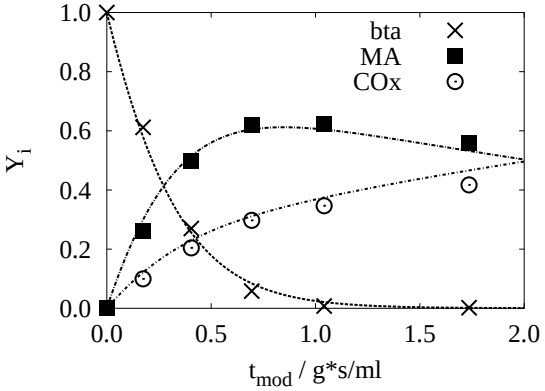

(a) Dimensionless molar fractions related to carbon

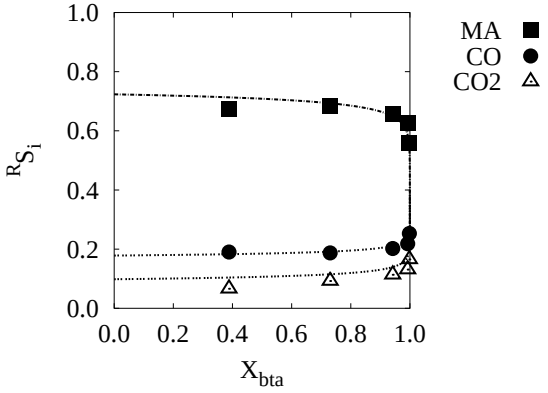

(b) Reactor selectivities related to carbon

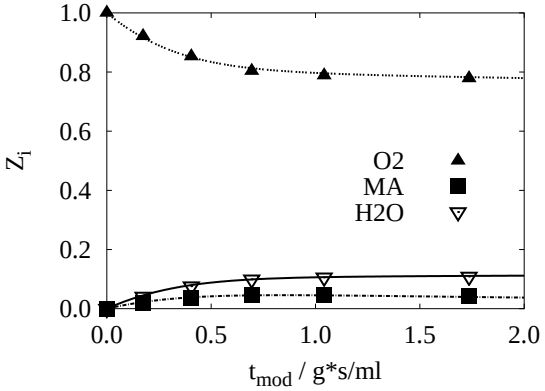

(c) Dimensionless molar fractions related to oxygen

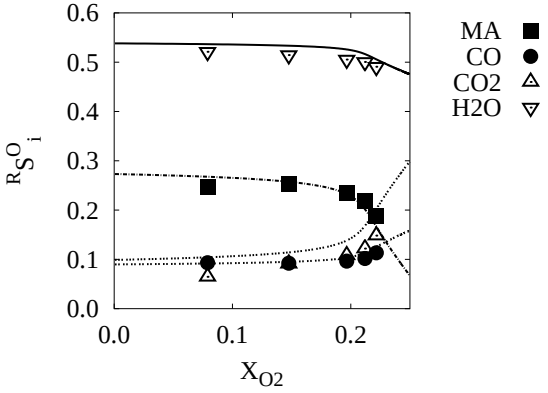

(d) Reactor selectivities related to oxygen

Fig. 4.1: *Partial oxidation of 1% n/n of n-butane in air at 400 °C over a VPO-50 catalyst. The dimensionless molar fractions are plotted against the modified residence time, the reactor selectivities against the conversion levels. The symbols represent the experimental values, the lines represent the calculations based on the modelled reaction kinetics.*

Fig. 4.1(a) shows the normalised dimensionless molar fractions related to carbon for the species *n*-butane, maleic anhydride and carbon oxides as a function of the modified residence time. These species were the only carbon containing species in significant amounts that were detected in the gas phase. There were also small amounts of acrylic and acetic acid. However, the acids showed yields below 1% and are, therefore, omitted in the plots.

At the reactor inlet ($t_{\mathrm{mod}} = 0$ (g s)/ml), the only carbon containing species was *n*-butane. The fraction of *n*-butane decreased steadily with increasing residence time. The initial slope of the curve of the dimensionless fractions of *n*-butane can be approximated by the differences in fraction and residence time of the first two experimental data points. Therefore, the activity parameter of this reaction can be estimated[1] to 0.41 mol/(s kg MPa). A higher value of the activity parameter corresponds to a lower residence time that is necessary to achieve a specific conversion level.

The *n*-butane feedstock is converted to maleic anhydride and carbon oxides as proposed by the two parallel reactions in the reaction network. The fraction of maleic anhydride increases up to a maximum of about 62% at a residence time of about 0.8 (g s)/ml. At this residence time, the conversion level of *n*-butane is about 96%. The maximum fraction and therefore also the maximum yield[2] of maleic anhydride has a value of slightly above 60%. The decrease in the fraction of maleic anhydride for higher residence times results from the consecutive reaction of maleic anhydride to carbon oxides. The fractions of the carbon oxides increase steadily with increasing residence time and reach a yield of 100% at sufficiently long residence times since they are the thermodynamically most favoured products.

The relative importance of the three reactions can be recognised in Fig. 4.1(b) where the reactor selectivities related to carbon are presented as functions of the conversion level of *n*-butane. The catalyst body selectivity[3] of maleic anhydride amounts to slightly above 70%. The catalyst body selectivity is a measure for the relative importances of the two parallel reactions of *n*-butane. A fraction of 30% of the *n*-butane reacts directly to carbon oxides. The reactor selectivity of maleic anhydride decreases slightly up to a conversion level of about 90%, followed by a sharp decrease at higher conversion levels. Compared to other partial oxidation reactions, the reactor selectivity remains at relatively high values even at a conversion level of about 90%. This behaviour is a sign that the stability of maleic anhydride towards subsequent oxidation reactions is high. A high stability is a desired property for the reactor performance and results from a high ratio of the rate constants of the formation reaction of maleic anhydride and of its consecutive oxidation. The sharp decrease in reactor selectivity of maleic anhydride for conversion levels above 90% results from the high fractions of maleic anhydride and low fractions of *n*-butane at these conversion levels. They influence the rates of the consecutive reaction and the formation reaction, respectively. For sufficiently high residence times, all *n*-butane and all maleic anhydride are converted to carbon oxides, and the reactor selectivity of maleic anhydride equals 0.

---

[1] $\left.\frac{\mathrm{d}Y_{\mathrm{HC}}}{\mathrm{d}t_{\mathrm{mod}}}\right|_{X_{\mathrm{HC}}=0} = -RT \times {}^{\mathrm{B}}k_{\mathrm{a}}$, see section 3.1.3 for details.

[2] The dimensionless normalised molar fractions equal the yields in case of products.

[3] It is assumed that external mass transport resistances in the laboratory reactor were negligible. Then the extrapolation of the reactor selectivities to zero conversion levels equal the catalyst body selectivities. See section 3.1.3 for details of the definition of catalyst body selectivities. The influences of external transport resistances are discussed in section 5.4.2.

The catalyst body selectivities of carbon monoxide and carbon dioxide have values of about 18% and 10%, respectively. The reactor selectivities increase only slightly for n-butane conversion levels below 90%, as it is expected considering the selectivity curve of maleic anhydride. The ratio of the selectivities and, therefore, the ratio of the fractions of carbon monoxide and carbon dioxide are about 1.8 to 1. For small conversion levels ($X \rightarrow 0$), almost no maleic anhydride is present in the gas phase and, therefore, the predominant formation of carbon oxides results from the total oxidation of n-butane. The ratio of the fractions of the carbon oxides at low conversion levels are thus directly related to the stoichiometric parameter s_{bta} of the total oxidation reaction of n-butane. A value of $s_{\mathrm{bta}} = 64\%$ results from the estimated fraction ratio. Per mole of n-butane that is converted to carbon oxides, 4×0.64 moles of carbon monoxide and 4×0.36 moles of carbon dioxide are formed. The fraction ratio of the carbon oxides decreases slightly with increasing conversion levels above 90%. The consecutive reaction gains importance and the stoichiometric parameter for the total oxidation reaction of maleic anhydride must be lower than the corresponding constant for the total oxidation of n-butane to result in the decrease in the fraction ratio. The formation of carbon dioxide instead of carbon monoxide in the total oxidation of maleic anhydride is therefore more favoured than the formation of carbon dioxide instead of carbon monoxide directly from n-butane.

The two plots discussed above show the fractions and selectivities related to carbon atoms. The next two plots in Fig. 4.1(c) and Fig. 4.1(d) focus on the oxygen containing species and the corresponding reactor selectivities. Fig. 4.1(c) displays the profiles of the dimensionless fractions related to oxygen. Oxygen was the only oxygen containing species in the reactor feed and therefore equalled one for zero residence time. The conversion level of oxygen at the residence time where the maximum yield of maleic anhydride is achieved is slightly above 20%. Thus, the sum of the yields of all products related to oxygen cannot be higher than 20% at this residence time. The maximum fraction of maleic anhydride related to oxygen, for example, is 5%. The yield of water increases steadily since water is formed in every individual oxidation reaction and is, like the carbon oxides, an end product. For sufficiently long residence times, the fraction of maleic anhydride equals 0 again and both fractions of oxygen and water reach limiting values since no carbon containing species are present in the gas phase that could be further oxidised. The limiting values depend on the ratio of the fractions of carbon monoxide and carbon dioxide formed.

In Fig. 4.1(d), the reactor selectivities related to oxygen are presented as functions of the conversion level of oxygen. The selectivity of water has the highest value of about 54%, although water contains only one oxygen atom. Water is formed in each of the oxidation reactions and the formation is consequently coupled to the conversion of each individual hydrocarbon. The high value of the selectivity of water results from the necessary oxidative dehydrogenation during the oxidation reactions. For the conversion of n-butane to maleic anhydride, for example, eight hydrogen atoms have to be removed from the hydrocarbon resulting in the formation of four water molecules. The selectivity of maleic anhydride related to oxygen has a value of about 27%.

At conversion levels of oxygen of above 20%, the selectivity of maleic anhydride decreases and the selectivities of the carbon oxides increase sharply. The conversion level of oxygen of 20% corresponds to the conversion level of n-butane of 90%. For higher conversion levels, the consecutive reaction of maleic anhydride becomes dominant. The selectivity of carbon dioxide increases faster than the selectivity of carbon monoxide. This

can be attributed to the two oxygen atoms in a carbon dioxide molecule. Only one oxygen atom is present in a carbon monoxide molecule. The selectivity of carbon dioxide must increase twice as fast as the selectivity of carbon monoxide to result in a constant ratio of the fractions of both species.

The decrease in the reactor selectivity of water for conversion levels of oxygen of above 20% results also from the consecutive reaction. In this reaction of maleic anhydride to carbon oxides, only two hydrogen atoms have to be removed. This amount is small compared to the eight hydrogen atoms that have to be removed from *n*-butane to form maleic anhydride.

4.2.1 Quantification of Reaction Kinetics and Catalyst Parameters

The lines in Fig. 4.1 represent the fraction profiles and reactor selectivities calculated by using the kinetic model that was developed in the present work. The calculated and experimentally determined profiles are in good agreement. Equation (3.39) was adopted for the partial oxidation of *n*-butane through removing the inhibition expressions for *n*-butenes and IP, and the rate equation

$$r_{i,j} = \frac{k_{i,j} p_i \sqrt{p_{\mathrm{O2}}/p^+}}{1 + b_{\mathrm{bta}} p_{\mathrm{bta}} + b_{\mathrm{H2O}} p_{\mathrm{H2O}}} \tag{4.1}$$

was obtained. The formulation of three rate equations is necessary to represent the three reactions. The model consists of 10 parameters that had to be determined: three rate constants, three activation energies, two inhibition constants and two stoichiometric parameters. All experiments carried out at temperatures between 360 °C and 420 °C and with fractions of *n*-butane in the feed between 1.0 and 2.5% n/n were used for the parameter determination. Therefore, 680 experimental values were available for the determination of the 10 parameters. The parameter estimation resulted in the residual error of $\chi^2 = 870$. The highest value of the cross correlation parameters is 0.79 for the rate constant $k_{\mathrm{bta,COx}}$ and the inhibition constant b_{bta}. The cross correlation parameters are all below a value of 0.9, indicating the absence of significant correlations between the estimated parameters. The kinetic and stoichiometric parameters for the oxidation of *n*-butane over the VPO-50 catalyst as well as their estimated confidence limits for a probability of 95% are listed in Tab. 4.1. The calculated enthalpies of reaction are also presented in the table.

i	j	$k_{i,j}(420\ ^\circ\mathrm{C})/k^+$		$E_{\mathrm{A},i,j}/E_{\mathrm{A}}^+$		$\frac{\Delta_{\mathrm{R}}H_{i,j}}{\Delta_{\mathrm{R}}H^+}$	other parameters		
bta	MA	0.948	±0.057	84.5	±3.2	−1266	b_{bta}/b^+	471	±50
bta	COx	0.422	±0.027	113.9	±4.1	−1931	b_{H2O}/b^+	6.2	±6.3
MA	COx	0.0925	±0.0092	136	±16	−892	s_{bta}	0.6448	±0.0087
							s_{MA}	0.444	±0.026

Tab. 4.1: *Kinetic, stoichiometric and thermodynamic parameters for the oxidation of n-butane over a VPO-50 catalyst. The reference values are* $k^+ = 1\,\frac{\mathrm{mol}}{\mathrm{s\,kg\,MPa}}$, $E_{\mathrm{A}}^+ = 1\,\frac{\mathrm{kJ}}{\mathrm{mol}}$, $\Delta_{\mathrm{R}}H^+ = 1\,\frac{\mathrm{kJ}}{\mathrm{mol}}$ *and* $b^+ = 1\,\mathrm{MPa}^{-1}$.

A measure of the quality of the parameter fit are parity plots which are presented in Fig. 4.2. All 680 experimental values are plotted in seven parity plots, one for each species and an extra plot for the absolute heat of reaction. In each individual plot, the calculated values are plotted against the corresponding experimental values. In the absence of experimental errors, the data points for the best model would be on the diagonal axis that is shown in each plot. Since all experimental values are falsified by statistical errors, deviations of the data points from the diagonal axis can be expected that correspond to the experimental errors, even for a perfect mathematical description of the physical reality. To quantify the deviations in each parity plot, two additional lines confine the area with relative errors smaller than 20%.

The absolute heat of reaction equals the cumulative heat flow out of the catalyst bed for all reactions up to the specified sampling port. In this case, the "experimental" values correspond to the heat flux that is calculated by summing up the contributions of all detected species (experimentally determined concentrations multiplied by the corresponding calculated heats of formation). The "calculated" values use the concepts as reported in section 3.4.2.

Most of the data points showed deviations smaller than 20%, especially the higher values of the fraction of maleic anhydride were well represented by the calculation. There were no visible systematic deviations between experimental and calculated values, except for a small deviation of the fractions of oxygen for values of about 0.4.

The kinetic constants in Tab. 4.1 have been calculated for a temperature of 420 °C. The corresponding values for the previously presented experiment that was carried out at a temperature of 400 °C result to $k_{\mathrm{bta,MA}} = 0.613\,\frac{\mathrm{mol}}{\mathrm{s\,kg\,MPa}}$, $k_{\mathrm{bta,COx}} = 0.234\,\frac{\mathrm{mol}}{\mathrm{s\,kg\,MPa}}$ and $k_{\mathrm{bta,MA}} = 0.0458\,\frac{\mathrm{mol}}{\mathrm{s\,kg\,MPa}}$. In all experiments, the pressure was 1.3 bar and the feed fraction of oxygen amounted to 20% n/n. Thus, the root expression containing the oxygen dependence in equation (4.1) equals unity in all experiments at zero conversion levels. For a typical conversion level of oxygen of 20%, the root expression still equals 0.89. Since no water was fed to the reactor, no inhibition of water has to be considered for zero conversion levels. The activity parameter of the partial oxidation of *n*-butane results in

$$ {}^{\mathrm{B}}k_{\mathrm{a}}(\mathbf{p}_0, T) = (r_{\mathrm{bta,MA}} + r_{\mathrm{bta,COx}})\big|_{\mathbf{p}_0,T} = \frac{k_{\mathrm{bta,MA}}(T) + k_{\mathrm{bta,COx}}(T)}{1 + b_{\mathrm{bta}} p_{\mathrm{bta},0}}. \tag{4.2} $$

The activity parameter depends on the reaction temperature and the partial pressure of *n*-butane in the feed. For the oxidation of 1% n/n of *n*-butane at 400 °C, the activity parameter amounts to 0.53 $\frac{\mathrm{mol}}{\mathrm{s\,kg,MPa}}$, which is slightly higher than estimated from the differences in the plot of dimensionless fractions in the previous section.

The catalyst body selectivity of maleic anhydride for $X \to 0$ results in

$$ {}^{\mathrm{B}}S_{\mathrm{MA}}(X \to 0) = \left.\frac{R_{\mathrm{MA}}}{-R_{\mathrm{bta}}}\right|_{\mathbf{p}_0,T} = \left.\frac{r_{\mathrm{bta,MA}}}{r_{bta,MA} + r_{bta,COx}}\right|_{\mathbf{p}_0,T} = \left.\frac{k_{\mathrm{bta,MA}}}{k_{\mathrm{bta,MA}} + k_{\mathrm{bta,COx}}}\right|_{T} \tag{4.3} $$

and depends only on the temperature. At 400 °C, the calculated catalyst body selectivity of maleic anhydride amounts to 72%. The corresponding calculated values for carbon monoxide and carbon dioxide are 18% and 10%, respectively. These values agree with the qualitative considerations carried out in the previous section in the discussion of the plot of the reactor selectivities.

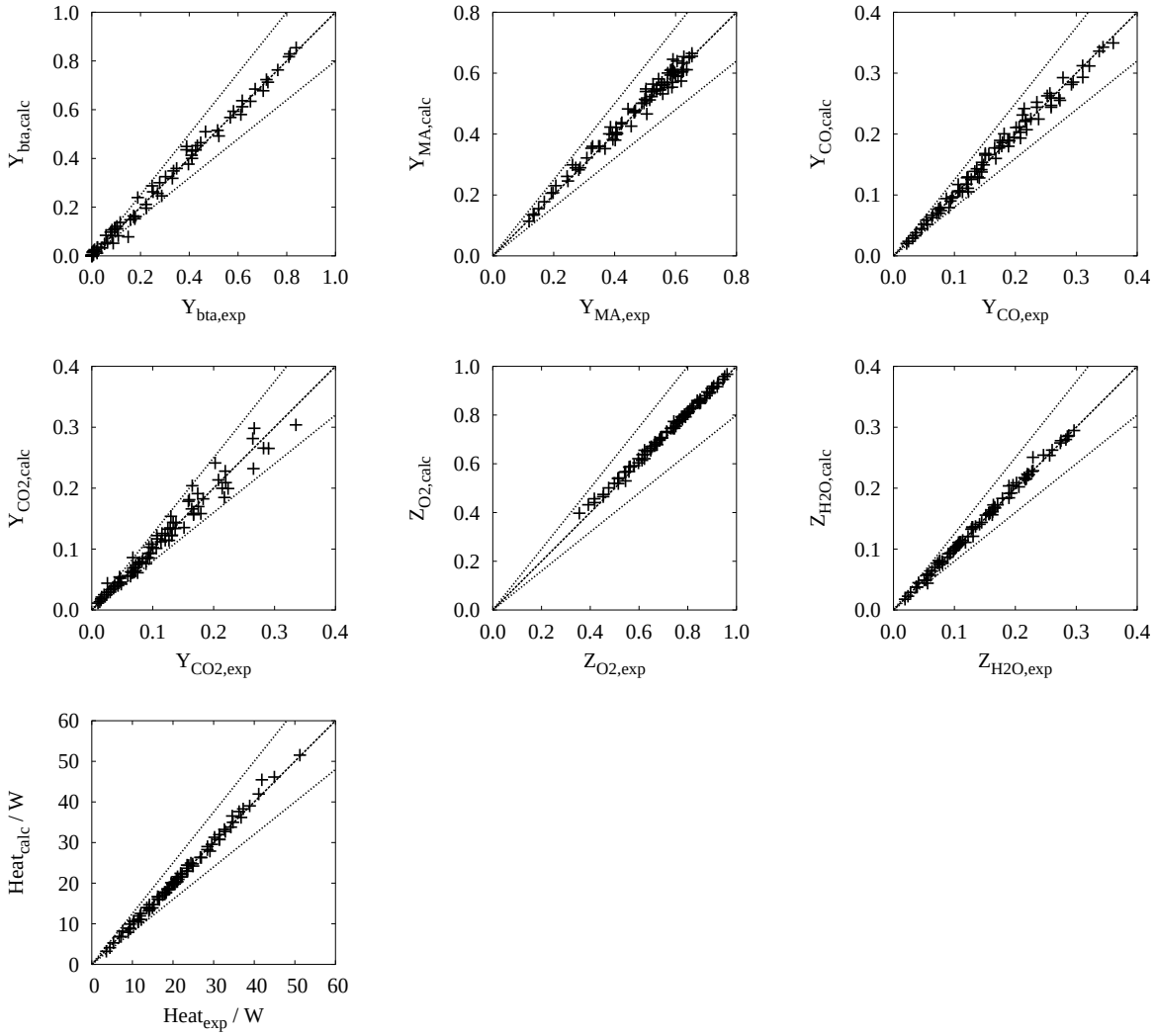

Fig. 4.2: *Parity plots for the oxidation of n-butane over a VPO-50 catalyst.*

The stability of maleic anhydride as an intermediate in the total oxidation of n-butane depends on the ratio of the two reaction rates for the formation of maleic anhydride and its total oxidation. The ratio of the reaction rates can be expressed as

$$\frac{r_{\mathrm{bta,MA}}}{r_{\mathrm{MA,COx}}} = \frac{k_{\mathrm{bta,MA}}}{k_{\mathrm{MA,COx}}} \times \frac{p_{\mathrm{bta}}}{p_{\mathrm{MA}}}. \tag{4.4}$$

This ratio is independent of the reactor type. It is a catalyst body property denoted as catalyst body stability of maleic anhydride

$${}^{\mathrm{B}}\lambda_{\mathrm{MA}} = \frac{k_{\mathrm{bta,MA}}}{k_{\mathrm{MA,COx}}}. \tag{4.5}$$

Its value depends on the temperature. At a temperature of 400 °C, it amounts to a value of about 13. A higher value denotes a higher stability of maleic anhydride and leads to a lower initial decrease in the reactor selectivity with increasing conversion levels.

The stoichiometric parameter for the total oxidation of n-butane equals $s_{\mathrm{bta}} = 64\%$. This value shows a good agreement with the estimation given in the previous section. The corresponding stoichiometric parameter for the total oxidation of maleic anhydride has a value of $s_{\mathrm{MA}} = 44\%$ and agrees also with the statement in the previous section that the relative amount of carbon monoxide which is formed in the total oxidation of maleic anhydride is smaller than the relative amount of carbon monoxide which is formed in the total oxidation of n-butane.

The enthalpies of reaction of the formation of maleic anhydride and the total oxidation of maleic anhydride are −1266 and −892 kJ/mol, respectively. The corresponding enthalpy of the total oxidation of n-butane (−1931 kJ/mol) deviates from the sum of the two latter values, which amounts to −2158 kJ/mol. It has to be considered that the different stoichiometric parameters for the two total oxidation reactions lead to different amounts of carbon monoxide and carbon dioxide. Even for residence times at which all maleic anhydride is completely oxidised, the relative amounts of the carbon oxides and, consequently, the total heat of reaction depend on the amount of maleic anhydride that was formed at lower residence times.

4.2.2 Variation of the Reaction Temperature

The oxidation of n-butane was investigated at reaction temperatures in the range from 360 up to 420 °C. The activity parameters, catalyst body selectivities and stability parameters of maleic anhydride depend on the temperature. The activity parameter always increases with increasing temperature since all rate constants increase. The activation energy of the formation of maleic anhydride equals 84.5 kJ/mol which is smaller than the corresponding value of 114 kJ/mol for the total oxidation of n-butane. Therefore, the catalyst body selectivity of maleic anhydride decreases with increasing temperature. The activation energy of the formation of maleic anhydride is also smaller than the activation energy of its total oxidation (136 kJ/mol). Therefore, also the stability of maleic anhydride decreases with increasing temperature. Both effects lead to a decrease in the maximum yield of maleic anhydride with increasing temperature. The temperature dependences of the activity parameter, the catalyst body selectivities and the stability are presented in Fig. 4.3. Because of the exponential dependence of the individual rate constants on the

temperature, the activity parameter also increases exponentially from a value of about 0.2 $\frac{\text{mol}}{\text{s kg MPa}}$ at 360 °C to a value of about 0.85 $\frac{\text{mol}}{\text{s kg MPa}}$ at 420 °C. The latter value is a factor of 4.25 higher than the value at the lower temperature. The catalyst body selectivity decreases from 78% to 69% in this temperature range. The catalyst body selectivities of the carbon oxides increase correspondingly. The stability parameter drops from a value of 24 to a value of about 10. The values are also listed in Tab. 4.2.

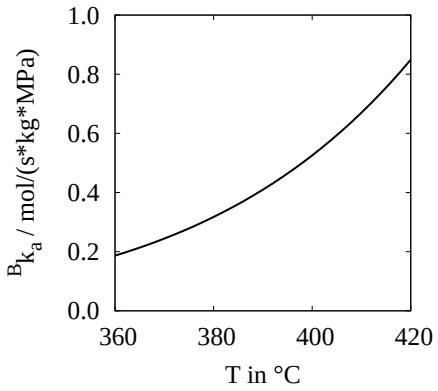

(a) Activity parameter

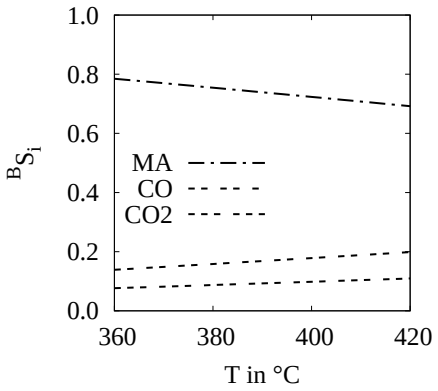

(b) Catalyst body selectivities

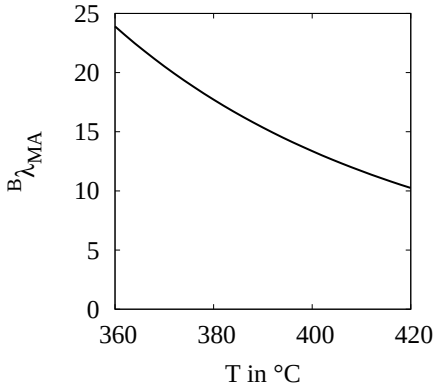

(c) Stability parameter

Fig. 4.3: *Activity parameter, catalyst body selectivities and stability of maleic anhydride as functions of the temperature for the partial oxidation of n-butane over a VPO-50 catalyst.*

It can be summarised that the kinetic model suggests that increasing the temperature decreases the modified residence time which is necessary to achieve the maximum yield of maleic anhydride. However, the value of the maximum yield also decreases with raising temperature.

The experimentally determined as well as the calculated fraction profiles and reactor selectivities at different temperatures are presented in Fig. 4.4. The fraction profiles of *n*-butane are plotted in Fig. 4.4(a). They show that the conversion rate increases with increasing temperature. Experiment and calculation show a good agreement. At a temperature of 420 °C, the conversion level is practically 100% at a modified residence time of about 0.7 (g s)/ml. At 360 °C, the conversion level is still about 90% at a modified residence time of 2 (g s)/ml. Fig. 4.4(c) shows the yields of maleic anhydride. Higher

temperatures lead to lower residence times at which the maximum yield is achieved. At 420 °C, the maximum yield is achieved at a residence time of about 0.5 (g s)/ml. At 360 °C, however, the maximum yield is not yet reached at 2 (g s)/ml. The value of the maximum yield decreases with increasing temperature as expected. However, as can be seen in Fig. 4.4(d), the calculated yield amounts to a value of about 70%. The maximum yields and their corresponding residence times are listed in Tab. 4.2. The maximum yield decreased from the estimated 70% at 360 °C to about 56% at 420 °C. The calculated maximum yields and their corresponding residence times agree well with the experimental values. The highest difference is about 3% absolute (see Fig. 4.4(d)). The reactor selectivities of maleic anhydride are presented in Fig. 4.4(b). The trends of the decreasing reactor selectivities with increasing temperatures are well represented by the calculations. However, the calculated values are about an absolute value of 3% higher than the experimental values. The experimental values of the reactor selectivities in the region of conversion levels below 80% are listed in Tab. 4.2 in the column named ${}^{\mathrm{R}}S_{\mathrm{MA}}^{\mathrm{const}}$. These values are about an absolute value of 4% smaller than the corresponding calculated catalyst body selectivities.

T in °C	${}^{\mathrm{B}}k_{\mathrm{a}}$ / $\frac{\mathrm{mol}}{\mathrm{s\,kg\,MPa}}$	${}^{\mathrm{B}}S_{\mathrm{MA}}$	${}^{\mathrm{B}}\lambda_{\mathrm{MA}}$	${}^{\mathrm{R}}S_{\mathrm{MA}}^{\mathrm{const}}$	${}^{\max}Y_{\mathrm{MA}}$	${}^{\max}t_{\mathrm{mod}}$ / $\frac{\mathrm{g\,s}}{\mathrm{ml}}$
360	0.19	78%	24	74%	(70%)	
380	0.32	75%	18	71%	(65%)	(1.6)
400	0.53	72%	13	68%	62%	0.8
420	0.85	69%	10	(65%)	56%	0.5

Tab. 4.2: *Calculated parameters of the oxidation of 1% n/n of n-butane over a VPO-50 catalyst at different temperatures. Values in parentheses are affected by large uncertainties.*

4.2.3 Variation of the Hydrocarbon Fraction in the Feed

The molar fraction of *n*-butane in the feed was varied between 1.0% and 2.5%. In this section, the experiments carried out at 400 °C with hydrocarbon fractions of 1.0, 1.5, 2.0 and 2.5% n/n in the feed are presented. The catalyst body parameters calculated for each of the feed compositions are listed in Tab. 4.3. The activity parameter depends on the partial pressure of *n*-butane in the feed because of the inhibiting effect of *n*-butane. The activity parameter decreases with increasing feed fraction from a value of 0.53 $\frac{\mathrm{mol}}{\mathrm{s\,kg\,MPa}}$ for a fraction of 1.0% to a value of 0.34 $\frac{\mathrm{mol}}{\mathrm{s\,kg\,MPa}}$ for a fraction of 2.5%. The factor between the lowest and highest value is 1.56. The catalyst body selectivity and the catalyst body stability of maleic anhydride depend only on the temperature and therefore have constant values of 72% and 13, respectively.

The fraction profiles and reactor selectivities for different feed fractions are presented in Fig. 4.5. The fraction profiles of *n*-butane are displayed in Fig. 4.5(a). Higher residence times are necessary to achieve the same conversion level for higher feed fractions. This behaviour results from the inhibition of the reaction by *n*-butane. It is well represented by the calculations. The residence time required for a maximum yield of maleic anhydride

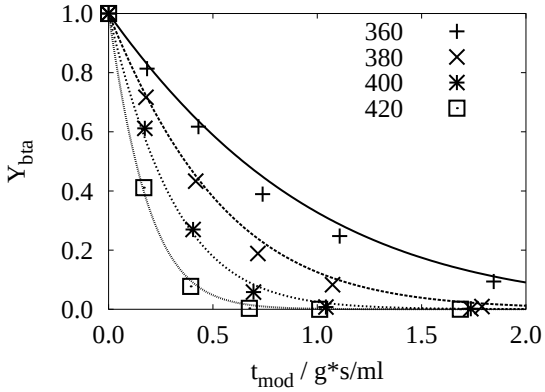

(a) Fraction profiles of *n*-butane

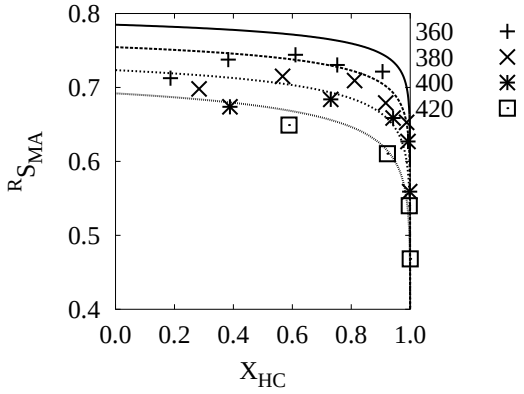

(b) Reactor selectivities of maleic anhydride

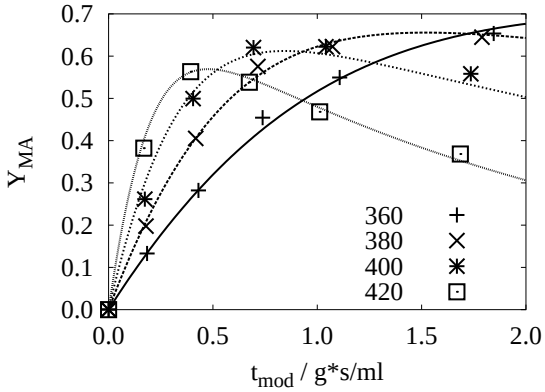

(c) Fraction profiles of maleic anhydride

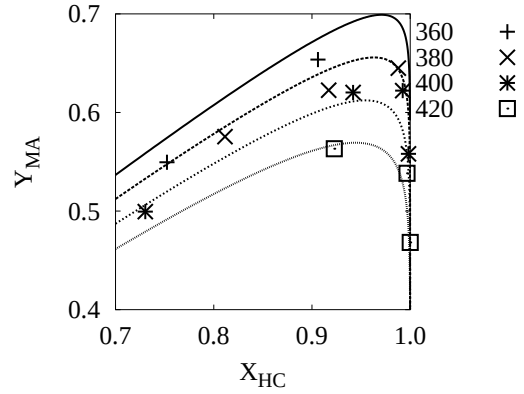

(d) Yields of maleic anhydride as a function of the conversion level

Fig. 4.4: *Variation of the reaction temperature (values are given in* °C*) in the oxidation of 1% n/n of n-butane in air. The normalised fractions of n-butane and maleic anhydride as functions of the modified residence time, reactor selectivities of maleic anhydride as functions of the conversion level and the yield of maleic anhydride also as functions of the conversion level are presented.*

also increases with increasing hydrocarbon fraction (Fig. 4.5(c)). For a given residence time below 1 (g s)/ml, the yields of maleic anhydride increase with decreasing feed fraction. Above this residence time, the yields of maleic anhydride drop with decreasing feed fraction. The calculated values at the inversion at 1 (g s)/ml are almost identical. At the same residence time, the experimental values range from 60 to 63%. The differences in the experimental values are in the range of the estimated relative errors of the measurements of 5%. Obviously, experiment and calculation show a good agreement.

Fig. 4.5(d) shows the yields of maleic anhydride as functions of the conversion level of *n*-butane. The constant catalyst body selectivity and catalyst body stability of maleic anhydride results in a constant relation between yield of maleic anhydride and conversion level of *n*-butane. A maximum yield of maleic anhydride of 61% at a conversion level of 96% is predicted, independently of the feed composition. The maximum yields determined experimentally were in the range of 60 to 63%. The difference between these two values is in the same order as the estimated measuremental errors.

The reactor selectivities are presented in Fig. 4.5(b). The calculated catalyst body selectivity has a value of 72%. The reactor selectivities at conversion levels between 20% and 70% are about 68%. The selectivity profiles can be regarded as being independent of the hydrocarbon fraction in the feed.

It can be concluded that an increase in the hydrocarbon fraction of the feed has no influence on the value of the maximum yield of maleic anhydride, but a higher residence time is required to obtain this maximum yield.

$x_{\mathrm{bta},0}$	${}^{\mathrm{B}}k_{\mathrm{a}}$ / $\frac{\mathrm{mol}}{\mathrm{s\,kg\,MPa}}$	${}^{\mathrm{B}}S_{\mathrm{MA}}$	${}^{\mathrm{B}}\lambda_{\mathrm{MA}}$	${}^{\mathrm{R}}S_{\mathrm{MA}}^{\mathrm{const}}$	${}^{\mathrm{max}}Y_{\mathrm{MA}}$	${}^{\mathrm{max}}t_{\mathrm{mod}}$ / $\frac{\mathrm{g\,s}}{\mathrm{ml}}$
1.0%	0.53	72%	13	68%	62%	0.8
1.5%	0.44	72%	13	68%	63%	0.9
2.0%	0.38	72%	13	69%	62%	1.0
2.5%	0.34	72%	13	69%	60%	1.4

Tab. 4.3: *Calculated parameters of the oxidation of n-butane at a temperature of 400 °C over a VPO-50 catalyst with different molar fractions of n-butane in the feed.*

4.2.4 Comparison with Results in the Literature

There are some literature references where kinetic models were proposed for the oxidation of pure *n*-butane. The investigations were carried out with different types of VPO catalysts. Nevertheless, the order of magnitude of the parameters can be compared with those obtained from the present work.

The general reaction progress and the absence of organic by-products experienced in the present work show a good agreement with the reports in the literature. The yields and selectivities are similar to those that are reported in the literature. Four examples are given:

1. Hodnett presents a plot of reactor selectivities as functions of the conversion level for many experimental values from the literature [21]. The best values show a catalyst

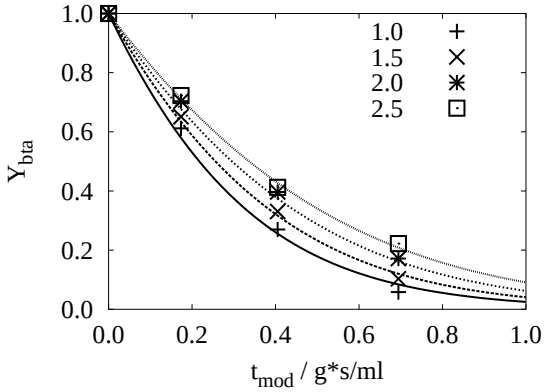

(a) Fraction profiles of *n*-butane

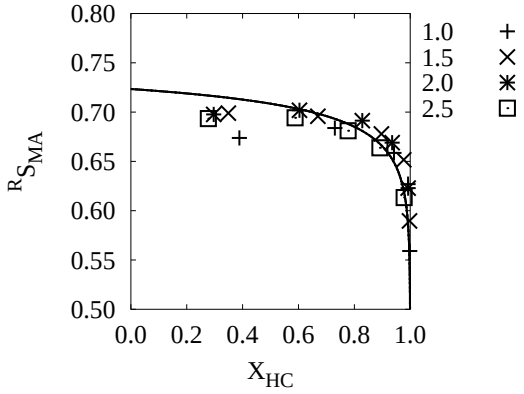

(b) Reactor selectivities of maleic anhydride

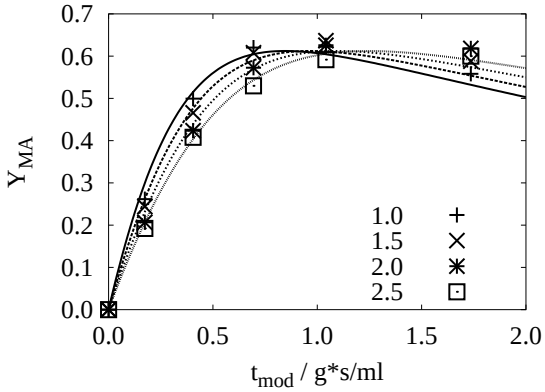

(c) Fraction profiles of maleic anhydride

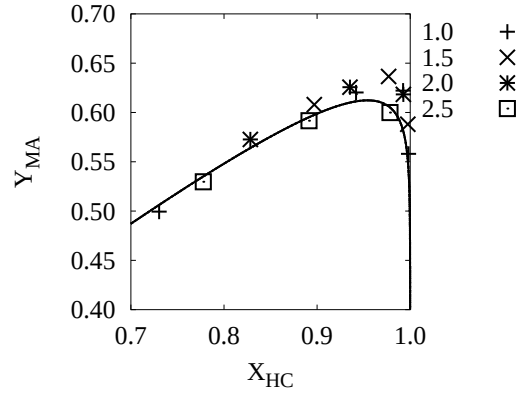

(d) Yields of maleic anhydride as functions of the conversion level

Fig. 4.5: *Variation of the n-butane fraction in the feed (values are given in % n/n) at 400 °C. The normalised fractions of n-butane and maleic anhydride as functions of the modified residence time, the reactor selectivities of maleic anhydride as functions of the conversion level and the yields of maleic anhydride as functions of the conversion level are presented.*

body selectivity of about 80% and a maximum yield of 62% at a conversion level of 95%. These values are almost identical to the values determined in the present work with catalyst body selectivities of about 75% and a maximum yield of about 65% at 380 °C.

2. Quast experimentally determined a maximum yield of about 63% at a temperature of 380 °C. The modified residence time to achieve maximum yield was about 5 (g s)/ml. The conversion level of *n*-butane had a value of about 96% [16]. In the present work, a maximum yield of about 65% was achieved at a residence time of about 1.5 (g s)/ml and a conversion level of about 96% with the VPO-50 catalyst at 380 °C. Except for the higher activity of the VPO-50 catalyst, the experimental results show good agreement.

3. In [18], a maximum yield of maleic anhydride of 60% was achieved at a conversion level of about 92% at a temperature of 420 °C. A feed fraction of 0.654% n/n of *n*-butane and 10.25% n/n of oxygen was used. In the present work, a maximum yield of 56% was achieved at 420 °C with 1% n/n of *n*-butane and 20% n/n of oxygen. The conversion level was 96%.

4. Becker achieved a yield of maleic anhydride of 57% at a conversion level of about 90% at 420 °C with a molar fraction of *n*-butane of 1.5% in the feed. This corresponds well to the yield of 55% that was achieved in the present work at the same temperature but with a feed fraction of 1% [8].

In most of the investigations, the trends in the variation of temperature and feed fraction were investigated at constant residence times. In those cases, conversion levels, reactor selectivities and yields change simultaneously. No statement can be given to what extent the reactor selectivity had changed because of the change in the conversion level and to what extent it had changed because of the change in catalyst body properties. Quast determined catalyst body parameters from a first order model [16], Becker [8] and Uihlein [29] presented Eley-Rideal models from which the catalyst body parameters can be determined.

Some catalyst body parameters, activation energies and inhibition constants found in or derived from kinetic parameters in the literature are compiled in Tab. 4.4. The activity parameters of the present work, from Uihlein, Becker and Quast are all of the same magnitude. The catalyst body selectivities range between 57% and 86% and the catalyst body stabilities range between 3.8 and 311. The models of Uihlein and Quast show the best agreement with the present catalyst body properties.

The activation energies of the desired reaction of *n*-butane to maleic anhydride are in the range of 60 to 114 kJ/mol. The activation energy of 85 kJ/mol as it was determined in the present work is well inside this range. The activation energies of the total oxidation of *n*-butane range between 77 and 132 kJ/mol. The value of 114 kJ/mol determined in the present work is the second highest value of the list. The determined value of 136 kJ/mol for the activation energy of the total oxidation of maleic anhydride is well in the range of 46 to 162 kJ/mol of all activation energies found in the literature.

Uihlein and Becker used nearly the same Eley-Rideal model as it was used in the present work. The only difference is the power of the partial pressure of oxygen for the consecutive reaction in the model of Uihlein which amounts to 0.25 instead of 0.5 that

was used in the present work and in the work by Becker. The inhibition constants of the Eley-Rideal approaches can be compared. The inhibition constants for *n*-butane that were determined in the present work and the constants that were determined by Uihlein are in the same order of magnitude. Becker reports a constant two orders of magnitude higher. The inhibition constants of water in the three models differ strongly.

(a) References

	authors	source	model type
thesis	present thesis		Eley–Rideal
Uihlein	Uihlein	[29]	Eley–Rideal
Becker	Becker	[8]	Eley–Rideal
Quast	Quast	[16]	first order
Sharma	Sharma, Cresswell	[27]	Redox
Dente	Dente et al.	[17]	Langmuir-Hinshelwood
Varma	Varma, Saraf	[31]	Mars van Krevelen
Bej	Bej, Rao	[24]	Mars van Krevelen

(b) Properties

	parameters at 400 °C			$E_{A,i,j}$ / kJ/mol			b_i / MPa^{-1}	
	${}^{B}k_a$ / $\frac{mol}{s\,kg\,MPa}$	${}^{B}S_{MA}$	${}^{B}\lambda_{MA}$	bta,MA	bta,COx	MA,COx	bta	H2O
thesis	0.53	72%	13	85	114	136	471	6
Uihlein	0.64	76%	3.8	114	132	97	680	580
Becker	1.35	57%	311	97	96	117	45900	34700
Quast	0.21	70%	15					
Sharma	40.7	86%		93	93	155		
Dente				79		48		
Varma				60	77	46		
Bej				103	112	162		

Tab. 4.4: *Comparison of catalyst body parameters, activation energies and inhibition constants taken from the present work and derived from kinetic parameters in published studies.*

It can be concluded that the present investigations agree well with the investigations carried out elsewhere. The best agreement was found with the investigations by Uihlein and Quast.

4.3 Oxidation of *n*-Butenes over VPO-50

There are fewer articles in the literature available about the oxidation of *n*-butenes than about the oxidation of *n*-butane. Apart from Quast [16] who used first order rate equations, no recent articles about the reaction kinetics of the oxidation of *n*-butenes were found in the literature. Quast proposed the reaction network which has also been used in the present work. The reaction network is presented in section 3.3.1 and is displayed

in Fig. 3.6. In contrast to the oxidation of *n*-butane, additional organic intermediates are formed during the oxidation of *n*-butenes which are lumped together into the pseudo-species IP.

The experiments in the present work were carried out with 1-butene as the hydrocarbon feedstock. The VPO-50 catalyst type was used. The temperature was varied in a range from 340 to 420 °C. The feed fractions were varied between 1.0% and 2.5% n/n of 1-butene in air.

The fraction profiles and reactor selectivities concerning the partial oxidation of 1-butene at 400 °C with a molar fraction of 1% of 1-butene in the feed are presented in Fig. 4.6. Fig. 4.6(a) shows the fraction profiles of *n*-butenes, intermediates (IP), maleic

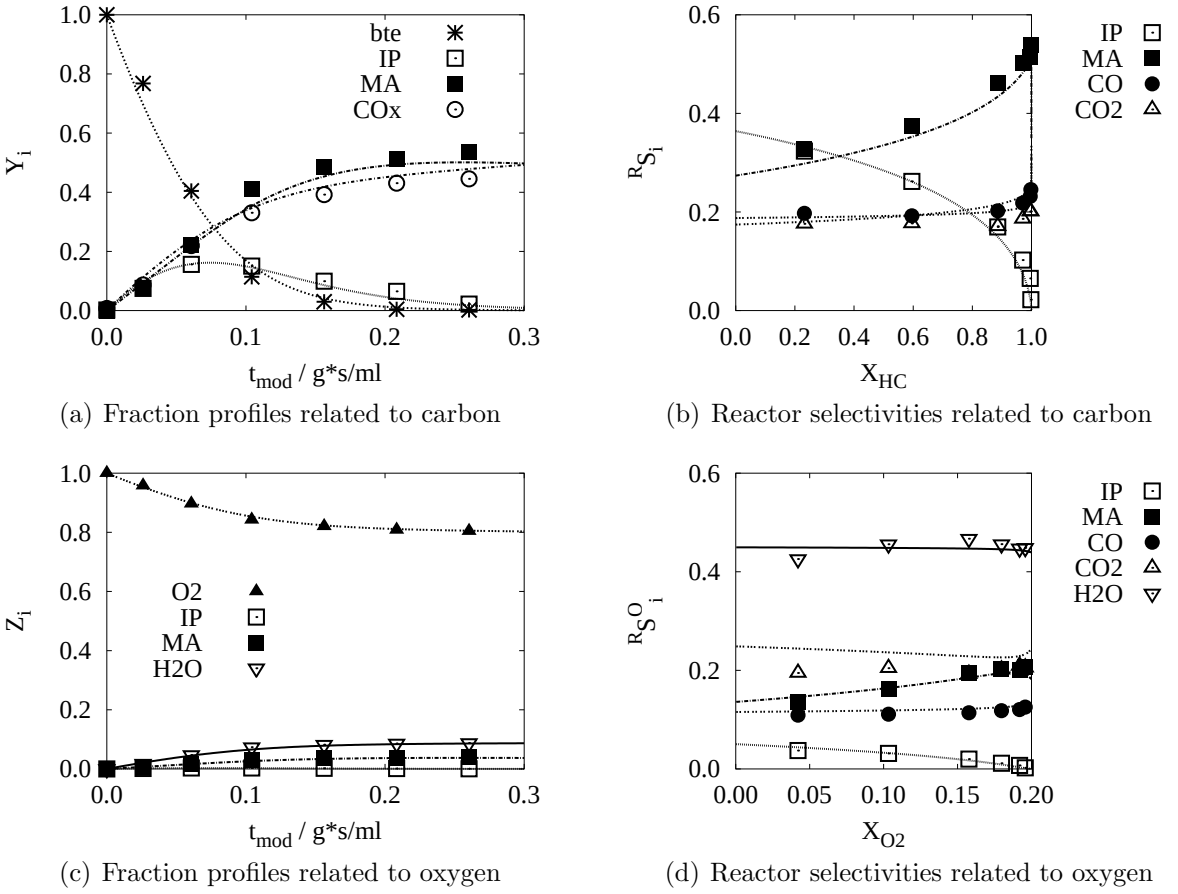

(a) Fraction profiles related to carbon

(b) Reactor selectivities related to carbon

(c) Fraction profiles related to oxygen

(d) Reactor selectivities related to oxygen

Fig. 4.6: *Partial oxidation of 1% n/n of 1-butene in air at 400 °C over a VPO-50 catalyst. The fraction profiles are plotted against the modified residence time, the reactor selectivities against the conversion levels. The symbols represent the experimental values, the lines represent the calculations based on the modelled reaction kinetics.*

anhydride and carbon oxides as functions of the modified residence time. At the reactor inlet, 1-butene is the only carbon containing species. It is completely converted at a modified residence time of about 0.2 (g s)/ml. The necessary residence time for complete conversion of *n*-butane for the same reaction conditions is about 1 (g s)/ml. At the same

flow rate, the mass of catalyst in the reactor must be four times higher in case of the *n*-butane oxidation to achieve complete conversion. The graphical estimation of the activity parameter of the *n*-butenes oxidation results in ${}^{\mathrm{B}}k_{\mathrm{a}} = 2.29\ \frac{\mathrm{mol}}{\mathrm{s\,kg\,MPa}}$. That is a factor of 4.3 higher than the corresponding activity parameter of the oxidation of *n*-butane.

The yield of organic intermediates (IP) shows a maximum at a residence time of about 0.08 (g s)/ml with a value below 20%. At residence times above 0.25 (g s)/ml, organic intermediates are no longer present in the gas phase.

The experimentally determined yield of maleic anhydride increases steadily with increasing modified residence time. No maximum of the yield was reached in the presented experiment. Experiments at other temperatures showed that the oxidation of maleic anhydride to carbon oxides results in the existence of a maximum at higher residence times. The calculated yields of maleic anhydride show a maximum yield of about 50% at a residence time of about 0.27 (g s)/ml. The highest yield of maleic anhydride that was experimentally determined was about 53%. This value is clearly lower than the maximum yield of 62% that was achieved in the oxidation of *n*-butane.

The reactor selectivities of IP, maleic anhydride and the carbon oxides as functions of the conversion level of *n*-butenes are presented in Fig. 4.6(b). The catalyst body selectivity of IP and maleic anhydride are about 36% and 27%, respectively. Therefore, 36% of the *n*-butenes are converted to IP, 27% are directly converted to maleic anhydride and 37% of the *n*-butenes are directly oxidised to carbon oxides. The intermediates IP in the oxidation of *n*-butenes are not as stable as maleic anhydride in the oxidation of *n*-butane. The reactor selectivity of IP in the *n*-butenes conversion decreases faster with increasing conversion level than the reactor selectivity of maleic anhydride in the *n*-butane conversion. Part of IP is converted to maleic anhydride. This leads to an increase in the reactor selectivity of maleic anhydride up to a conversion level of almost 100%. The stability of maleic anhydride upon conversion of *n*-butenes is higher than in case of the conversion of *n*-butane. For sufficiently high residence times, the reactor selectivity of maleic anhydride decreases to a value of 0.

The reactor selectivity of the carbon oxides remains almost constant up to a conversion level of about 70%. At this conversion level, the maximum yield of IP is achieved. Both, carbon monoxide and carbon dioxide have equal reactor selectivities up to this conversion level. The stoichiometric parameter for the total oxidation of 1-butene must therefore be about 50%. At a conversion level of about 90%, the reactor selectivity of carbon dioxide is significantly smaller than the reactor selectivity of carbon monoxide. At this conversion level, IP can be expected to be the main source for the formation of carbon oxides, and the stoichiometric parameter of the total oxidation of IP must be significantly above 50%.

Fig. 4.6(c) shows the fraction profiles related to oxygen. The conversion level of oxygen results in a value of about 20% when all *n*-butenes are converted. Only small yields of IP and maleic anhydride related to oxygen are achieved. Most of the oxygen is used for the oxidative dehydrogenation. Fig. 4.6(d) shows the reactor selectivities related to oxygen. The reactor selectivity of water has an almost constant value of about 45%. This corresponds to the relative amount of oxygen that is used for the oxidative dehydrogenation of the hydrocarbons. The selectivity of water in the conversion of *n*-butenes is smaller than the corresponding selectivity with a value of 54% in the conversion of *n*-butane. The higher selectivity of water in the conversion of *n*-butane can be attributed to the higher number of hydrogen atoms in the *n*-butane molecules that have to be removed.

4.3.1 Quantification of Reaction Kinetics and Catalyst Parameters

The calculated lines in the plots of Fig. 4.6 result from reaction kinetics with parameters that were determined for the partial oxidations of pure 1-butene, pure *n*-butane and all mixtures thereof. From the experiments with pure *n*-butane, only those were considered that were carried out after the catalyst had been subjected to a 1-butene flow. The catalyst changes its behaviour in the conversion of *n*-butane irreversibly after it has been used for the conversion of *n*-butenes. These irreversible changes are discussed in section 4.8. Fig. 4.6 shows that calculation and experiment are in good agreement despite the fact that no kinetic parameters were determined for the oxidation of pure *n*-butenes alone. Since the agreement was very good, a parameter estimation for the conversion of pure *n*-butenes was omitted. In Tab. 4.5, the parameters concerning the conversion of *n*-butenes that are extracted from the parameter set for the conversion of the mixtures are presented.

i	j	$k_{i,j}(420\ ^\circ\mathrm{C})/k^+$		$E_{\mathrm{A},i,j}/E_\mathrm{A}^+$		$\frac{\Delta_\mathrm{R}H_{i,j}}{\Delta_\mathrm{R}H^+}$	other parameters		
bte	IP	2.89	±0.20	71.0	±6.9	−245	b_bte/b^+	1096	±117
bte	MA	2.29	±0.20	80.7	±8.8	−1150	b_IP/b^+	0	±310
bte	COx	2.70	±0.18	58.7	±2.9	−1996	b_H2O/b^+	0	±8.4
IP	MA	3.53	±0.37	56	±14	−905	s_bte	0.482	±0.012
IP	COx	1.39	±0.25	147	±20	−1355	s_IP	0.826	±0.073
MA	COx	0.155	±0.016	54	±12	−858	s_MA	0.472	±0.040

Tab. 4.5: *Kinetic, stoichiometric and thermodynamic parameters for the oxidation of n-butenes over a VPO-50 catalyst. The reference values are* $k^+ = 1\,\frac{\mathrm{mol}}{\mathrm{s\,kg\,MPa}}$, $E_\mathrm{A}^+ = 1\,\frac{\mathrm{kJ}}{\mathrm{mol}}$, $\Delta_\mathrm{R}H^+ = 1\,\frac{\mathrm{kJ}}{\mathrm{mol}}$ *and* $b^+ = 1\,\mathrm{MPa}^{-1}$.

Because of the normalised oxygen expression in the rate equations and because no water was fed to the reactor, the activity parameter for the experimental reaction conditions in the present work equals

$$ {}^\mathrm{B}k_\mathrm{a}(T, p_\mathrm{bte,0}) = \frac{k_\mathrm{bte,IP}(T) + k_\mathrm{bte,MA}(T) + k_\mathrm{bte,COx}(T)}{1 + b_\mathrm{bte} p_\mathrm{bte,0}}. \tag{4.6} $$

For a temperature of 400 °C and a feed fraction of *n*-butenes of 1% n/n, the activity parameter equals 2.27 $\frac{\mathrm{mol}}{\mathrm{s\,kg\,MPa}}$. The estimation of the activity parameter from the plots in the last section was 2.29 $\frac{\mathrm{mol}}{\mathrm{s\,kg\,MPa}}$.

The catalyst body selectivities of IP and maleic anhydride amount to 36% and 27%, respectively. The catalyst body selectivity of maleic anhydride cannot be compared to the much higher value of 72% for the oxidation of *n*-butane, since some of the IP that is formed from 27% of the *n*-butenes is also converted to maleic anhydride. A partial catalyst body selectivity can be defined that quantifies the relative amount of the fraction of IP that can be converted to maleic anhydride by

$$ {}^\mathrm{B}_\mathrm{IP}S_\mathrm{MA} = \frac{r_\mathrm{IP,MA}}{r_\mathrm{IP,MA} + r_\mathrm{IP,COx}} = \frac{k_\mathrm{IP,MA}(T)}{k_\mathrm{IP,MA}(T) + k_\mathrm{IP,COx}(T)}. \tag{4.7} $$

The partial catalyst body selectivity of maleic anhydride from IP depends solely on the temperature. It amounts to 80% for a temperature of 400 °C. If no further oxidation of maleic anhydride is considered, a total selectivity of maleic anhydride can be obtained after total conversion of all *n*-butenes and IP of

$$ {}^{\mathrm{B}}S_{\mathrm{MA}}^{\max} = {}^{\mathrm{B}}S_{\mathrm{MA}} + {}^{\mathrm{B}}S_{\mathrm{IP}} \times {}^{\mathrm{B}}_{\mathrm{IP}}S_{\mathrm{MA}} = 56\%. \tag{4.8} $$

This can be regarded as a hypothetical catalyst body selectivity of maleic anhydride and can be compared to the catalyst body selectivity of maleic anhydride of the *n*-butane oxidation of 72%. The parallel reaction of the *n*-butenes directly to carbon oxides is responsible for the lower yields that are experienced in the partial oxidation of *n*-butenes. The formation of the intermediate products IP leads to a loss of hydrocarbon material in the total oxidation of $0.27 \times 0.20 = 5\%$ and cannot be regarded as the reason for lower yields.

Maleic anhydride is formed through oxidation of *n*-butenes and IP. No overall stability parameter can be defined. Instead, partial stabilities have to be introduced. A partial stability of a species i related to its formation by conversion of species j is defined as

$$ {}^{\mathrm{B}}_{j}\lambda_{i} = \frac{k_{\mathrm{j,i}}}{\sum_{l} k_{\mathrm{i,l}}}. \tag{4.9} $$

The partial stability of IP that is formed by conversion of *n*-butenes equals

$$ {}^{\mathrm{B}}_{\mathrm{bte}}\lambda_{\mathrm{IP}} = \frac{k_{\mathrm{bte,IP}}}{k_{\mathrm{IP,MA}} + k_{\mathrm{IP,COx}}} \tag{4.10} $$

and amounts to 0.61 for a reaction temperature of 400 °C. The low amount of this stability compared to the corresponding stability of maleic anhydride in the partial oxidation of *n*-butane with a value of 13 explains the low value of the maximum yield of IP of about 17% despite the catalyst body selectivity of IP of about 36%. The partial stabilities of maleic anhydride from *n*-butenes and IP are 13 and 22, respectively.

Three reactions are involved in the oxidation of *n*-butane. The respective rate constants can be transformed into three catalyst body parameters (activity parameter, catalyst body selectivity, catalyst body stability). In the case of the oxidation of the *n*-butenes, six rate constants are involved but seven catalyst body parameters are defined. Indeed, the catalyst body properties are fully determined if only five of the six selectivity and stability parameters are given, because of the general relation between catalyst body selectivities and catalyst body stabilities

$$ \frac{{}^{\mathrm{B}}_{\mathrm{bte}}\lambda_{\mathrm{IP}} \times {}^{\mathrm{B}}_{\mathrm{IP}}\lambda_{\mathrm{MA}}}{{}^{\mathrm{B}}_{\mathrm{bte}}\lambda_{\mathrm{MA}}} = \frac{{}^{\mathrm{B}}S_{\mathrm{IP}} \times {}^{\mathrm{B}}_{\mathrm{IP}}S_{\mathrm{MA}}}{{}^{\mathrm{B}}S_{\mathrm{MA}}}. \tag{4.11} $$

The stoichiometric parameter of the total oxidation of *n*-butenes is 48% and confirms the estimation of 50% from the previous section. The corresponding value of the total oxidation of IP is 83%. The formation of carbon monoxide is much more favoured over the formation of carbon dioxide in the case of the total oxidation of IP. The value for the oxidation of maleic anhydride amounts to 47% and is similar to the corresponding value of 44% that was found in the parameter estimation for the oxidation of *n*-butane.

The rate constants and activation energies of the total oxidation of maleic anhydride differ in the two sets of kinetic parameters for the oxidation of pure *n*-butane and for the oxidation of mixtures of *n*-butane and *n*-butenes. The values at 420 °C are 0.093 $\frac{\text{mol}}{\text{s kg MPa}}$ for the parameter set of the *n*-butane oxidation and 0.155 $\frac{\text{mol}}{\text{s kg MPa}}$ for the parameter set of the oxidation of the mixtures. The activation energies are 136 kJ/mol and 54 kJ/mol, respectively. The differences in these values can be attributed to the irreversible change of the catalyst as described in section 4.8, or to the different influences of pore transport resistances on the catalyst performance. The transport resistances are surely the same as in the case of the pure *n*-butane oxidation. The effects of these resistances on the catalyst performance, however, depend on the reaction rates. The oxidation of *n*-butenes leads to a higher formation rate of maleic anhydride. It could be assumed that the higher formation rate leads to a higher mean fraction level of maleic anhydride in the catalyst body and therefore to a higher apparent decomposition rate of maleic anhydride. The lower value of the corresponding activation energy could be explained by the lower temperature dependence of the transport properties.

The inhibition constant of *n*-butenes amounts to about 1100 MPa^{-1} which is higher than the inhibition constant for the pure *n*-butane conversion of 470 MPa^{-1}. It can therefore be assumed that the *n*-butenes adsorb stronger on the VPO catalyst. The higher catalyst body selectivities of carbon oxides, however, lead to the conclusion that *n*-butenes are adsorbed on less selective sites. The inhibitions by IP and water were considered in the parameter estimation. The best fit, however, was achieved by excluding the inhibition effects caused by IP and water.

4.3.2 Variation of the Reaction Temperature

The oxidation of 1-butene was carried out at temperatures between 340 and 420 °C. The progress of the reaction at 340 °C deviates much from the observations made at the other temperatures. Data obtained at 340 °C were not considered in the parameter estimation. The deviation is described in the following.

The calculated catalyst body parameters for the temperatures from 360 to 420 °C are listed in Tab. 4.6. The activity parameter increases from 1.05 $\frac{\text{mol}}{\text{s kg MPa}}$ to 3.25 $\frac{\text{mol}}{\text{s kg MPa}}$ in this temperature range. The factor between the two values is 3.1. The corresponding factor for the oxidation of *n*-butane is 4.8, resulting from the higher activation energies of the pure *n*-butane oxidation.

T in °C	${}^{\text{B}}k_{\text{a}}$ / $\frac{\text{mol}}{\text{s kg MPa}}$	${}^{\text{B}}S_{\text{IP}}$	${}^{\text{B}}S_{\text{MA}}$	${}^{\text{B}}_{\text{IP}}S_{\text{MA}}$	${}^{\text{B}}_{\text{bte}}\lambda_{\text{IP}}$	${}^{\text{B}}_{\text{bte}}\lambda_{\text{MA}}$	${}^{\text{B}}_{\text{IP}}\lambda_{\text{MA}}$
360	1.05	36%	24%	92%	0.59	9.4	22
380	1.56	36%	26%	87%	0.61	11.0	22
400	2.27	36%	27%	80%	0.61	12.8	22
420	3.25	37%	29%	72%	0.59	14.7	23

Tab. 4.6: *Calculated catalyst body properties of the oxidation of 1% n/n of n-butenes over a VPO-50 catalyst at different temperatures.*

Since the activation energy of the reaction of *n*-butenes to maleic anhydride with a

value of 81 kJ/mol has the highest value of the corresponding activation energies of the three reactions of *n*-butenes, the calculated catalyst body selectivity of maleic anhydride increases with increasing temperature. The value of the activation energy of the reaction of IP to maleic anhydride is almost three times higher than the corresponding activation energy of the total oxidation of IP. The partial catalyst body selectivity of maleic anhydride from IP therefore decreases with increasing temperature. The catalyst body selectivity of IP remains almost constant in the considered temperature range. The partial stability of maleic anhydride from *n*-butenes increases with increasing temperature. Both of the other stabilities remain constant.

Since both, the catalyst body selectivity as well as the catalyst body stability of IP do not change much in the temperature range from 360 to 420 °C, it can be expected that the maximum yield of IP does not change much in this range.

No statement based on the catalyst body parameters can be given, however, about the change in the amount of the maximum yield of maleic anhydride. The catalyst body selectivities and catalyst body stabilities show different trends at varying temperatures.

The experimental results and the results of the calculations for the individual reaction temperatures are compared in the plots in Fig. 4.7. Fig. 4.7(a) shows the fraction profiles of *n*-butenes as functions of the modified residence time. Except for the temperature of 340 °C, the results of the calculations agree with the experimental results. For 340 °C, the calculated fractions are below those that were experimentally determined. The apparent activation energies of the conversion reactions of *n*-butenes between 340 °C and 360 °C seem to be higher than the activation energies which were determined in the parameter estimation. The activation energies that were determined in the parameter estimation lead to a good agreement of calculations and experiments for the higher temperatures. One possibility to elucidate the deviation for a temperature of 340 °C might be the influence of pore transport effects on the apparent reaction kinetics. For Thiele numbers $\phi > 2$, the apparent activation energies are about the half of the intrinsic activation energies[4]. For small values of the Thiele number ($\phi < 0.3$), it can be assumed that the apparent and intrinsic activation energies are equal. The Thiele number increases with increasing temperature. If the Thiele number equalled $\phi = 2$ somewhere in the range of 340 and 360 °C, the apparent activation energies would be constant for temperatures above 360 °C, but can deviate for temperatures below this value. This explanation corresponds to the behaviour found in the experimental investigations.

The fraction profiles of IP as functions of the modified residence time are presented in Fig. 4.7(c). The experimentally determined maximum yields of IP are about 17% for temperatures of 360 °C and are almost independent of the temperature as stated above in the discussion of the temperature dependences of the catalyst body properties. The maximum yield was not reached in the experiment at 340 °C. The residence time for achieving the maximum yield decreases from about 0.2 (g s)/ml for a temperature of 360 °C to a value of about 0.07 (g s)/ml for a temperature of 420 °C.

For the temperature of 340 °C, the experimentally determined and calculated fractions of IP agree well. This agreement is surprising considering the deviations in the fraction profile of *n*-butenes and also the deviations in the fraction profile of maleic anhydride (Fig. 4.7(e)) at this temperature. The lower conversion rate of *n*-butenes, however, is compensated for by a higher reactor selectivity of IP, as can be seen in Fig. 4.7(d).

[4]See section 3.1.4 for details.

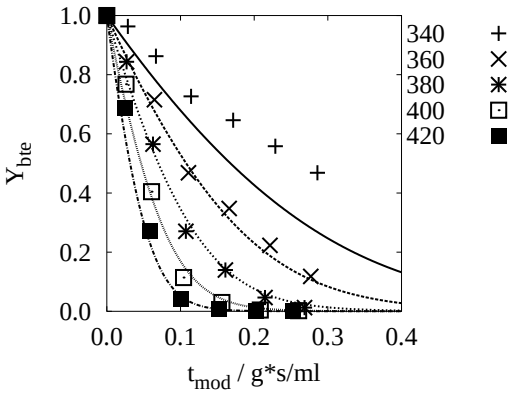

(a) Fraction profiles of *n*-butenes

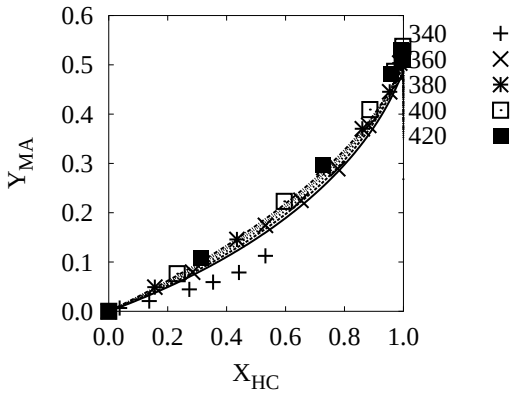

(b) Yields of maleic anhydride as functions of the conversion level

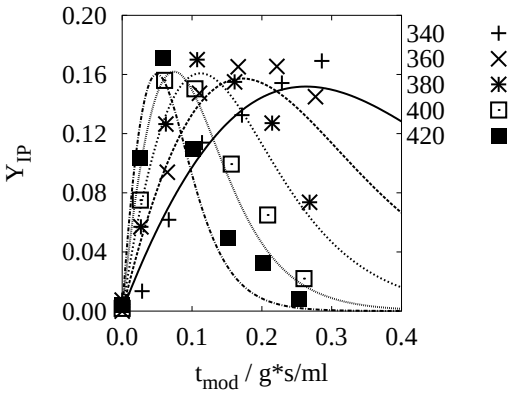

(c) Fraction profiles of IP

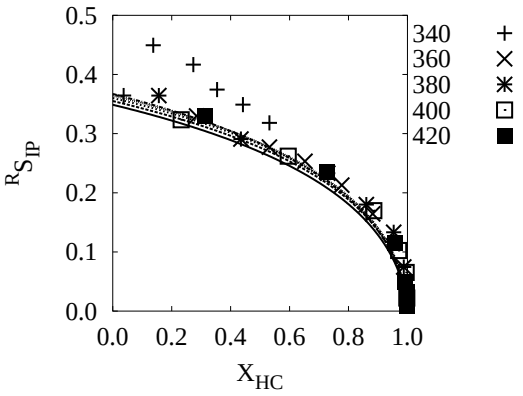

(d) Reactor selectivities of IP

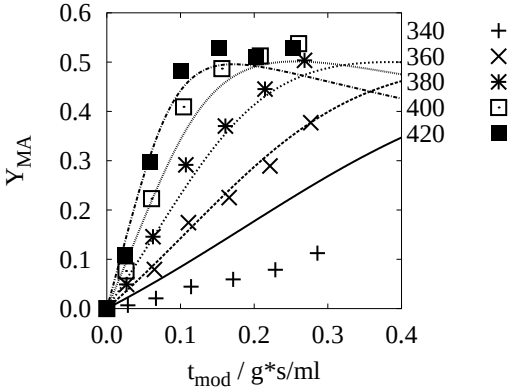

(e) Fraction profiles of maleic anhydride

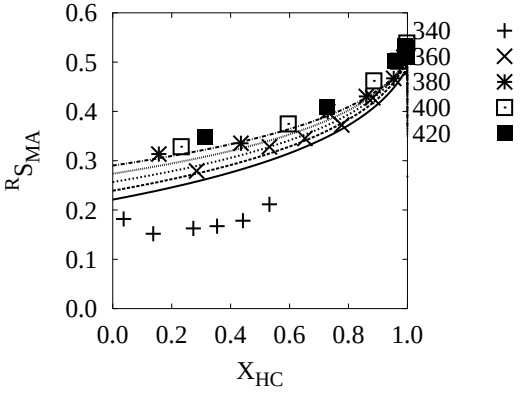

(f) Reactor selectivities of maleic anhydride

Fig. 4.7: *Variation of the reaction temperature (values are given in* °C*) in the oxidation of 1% n/n of 1-butene in air. The fraction profiles and reactor selectivities are presented.*

This results in a presumably coincidental agreement of the calculated and experimental determined fractions of IP. The reactor selectivities of IP are well represented by the calculations and can be regarded as temperature independent, except for the above mentioned higher reactor selectivity for a reaction temperature of 340 °C. The higher selectivity can again be elucidated by the change in the Thiele number and the accompanying change in selectivity. IP is an intermediate with a low stability. Therefore, the intrinsic selectivity of IP should be higher than the catalyst body selectivities of about 36% as determined in the experiments. It can be assumed that the Thiele number for temperatures of 360 °C and above is high enough for the catalyst body selectivity of IP to become independent of changes in the Thiele number. In case of a reaction temperature of 340 °C, however, the sensitivity of the catalyst body selectivity with changing Thiele number seems to be much higher. On the other hand, the reactor selectivity of maleic anhydride as displayed in Fig. 4.7(f) shows much lower values at a temperature of 340 °C than the corresponding selectivities at the other temperatures. Maleic anhydride is an intermediate that is much more stable than IP and can be thus regarded as an almost inert species compared to IP. As the carbon oxides in the triangular scheme of the three species *n*-butane, maleic anhydride and carbon oxides, maleic anhydride can be considered as the end product in the triangular scheme of the three species *n*-butenes, IP and maleic anhydride. The decreasing Thiele number therefore leads to an increase in the catalyst body selectivity of IP and to a decrease in the catalyst body selectivity of maleic anhydride, correspondingly.

The fraction profiles of maleic anhydride are presented in Fig. 4.7(e). Except for the temperature of 420 °C, the maximum yield of maleic anhydride was not achieved. The amount of the maximum yield at this temperature is about 52%. For higher temperatures, the calculated fractions have values slightly below the experimental values. The calculated fractions of maleic anhydride for a reaction temperature of 340 °C show higher values than the experimentally determined fractions.

Fig. 4.7(b) displays the yields of maleic anhydride as functions of the conversion level. The profiles are almost independent of the temperature and show that the maximum yield of maleic anhydride is achieved for almost total conversion of the *n*-butenes.

4.3.3 Variation of the Hydrocarbon Fraction in the Feed

The only temperature at which the hydrocarbon fraction was varied in the partial oxidation of pure 1-butene was 340 °C. The feed fraction of 1-butene was varied between 1.0% and 2.5% n/n. Because of the high deviations between experimentally determined and calculated values at this temperature, only trends can be compared. The fraction profiles and reactor selectivities are presented in Fig. 4.8. The trend in the inhibition of the hydrocarbon conversion is well represented by the calculation, as it can be seen in the plot of the fraction profiles of *n*-butenes (Fig. 4.8(a)).

Fig. 4.8(c) presents the reactor selectivities of IP. The experimentally determined reactor selectivities as well as the calculated selectivities are independent of the feed fraction. The experimental values for conversion levels below 10% are strongly deviating. This could be attributed to inaccurate measurement since small differences in fractions had to be determined by measuring high absolute fractions. The reactor selectivity of maleic anhydride decreases slightly with increasing feed fraction. This dependence is not represented by the calculation. This behaviour cannot be related to changes in the Thiele

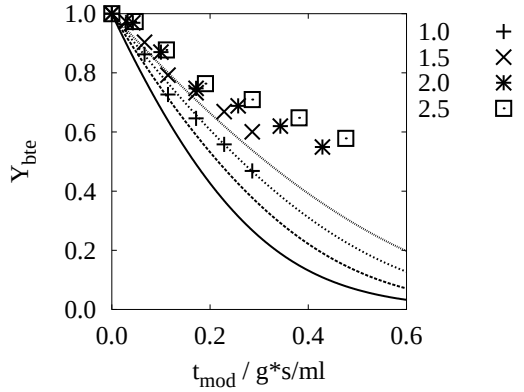

(a) Fraction profiles of *n*-butenes

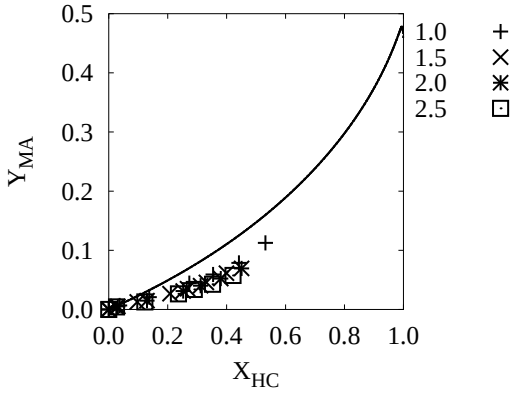

(b) Yields of maleic anhydride as functions of the conversion level

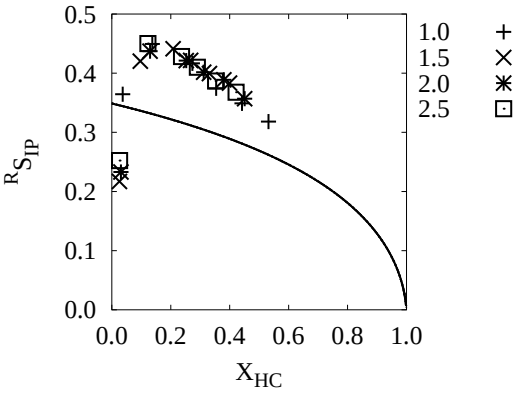

(c) Reactor selectivities of IP

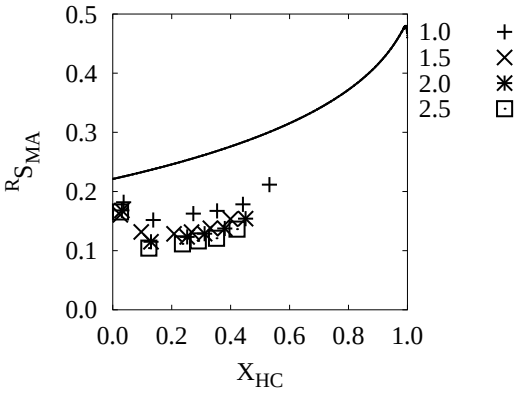

(d) Reactor selectivities of maleic anhydride

Fig. 4.8: *Variation of the hydrocarbon fraction of 1-butene in the feed (values are given in % n/n) in the oxidation of 1-butene at 340* °C.

number since no change in the reactor selectivity of IP can be seen. Centi stated in [43] that *n*-butenes adsorb stronger on the VPO catalyst and that high coverages lead to an inhibition of the chemisorption of oxygen. Lower feed fractions are obviously more suitable for the oxidation of *n*-butenes.

4.3.4 Isomerisation of the *n*-Butenes

Quast investigated the partial oxidation of the *n*-butene isomers 1-butene, *cis*-2-butene and *trans*-2-butene individually at a temperature of 340 °C and with a hydrocarbon fraction in the feed of 0.6% n/n in air [16]. Only small differences in the reaction performance were observed between the individual isomers. Above a conversion level of about 20%, the relative amounts of the individual isomers corresponded to those of the isomerisation equilibrium and remained constant for higher conversion levels. It was concluded that no statement could be given about the individual performances of the three isomers, since the relative amounts of the isomers above conversion levels of 20% are independent of the type of isomer that was fed to the reactor.

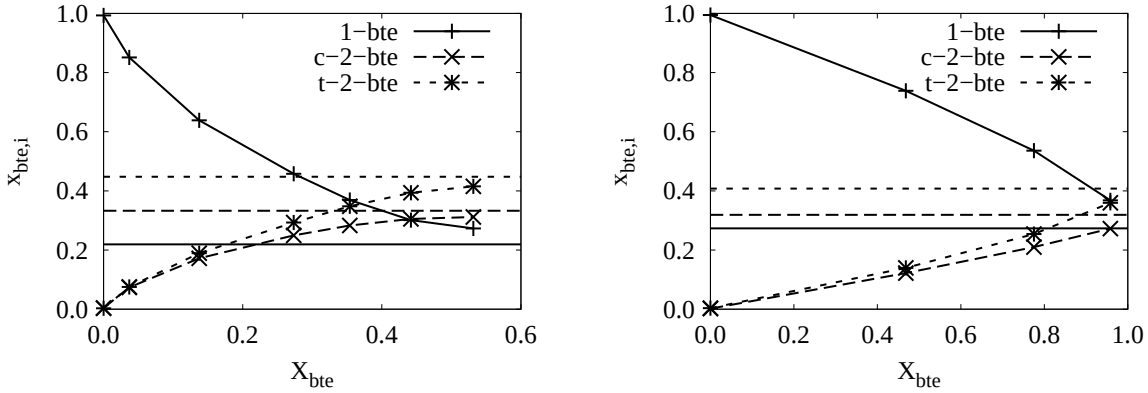

(a) 1-Butene, 340 °C

(b) Raffinate II, 450 °C

Fig. 4.9: *Isomer fractions during the conversion of 1-butene (1% n/n) at 340* °C *and during conversion of synthetic raffinate II (1%) at 450* °C *as a function of the conversion level of n-butenes. The horizontal lines represent the thermodynamic equilibrium.*

The plots in Fig. 4.9 present the relative amounts of the *n*-butene isomers in two different experiments. The first experiment was carried out with 1% n/n of 1-butene at 340 °C. The second was carried out with 1% n/n of synthetic raffinate II at 450 °C over the VPO-50 catalyst. Both plots show the isomer fractions

$$x_{\mathrm{bte},i} = \frac{x_i}{x_{1-\mathrm{bte}} + x_{\mathrm{c}-2-\mathrm{bte}} + x_{\mathrm{t}-2-\mathrm{bte}}} \tag{4.12}$$

as functions of the conversion level of the *n*-butenes. The connected symbols represent the measurements, the horizontal lines show the corresponding levels at thermodynamic equilibrium calculated as described in section 3.4.3. In contrast to the investigations of Quast, the isomerisation equilibrium is not achieved for conversion levels below 50% at a

temperature of 340 °C. At a temperature of 450 °C, the isomerisation remains incomplete even for conversion levels of about 90%. The experimental values at the conversion level of about 97% in Fig. 4.9(b) exhibit a large experimental error since the relative amounts were difficult to determine for low absolute fractions of the *n*-butenes.

The statement of Quast that there are no significant differences in the reaction behaviour between the *n*-butene isomers does not hold for the present catalyst. Here, the isomers were not in equilibrium during most part of the oxidation process. The reason for this is unclear. This difference might be explained by different natures or amounts of acidic sites of the two catalysts leading to different isomerisation capabilities.

4.3.5 Composition of the Pseudo-Species IP

The pseudo-species IP represents a lump of seven detected species, among which 1,3-butadiene and furan are the predominant substances. The fraction profiles of the individual species in the conversion of 1% n/n of synthetic raffinate II in air at a temperature of 400 °C over a VPO-50 catalyst are presented in Fig. 4.10.

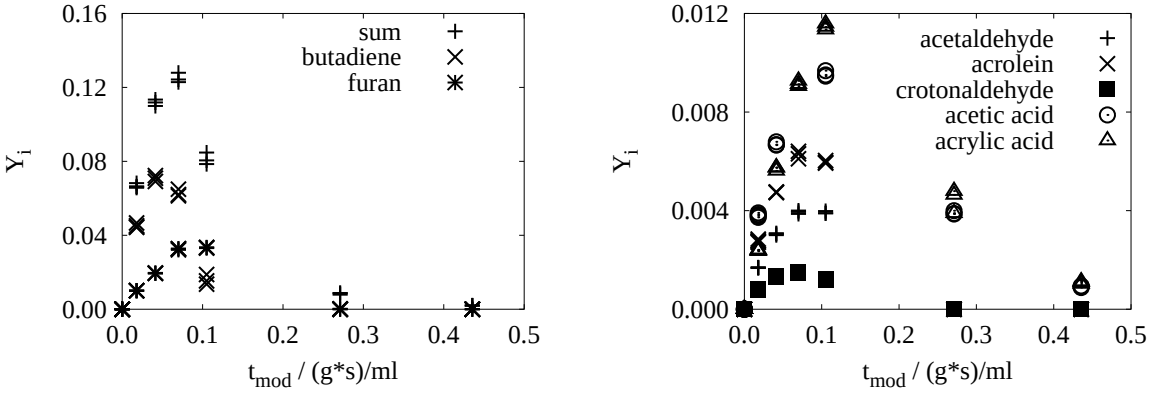

(a) Major components and sum of IP

(b) Minor components of IP

Fig. 4.10: *Fractions of organic intermediates that are lumped together into IP as functions of the modified residence time. The results stem from the partial oxidation of synthetic raffinate II (1% n/n in air) at 400* °C *over a VPO-50 catalyst.*

Fig. 4.10(a) shows the fractions of the two major components 1,3-butadiene and furan as well as the sum fraction of IP. The most dominant species is 1,3-butadiene with a maximum yield of about 8%, followed by furan with a maximum yield of about 4%. The maximum yield of furan is obtained at a modified residence time of about 0.1 (g s)/ml. The maximum yield of 1,3-butadiene is achieved at a lower residence time of 0.05 (g s)/ml. The locations of the maxima fit well into the mechanistic picture saying that furan is the product of the consecutive reaction of 1,3-butadiene. Crotonaldehyde is the only species among the proposed intermediates on the *main* pathway to maleic anhydride that is presented in Fig. 2.3. The maximum yield of this species is about 0.2%. The maximum is achieved at a residence time of about 0.07 (g s)/ml and therefore lies in between the maxima of 1,3-butadiene and furan. This result fits also well into the mechanistic picture

of two parallel reaction paths, one including 1,3-butadiene and furan, the other including crotonaldehyde.

There are also decomposition products present in the gas phase. The only C_3 products that were detected are acrolein and acrylic acid with maximum yields of about 0.6% and 1.2%, respectively. The maximum yield of acrolein is reached at a smaller residence time of about 0.07 (g s)/ml than the maximum yield of acrylic acid (about 1 (g s)/ml). Two C_2 products were also detected: acetaldehyde and acetic acid. The maximum yields are 0.4% and 1.0%, respectively. Again, the maximum yield of the aldehyde is reached at a lower residence time than the maximum yield of the corresponding acid. The acids are the most stable intermediates of IP and are the only components left at residence times above 0.25 (g s)/ml with a yield of about 0.4%, each. It seems that the decomposition reactions lead to the formation of C_2 and C_3 aldehydes. The aldehydes are then converted to their corresponding acids.

The composition of IP changes with proceeding reaction. For the species balances in the present work, however, a specific sum formula of IP had to be used which fullfills the carbon, hydrogen and oxygen balances satisfactorily. The sum formula was determined by averaging the amounts of the individual elements of the species in IP for residence times where mostly 1,3-butadiene and furan are present. The sum formula amounts to $C_{3.6}H_5O_{0.75}$.

The partial oxidation of *n*-butenes to IP and the oxidation of IP to maleic anhydride can then be formally written as

$$C_4H_8 + 3\,O_2 \longrightarrow \frac{10}{9}\,C_{3.6}H_5O_{0.75} + \frac{71}{36}\,O_2 + \frac{11}{9}\,H_2O \longrightarrow C_4H_2O_3 + 3\,H_2O. \quad (4.13)$$

It is clear that maleic anhydride is only formed from hydrocarbon species with four carbon atoms. Nevertheless, this sum formula represents the sum of the individual species in IP best. To explain why the sum formula can be used, Fig. 4.11 gives a graphical representation of the chosen model of the reaction network utilising the pseudo-species IP compared to a more detailed model where IP is split into intermediate products and decomposition products. In the upper scheme, the intermediates are divided into two pseudo-species: precursors for the production of maleic anhydride (1,3-butadiene, furan, and crotonaldehyde) and decomposition species (the aldehydes and the acids). Two reactions lead to the formation of these two pseudo-species. Only the precursors can be converted to maleic anhydride, but both pseudo-species can be oxidised to carbon oxides. Additionally, a reaction of the precursors to the composition products is considered[5]. The lower scheme shows the reactions of the pseudo-species IP as considered in the present work. The reactions of the two divided pseudo-species are lumped together and instead of the five reactions which have to be considered in the more complex scheme, only three have to be considered in the lower scheme. The detailed network can be safely abandoned since the reaction rates of the less complex network are sufficient to describe the key reactions like the formation of maleic anhydride and carbon oxides.

The additional knowledge of the existence of the two subclasses leads to the insight that some part of IP *has* to be converted to carbon oxides. The partial catalyst body selectivity of maleic anhydride from IP cannot reach 100%.

[5]As it can be seen in the partial oxidation of *n*-butane, the decomposition of maleic anhydride produced mainly carbon oxides. Only small amounts of acrylic and acetic acids were formed. The formation of the acids from maleic anhydride is therefore not considered in Fig. 4.11.

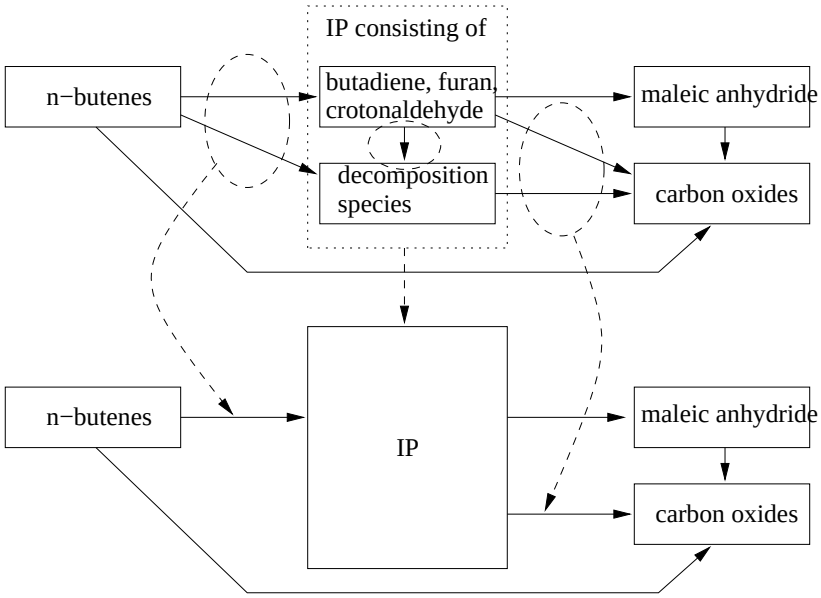

Fig. 4.11: *Differently complex reaction networks describing the oxidation of n-butenes are shown. The upper scheme is the more complex one. The lower scheme shows the network used in the present work with the pseudo-species IP. The dashed lines show the reactions and species that are combined and therefore reduced when the complexity is reduced from the upper to the lower scheme.*

4.3.6 Comparison with Results in the Literature

Most of the literature about the partial oxidation of *n*-butenes to maleic anhydride over VPO catalysts was published around 1970. A technical review was given by Varma and Saraf in 1978 [31]. They reported a broad range of maximum yields between 35% and 62% for the oxidation of pure *n*-butenes over VPO catalysts. Most of the yields were about 60%. The higher yields resulted possibly from the optimisation of the VPO catalyst for the *n*-butene oxidation. The VPO catalyst used in the present work was optimised for the *n*-butane conversion and maximum yields of slightly above 50% were achieved.

Centi and Trifirò reported typical yields of their VPO catalysts of about 50% at total conversion of *n*-butenes [22]. That corresponds to the behaviour of the present catalyst.

Quast carried out experiments with *n*-butenes at temperatures in the range of 340 to 380 °C [16]. At 360 °C, the activity parameter for the conversion of 1% n/n of 2-butene in air amounted to 1.0 $\frac{\text{mol}}{\text{s kg MPa}}$. That is identical to the activity parameter of 1.05 $\frac{\text{mol}}{\text{s kg MPa}}$ as found in the present work. The catalyst body selectivity of maleic anhydride had a value of 22%. This value is also very similar to the value of 24% which was found in the present work.

Quast had mainly used a hydrocarbon fraction of 0.6% n/n in the feed, since the yield of maleic anhydride increased from 44% for 1.0% of 2-butene to 51% for 0.6% of 2-butene. The tendency to higher yields for decreasing fractions of hydrocarbons in the feed was also observed in the present work.

The maximum yield depends on the temperature. In the investigations by Quast, the yields were raised from 44% to 54% through increasing the temperature from 340 to

380 °C [16]. The maxima of the fraction profiles at these temperatures were not achieved in the present work, but the temperature dependence seems to be weaker with the VPO-50 catalyst.

At 340 °C and with a fraction of 0.6% n/n of 2-butene in the feed, Quast determined a maximum yield of intermediates of slightly above 20%. The maximum yield in the present work was about 17% for higher temperatures and higher hydrocarbon fractions in the feed.

It can be concluded that the differences between the individual experiments reported in the literature are higher for the oxidation of *n*-butenes than those for the oxidation of *n*-butane. The yields of maleic anhydride with the 'more modern' VPO catalysts are lower since they have been optimised for the conversion of *n*-butane.

4.4 Oxidation of Raffinate II over VPO-50

The partial oxidation of raffinate II combines the partial oxidations of its two main components *n*-butenes and *n*-butane. The resulting reaction network is presented in section 3.3.1 and is displayed in Fig. 3.7. The experiments were carried out with the synthetic raffinate II mixture described in section 3.2.2. It contained 75% n/n of 1-butene, 16% n/n of *n*-butane and 9% of nitrogen. Since the normalised fractions are related to the carbon content, the 9% of nitrogen are not considered in the data evaluation. The fractions and yields are rather related to the amount of the linear C_4 hydrocarbons. The yields in processing of a real raffinate II mixture are about

$$Y_i^{\text{real}} \approx 0.91 \times Y_i. \tag{4.14}$$

The measurements were carried out at temperatures in the range of 400 to 450 °C. The hydrocarbon fraction in the feed was varied between 1.0% n/n and 2.0% n/n of synthetic raffinate II in air.

The results of the partial oxidation of 1% n/n of synthetic raffinate II in air at a temperature of 410 °C are presented in the plots in Fig. 4.12. Fig. 4.12(a) shows the fraction profiles of *n*-butenes and *n*-butane as well as the calculated sum fraction of both. At $t_{\text{mod}} = 0$, the sum fraction equals 1. Since the fractions are related to carbon, the fractions of 75% of *n*-butenes and 16% of *n*-butane of the synthetic raffinate II mixture lead to dimensionless fractions of 82% and 17.5%, respectively. The *n*-butenes are almost completely converted at a residence time of about 0.1 (g s)/ml. At this residence time, the conversion level of *n*-butane is below a value of about 15%. Because of the difficulties in determining the fractions of *n*-butane and 1,3-butadiene simultaneously, the experimental values of the fractions of these species are quite inaccurate at residence times below 0.1 (g s)/ml[6]. The experimental values of the fraction of *n*-butane have constant values at these residence times. The constantness can be attributed to the assumptions made in the evaluation of the chromatographic data that *n*-butane is converted only if there is no butadiene present. It can be expected instead that the fraction of *n*-butane decreases slightly with increasing residence time in the way the calculation shows. Because of the different conversion rates of *n*-butenes and *n*-butane, the resulting hydrocarbon sum curve

[6]See section 3.2.3 for details.

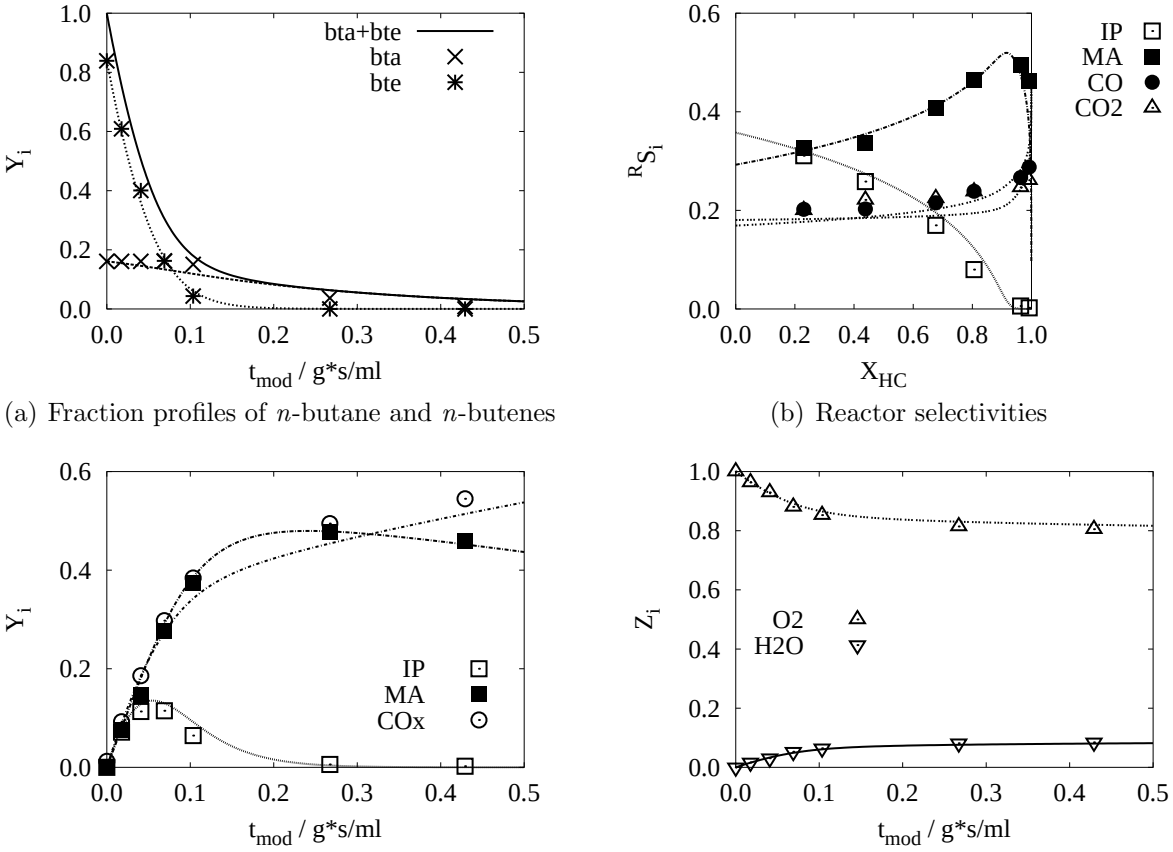

(a) Fraction profiles of n-butane and n-butenes

(b) Reactor selectivities

(c) Fraction profiles of the products

(d) Fraction profiles of oxygen and water

Fig. 4.12: *Partial oxidation of 1% n/n of synthetic raffinate II in air at 410 °C over a VPO-50 catalyst. The fraction profiles are plotted against the modified residence time, the reactor selectivities against the conversion level of raffinate II. The symbols represent the experimental values, the lines represent the calculations based on the modelled reaction kinetics.*

shows a sharp bend at a modified residence time of about 0.1 (g s)/ml, where almost all of the *n*-butenes are converted.

Fig. 4.12(c) shows the fraction profiles of the products. The maximum yield of IP amounts to about 12% and is achieved at a residence time of about 0.05 (g s)/ml. The maximum yield of IP in the conversion of pure 1-butene is about 17%. The smaller value of the maximum yield for the raffinate II conversion can be attributed to the fact that only 82% of the hydrocarbons in the feed are 1-butene. The residence time where the maximum yield is reached in the conversion of pure 1-butene is about 0.06 (g s)/ml.

The large uncertainties in the fractions of 1,3-butadiene and *n*-butane lead to the underestimation of the fraction of IP. The kinetic parameters, however, are based on both measurements with pure 1-butene and raffinate II. In the 1-butene conversions, the fraction of 1,3-butadiene and IP were determined exactly. The calculations agree well with the experimental results obtained with both types of feedstock. Therefore, the approximations in the experimental determination of the fractions of *n*-butane and 1,3-butadiene are sufficiently good.

The maximum yield of maleic anhydride amounts to about 47% for synthetic raffinate II. This value is not in-between the values of the maximum yields that were achieved in the conversions of the pure components *n*-butenes (52%) and *n*-butane (58%). The lower yield can be attributed to the higher residence time that is necessary to convert the amount of *n*-butane in raffinate II after the *n*-butenes have been converted. The amount of maleic anhydride that has been formed during the conversion of the *n*-butenes at lower residence times is then subjected to decomposition during the slow *n*-butane conversion. The yield related to a real raffinate II mixture amounts to about 43%.

Fig. 4.12(b) shows the reactor selectivities as functions of the conversion level of raffinate II. The *n*-butenes are converted at low residence times. The conversion of *n*-butane is insignificant as long as *n*-butenes are present. The selectivity of raffinate II at low conversion levels is therefore solely characterised by the performance of the *n*-butenes. The catalyst body selectivities of IP and maleic anhydride amount to about 36% and 29%, respectively, and are therefore identical to the corresponding catalyst body selectivities obtained with pure 1-butene as a feedstock. The selectivity in the conversion of *n*-butenes is not influenced by the presence of *n*-butane.

Since the organic intermediates are formed during the oxidation of the *n*-butenes only, the reactor selectivity of IP decreases to about 0 for a conversion level of slightly above 90%. The reactor selectivity of maleic anhydride increases with increasing conversion levels at conversion levels below 90%. For higher conversion levels, the reactor selectivity drops sharply. This phenomenon can be clearly understood as the superposition of the performances of the pure components. The superposition of the two reactor selectivity curves for the conversion of the pure hydrocarbons are presented qualitatively in Fig. 4.13. Since the *n*-butenes in raffinate II are completely converted at a conversion level of raffinate II of about 85%, the selectivity curve of maleic anhydride for the conversion of raffinate II achieves the same value at a conversion level of 85% as the reactor selectivity for the conversion of pure *n*-butenes at a conversion level of 100%. A further increase in the reactor selectivity for the raffinate II conversion results from the conversion of *n*-butane. The decomposition of maleic anhydride results in a sharp decrease of its reactor selectivity at conversion levels above 95%.

Fig. 4.12(d) shows that the conversion level of oxygen is about 20% after most of the

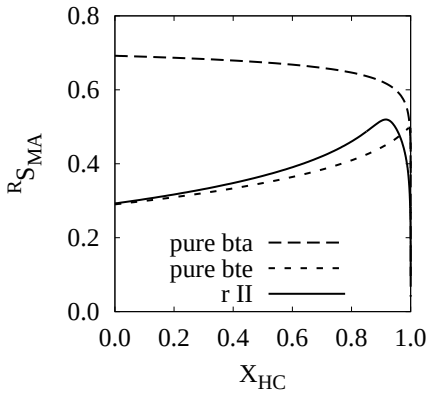

Fig. 4.13: *Qualitative representation of calculated reactor selectivity curves in the conversion of pure n-butane, pure n-butenes and raffinate II, the latter as a superposition of the both former curves.*

hydrocarbons have been converted. This is about the same conversion level as experienced in the conversions of the pure hydrocarbons.

4.4.1 Quantification of Reaction Kinetics and Catalyst Parameters

The rate equations of the conversion of pure *n*-butenes and mixtures of *n*-butenes and *n*-butane were assumed to be of the type of equation (3.39). All experiments carried out at temperatures between 360 and 450 °C with pure *n*-butenes as well as with mixtures of *n*-butenes and *n*-butane were used for the parameter estimation. The effect of decreasing reactor selectivities of maleic anhydride with increasing hydrocarbon fractions in the feed in the conversion of pure 1-butene is discussed in section 4.3.3. This effect cannot be represented through the rate equations used in this work. Therefore, the parameter estimation was restricted to feed fractions below 2.0%. Measurements with pure *n*-butane in the feed were also used for the parameter estimation, but only those measurements were considered that were carried out after the catalyst had been used for the conversion of *n*-butenes.

The kinetic model consists of 24 model parameters that were determined by the use of 1096 experimentally determined fractions. The parameter estimation resulted in a residual error of $\chi^2 = 1985$. The highest value of the cross correlation parameters is 0.85 for the correlation of the rate constant $k_{\mathrm{bte,COx}}$ and the inhibition constant b_{bte}. The cross correlation parameters are therefore all below a value of 0.9, indicating the absence of significant correlations between the estimated parameters. The kinetic and stoichiometric parameters for the oxidation of mixtures of *n*-butenes and *n*-butane over the VPO-50 catalyst as well as their estimated confidence limits are listed in Tab. 4.7. The calculated enthalpies of reaction are also presented in the table. The parameter estimation resulted in zero values of the inhibition constants of IP and water. Therefore, the rate equations can be simplified to

$$r_{i,j} = \frac{k_{i,j} p_i \sqrt{p_{\mathrm{O2}}/p^+}}{1 + b_{\mathrm{bta}} p_{\mathrm{bta}} + b_{\mathrm{bte}} p_{\mathrm{bte}}}. \tag{4.15}$$

i	j	$k_{i,j}(420\ ^\circ\mathrm{C})/k^+$		$E_{\mathrm{A},i,j}/E_\mathrm{A}^+$		$\frac{\Delta_\mathrm{R}H_{i,j}}{\Delta_\mathrm{R}H^+}$	other parameters		
bta	MA	0.692	±0.033	62.2	±4.5	−1266	b_bta/b^+	213	±37
bta	COx	0.273	±0.018	163.7	±9.0	−1943	b_bte/b^+	1096	±117
bte	MA	2.29	±0.20	80.7	±8.8	−1150	b_IP/b^+	0	±310
bte	IP	2.89	±0.20	71.0	±6.9	−245	b_H2O/b^+	0	±8.4
bte	COx	2.70	±0.18	58.7	±2.9	−1996	s_bta	0.625	±0.015
IP	MA	3.53	±0.37	56	±14	−905	s_bte	0.482	±0.012
IP	COx	1.39	±0.25	147	±20	−1355	s_MA	0.472	±0.040
MA	COx	0.155	±0.016	54	±12	−858	s_IP	0.826	±0.073

Tab. 4.7: *Kinetic, stoichiometric and thermodynamic parameters of the oxidation of mixtures of n-butenes and n-butane over a VPO-50 catalyst. The reference values are* $k^+ = 1\,\frac{\mathrm{mol}}{\mathrm{s\,kg\,MPa}}$, $E_\mathrm{A}^+ = 1\,\frac{\mathrm{kJ}}{\mathrm{mol}}$, $\Delta_\mathrm{R}H^+ = 1\,\frac{\mathrm{kJ}}{\mathrm{mol}}$ *and* $b^+ = 1\,\mathrm{MPa}^{-1}$.

The parity plots for the parameter estimation are presented in Fig. 4.14. All 1096 experimentally determined fractions are plotted in nine parity plots, one for each species and one for the absolute heat of reaction. In every individual plot, the calculated values are plotted against the corresponding experimental values. The diagonal axis and the lines that confine the area with relative errors smaller than 20% are also presented. Most of the calculated values lie in this area with relative errors smaller than 20%. It has to be considered that the experimental determination of the fractions of IP and the smaller fractions of *n*-butane below 0.2 were subjected to uncertainties in case of the oxidation of the mixtures.

In the present work, the activity parameter is defined as

$$^\mathrm{B}k_\mathrm{a} = -\frac{^\mathrm{B}R_\mathrm{HC,0}}{p_\mathrm{HC,0}}. \tag{4.16}$$

It is possible to define activities concerning the individual species *n*-butenes and *n*-butane. The partial activity concerning a species i can be defined as

$$^\mathrm{B}k_{\mathrm{a},i} = -\frac{^\mathrm{B}R_{i,0}}{p_{i,0}}. \tag{4.17}$$

The relation of the activity parameter and the partial activity parameters can be expressed as

$$^\mathrm{B}k_\mathrm{a} = x_\mathrm{bte}^\mathrm{HC} \times {}^\mathrm{B}k_\mathrm{a,bte} + x_\mathrm{bta}^\mathrm{HC} \times {}^\mathrm{B}k_\mathrm{a,bta}, \tag{4.18}$$

with the molar fraction of species i in the hydrocarbon feedstock

$$x_i^\mathrm{HC} = \frac{x_{i,0}}{x_\mathrm{bte,0} + x_\mathrm{bta,0}}. \tag{4.19}$$

The partial activity parameters are related to the negative slopes of the corresponding fraction curves as functions of the modified residence time:

$$\left.\frac{\mathrm{d}Y_i}{\mathrm{d}t_\mathrm{mod}}\right|_{X_\mathrm{HC}=0} = -\frac{RT}{x_\mathrm{i}^\mathrm{HC}} \times {}^\mathrm{B}k_{\mathrm{a},i}. \tag{4.20}$$

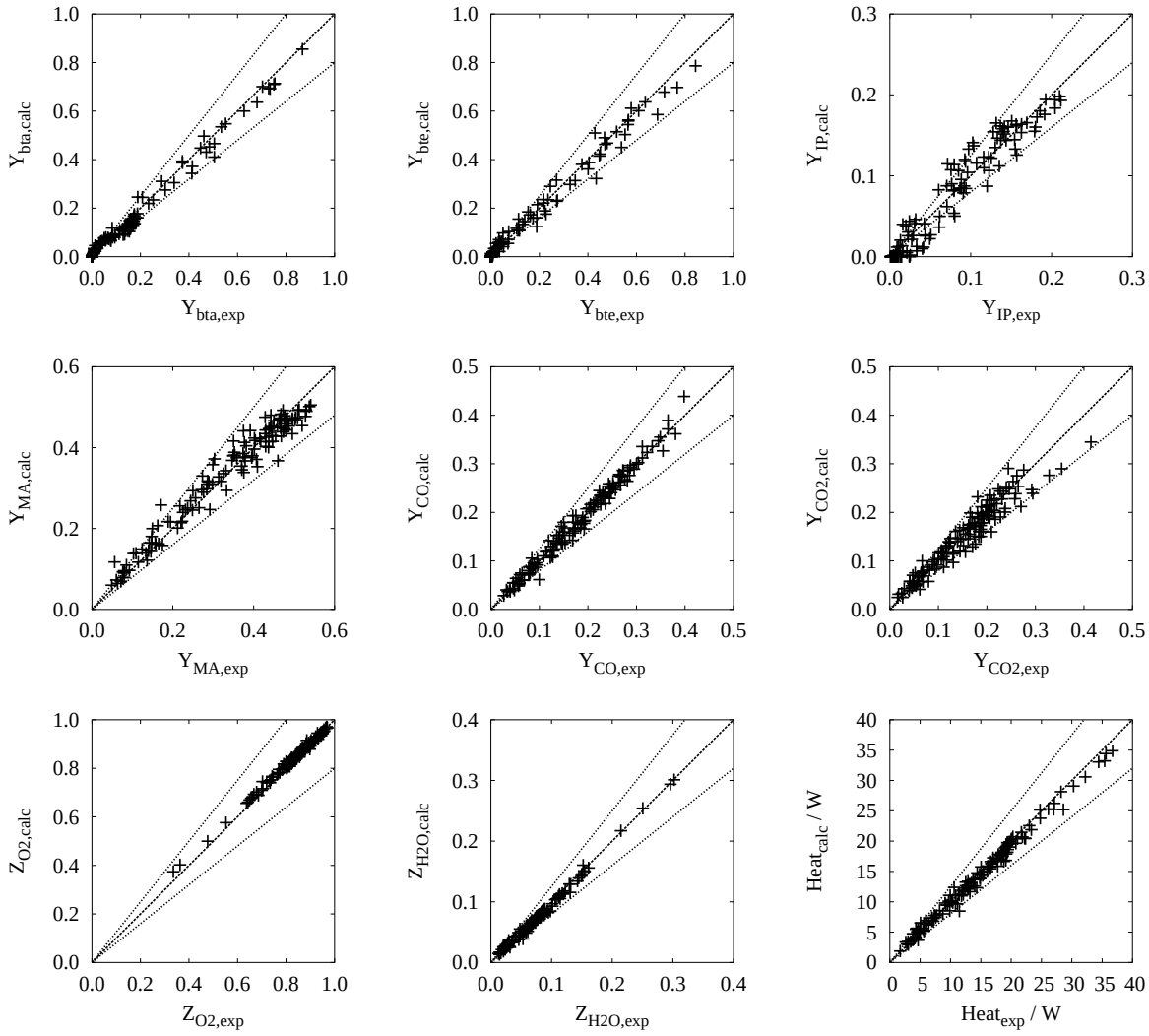

Fig. 4.14: *Parity plots for the oxidation of mixtures of n-butenes and n-butane over a VPO-50 catalyst.*

Because of the constant oxygen content that was used in all experiments and the absence of water in the feed, the partial activity parameters can be calculated from following simplified rate equations:

$$ {}^{\mathrm{B}}k_{\mathrm{a,bte}} = \frac{k_{\mathrm{bte,IP}} + k_{\mathrm{bte,MA}} + k_{\mathrm{bte,COx}}}{1 + b_{\mathrm{bta}}p_{\mathrm{bta},0} + b_{\mathrm{bte}}p_{\mathrm{bte},0}}, \tag{4.21} $$

$$ {}^{\mathrm{B}}k_{\mathrm{a,bta}} = \frac{k_{\mathrm{bta,MA}} + k_{\mathrm{bta,COx}}}{1 + b_{\mathrm{bta}}p_{\mathrm{bta},0} + b_{\mathrm{bte}}p_{\mathrm{bte},0}}. \tag{4.22} $$

In the conversion of the synthetic raffinate II mixture at 410 °C, the partial activity parameters for n-butenes and n-butane amount to 3.12 and 0.36 $\frac{\mathrm{mol}}{\mathrm{s\,kg\,MPa}}$, respectively. The corresponding values for the conversions of the pure hydrocarbons are 3.19 and 0.74 $\frac{\mathrm{mol}}{\mathrm{s\,kg\,MPa}}$. The inhibition of the conversion of n-butane by the presence of n-butenes is clearly visible, whereas the inhibition of the conversion of n-butenes by the presence of n-butane is insignificantly small. The higher reaction rates of n-butenes compared to the reaction rates of n-butane can be expressed in terms of the relative reaction rate

$$ a_{\mathrm{bte}} = \frac{R_{\mathrm{bte}}}{R_{\mathrm{HC}}} = \frac{x_{\mathrm{bte}}^{\mathrm{HC}} \times {}^{\mathrm{B}}k_{\mathrm{a,bte}}}{{}^{\mathrm{B}}k_{\mathrm{a}}} \tag{4.23} $$

which amounts to 98% at $t_{\mathrm{mod}} = 0$. Therefore, at low residence times, only the n-butenes are converted in significant amounts.

The catalyst body selectivities of IP and maleic anhydride depend on the relative reaction rate and on the respective partial catalyst body selectivities. The partial catalyst body selectivities, in turn, depend solely on the temperature and amount to ${}_{\mathrm{bta}}^{\mathrm{B}}S_{\mathrm{MA}} = 77\%$, ${}_{\mathrm{bte}}^{\mathrm{B}}S_{\mathrm{IP}} = 37\%$ and ${}_{\mathrm{bta}}^{\mathrm{B}}S_{\mathrm{MA}} = 28\%$ for a temperature of 410 °C. The partial catalyst body selectivities of IP and maleic anhydride for the conversion of n-butenes in the mixture are identical to the corresponding catalyst body selectivities of the conversion of pure n-butenes. The catalyst body selectivity of maleic anhydride in the conversion of pure n-butane has a value of 71%. It is unlikely that the catalyst body selectivity of maleic anhydride for the conversion of pure n-butane is lower than the catalyst body selectivity of maleic anhydride in the experiments with the hydrocarbon mixture. Nevertheless, the estimated parameters describe the optimum representation of all measurements with the proposed rate equations. More experiments with pure n-butane would probably lead to lower estimated values of the partial catalyst body selectivity of maleic anhydride for the conversion of n-butane, but also to a worse agreement between the calculated and the experimental determined values for the conversion of the mixtures.

The catalyst body selectivities of IP and maleic anhydride are related to the partial catalyst body selectivities according to

$$ {}^{\mathrm{B}}S_i = a_{\mathrm{bte}} \times {}_{\mathrm{bte}}^{\mathrm{B}}S_i + a_{\mathrm{bta}} \times {}_{\mathrm{bta}}^{\mathrm{B}}S_i. \tag{4.24} $$

The relative reaction rates depend on the fraction ratio of n-butenes and n-butane and on the temperature. The values of the catalyst body selectivities of IP and maleic anhydride for the experiment that is presented in the previous section equal 36% and 29%, respectively. These values are almost identical to the partial catalyst body selectivities based on n-butenes, since the conversion of n-butane is negligible for small residence times.

The partial catalyst body stabilities related to n-butenes and IP are the same as in the oxidation of pure n-butenes as presented in section 4.3.1, since they depend on temperature

only. The partial catalyst body stability of maleic anhydride related to n-butane amounts to ${}^{\mathrm{B}}_{\mathrm{bta}}\lambda_{\mathrm{MA}} = 4.4$. This value is clearly lower than the corresponding value of 11.7 for the conversion of pure n-butane at the same temperature. No exact statement can be given as to which extent this difference can be attributed to the irreversible change in the catalytic behaviour of the active catalyst or to pore transport effects.

The stoichiometric parameters for the total oxidation of n-butane and for the total oxidation of maleic anhydride have values of 63% and 47%, respectively. The values agree with the corresponding values of 64% and 44% that were found for the conversion of pure n-butane.

4.4.2 Variation of the Reaction Temperature

The synthetic raffinate II mixture was converted at temperatures between 400 and 450 °C. The activation energies for the reactions which are also involved in the oxidation of pure n-butenes are discussed in section 4.3.2. The activation energy of the reaction of n-butane to maleic anhydride has a value of 62 kJ/mol. This is about 27% smaller than the corresponding activation energy of the conversion of pure n-butane. The activation energy of the total oxidation of n-butane of 164 kJ/mol is much higher than the value of 114 kJ/mol that was found for conversion of pure n-butane. No statements can be given whether these differences result from the irreversible changes of the catalyst, from the pore transport effects or from the low number of experiments with pure n-butane that were considered in the parameter estimation.

The calculated catalyst body parameters are listed in Tab. 4.8. The activity parameters show the typical increase with increasing temperature. The relative reaction rate of n-butenes for $t_{\mathrm{mod}} = 0$ remains at a constant value of about 97%. Most of the catalyst body selectivities and stabilities do not change much in the temperature range. The increase in the catalyst body selectivity from n-butenes to maleic anhydride as well as the corresponding catalyst body stability can be attributed to increasing effects of transport resistances in the catalyst body. The catalyst body selectivity of maleic anhydride related to n-butane decreases sharply from 81% at 400 °C to a value of 55% at 450 °C because of the high activation energy of the total oxidation reaction of n-butane. As stated above, this calculation result can stem from the low number of experiments with pure n-butane that were considered in the parameter estimation.

The fraction profiles and reactor selectivities for the individual reaction temperatures are displayed in Fig. 4.15. The increase in the conversion rate of n-butenes with increasing temperature is represented well by the calculations as shown in Fig. 4.15(a). On the other hand, the increase in the conversion rate of n-butane is represented only qualitatively. The maximum fraction of n-butane, however, is about 16% and is therefore small compared to the fractions of n-butenes and maleic anhydride. The calculated values agree better with the experimental values for higher temperatures. The fraction profiles of IP are presented in Fig. 4.15(c). Because of the uncertainties in the determination of their experimental values, the deviations between calculation and experiment are relatively high but remain small in terms of absolute values. The fraction profiles of maleic anhydride are well represented by the calculations. The highest deviations are present for high temperatures and high residence times.

Plots 4.15(e) and 4.15(f) show the reactor selectivities of IP and maleic anhydride,

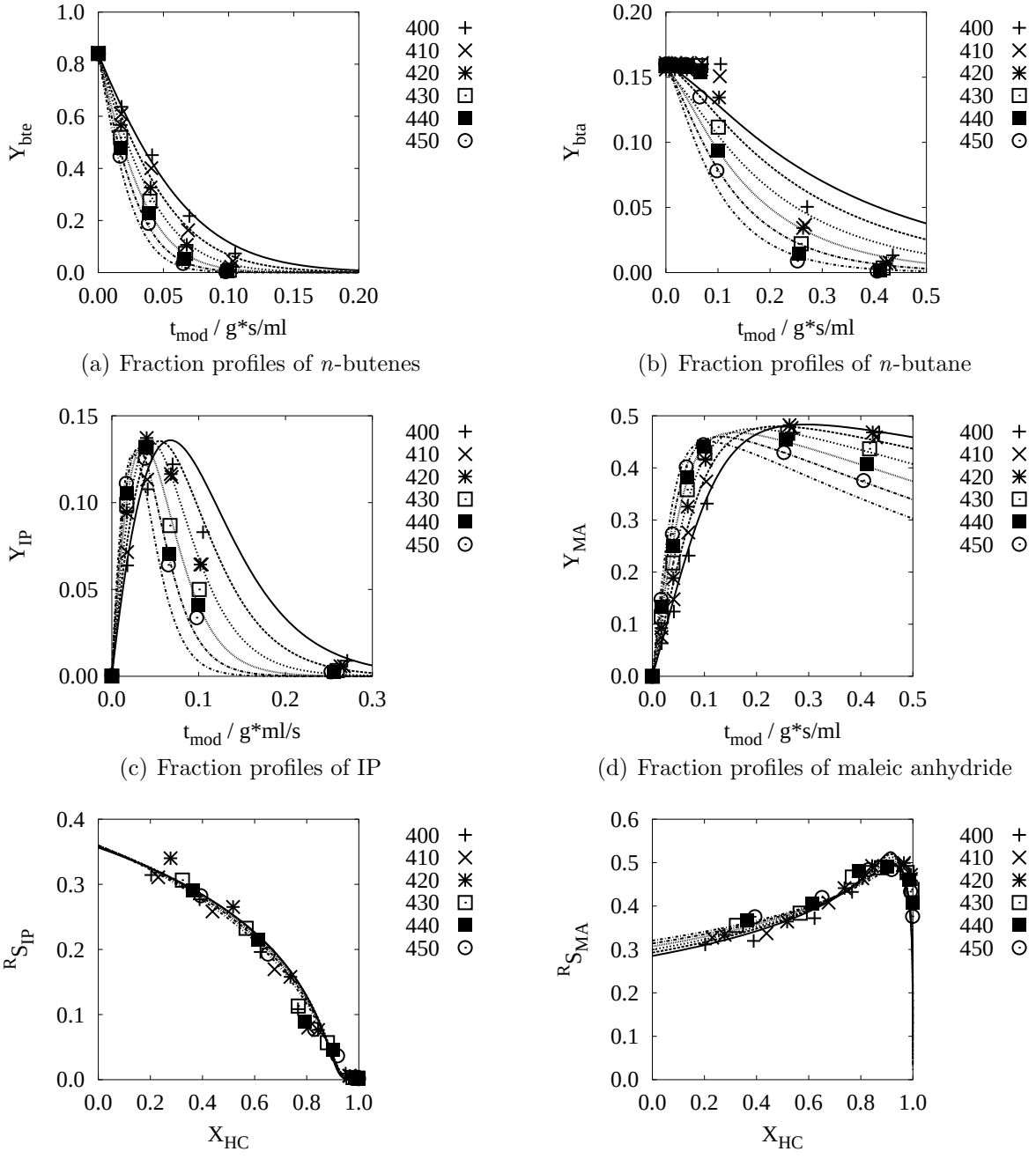

(a) Fraction profiles of n-butenes

(b) Fraction profiles of n-butane

(c) Fraction profiles of IP

(d) Fraction profiles of maleic anhydride

(e) Reactor selectivities of IP

(f) Reactor selectivities of maleic anhydride

Fig. 4.15: *Variation of the reaction temperature (values are given in °C) in the oxidation of 1% n/n of synthetic raffinate II in air. The fraction profiles and reactor selectivities are presented.*

T in °C	${}^{\mathrm{B}}k_{\mathrm{a,bte}}$ / $\frac{\mathrm{mol}}{\mathrm{s\,kg\,MPa}}$	${}^{\mathrm{B}}k_{\mathrm{a,bta}}$ / $\frac{\mathrm{mol}}{\mathrm{s\,kg\,MPa}}$	${}^{\mathrm{B}}k_{\mathrm{a}}$ / $\frac{\mathrm{mol}}{\mathrm{s\,kg\,MPa}}$	${}^{\mathrm{B}}_{\mathrm{bte}}\lambda_{\mathrm{IP}}$	${}^{\mathrm{B}}_{\mathrm{bte}}\lambda_{\mathrm{MA}}$	${}^{\mathrm{B}}_{\mathrm{bta}}\lambda_{\mathrm{MA}}$	${}^{\mathrm{B}}_{\mathrm{IP}}\lambda_{\mathrm{MA}}$
400	2.61	0.29	2.20	0.61	13	4.3	22
410	3.12	0.36	2.64	0.60	14	4.4	23
420	3.73	0.46	3.15	0.59	15	4.5	23
430	4.43	0.58	3.75	0.57	16	4.6	23
440	5.23	0.73	4.44	0.55	17	4.7	23
450	6.16	0.93	5.24	0.52	18	4.7	23
	a_{bte}	${}^{\mathrm{B}}_{\mathrm{bte}}S_{\mathrm{IP}}$	${}^{\mathrm{B}}S_{\mathrm{IP}}$	${}^{\mathrm{B}}_{\mathrm{bte}}S_{\mathrm{MA}}$	${}^{\mathrm{B}}_{\mathrm{bta}}S_{\mathrm{MA}}$	${}^{\mathrm{B}}S_{\mathrm{MA}}$	${}^{\mathrm{B}}_{\mathrm{IP}}S_{\mathrm{MA}}$
400	98%	36%	36%	27%	81%	29%	80%
410	98%	37%	36%	28%	77%	29%	76%
420	97%	37%	36%	29%	72%	30%	72%
430	97%	37%	36%	30%	66%	31%	67%
440	97%	37%	36%	31%	61%	31%	62%
450	97%	37%	36%	31%	55%	32%	57%

Tab. 4.8: *Calculated catalyst body properties in the oxidation of 1% n/n of synthetic raffinate II over a VPO-50 catalyst at different temperatures.*

respectively. The reactor selectivities are almost independent of temperature. The calculations and the experimental values show good agreement. Even the small increase in the catalyst body selectivity of maleic anhydride with increasing temperature is well represented. At higher conversion levels of about 90%, the maximum reactor selectivities are achieved. This region is displayed in more detail in Fig. 4.16(a). The calculated values decrease with increasing temperature from about 52% to about 48%. The experimentally determined maximum reactor selectivities of maleic anhydride are independent of temperature considering measuremental errors and have values of about 49%. The resulting yields are displayed in Fig. 4.16(b). The maximum experimental yields tend to be around 47% at a conversion level of about 96%. The calculated maximum yields decrease with increasing temperature from 48% to 45% and are achieved at a conversion level of about 95%. Considering the broad range of reaction conditions presented by the rate equations used in the present work and considering the experimental errors, it can be stated that a good agreement between experiments and calculations was achieved.

4.4.3 Variation of the Hydrocarbon Fraction in the Feed

The conversion of raffinate II was carried out with varying hydrocarbon fractions in the feed. In this section, the experiments carried out at a reaction temperature of 420 °C are presented. The fractions of synthetic raffinate II of 1.0%, 1.5% and 2.0% in the feed correspond to hydrocarbon fractions of 0.9%, 1.4% and 1.8%, respectively, because of the nitrogen content in the synthetic raffinate II mixture.

Only the activity parameters change upon variation of the raffinate fraction in the feed. The values of the activity parameters of *n*-butenes, *n*-butane and both hydrocarbons decrease from 3.73, 0.46 and 3.15 $\frac{\mathrm{mol}}{\mathrm{s\,kg\,MPa}}$ for feed fractions of 1.0% n/n to values of 2.44, 0.31 and 2.06 $\frac{\mathrm{mol}}{\mathrm{s\,kg\,MPa}}$ for feed fractions of 2.0% n/n, respectively.

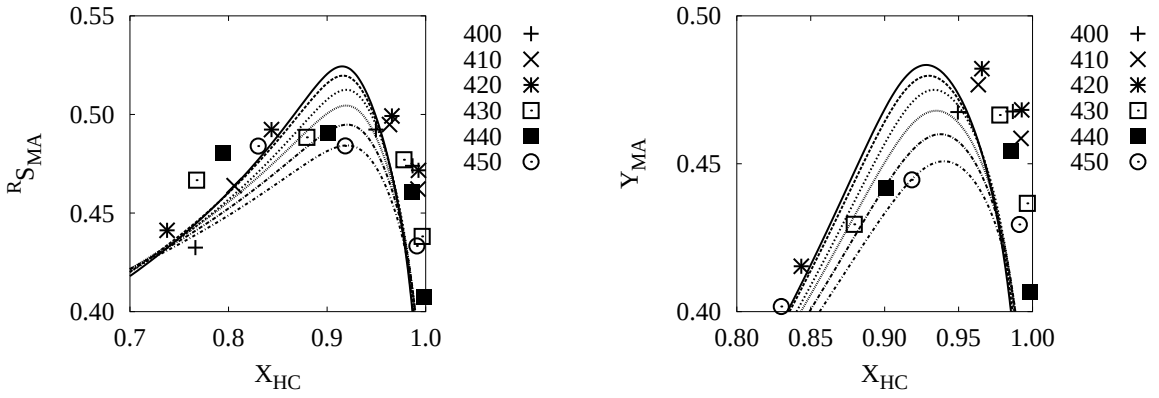

(a) Reactor selectivities (b) Yields

Fig. 4.16: *Reactor selectivities and yields of maleic anhydride at high conversion levels for the oxidation of synthetic raffinate II (1% n/n in air) at various temperatures.*

The results of the experiments and the corresponding calculations are presented in Fig. 4.17. The inhibition effects are well represented by the calculation as shown in the plots of the fraction profiles of the individual hydrocarbons. The reactor selectivities of maleic anhydride decrease only slightly with increasing hydrocarbon fractions in the feed. The rate equations cannot represent this dependence.

4.4.4 Comparison with Results in the Literature

The most detailed report on the oxidation of raffinate II in the literature is the investigation carried out by Quast [16]. He studied the conversion of a real raffinate II mixture at 380 °C and achieved a maximum conversion level of 80%. The reactor selectivity of maleic anhydride was about 50% at this conversion level. The corresponding reactor selectivity in the present work at 400 °C is about 45%.

The Bayer process of converting raffinate II to maleic anhydride is reported in [9]. The complete conversion of *n*-butenes and a yield of maleic anhydride of 34% was achieved at temperatures between 400 and 440 °C. The yields in the present work related to the linear C_4 hydrocarbons are around 47%. That corresponds to a yield for the conversion of raffinate II of about 43%. This yield is clearly higher than the yield of maleic anhydride in the Bayer Process.

4.5 Variation of the *n*-Butane/*n*-Butene-Ratio

The previous sections covered the conversion of pure *n*-butane, pure *n*-butenes and synthetic raffinate II. In this section, the effects of changes in the composition of the hydrocarbon feedstock on the reaction behaviour are discussed. The experiments which are presented in this section were carried out at a reaction temperature of 420 °C and with a total hydrocarbon fraction of 1% n/n in the feed. The experiments with pure *n*-butane, with 25% of 1-butene, with 82% of 1-butene (raffinate II) and with pure 1-butene are

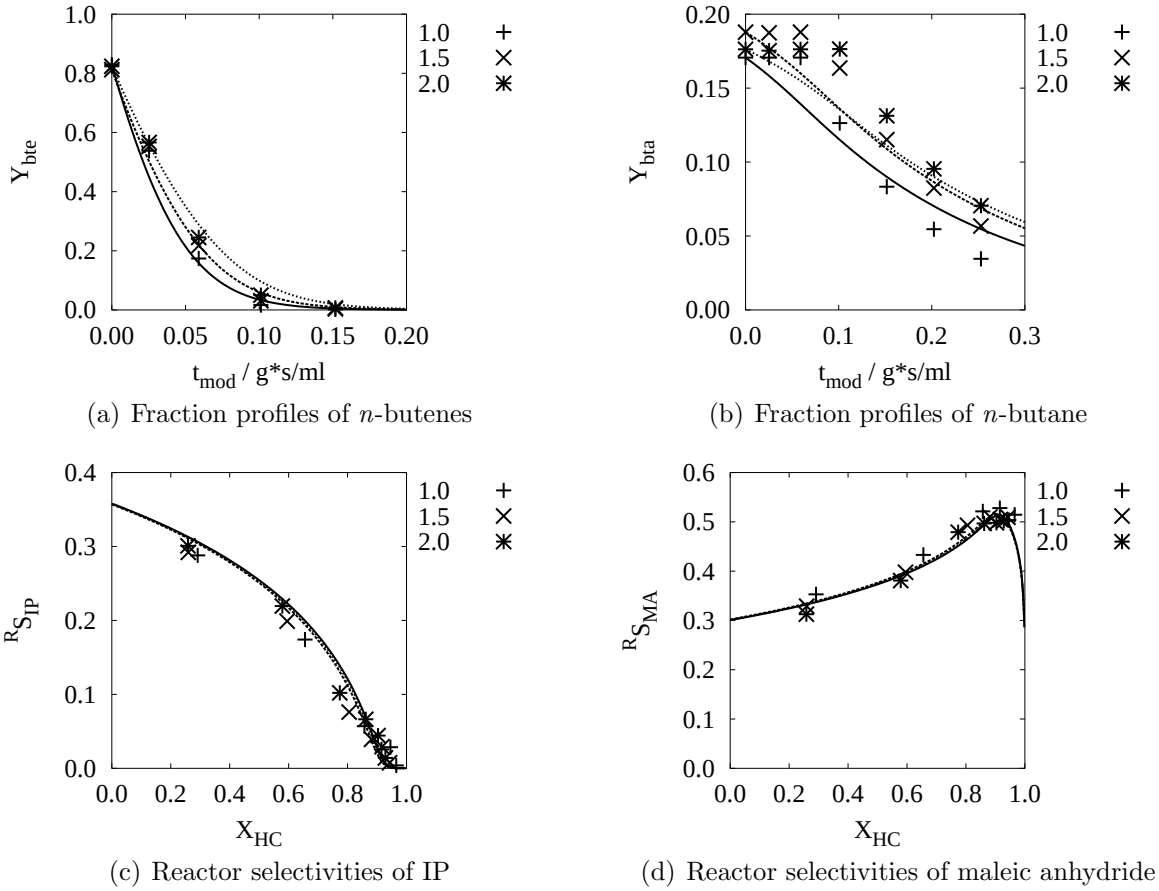

(a) Fraction profiles of *n*-butenes

(b) Fraction profiles of *n*-butane

(c) Reactor selectivities of IP

(d) Reactor selectivities of maleic anhydride

Fig. 4.17: *Variation of the fraction of synthetic raffinate II in the feed (values are given in % n/n) at 420* °C.

discussed in the present section.

The calculated catalyst body properties for these reaction conditions are listed in Tab. 4.9. Additionally, the catalyst body properties for a 1:1 composition of *n*-butane and *n*-butenes are presented as they result from the modelled reaction kinetics. Only those properties are listed that change with the variation of the hydrocarbon composition.

The oxidation reactions are more inhibited by the presence of *n*-butenes than by the presence of *n*-butane. Therefore, the partial activity parameters decrease with increasing relative amount of *n*-butenes in the feed. The rate constants for the conversion of *n*-butenes are higher than the rate constants for the conversion of *n*-butane. Therefore, the overall activity parameter increases with increasing relative amount of *n*-butenes. The relative reaction rate of the *n*-butenes for a relative amount of only 25% of *n*-butenes in the feed already has a value of 73%. The conversion reactions of *n*-butenes are dominating even for small relative amounts of *n*-butenes in the feed.

The catalyst body selectivity of IP increases with increasing relative amount of *n*-butenes since more *n*-butenes in the feed accelerate the formation of IP. The catalyst body selectivity of maleic anhydride decreases with increasing relative amount of *n*-butenes, since the direct formation of maleic anhydride by the conversion of *n*-butane decreases.

$x_{\mathrm{bte}}^{\mathrm{HC}}$	$x_{\mathrm{bta}}^{\mathrm{HC}}$	${}^{\mathrm{B}}k_{\mathrm{a,bta}}$ / $\frac{\mathrm{mol}}{\mathrm{s\,kg\,MPa}}$	${}^{\mathrm{B}}k_{\mathrm{a,bte}}$ / $\frac{\mathrm{mol}}{\mathrm{s\,kg\,MPa}}$	${}^{\mathrm{B}}k_{\mathrm{a}}$ / $\frac{\mathrm{mol}}{\mathrm{s\,kg\,MPa}}$	a_{bte}	${}^{\mathrm{B}}S_{\mathrm{IP}}$	${}^{\mathrm{B}}S_{\mathrm{MA}}$	${}^{\mathrm{max}}Y_{\mathrm{MA}}$
0%	100%	0.76	6.2	0.76	0%	0%	72%	56%
25%	75%	0.62	5.0	1.7	73%	27%	40%	
50%	50%	0.52	4.3	2.4	89%	33%	34%	
82%	18%	0.43	3.6	3.0	97%	36%	30%	48%
100%	0%	0.40	3.3	3.3	100%	37%	29%	53%

Tab. 4.9: *Calculated catalyst body properties of the conversion of 1% n/n of hydrocarbons with different compositions over a VPO-50 catalyst at a reaction temperature of 420* °C.

The fraction profiles and reactor selectivities that were determined in the experiments and the corresponding calculated values are presented in Fig. 4.18. Fig. 4.18(b) shows the fraction profiles of *n*-butenes as functions of the modified residence time. The different amounts of *n*-butenes in the feed lead to different values for the dimensionless fractions at $t_{\mathrm{mod}} = 0$. The dimensionless fractions equal $x_{\mathrm{bte}}^{\mathrm{HC}}$ in this case. The profiles show a good agreement of experiments and calculations. This also holds for the profiles presented in Fig. 4.18(b) except for the case of the conversion of pure *n*-butane. In this case, the calculated values are higher than the experimental ones. The experimental values were obtained in an experiment with a freshly activated catalyst that had not yet been used in the oxidation of *n*-butenes. The calculations, however, are based on the reaction kinetics for the conversion of the mixtures.

Fig. 4.18(c) shows the fraction profiles of IP. The calculations and the experimental values show a good agreement. The maximum yields as well as the residence times of the maxima decrease with increasing relative amounts of *n*-butenes in the feed. The catalyst body selectivities of IP increase for increasing relative amounts of *n*-butenes. Additionally, the conversion levels where the reactor selectivities achieve the value 0 increase. The deviation of the calculated and experimental values for the experiment with 25% of *n*-butenes

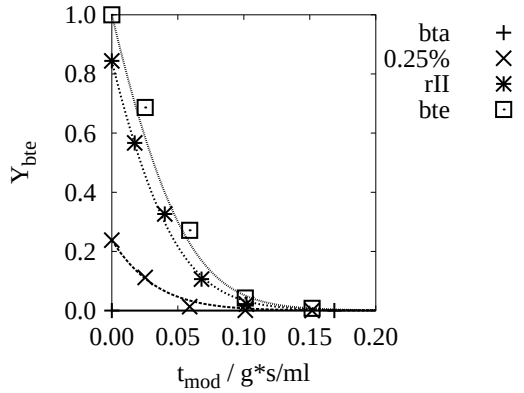

(a) Fraction profiles of *n*-butenes

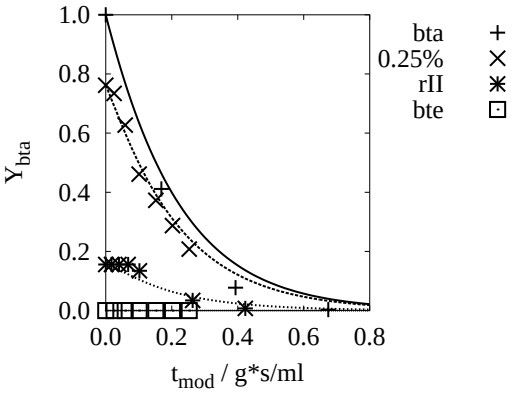

(b) Fraction profiles of *n*-butane

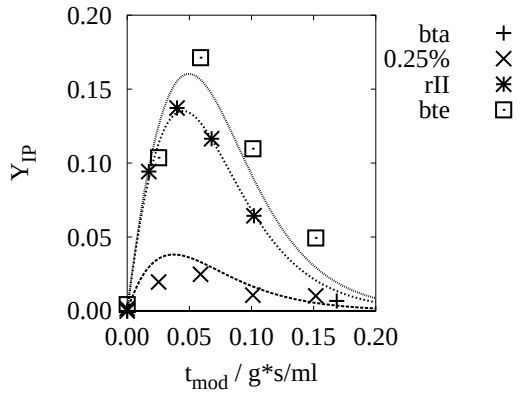

(c) Fraction profiles of IP

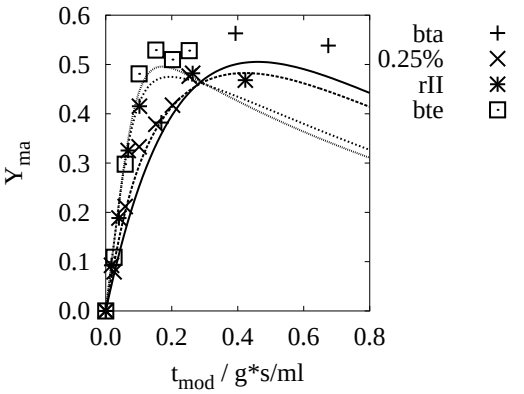

(d) Fraction profiles of maleic anhydride

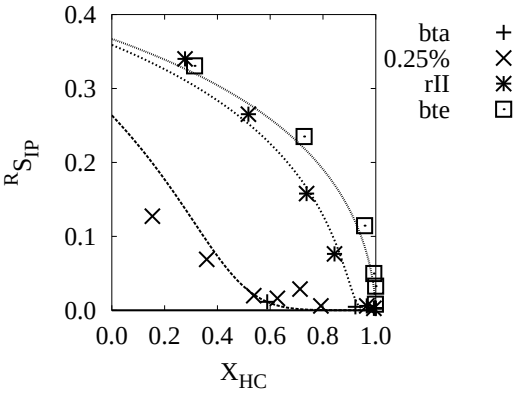

(e) Reactor selectivities of IP

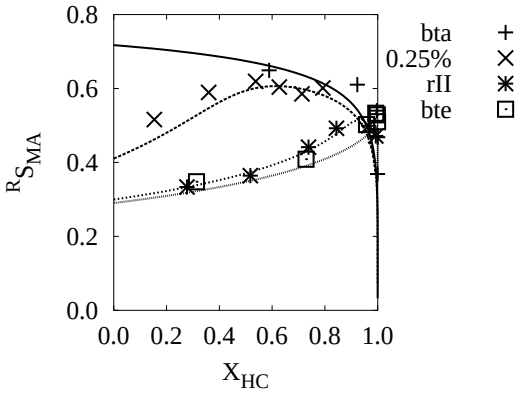

(f) Reactor selectivities of maleic anhydride

Fig. 4.18: *Variation of the butane and butene contents at 420* °C *and 1% of hydrocarbons in the feed over a VPO-50 catalyst. The labels 'bta', '0.25%', 'rII' and 'bte' denote the conversion of pure n-butane, conversion of 25% of n-butenes in the hydrocarbon feedstock, conversion of raffinate II and conversion of pure n-butenes, respectively.*

may be explained by the uncertainty of the experimental determination of the fraction of 1,3-butadiene.

The reactor selectivities of maleic anhydride are displayed in Fig. 4.18(f). The catalyst body selectivities of maleic anhydride decrease with increasing relative amounts of *n*-butenes. The calculated values for the pure *n*-butane conversion for conversion levels of about 90% are lower than the experimental values. This deviation can be attributed to the different behaviour of the catalyst after the conversion of *n*-butenes. The yields for maleic anhydride are presented in Fig. 4.18(d). The experimentally determined maximum yields are also listed in Tab. 4.9. The highest yield of 56% was achieved with pure *n*-butane, the lowest yield with a value of 48% with the synthetic raffinate II mixture. The maximum yield of the conversion of pure *n*-butenes is in-between these two values and amounts to 53%. The reason for the smaller yield obtained with raffinate II has already been explained in section 4.4. The maximum yield for the hydrocarbon mixture with 25% n/n of 1-butene was not achieved in the experiment. Higher relative amounts of *n*-butenes in the feed lead to smaller residence times where the maximum yield is reached.

In Fig. 4.19, the yields of maleic anhydride are plotted against the conversion levels. For higher relative amounts of *n*-butenes in the feed, the conversion levels required to achieve maximum yields of maleic anhydride shift to higher values.

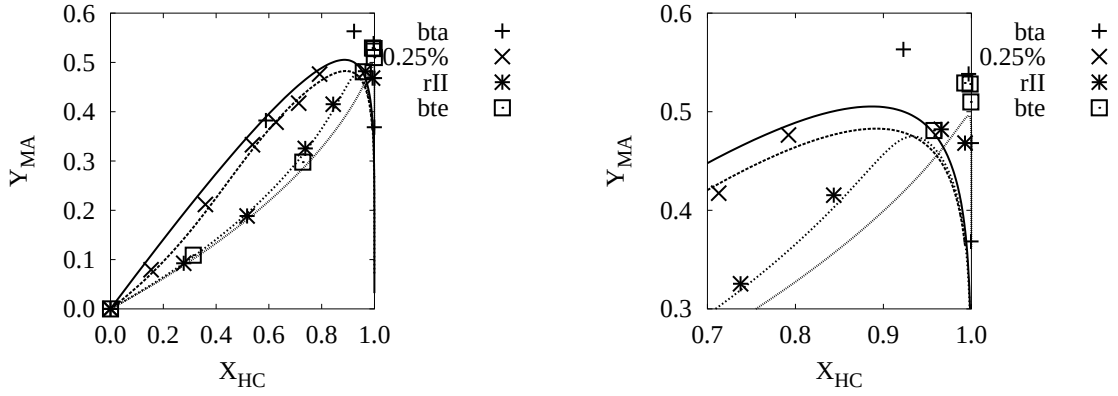

(a) Whole range (b) High conversion levels

Fig. 4.19: *Yields of maleic anhydride as functions of the conversion level for different compositions of the hydrocarbon feedstock at 420 °C. The feed fraction was 1% n/n. The labels 'bta', '0.25%', 'rII' and 'bte' denote the conversion of pure n-butane, conversion of 25% of n-butenes in the hydrocarbon feedstock, conversion of raffinate II and conversion of pure n-butenes, respectively.*

4.6 Oxidation of Isobutane over VPO-50

Raffinate II contains about 8% n/n of isobutane. In the present work, a synthetic mixture of *n*-butane and 1-butene containing the same concentrations as present in raffinate II was used. In this section, the reactivity of isobutane is discussed. Experiments were carried out with a feed fraction of 1% n/n of isobutane as the only hydrocarbon. The conversion

of isobutane was investigated at two temperatures: 420 °C and 450 °C. The fraction profiles and reactor selectivities for the oxidation of isobutane at 420 °C are plotted in Fig. 4.20. Fig. 4.20(a) shows the fraction profiles of isobutane, IP, maleic anhydride and carbon oxides as functions of the modified residence time. The oxidation of isobutane follows the same triangular scheme as the oxidation of *n*-butane. However, the maximum yield of maleic anhydride has a value of about 5% and most of the isobutane is directly converted to carbon oxides. Fig. 4.20(b) displays the reactor selectivities as functions of the conversion level. The catalyst body selectivity of maleic anhydride is about 10%. Intermediates are formed with a higher selectivity than the intermediates that are formed in the conversion of *n*-butane, but the value of the selectivity is still small. The catalyst body selectivities of carbon monoxide and carbon dioxide amount to about 50% and 40%, respectively. Therefore, the stoichiometric parameter for the total oxidation of isobutane is about 56%. The corresponding value for the total oxidation of *n*-butane is 64%. The formation of carbon dioxide is obviously more favoured in the oxidation of isobutane.

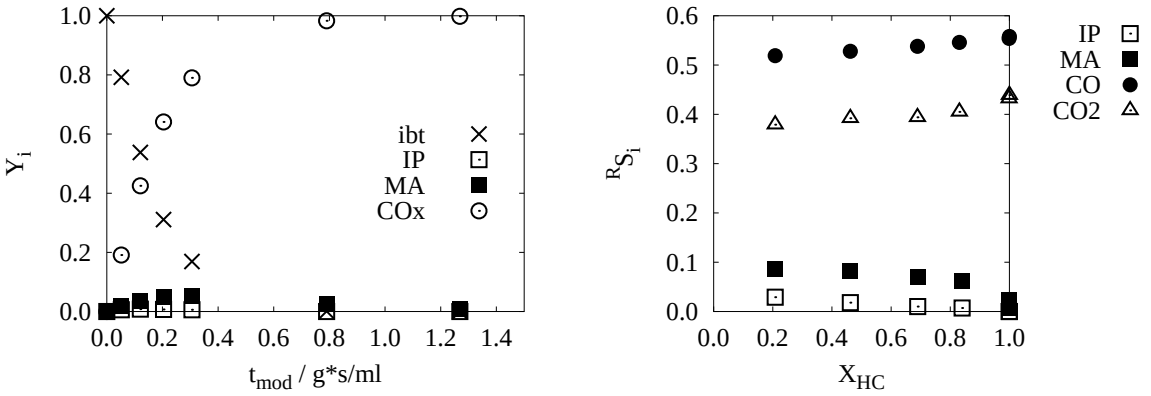

(a) Fraction profiles

(b) Reactor selectivities

Fig. 4.20: *Oxidation of 1% n/n of isobutane (ibt) in air at 420 °C over a VPO-50 catalyst. The fraction profiles are plotted against the modified residence time, the reactor selectivities against the conversion level.*

In Fig. 4.21 the fraction profiles of isobutane are plotted against the modified residence time for both temperatures, 420 °C and 450 °C. Additionally, the corresponding experimentally determined and calculated fraction profiles of *n*-butane for the oxidation of pure *n*-butane are included. The profiles of the individual hydrocarbons are coinciding at both temperatures. Therefore, it can be assumed that the reaction rates are identical. The selectivity of maleic anhydride, however, has a value of about 5% only.

4.7 Oxidation of Raffinate II over VPO-14

The variation of reaction temperature in the oxidation of pure *n*-butenes showed deviations from the expected rates at a temperature of 340 °C. Those deviations may result from changes in the effects of the pore transport resistances on the catalyst performance. To investigate the effects of the transport resistances in more detail, experiments were carried

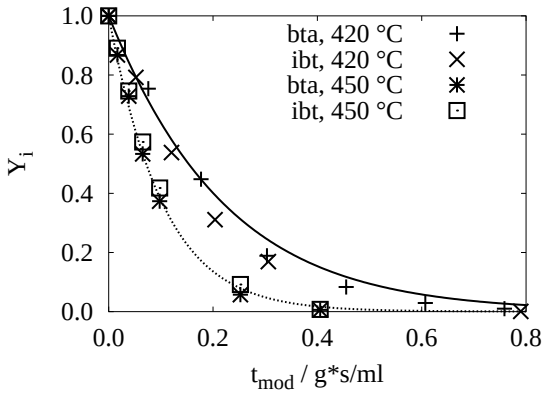

Fig. 4.21: *Comparison of the conversion of isobutane (ibt) and n-butane (bta) at temperatures of 420* °C *and 450* °C.

out with the VPO-14 catalyst. This catalyst type has an active layer with a thickness that is about six times lower than the thickness of the layer of the VPO-50 catalyst. This section shows the differences between the raffinate II oxidation by using the VPO-50 and VPO-14 catalyst. This section serves as an introduction to chapter 5, where a detailed comparison and the quantitative description of the differences are given.

The experiments concerning the oxidation of synthetic raffinate II over a VPO-14 catalyst were carried out in a temperature range from 350 °C to 430 °C. The hydrocarbon fraction in the feed was varied between 0.75% and 2%. The results of the conversion of raffinate II (1% n/n in air) at 410 °C are presented in Fig. 4.22. Fig. 4.22(a) shows the fraction profiles of the hydrocarbons *n*-butane and *n*-butenes as well as the sum of both. The *n*-butenes were completely converted at a modified residence time of about 0.05 (g s)/ml. This residence time is roughly a fourth of the corresponding residence time required for the complete conversion of *n*-butenes over a VPO-50 catalyst. At a given flow rate through the reactor, this means that four times the active mass of a VPO-50 catalyst is necessary than it is of a VPO-14 catalyst to achieve complete conversion. This can be attributed to a lower effectiveness factor when a VPO-50 catalyst is used. This, in turn, is a clear indication that transport resistances influence the catalyst performance of a VPO-50 catalyst.

The reactor selectivities are displayed in Fig. 4.22(b). The selectivity curves resemble those that were obtained for the VPO-50 catalyst, except for the higher catalyst body selectivity of IP and the lower selectivities of maleic anhydride. The catalyst body selectivity of maleic anhydride can be extrapolated to a value of 0 in case of the VPO-14 catalyst. The direct oxidation reaction of *n*-butenes to maleic anhydride can therefore be removed from the reaction network as it is displayed in Fig. 4.23. Fig. 4.22(c) shows the fraction profiles of the products. The higher reactor selectivities of IP and the lower reactor selectivities of maleic anhydride result in a higher maximum yield of IP and a lower maximum yield of maleic anhydride, respectively. The maximum yield of maleic anhydride was about 40% and was therefore clearly lower than the corresponding maximum yield of 47% obtained by using a VPO-50 catalyst for the same reaction conditions.

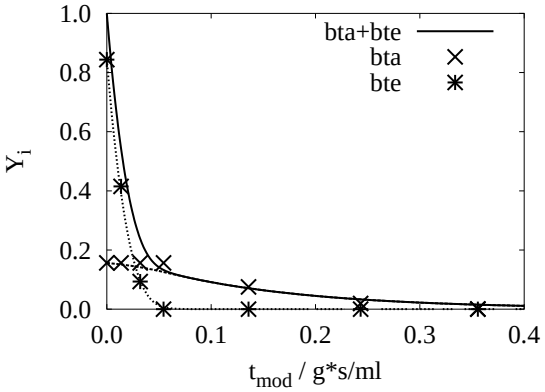

(a) Concentration profiles of *n*-butane and *n*-butenes

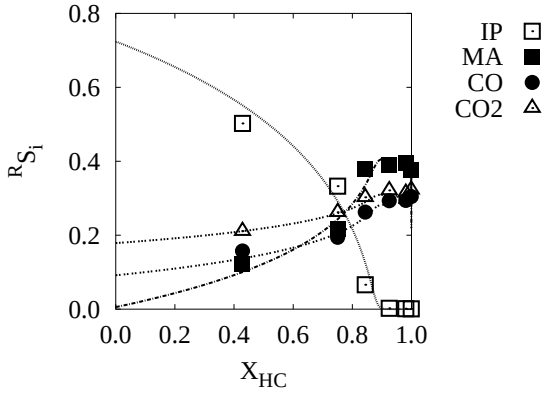

(b) Reactor selectivities

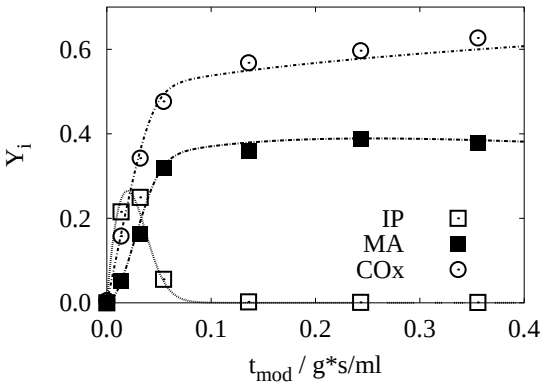

(c) Fraction profiles of the products

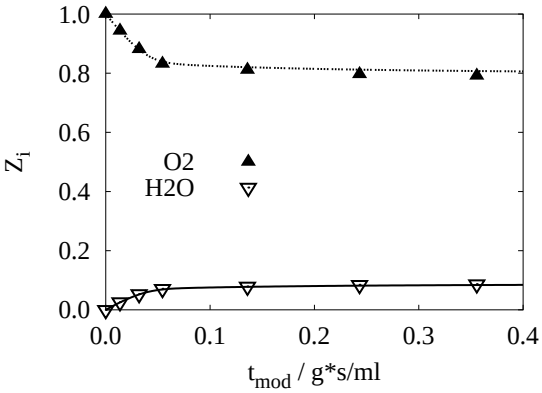

(d) Fraction profiles of oxygen and water

Fig. 4.22: *Partial oxidation of 1% n/n of synthetic raffinate II in air at 410 °C over a VPO-14 catalyst. The fraction profiles are plotted against the modified residence time, the reactor selectivities against the conversion level of raffinate II. The symbols represent the experimental values, the lines represent the calculations based on the modelled reaction kinetics.*

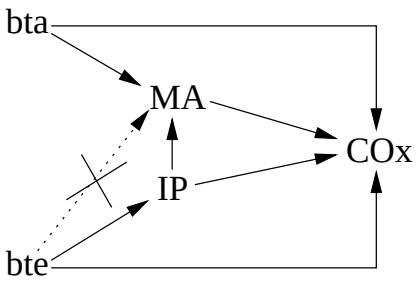

Fig. 4.23: *Reaction network for the oxidation of mixtures of n-butenes and n-butane over a VPO-14 catalyst.*

4.7.1 Quantification of Reaction Kinetics and Catalyst Parameters

As in the parameter estimations before, the rate equations are of the type of equation (3.39). The direct oxidation of *n*-butenes to maleic anhydride, however, was not considered. The measurements resulted in 704 experimental values that were used to determine 22 model parameters. After the parameter estimation, the residual error resulted in a value of $\chi^2 = 875$. The resulting parameters are shown in Tab. 4.10. Some of the correlation parameters have values higher than 0.9. These are listed in Tab. 4.11. A strong correlation was found between the rate constant of the total oxidation of *n*-butane and the inhibition constant of *n*-butane. Weak correlations exist between both rate constants of the *n*-butane oxidation reactions and between the rate constant of the total oxidation of *n*-butenes and the inhibition constant for *n*-butenes. The confidence limits of the corresponding parameters, however, show that the parameters are determined in a similar precision as the other parameters.

i	j	$k_{i,j}(420\ ^\circ\mathrm{C})/k^+$		$E_{\mathrm{A},i,j}/E_\mathrm{A}^+$		$\frac{\Delta_\mathrm{R}H_{i,j}}{\Delta_\mathrm{R}H^+}$	other parameters		
bta	MA	2.25	±0.28	88.1	±9.1	−1266	b_bta/b^+	961	±192
bta	COx	1.24	±0.16	119	±10	−1977	b_bte/b^+	5520	±1214
bte	MA						b_IP/b^+	3778	±1660
bte	IP	62	±12	141.3	±5.9	−245	b_H2O/b^+	216	±48
bte	COx	20.7	±4.5	101.9	±5.9	−2155	s_bta	0.601	±0.014
IP	MA	31.9	±6.0	165.5	±7.6	−905	s_bte	0.336	±0.023
IP	COx	26.4	±5.3	162	±10	−1683	s_MA	0.535	±0.090
MA	COx	0.181	±0.040	101	±45	−790	s_IP	0.582	±0.033

Tab. 4.10: *Kinetic, stoichiometric and thermodynamic parameters for the oxidation of mixtures of n-butenes and n-butane over a VPO-14 catalyst. The reference values are* $k^+ = 1\,\frac{\mathrm{mol}}{\mathrm{s\,kg\,MPa}}$, $E_\mathrm{A}^+ = 1\,\frac{\mathrm{kJ}}{\mathrm{mol}}$, $\Delta_\mathrm{R}H^+ = 1\,\frac{\mathrm{kJ}}{\mathrm{mol}}$ *and* $b^+ = 1\,\mathrm{MPa}^{-1}$.

parameters		value	type
$k_\mathrm{bta,MA}$	$k_\mathrm{bta,COx}$	0.91	weak
$k_\mathrm{bta,MA}$	b_bta	0.93	weak
$k_\mathrm{bta,COx}$	b_bta	0.95	strong
$k_\mathrm{bte,COx}$	b_bte	0.91	weak

Tab. 4.11: *Correlation parameters of the parameter estimation carried out for the oxidation of mixtures of n-butenes and n-butane over a VPO-14 catalyst.*

Most of the values of the rate constants and activation energies found for the VPO-14 catalyst are higher than the corresponding values found for VPO-50. The lower values for the VPO-50 catalyst confirm the assumption of the existence of significant transport resistances.

The inhibition constants have higher values than those of VPO-50. There is a factor of five between the corresponding values for the inhibition by *n*-butane and *n*-butenes. In contrary to the VPO-50 catalyst, the inhibition constants for IP and water have non-zero values in case of the VPO-14 catalyst. The stoichiometric parameters of the total oxidation of *n*-butane and maleic anhydride obtained for the VPO-50 catalyst differ from the corresponding values found for VPO-14 by values of about 4% and -12%, respectively. The differences in the stoichiometric values for the total oxidation of *n*-butenes and IP are about 43% and 42%, respectively.

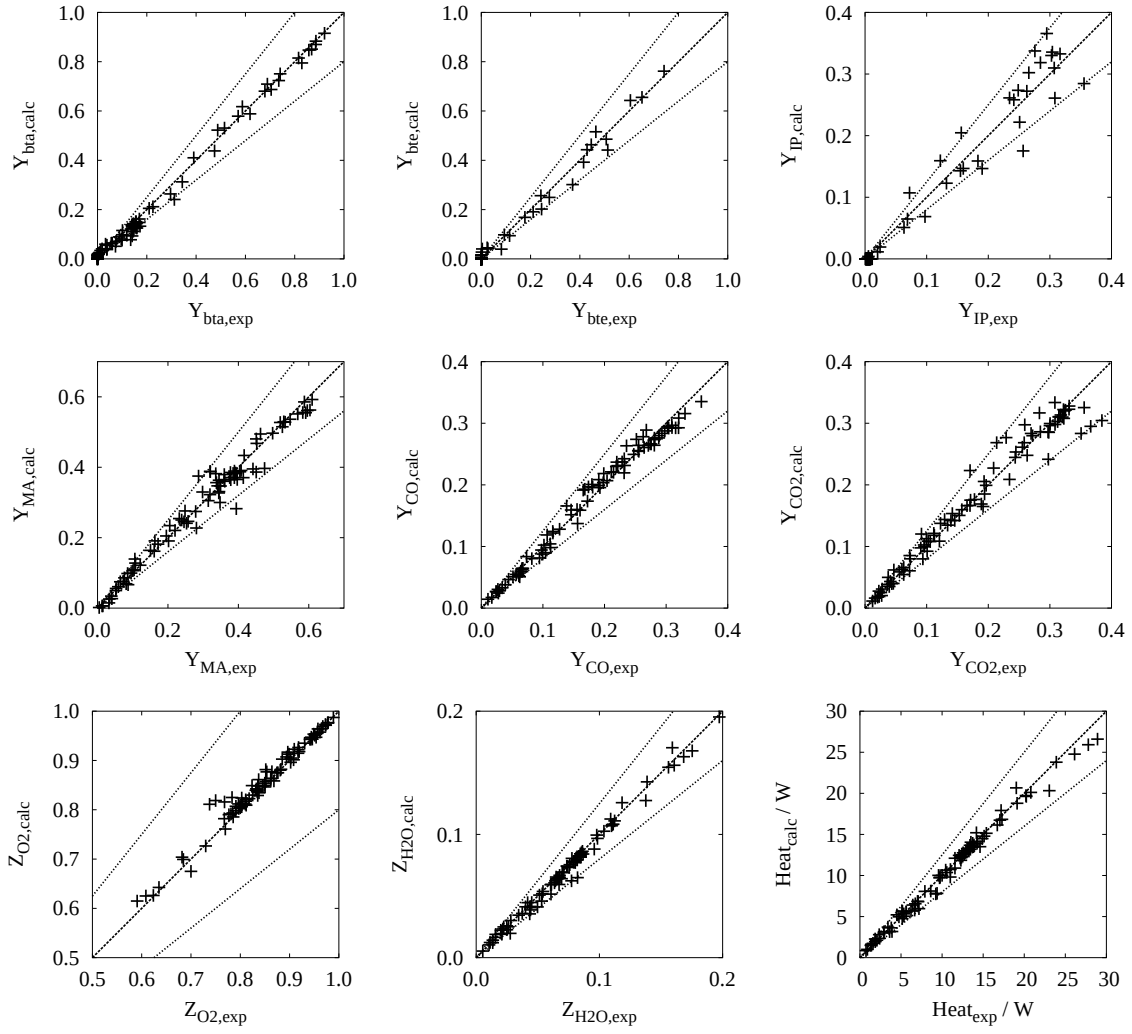

Fig. 4.24: *Parity plots for the oxidation of mixtures of n-butenes and n-butane over a VPO-14 catalyst.*

The parity plots for the oxidation of mixtures of *n*-butenes and *n*-butane over a VPO-14 catalyst are presented in Fig. 4.24. Most of the calculated values show deviations smaller than 20% from the experimental values.

4.7.2 Variation of the Temperature

The oxidation of the synthetic raffinate II mixture with the VPO-14 catalyst was carried out at temperatures between 350 °C and 420 °C. The calculated catalyst body parameters for these temperatures are listed in Tab. 4.12. The experimentally obtained fraction profiles and reactor selectivities as well as the corresponding calculated curves are presented in Fig. 4.25. Fig. 4.25(a) shows the fraction profiles of *n*-butenes as functions of the modified residence time. The temperature dependence is well represented by the calculations. For the fraction profiles of *n*-butane, however, only the tendencies agree. This can be seen in Fig. 4.25. Plots 4.25(c) and 4.25(d) which display the fraction profiles of IP and maleic anhydride, respectively. Except for the fraction profile of maleic anhydride for a reaction temperature of 430 °C, the calculated profiles agree with the experimental profiles. The experimentally determined fractions of maleic anhydride at a temperature of 430 °C as well as the corresponding reactor selectivities presented in Fig. 4.25(f) were higher than expected by the calculations. This difference could be attributed to pore diffusional effects even in the thin layer since the reaction temperature is high. Possibly, the catalyst is working in the transient regime between intrinsic reaction kinetics and effective kinetics with influences of pore diffusional transport. The experimentally determined reactor selectivity curves of IP are displayed in Fig. 4.25(e). They were found to be independent of the reaction temperature. The calculated curves, however, show catalyst body selectivities which are increasing with increasing temperature.

T in °C	${}^{\mathrm{B}}k_{\mathrm{a,bte}}$ / $\frac{\mathrm{mol}}{\mathrm{s\,kg\,MPa}}$	${}^{\mathrm{B}}k_{\mathrm{a,bta}}$ / $\frac{\mathrm{mol}}{\mathrm{s\,kg\,MPa}}$	${}^{\mathrm{B}}k_{\mathrm{a}}$ / $\frac{\mathrm{mol}}{\mathrm{s\,kg\,MPa}}$	${}^{\mathrm{B}}_{\mathrm{bte}}\lambda_{\mathrm{IP}}$	${}^{\mathrm{B}}_{\mathrm{bta}}\lambda_{\mathrm{MA}}$	${}^{\mathrm{B}}_{\mathrm{IP}}\lambda_{\mathrm{MA}}$
350	1.0	0.08	0.86	1.67	16	50
370	2.2	0.14	1.83	1.45	15	74
390	4.5	0.25	3.77	1.28	14	106
410	9.0	0.41	7.50	1.13	13	150
430	17.4	0.68	14.5	1.01	12	207
	a_{bte}	${}^{\mathrm{B}}_{\mathrm{bte}}S_{\mathrm{IP}}$	${}^{\mathrm{B}}S_{\mathrm{IP}}$	${}^{\mathrm{B}}_{\mathrm{bta}}S_{\mathrm{MA}}$	${}^{\mathrm{B}}S_{\mathrm{MA}}$	${}^{\mathrm{B}}_{\mathrm{IP}}S_{\mathrm{MA}}$
350	98%	58%	57%	77%	1%	53%
370	99%	64%	63%	73%	1%	54%
390	99%	69%	68%	70%	1%	54%
410	99%	73%	72%	66%	1%	55%
430	99%	77%	76%	63%	1%	55%

Tab. 4.12: *Calculated catalyst body properties of the oxidation of 1% n/n of synthetic raffinate II over a VPO-14 catalyst at different temperatures.*

4.7.3 Variation of the Hydrocarbon Fraction in the Feed

At a temperature of 410 °C the hydrocarbon fraction in the feed was varied between 0.75% n/n and 2% n/n. The results are presented in Fig. 4.26. Like in the oxidation of raffinate II over a VPO-50 catalyst, the fraction profiles of *n*-butenes, *n*-butane and IP are well represented by the calculations. The experimentally determined and calculated

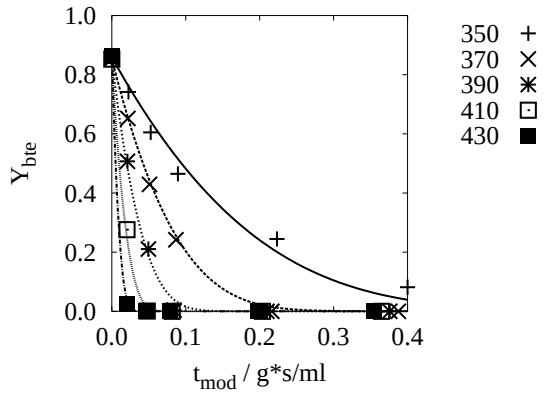

(a) Fraction profiles of *n*-butenes

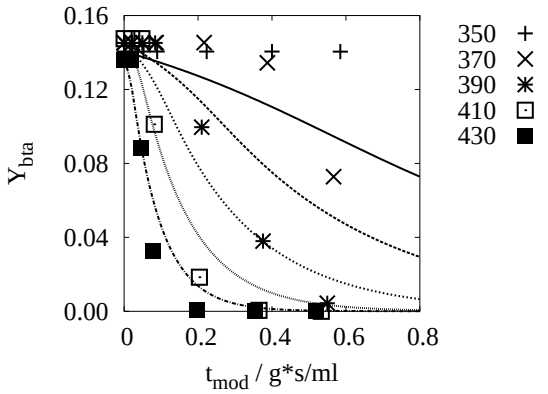

(b) Concentration profiles of *n*-butane

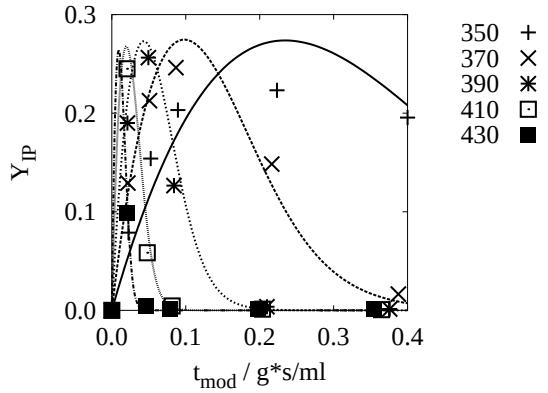

(c) Fraction profiles of IP

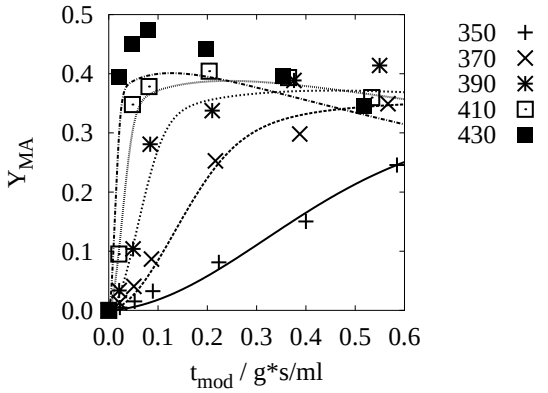

(d) Fraction profiles of maleic anhydride

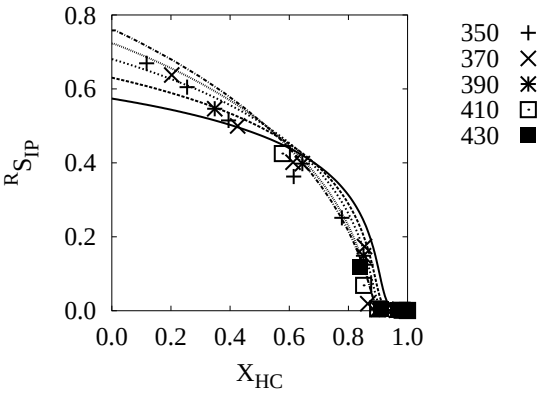

(e) Reactor selectivities of IP

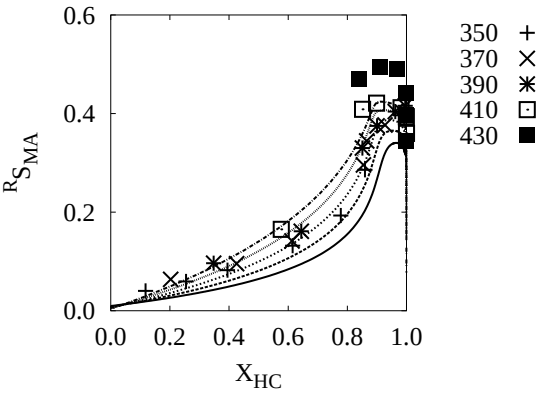

(f) Reactor selectivities of maleic anhydride

Fig. 4.25: *Variation of the reaction temperature (values are given in* °C*) in the oxidation of 1% n/n of synthetic raffinate II in air over a VPO-14 catalyst. The fraction profiles and reactor selectivities are presented.*

reactor selectivities of IP show also a good agreement. The reactor selectivities and yields of maleic anhydride were decreasing with increasing hydrocarbon fraction in the feed and show the same trend as the reactor selectivities in the oxidation of raffinate II over the VPO-50 catalyst.

4.8 Irreversible Changes in the Catalytic Performance

The value of the maximum yield and the residence time required to achieve this maximum yield are crucial for the process specifications. The catalyst behaviour, however, is changing with time, and the operation conditions of the reactor must be continuously adjusted to cope with the catalyst changes. It is therefore necessary to know how the catalyst properties vary over a period of time.

The catalyst changed irreversibly upon altering the operation conditions. For example, the catalyst may loose its desired properties, if the temperature in the reactor exceeds a critical value for some time. The performance of the catalyst may also be affected by changes in the amount of hydrocarbons in the feed. The catalyst may be irreversibly over-reduced or over-oxidised, if the hydrocarbon to oxygen ratio is increased or decreased, respectively. In the present work, an irreversible drop in the selectivity to maleic anhydride upon the conversion of pure *n*-butane was experienced after the catalyst was used for the conversion of *n*-butenes for some time.

4.8.1 Changes After Switching Between *n*-Butane and *n*-Butenes

Two experiments are compared in this section. In both experiments, pure *n*-butane was converted over the same VPO-14 catalyst at identical reaction conditions. The temperature was 415 °C, and the hydrocarbon fraction in the feed was 1.5% n/n. The first experiment was carried out after activation of the fresh catalyst. After the first experiment, the feed was switched to raffinate II for a few days. After switching back to pure *n*-butane, the second measurement was carried out. The fraction profiles of *n*-butane and the reactor selectivities of maleic anhydride determined in both experiments, first with fresh catalyst, and, second, the same catalyst after oxidation of raffinate II are presented in Fig. 4.27. The conversion rate of pure *n*-butane was slightly higher after the catalyst had been used for the oxidation of raffinate II: The fraction profile was shifted to lower values. The reactor selectivity of maleic anhydride also changed to lower values. While the reactor selectivity of maleic anhydride had been about 68% with the fresh catalyst, it had a value of about 63% for the catalyst used for the oxidation of raffinate II. This reactor performance remained constant over the next days. It was therefore assumed that the catalyst must have changed irreversibly.

4.8.2 Ageing During the Conversion of Raffinate II

The conversion of raffinate II (1% n/n in air) at 410 °C over a VPO-14 catalyst was studied during a longer runtime. The results of two measurements, one carried out after 8 days and one carried out after 35 days, are presented in Fig. 4.28. The changes in the catalytic behaviour for a period of 27 days are shown. The fraction profiles of *n*-butenes

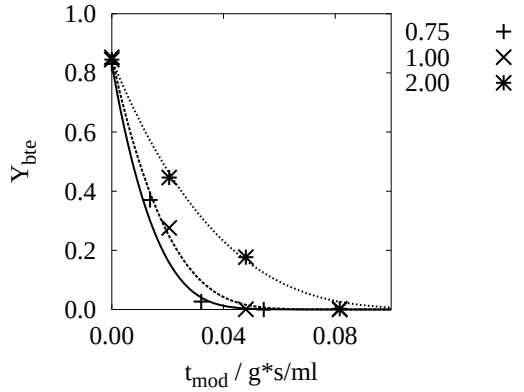

(a) Fraction profiles of *n*-butenes

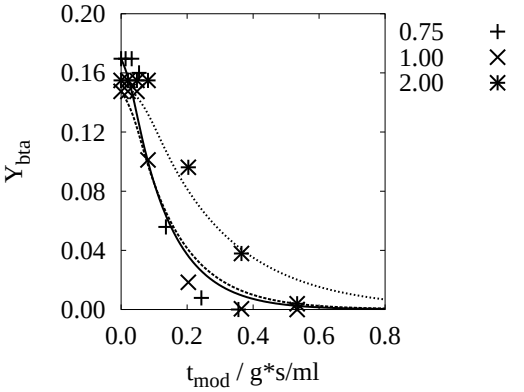

(b) Fraction profiles of *n*-butane

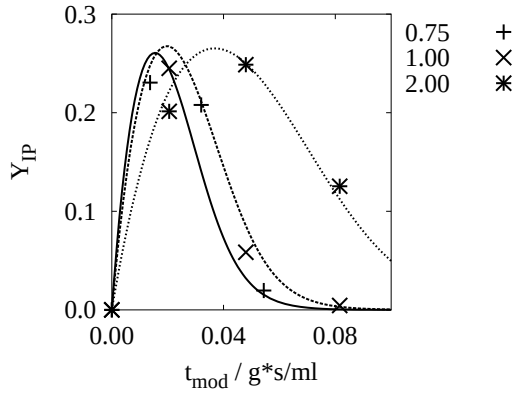

(c) Fraction profiles of IP

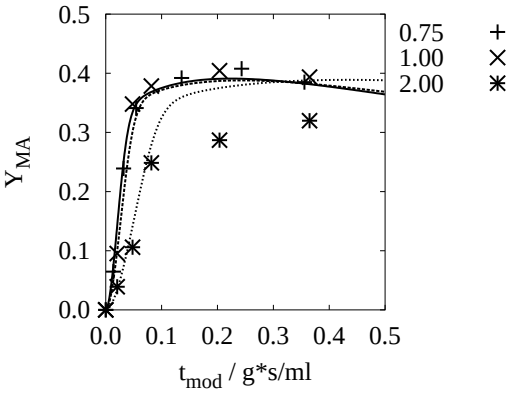

(d) Fraction profiles of maleic anhydride

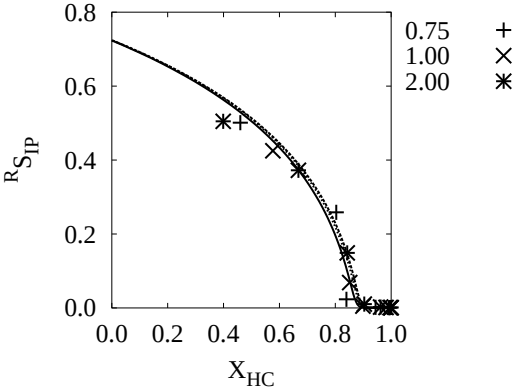

(e) Reactor selectivities of IP

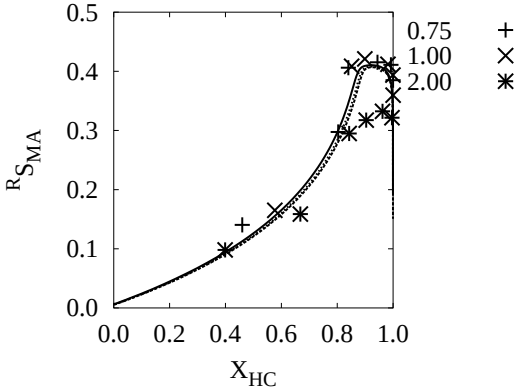

(f) Reactor selectivities of maleic anhydride

Fig. 4.26: *Variation of the hydrocarbon fraction of synthetic raffinate II in the feed (values are given in % n/n) in the conversion of raffinate II at 410* °C *over the VPO-14 catalyst.*

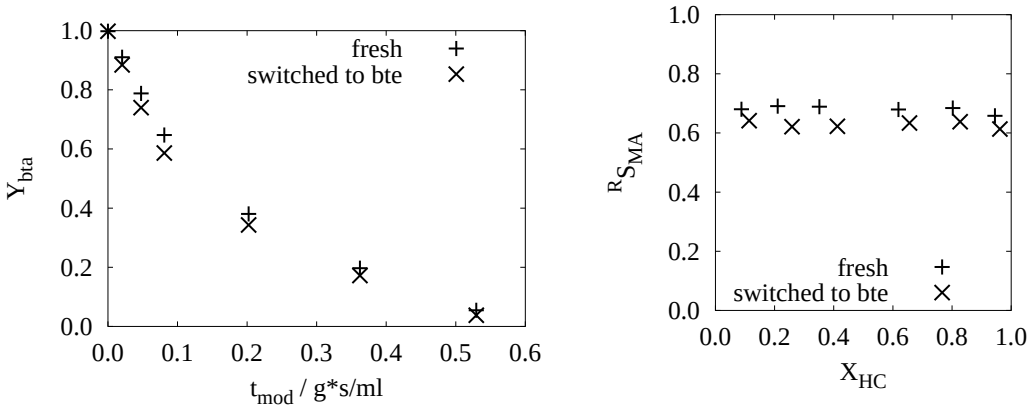

(a) Fraction profiles of *n*-butane

(b) Reactor selectivities of maleic anhydride

Fig. 4.27: *Oxidation of n-butane (1.5% n/n in air) at 415* °C *over the VPO-14 catalyst. The experiments with a fresh catalyst and with the same catalyst after switching back from raffinate II conversion are compared.*

and *n*-butane are presented in plots 4.28(a) and 4.28(c), respectively. It can be seen that the catalyst had become slightly more active upon the conversion of the hydrocarbon feedstock. The reactor selectivity curves of IP, plotted in Fig. 4.28(b), remained the same, despite the increasing activity. Fig. 4.28(d) shows the reactor selectivities of maleic anhydride. The reactor selectivity to maleic anhydride decreased slightly at higher conversion levels.

According to Cavani and Trifirò, the ageing of the VPO catalysts is mainly ascribed to the loss of phosphorus during reaction via hydrolysis by water. The catalyst lifetime is increased by continuous co-feeding of phosphorus compounds to the reactor during normal operation [44].

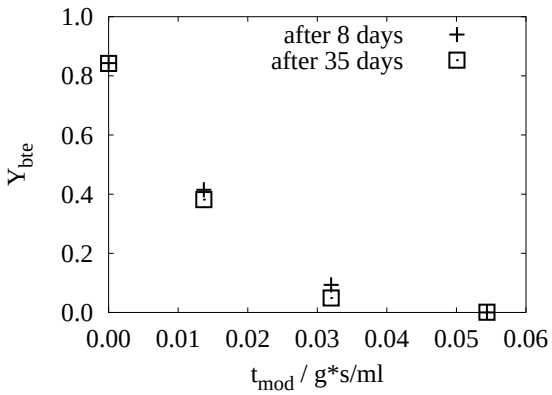

(a) Fraction profiles of *n*-butenes

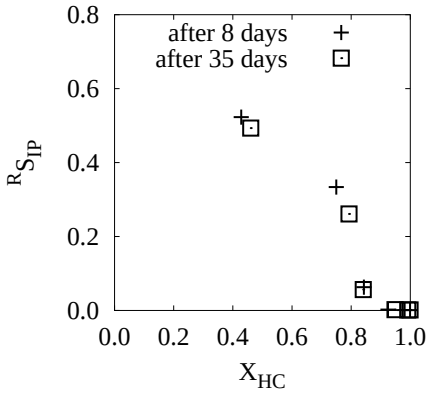

(b) Reactor selectivity of IP

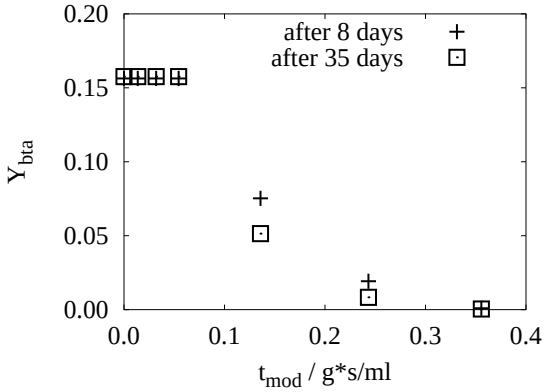

(c) Fraction profiles of *n*-butane

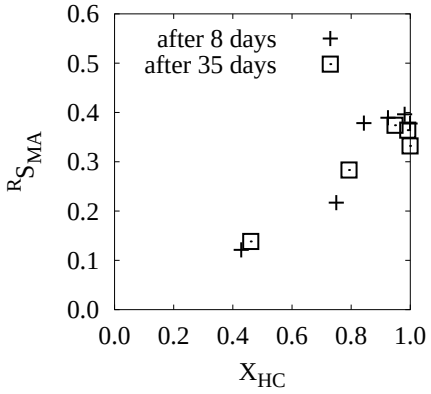

(d) Reactor selectivities of maleic anhydride

Fig. 4.28: *Ageing of the VPO-14 catalyst during the conversion of raffinate II (1% n/n) at 410* °C.

Chapter 5

Reaction and Transport

The results presented in the previous chapter demonstrate the different catalytic properties of VPO-50 and VPO-14. In this chapter, these differences are discussed in more detail regarding the oxidation of both, pure *n*-butane and raffinate II. This chapter also deals with the attempt to elucidate the differences between the two catalyst types by the simulation of coupled reaction and transport in the catalyst bodies. These simulations were, in turn, coupled with the simulation of an ideal plug flow reactor. Fraction profiles are presented and compared with those determined experimentally. The last section of this chapter discusses external transport resistances and their effects on reactor performance for both, laboratory and production scale reactors.

5.1 Comparison of VPO-50 and VPO-14

5.1.1 Oxidation of *n*-Butane

This section discusses the differences between the conversion of pure *n*-butane with the VPO-14 and VPO-50 catalyst types. Two experiments are compared in this section. Both were carried out at a temperature of 410 °C and with a feed fraction of 1% n/n of *n*-butane in air. The fraction profiles of *n*-butane and the reactor selectivities of maleic anhydride are presented in Fig. 5.1. The fractions of *n*-butane obtained for the VPO-14 catalyst are lower than the corresponding fractions obtained for the VPO-50 catalyst. Therefore, it can be stated that the activity of the VPO-14 catalyst is higher than the activity of VPO-50. More active mass is required at the same volumetric flow rate to achieve the same conversion level with VPO-50 since the active mass is less efficiently used as in case of VPO-14. In case of the VPO-50 catalyst, the reactor selectivity of maleic anhydride is lower than the corresponding selectivity obtained for the VPO-14 catalyst. The catalyst body selectivities are approximately 69% and 65% for the VPO-14 and VPO-50 catalysts, respectively. The explanation for the lower activity and selectivity obtained by using the VPO-50 catalyst type is presented in section 3.1.4. Accordingly, the lower activity results from the lower effectivity. The active mass is not used with equal efficiency in converting *n*-butane. The lower reactor selectivity of maleic anhydride obtained with the VPO-50 catalyst can be explained by the diffusional resistance of maleic anhydride: Some of the maleic anhydride molecules which had been formed on the catalyst surface were converted to carbon oxides before they could leave the active layer.

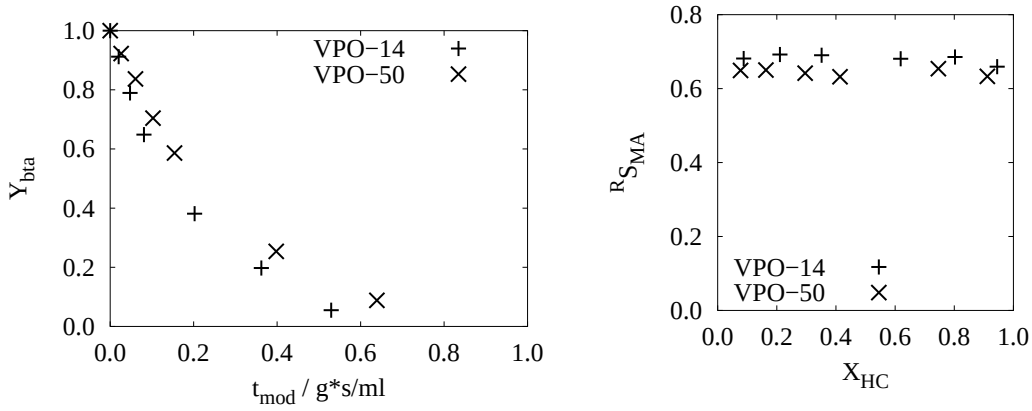

(a) Fraction profiles of *n*-butane

(b) Reactor selectivities of maleic anhydride

Fig. 5.1: *Comparison of the fraction profiles of n-butane and reactor selectivities of maleic anhydride in the conversion of pure n-butane over VPO-14 and VPO-50. The reactions were carried out with a feed fraction of 1% n/n of n-butane in air and at a temperature of 410* °C.

The differences between the conversion of *n*-butane by using the VPO-14 and the VPO-50 catalyst show that effects of transport resistances on the catalyst performance are significant even for the slowly reacting *n*-butane. The effects of transport resistances must be higher for the conversion of the more rapidly reacting *n*-butenes.

5.1.2 Oxidation of Raffinate II

The oxidation of raffinate II (1% n/n in air) over the VPO-14 and the VPO-50 catalysts is compared in Fig. 5.2. As already mentioned in the previous section, the lower activity of the VPO-50 catalyst is clearly seen in Fig. 5.2(a). The difference in activity is higher in the conversion of *n*-butenes than in the conversion of *n*-butane. The modified residence time required to achieve total conversion of the *n*-butenes is about 0.05 (g s)/ml and 0.20 (g s)/ml for the VPO-14 and VPO-50 catalysts, respectively. In order to achieve total conversion of *n*-butenes for the same reaction conditions, it is necessary to use a four times larger active mass of the VPO-50 catalyst than of the VPO-14 catalyst. Fig. 5.2(b) shows the fraction profiles of *n*-butane. The conversion of the *n*-butane fraction of the raffinate II feed is inhibited by the presence of *n*-butenes and begins to react significantly only at higher residence times. This delay is not represented well by the calculation. The differences between the experimentally determined fraction profiles of *n*-butane for the two catalyst types do not differ as much as the fraction profiles of *n*-butenes. The rate constants of the *n*-butane reactions are lower than the rate constants of the *n*-butenes reactions. Thus, the pore transport resistances have a lower impact on the conversion of *n*-butane.

The reactor selectivities of IP are displayed in Fig. 5.2(e). At low conversion levels, the reactor selectivities are higher for the VPO-14 catalyst. The catalyst body selectivities of IP are 72% and 36% for the VPO-14 and VPO-50 catalysts, respectively. The lower

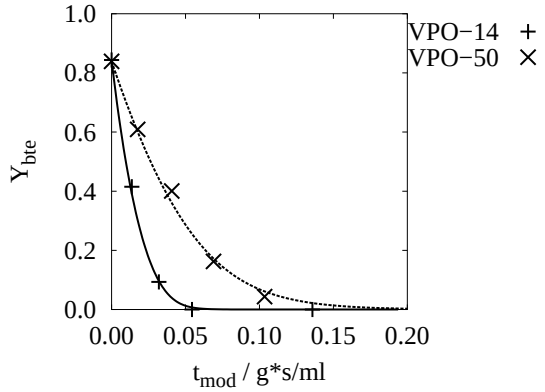

(a) Fraction profiles of *n*-butenes

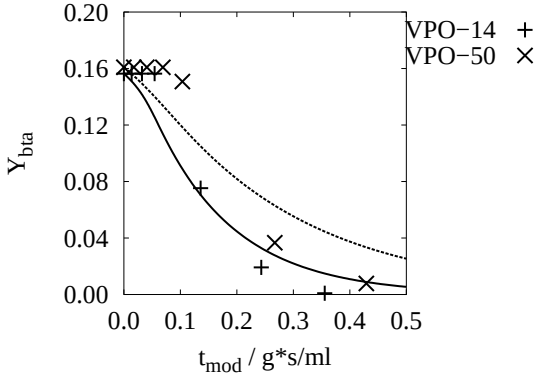

(b) Fraction profiles of *n*-butane

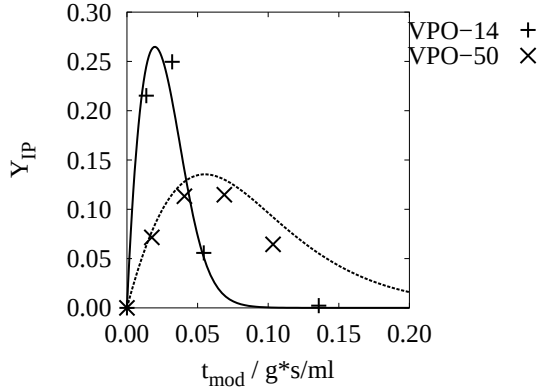

(c) Fraction profiles of IP

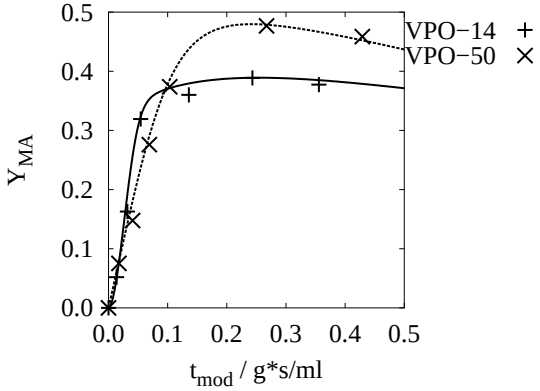

(d) Fraction profiles of maleic anhydride

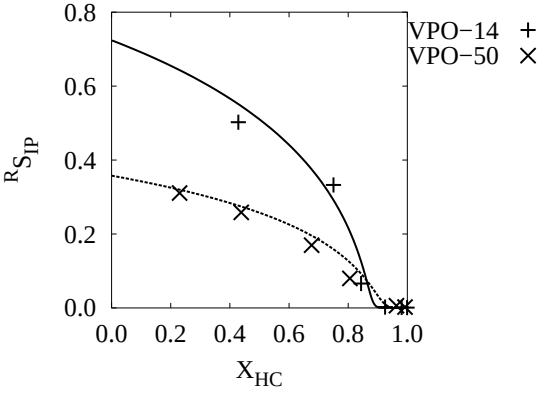

(e) Reactor selectivities of IP

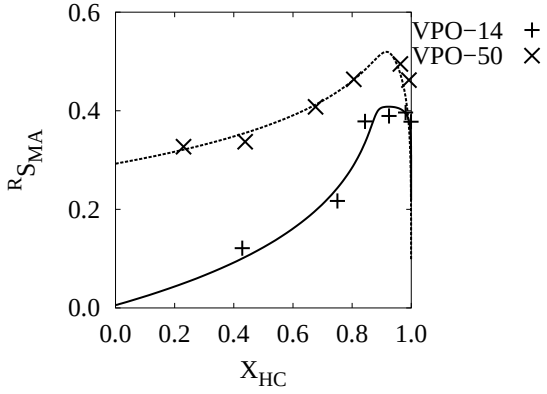

(f) Reactor selectivities of maleic anhydride

Fig. 5.2: *Comparison of the fraction profiles and reactor selectivities for the oxidation of synthetic raffinate II (1% n/n in air) over VPO-14 and VPO-50 catalysts at 410* °C.

value for the VPO-50 catalyst can be explained by considering the triangular reaction network of *n*-butenes, IP and maleic anhydride as shown in Fig. 5.3. The rate constant of the total oxidation reaction of maleic anhydride is much lower than the rate constants of the reactions of the above mentioned triangular reaction network. IP can therefore be regarded as an intermediate in the reaction of *n*-butenes to the *end product* maleic anhydride. The catalyst body selectivity and catalyst body stability of an intermediate of a triangular scheme is decreasing with increasing pore transport effects. This explains the lower values of IP in case of the VPO-50 catalyst. The *end product* is favoured in case of the VPO-50 catalyst and results in higher reactor selectivities of maleic anhydride as it can be seen in Fig. 5.2(f). While the catalyst body selectivity of maleic anhydride is 0 for the VPO-14 catalyst, which indicates the absence of the direct oxidation reaction of *n*-butenes to maleic anhydride, the catalyst body selectivity of maleic anhydride has a value of 29% for the VPO-50 catalyst. The fraction profiles of IP and maleic anhydride are presented in plots 5.2(c) and 5.2(d), respectively. Because of the higher selectivities of IP for the VPO-14 catalyst, the maximum yield is also higher than for the VPO-50 catalyst and amounts to about 25% compared to about 12% for the VPO-50 catalyst. Because of the higher activity of the VPO-14 catalyst, the maximum yield was achieved at lower residence times. The maximum yield of maleic anhydride (48%) was higher for the VPO-50. The corresponding value for the VPO-14 was about 38%. The formation rate of maleic anhydride during the conversion of the hydrocarbons was higher for the VPO-14 catalyst which results from the higher reaction rates of *n*-butenes and IP. The conversion rate of maleic anhydride, however, is higher for the VPO-50 catalyst. The higher conversion rate of maleic anhydride can be elucidated by the low rate constants for the decomposition reaction of maleic anhydride. A lower rate constant is less influenced by pore transport resistances. It can be assumed that these rate constants are equal for both catalyst types because they are not influenced by transport effects. Thus, the higher fraction level in case of the VPO-50 leads to higher decomposition rates. This statement agrees well with the experimental results.

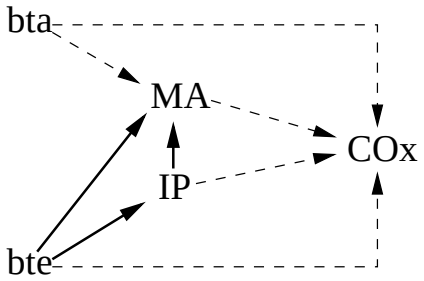

Fig. 5.3: *The triangular reaction network of n-butenes, IP and maleic anhydride (solid lines) as part of the complete reaction network.*

The differences between the two catalysts can be further discussed by comparing the kinetic constants and catalyst body parameters. These values are listed in Tab. 5.1. Each kinetic constant obtained for the VPO-50 catalyst is smaller than the corresponding constant obtained for the VPO-14 catalyst, except for the rate constant of the total oxidation reaction of maleic anhydride. The corresponding rate constants of this reaction are equal. This agrees well with the statement that reaction rates are more influenced by

	$k_{i,j}$ / $\frac{\text{mol}}{\text{s kg MPa}}$ for 410 °C							
	bte,IP	bte,MA	bte,COx	bta,MA	bta,COx	IP,MA	IP,COx	MA,COx
VPO-14	43.3		15.9	1.80	0.92	20.9	17.4	0.14
VPO-50	2.41	1.86	2.33	0.59	0.18	3.06	0.96	0.14
	$E_{\text{A},i,j}$ / kJ/mol							
	bte,IP	bte,MA	bte,COx	bta,MA	bta,COx	IP,MA	IP,COx	MA,COx
VPO-14	141		102	88	119	166	162	101
VPO-50	81	71	59	62	164	56	147	54
	inhibition constants and stoichiometric parameters							
	b_{bte}	b_{bta}	b_{IP}	b_{H2O}	s_{bte}	s_{bta}	s_{IP}	s_{MA}
VPO-14	5520	961	3778	216	34%	60%	54%	58%
VPO-50	1096	213	0	0	48%	63%	47%	83%
	catalyst body properties for 410 °C, activity parameters in $\frac{\text{mol}}{\text{s kg MPa}}$							
	${}^{\text{B}}k_{\text{a,bte}}$	${}^{\text{B}}k_{\text{a,bta}}$	${}^{\text{B}}k_{\text{a}}$	${}^{\text{B}}_{\text{bte}}\lambda_{\text{IP}}$	${}^{\text{B}}_{\text{bte}}\lambda_{\text{MA}}$	${}^{\text{B}}_{\text{bta}}\lambda_{\text{MA}}$	${}^{\text{B}}_{\text{IP}}\lambda_{\text{MA}}$	
VPO-14	9.0	0.41	7.50	1.13		13	150	
VPO-50	3.1	0.36	2.64	0.60	14	(4.4)	23	
	a_{bte}	${}^{\text{B}}_{\text{bte}}S_{\text{IP}}$	${}^{\text{B}}S_{\text{IP}}$	${}^{\text{B}}_{\text{bte}}S_{\text{MA}}$	${}^{\text{B}}_{\text{bta}}S_{\text{MA}}$	${}^{\text{B}}S_{\text{MA}}$	${}^{\text{B}}_{\text{IP}}S_{\text{MA}}$	
VPO-14	99%	73%	72%		66%	1%	55%	
VPO-50	98%	37%	36%	28%	(77%)	29%	76%	

Tab. 5.1: *Comparison of the calculated kinetic constants and catalyst body parameters in the oxidation of synthetic raffinate II over VPO-14 and VPO-50 catalysts. The values in parentheses appear unrealistic. See section 4.4 for a detailed discussion.*

transport resistances for higher values of the rate constants. As expected, almost all of the activation energies are higher for the VPO-14 catalyst than the corresponding activation energies for the VPO-50 catalyst.

The higher pore transport resistances in the VPO-50 catalyst lead to lower apparent inhibition constants. The inhibition constants are all smaller for the VPO-50 catalyst than for the VPO-14 catalyst. They are even 0 for the inhibition by IP and water in case of the VPO-50catalyst. There are also differences in the stoichiometric parameters. Especially the stoichiometric parameters of the total oxidation reactions of *n*-butenes and maleic anhydride have significantly different values. The values of the stoichiometric parameters of the total oxidation reaction of *n*-butenes amount to 48% and 34% for the VPO-50 and VPO-14 catalysts, respectively. The higher value of the VPO-50 catalyst can be elucidated by the combined formation and total oxidation of IP in the catalyst pores. This means that some carbon oxides are formed by the total oxidation of *n*-butenes, some are formed by the oxidation of *n*-butenes to IP and subsequent oxidation to carbon oxides in the pores of the VPO-50 catalyst. For reactions over the VPO-50 catalyst, these reactions appear to be partly lumped together. The stoichiometric parameter of *n*-butenes of the VPO-50 catalyst has therefore to be somewhere in-between the values of the stoichiometric parameters of *n*-butenes and IP of the VPO-14 catalyst. This is the case, since the value of 48% obtained for the VPO-50 catalyst is indeed in-between 34% and 54% which is obtained for the total oxidations of *n*-butenes and IP over VPO-14, respectively.

Each of the catalyst body activity parameters is lower for the VPO-50 catalyst than for the VPO-14 catalyst because of the lower effectiveness factor. The catalyst body stabilities are all lower for the VPO-50 catalyst as it can be expected for pore transport effects that become more dominant. The catalyst body selectivity of IP is higher for the VPO-14 catalyst whereas the catalyst body selectivity of maleic anhydride is higher for the VPO-50 catalyst. The catalyst body selectivity of maleic anhydride of 1% for the VPO-14 catalyst results from the conversion of small amounts of *n*-butane.

The variation of the reaction temperature in the oxidation of synthetic raffinate II on a VPO-14 catalyst is presented in section 4.7.2. There is a significant deviation of the calculated values from experimental values for a temperature of 430 °C while the calculations and the experiments show a good agreement for temperatures of 410 °C and below. Fig. 5.4 displays the plots of fraction profiles and reactor selectivities for a reaction temperature of 430 °C obtained by using the VPO-14 and by using the VPO-50 catalysts. The fraction profiles of the hydrocarbons *n*-butenes and *n*-butane resemble those of the experiments carried out at 410 °C. The reactor selectivities and yields of IP and maleic anhydride, however, deviate from the behaviour that was expected by the calculation.

The reactor selectivities of maleic anhydride are displayed in Fig. 5.4(f). While the calculated values for the VPO-14 catalyst are clearly below those of the VPO-50 catalyst, the experimentally determined values for both catalyst types lie on the same selectivity curve calculated for the VPO-50 catalyst. The higher temperature of 430 °C causes more predominant transport resistances. The effects of transport resistances on both catalyst types and therefore the behaviour of both catalyst types are more similar at this temperature.

The yields of maleic anhydride as functions of the modified residence time are displayed in Fig. 5.4(d). The reactor selectivities of maleic anhydride are identical for both catalyst types. This leads also to identical values of the maximum yield of about 48%. The

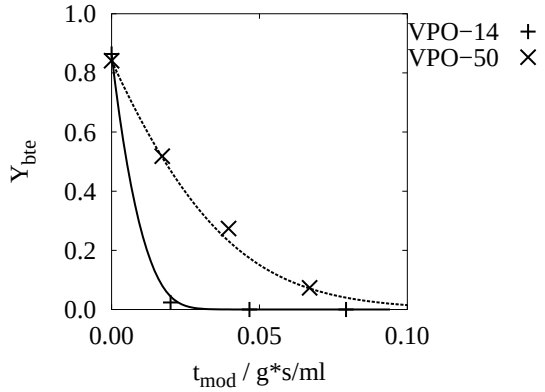

(a) Fraction profiles of *n*-butenes

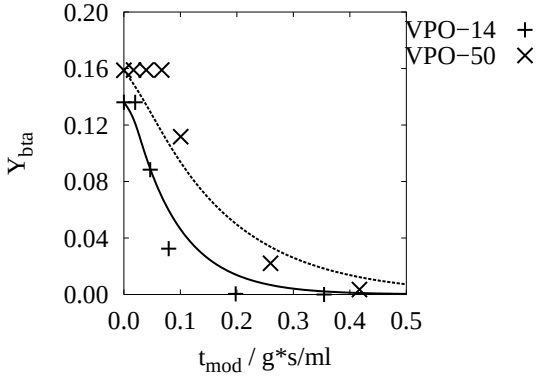

(b) Fraction profiles of *n*-butane

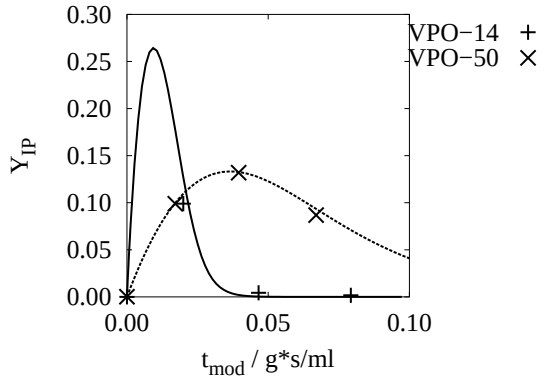

(c) Fraction profiles of IP

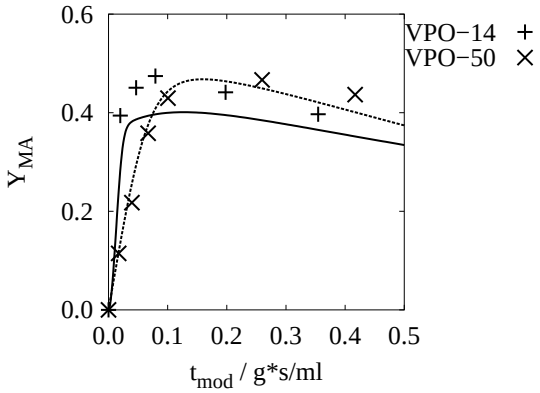

(d) Fraction profiles of maleic anhydride

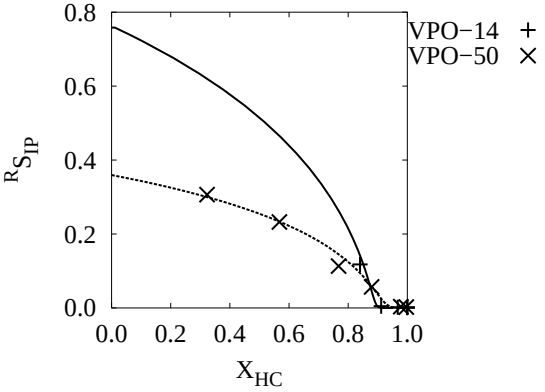

(e) Reactor selectivities of IP

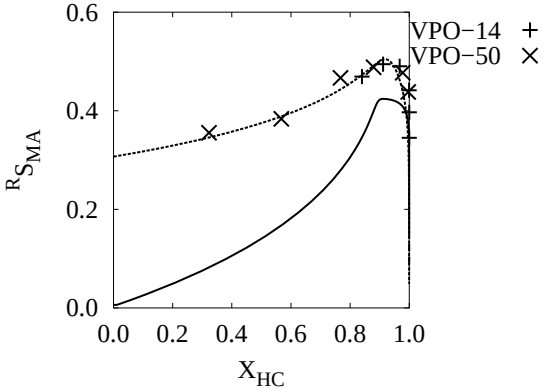

(f) Reactor selectivities of maleic anhydride

Fig. 5.4: *Comparison of the fraction profiles and reactor selectivities for the oxidation of synthetic raffinate II (1% n/n in air) over VPO-14 and VPO-50 catalysts at 430* °C.

maximum yield that was determined for the VPO-14 catalyst type, however, was achieved at a lower residence time of about 0.1 (g s)/ml compared to the value of about 0.3 (g s)/ml determined for the VPO-50 catalyst. The effectiveness factors are higher for the VPO-14 catalyst despite the positive influence of transport resistances on the reactor selectivities.

5.2 Simulation of Simultaneous Reaction and Transport in the Catalyst

This section describes the catalyst body simulations carried out to predict the differences in the behaviour between the two catalyst types. The catalyst body simulations are based on the coupled reaction and transport mechanisms that are important in the active layer of the catalyst body. One of the uncertainties affecting the simulations, however, is the missing information about the intrinsic reaction rates. It was assumed that the reaction kinetics over the VPO-14 catalyst are not influenced by pore transport resistances because of the low thickness of the active layer. In this case, the catalyst body reaction rates would coincide with the intrinsic reaction rates.

The catalytically active layer is treated as a pseudo-homogeneous phase in which the individual species are transported according to Fick's law. The distribution of active material is assumed to be homogeneous. The active layer is a shell surrounding the inert support. Since the shell thickness is small compared to the radius of the cylindrical shell, the curvature of the shell is negligible. It is further assumed that there are no fraction gradients in tangential directions. The problem results in a set of differential equations which can be solved to obtain the fraction profiles perpendicular to the catalyst surface. The depth in the layer is denoted by x with $x = 0$ at the surface of the catalyst and $x = L$ at the inner interface between the active layer and the support. The resulting differential balance for species i can be expressed as

$$D_i^{\text{body}} \frac{\partial^2 c_i}{\partial x^2} + \rho^{\text{body}} \times {}^{\text{I}}R_i = 0. \tag{5.1}$$

The fraction profiles in the active layer are obtained by solving equation (5.1) with the boundary conditions

$$\mathbf{c}\big|_{x=0} = \mathbf{c}^{\text{S}}, \tag{5.2}$$

$$\left.\frac{\partial \mathbf{c}}{\partial x}\right|_{x=L} = 0. \tag{5.3}$$

Boundary condition (5.2) states that the concentration of the species in the opening of the pores at the outer surface of the catalyst body equal those of the gas phase directly surrounding the body. Boundary condition (5.3) expresses that the catalyst support is non-porous and therefore no molecule can enter the support: the flux equals 0.

The constants D_i^{body} are the effective diffusivities of species i in the catalyst layer. The intrinsic formation rates related to catalyst mass ${}^{\text{I}}R_i$ are assumed to be the catalyst body formation rates over the VPO-14 catalyst for the reasons given above. The concentration profiles in the active layer were calculated in Matlab by using a finite differences solver coupled with a relaxation method and a non-linear root finder. The catalyst body

formation rates can be calculated by using Fick's law at the catalyst body surface:

$$^{\mathrm{B}}R_i = \frac{A_{\mathrm{geo}}^{\mathrm{body}}}{m_{\mathrm{active}}^{\mathrm{body}}} \times j_i = \frac{A_{\mathrm{geo}}^{\mathrm{body}}}{m_{\mathrm{active}}^{\mathrm{body}}} \times D_i^{\mathrm{body}} \left.\frac{\partial c_i}{\partial x}\right|_{x=0}. \tag{5.4}$$

However, the gradient cannot be calculated numerically in the necessary precision. Another way was therefore chosen to determine the catalyst body formation rates. The molar flow of a specific species i out of the catalyst body equals the molar formation rate of this species within the catalyst body. Since the reaction rates in the active layer depend on the position, the overall catalyst body formation rates are obtained by integration:

$$^{\mathrm{B}}R_i = \frac{1}{L}\int_0^L {}^{\mathrm{I}}R_i(\mathbf{c}(x), T, p)\,\mathrm{d}x. \tag{5.5}$$

5.2.1 Effective Diffusivities in the Catalyst Bodies

The effective diffusivities are related to the corresponding diffusivities of the species in cylindrical pores with a specific pore diameter:

$$D_i^{\mathrm{body}} = \frac{\epsilon}{\tau} D_i^{\mathrm{pore}}. \tag{5.6}$$

The porosity of the catalyst layer (ϵ) can be regarded as the fraction of imaginary cylindrical pores in the active layer. However, the pores are typically branched or even interconnected and do not have the same pore diameters. Also, they are not necessarily cylindrical. The effective diffusivities have to be corrected by the tortuosity factor τ. This factor has typically values in the range of 3 to 7 [34]. The tortuosity can be calculated by assuming specific pore structures. In the present work, however, the tortuosity has been determined by comparison of the performance of the two catalysts. This is discussed in section 5.2.3.

Two diffusional transport mechanisms have to be considered to calculate the diffusivity of a species i in a cylindrical pore: the molecular diffusion and the Knudsen diffusion. The molecular diffusion assumes that the collisions of molecules with the pore wall are negligible compared to the collisions between molecules. The Knudsen diffusion, on the other hand, is based on the assumption that the collisions of the molecules of species i with the wall are dominant. The molecular diffusion mechanism is therefore valid for high gas pressures and large pore diameters. The Knudsen diffusion mechanism is applicable for low gas pressures and small pore diameters. The gas pressures and pore diameters in catalyst bodies are typically in-between such extreme conditions. By assuming equimolar fluxes, the diffusivities in the transition region can be calculated by considering both mechanisms [45] and result in

$$D_i^{\mathrm{pore}} = \left(\left(D_i^{\mathrm{mol}}\right)^{-1} + \left(D_i^{\mathrm{kn}}\right)^{-1}\right)^{-1}. \tag{5.7}$$

The Knudsen diffusivities result from the assumption of a cylindrical pore with a specific radius. In the present work, the mean pore radius was used. The diffusivity of a species i is directly proportional to the inverse root of its molecular weight and can be expressed as

$$D_i^{\mathrm{kn}} = \frac{2\bar{r}_{\mathrm{pore}}}{3}\sqrt{\frac{8RT}{\pi M_i}}. \tag{5.8}$$

The molecular diffusivities were calculated by assuming that the concentrations of the species involved in the reactions are small compared to the carrier gas and interactions between these species are negligible. The molecular diffusivities then equal the molecular diffusivities of binary mixtures of the considered species and air. The binary molecular diffusivities were calculated according to [42]. The diffusivity of IP was obtained by treating all intermediates lumped together as a virtual species with the corresponding sum formula.

The dependence of molecular diffusivities on temperature and pressure is

$$D_i^{\mathrm{mol}} \propto \frac{T^{1.75}}{p}. \tag{5.9}$$

The temperature dependence of the Knudsen diffusivities is even weaker. Both temperature dependences are much weaker than the temperature dependences of the reaction rates. The calculated values of the molecular diffusivities are presented in Tab. 5.2. The corresponding effective catalyst body diffusivities are about two magnitudes lower than the molecular diffusivities.

Species	$D_i^{\mathrm{mol}}/(\mathrm{cm}^2/\mathrm{s})$	
	340 °C	450 °C
butane	0.264	0.352
butene	0.271	0.361
IP	0.280	0.373
MA	0.245	0.327
CO	0.539	0.720
CO_2	0.432	0.577
O_2	0.545	0.727
H_2O	0.693	0.925

Tab. 5.2: *Calculated molecular diffusivities of the individual reaction species.*

5.2.2 Typical Concentration Profiles in the Catalyst Bodies

The catalyst body simulation can be used to calculate the concentration profiles in the active layer for given concentrations in the gas phase surrounding the catalyst body. In this section, a specific situation and the resulting calculated concentration profiles in the active layer are presented. The calculations were carried out for a VPO-50 catalyst body directly located at the reactor inlet. The catalyst body was assumed to be surrounded by a feed gas containing 1% of synthetic raffinate II in air. A temperature of 410 °C was assumed. The resulting concentration profiles of *n*-butenes, *n*-butane, IP and maleic anhydride are presented in Fig. 5.5 as functions of a dimensionless position or depth x_{layer}. A position of $x_{\mathrm{layer}} = 0$ denotes the catalyst body surface and a position of $x_{\mathrm{layer}} = 1$ denotes the interface between active layer and catalyst support. A tortuosity factor of $\tau = 3$ was assumed.

In case of negligible transport resistances, the concentrations would be equal for every position in the layer. The hydrocarbons, however, cannot move fast enough through the

active layer to achieve equal concentrations at every position. Instead, both hydrocarbon concentrations decrease with increasing depth. Because of the higher reaction rates of the conversion reactions of *n*-butenes compared to those of *n*-butane, the corresponding concentrations achieve values of almost 0 in the vicinity of the support surface.

The products IP and maleic anhydride exhibit higher concentrations in the catalyst body compared to the gas phase surrounding the catalyst body. In the gas phase, no products are present at the reactor inlet. The concentration of maleic anhydride is highest directly at the boundary between the active layer and the catalyst support. The concentration profile of IP, however, shows a maximum at about $x_{\text{layer}} = 0.3$. For $x_{\text{layer}} > 0.3$, the concentrations of *n*-butenes and *n*-butane are low which results in low conversion rates of the hydrocarbons to IP. The presence of maleic anhydride in the catalyst body leads to a catalyst body selectivity of maleic anhydride of ${}^{\text{B}}S_{\text{MA}} > 0$. The effectiveness factor of the hydrocarbon conversion equals 37%.

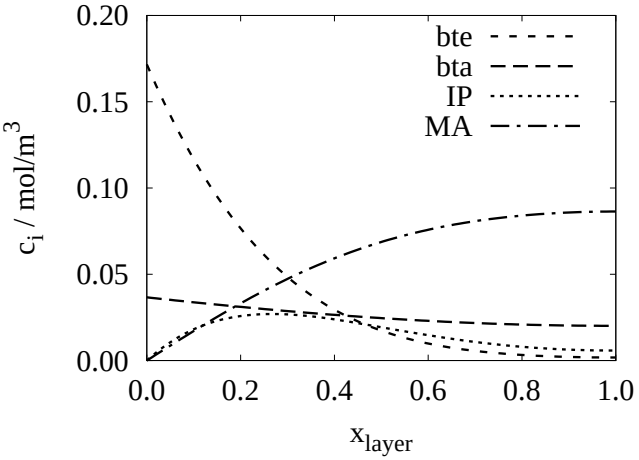

Fig. 5.5: *Concentration profiles in the active layer of a VPO-50 catalyst body located directly at the reactor inlet with 1% of raffinate II in the gas phase at 410* °C*. The effectiveness factor of the hydrocarbon conversion is 37%. The tortuosity factor was assumed to be* $\tau = 3$*.*

5.2.3 Effect of Layer Thickness and Tortuosity on Catalyst Performance

In the previous section, the tortuosity was assumed to be $\tau = 3$. In this section, the sensitivity of the calculation towards the choice of the tortuosity factor is presented. The resulting values of the effectiveness factor and catalyst body selectivities of IP and maleic anhydride are compared to the corresponding values calculated by using the effective kinetics of the VPO-50 catalyst. The layer thickness was also varied. The calculations were carried out for a reaction temperature of 410 °C and a gas phase with the composition of the reactor feed: 1% n/n of synthetic raffinate II in air. Fig. 5.6 displays the calculated effectiveness factor η and catalyst body selectivities of IP and maleic anhydride plotted

against the dimensionless thickness of the active layer

$$t_{\text{layer}} = \frac{L}{L_{\text{VPO}-50}}. \tag{5.10}$$

The dimensionless thickness relates the actual thickness to the thickness of the layer of the VPO-50 catalyst. The different curves represent calculations for different tortuosity

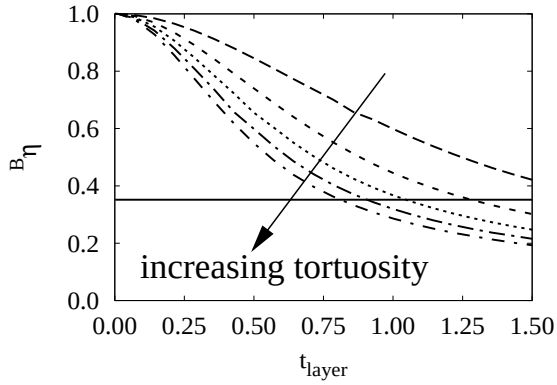

(a) Effectiveness factors

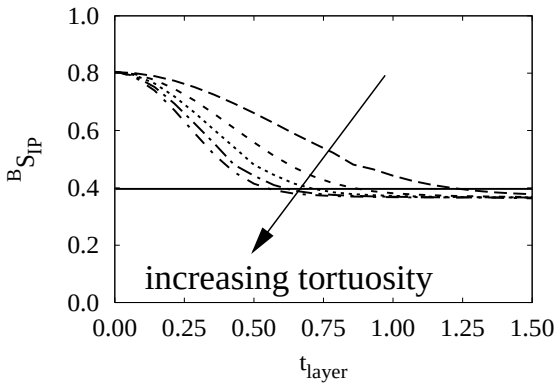

(b) Body selectivities of IP

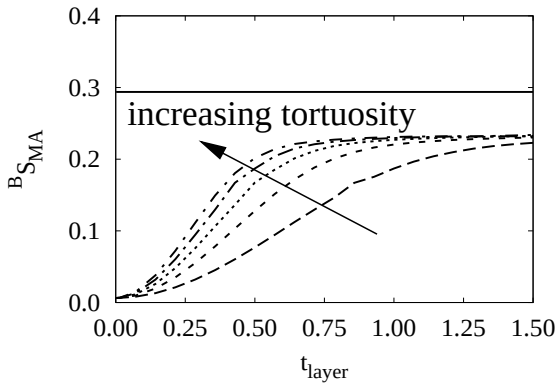

(c) Body selectivities of maleic anhydride

Fig. 5.6: *Influence of layer thickness and tortuosity on the catalyst body performance at 410* °C *with 1.0% n/n of synthetic raffinate II in the gas phase. Presented are the effectiveness factors and catalyst body selectivities of IP and maleic anhydride as functions of the dimensionless layer thickness. The individual curves represent the calculation for tortuosity factors ranging from 1 to 5. The arrows show the direction of increasing tortuosity values. The horizontal lines represent the values obtained by using the effective kinetics model of the VPO-50 catalyst.*

factors, ranging from 1 to 5. The horizontal lines show the corresponding values obtained by using the kinetic model of the VPO-50 catalyst. Fig. 5.6(a) shows the effectiveness factors as functions of the dimensionless layer thickness. Since no transport effects are present for zero thickness the effectiveness factor equals 1 for $t_{\text{layer}} = 0$. The effectiveness

factor is decreasing with increasing layer thickness and tortuosity. The effectiveness factor reaches a constant value of 0 for sufficiently high values of the thickness. For a tortuosity factor of $\tau = 3$, the best agreement between the effectiveness factors calculated by the catalyst body model and the effective kinetics of the VPO-50 ($t_{\text{layer}} = 1$) is obtained. Therefore, $\tau = 3$ was chosen for all subsequent calculations.

Fig. 5.6(b) shows the catalyst body selectivities of IP. The value of the catalyst body selectivity for a thickness of $t_{\text{layer}} = 0$ is identical to the intrinsic selectivity. It is assumed that the effective kinetics of the VPO-14 catalyst equals the intrinsic kinetics and the intrinsic selectivity of IP is therefore assumed to be 80% at 410 °C. The catalyst body selectivity is decreasing with increasing thickness and reaches a value of 38% for higher values of the thickness. At a lower tortuosity factor, the limit of 38% is achieved at a lower thickness. The corresponding value which is obtained by using the effective kinetics of the VPO-50 catalyst is about 40%. This is a good agreement for $\tau = 3$. The catalyst body selectivity of maleic anhydride is presented in Fig. 5.6(c). The intrinsic selectivity is assumed to be 1%. No *n*-butenes are directly converted to maleic anhydride, but some maleic anhydride is directly formed through conversion of *n*-butane. The catalyst body selectivity of maleic anhydride is increasing with increasing layer thickness and also reaches a limit for higher values of the thickness. This constant value is about 23% and is therefore lower than 29% which is obtained by using the effective kinetics of the VPO-50 catalyst. The constant values are independent of the tortuosity. The tortuosity determines, however, at which thickness the constant values are achieved.

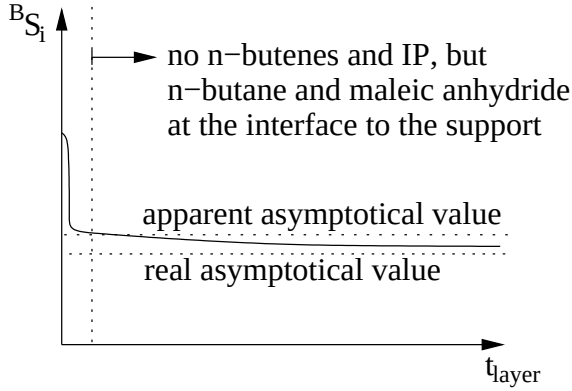

Fig. 5.7: *Schematic plot of the catalyst body selectivity as a function of the thickness of the active layers. The zone on the right hand side of the vertical line represents the lower decrease of the catalyst body selectivity because of the lower reaction rates of the conversion reactions of n-butane and maleic anhydride.*

The existence of asymptotical values of the catalyst body selectivities for $t_{\text{layer}} \to \infty$ have already been explained in section 3.1.4. The same types of plots as in Fig. 5.6 are displayed for a first order reaction network in Fig. 3.3. The constant values as reported above, however, are not yet the asymptotical values. The latter are achieved for a thickness at which no more carbon containing species except for the carbon oxides are present at the interface between the active layer and the support. However, *n*-butane and maleic anhydride are still present at this interface as displayed in Fig. 5.5. Fig. 5.7 shows the

catalyst body selectivities schematically for higher values of the layer thickness. The plots presented in Fig. 5.6 represent only the part of the plot in Fig. 5.7 that is on the left hand side of the vertical line. On the right hand side of this line, no *n*-butenes and IP are present at the interface of the support, and the subsequent decrease in the catalyst body selectivities result from the much lower rate constants of the conversion reactions of *n*-butane and maleic anhydride.

5.2.4 Variation of Temperature

The temperature dependence of the diffusivities is much weaker than the temperature dependence of the reaction rates. Therefore, the effects of transport resistances on the catalyst body performance are increasing with increasing temperature. The effectiveness factors and catalyst body selectivities were calculated for temperatures between 340 °C and 450 °C. The results are presented in Fig. 5.8. Each plot shows four curves. For both of the catalyst types VPO-14 and VPO-50, the properties calculated from the corresponding effective kinetics are displayed, labelled 'kin-14' and 'kin-50', respectively. The results from the catalyst body simulations are also presented, labelled 'sim-14' and 'sim-50', respectively. The gas phase surrounding the catalyst body is assumed to consist of 1% n/n of synthetic raffinate II in air.

Fig. 5.8(a) displays the effectiveness factors. The curve labelled 'kin-14' is a horizontal line at $\eta = 1$, since it is assumed that the catalyst body kinetics of the VPO-14 equal the intrinsic kinetics. The curve labelled 'sim-14' is calculated by using the catalyst body simulations for the VPO-14 catalyst. It decreases with increasing temperature and reaches a value of about 80% at 450 °C. This result indicates that the effective kinetics of VPO-14 are probably[1] influenced by transport resistances.

Curve 'kin-50' shows the effectiveness factor as calculated from the effective kinetics of the VPO-50 catalyst. For temperatures around 340 °C, it is about $\eta \approx 1$. The experiments carried out with pure *n*-butenes showed a deviation at this temperature. The calculated conversion rate was higher than the experimentally determined rate. It is clear that the reaction rates which are achieved by using the VPO-50 catalyst cannot be higher than the reaction rates which are achieved by using the VPO-14 catalyst. Curve 'sim-50' shows the effectiveness factor for the simulation of the VPO-50 catalyst body. The values of the simulation and the effective kinetics agree for temperatures above 370 °C. For temperatures below 370 °C, however, the effectiveness factors calculated in the simulation have lower values and a value of about 83% is achieved at a temperature of 340 °C. The qualitative result of the simulation is physically more probable than the results obtained with the effective kinetics. The model of the effective kinetics cannot represent the changes in influences of transport resistances on the catalyst body performance.

Fig. 5.8(b) shows the catalyst body selectivities of IP. The catalyst body selectivities obtained by using the effective kinetics of the VPO-14 shows the strongest temperature dependence which results in an increase from 60% for a temperature of 340 °C to a value of above 80% for a temperature of 450 °C. The catalyst body selectivity of IP which was obtained by the simulation of the VPO-14 catalyst is labelled 'sim-14'. The values of the catalyst body selectivities differ significantly between the effective kinetics

[1]The effective kinetics are influenced by transport resistances if the simulation of transport processes in the catalyst body is accurate.

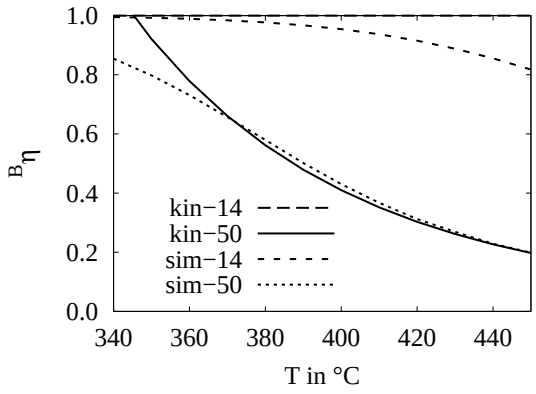

(a) Effectiveness factors

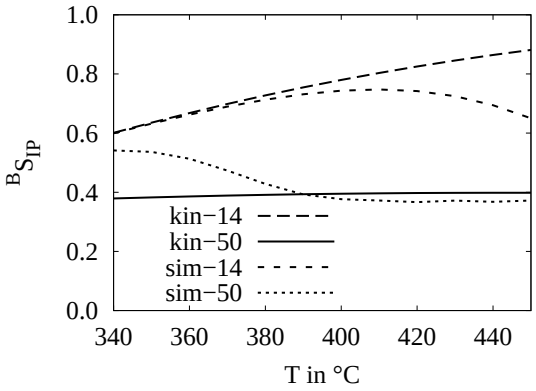

(b) Body selectivities of IP

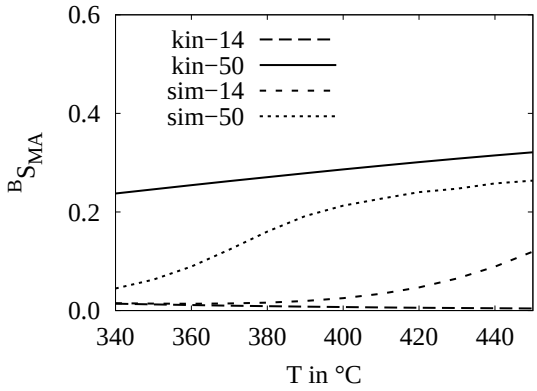

(c) Body selectivities of maleic anhydride

Fig. 5.8: *Influence of reaction temperature on the calculated effectiveness factors and the catalyst body selectivities of IP and maleic anhydride. Four curves are presented in each plot. Two of these curves are calculated by using the effective kinetics of VPO-14 ('kin-14') and VPO-50 ('kin-50'). The two remaining curves are calculated by assuming that the effective kinetics of VPO-14 equals the intrinsic kinetics and by simulating the catalyst bodies of VPO-14 ('sim-14') and VPO-50 ('sim-50').*

and the simulation of the catalyst body for temperatures above 390 °C. The catalyst body selectivities obtained by simulation are lower for higher temperatures. This result is a further sign of transport resistances that influence the catalyst performance of the VPO-14.

Curve 'kin-50' shows the catalyst body selectivity of IP obtained by using the effective kinetics of the VPO-50 catalyst. The catalyst body selectivities for the VPO-50 catalyst type are about 40% and remain almost constant in the investigated temperature range. The catalyst body selectivities calculated in the simulation of the VPO-50 catalyst are labelled 'sim-50'. They are higher than the corresponding values obtained by using the effective kinetics for temperatures below 390 °C. For temperatures above 390 °C, the catalyst body selectivity has a constant value of about 38%. The curves calculated in the simulation and from the effective kinetics of the VPO-50 agree for temperatures above 390 °C.

The catalyst body selectivities of maleic anhydride are displayed in Fig. 5.8(c). The catalyst body selectivity of maleic anhydride is almost 0 for the VPO-14 model, since there is no direct reaction of *n*-butenes to maleic anhydride and only a small conversion of *n*-butane to maleic anhydride. The curve of the simulated VPO-14 catalyst deviates from the effective kinetics at temperatures above 390 °C. This behaviour corresponds to that shown in the curves of the other catalyst body parameters which also deviate at temperatures higher than 390 °C. As expected, the transport resistances lead to higher catalyst body selectivities at higher temperatures.

The curve labelled 'kin-50' shows the catalyst body selectivities obtained by using the effective kinetics of the VPO-50. The values of this catalyst body selectivity is increasing steadily from about 25% at 340 °C to about 33% at 450 °C. The catalyst body selectivities which were calculated in the simulation of the catalyst bodies of VPO-50 are lower in the considered temperature range. For temperatures above 390 °C, the catalyst body selectivities of maleic anhydride show a temperature dependence resembling that of the catalyst body selectivities which were obtained by using effective kinetics, but differ by a value of about 5%. In contrast to the other parameters, the catalyst body selectivity of maleic anhydride is not represented well by the simulation of the VPO-50 catalyst.

At low temperatures, the temperature dependence of the catalyst body properties coincides with that of the intrinsic properties. For high temperatures, an effective kinetic model can be proposed with lower activation energies than the intrinsic activation energies.

It can be summarised that the effective kinetics of the VPO-14 catalyst are influenced by pore transport resistances for higher temperatures, presumably above 390 °C. The simulation shows that below this temperature, the effective kinetics equal the intrinsic kinetics in case of the VPO-14 catalyst.

The simulation showed that the effective kinetics of the VPO-50 catalyst differ from the intrinsic kinetics in the entire temperature range.

5.3 Coupled Catalyst and Reactor Simulations

The previous section presented results obtained by simulation of the catalyst bodies in the feed stream of the reactor. This section presents simulations in which the catalyst simulations are coupled to the simulation of an ideal fixed-bed reactor. For each differential element of the fixed-bed reactor, the simultaneous reaction and transport processes in the

catalyst body was simulated for the local gas phase composition[2]. The formal formation rates calculated in the catalyst simulations were used as the differential formation rates in the reactor balance.

First, the coupled simulation of the oxidation of pure *n*-butenes will be presented. The oxidation of the *n*-butenes is the reaction that is affected most by transport resistances. By omitting the presence of *n*-butane in this first simulation, the simulation results can be discussed more clearly. After that, the simulation of the oxidation of raffinate II will be presented.

5.3.1 Oxidation of *n*-Butenes

This section discusses the coupled catalyst and reactor simulation for the conversion of pure *n*-butenes with the VPO-50 catalyst for the same reaction conditions as described in section 4.3.2. Fig. 5.9 shows the experimentally determined and calculated values from the coupled simulations for the conversion of pure *n*-butenes (1% n/n in air) in a temperature range from 340 °C to 420 °C.

Fig. 5.9(a) displays the fraction profiles of *n*-butenes as functions of the modified residence time. The experiments and the simulations agree well. The measurement for 340 °C is better represented by the simulation than by the effective kinetics.

The reactor selectivities of IP are displayed in Fig. 5.9(c). The experimentally determined selectivities are independent of temperature for all temperatures of 360 °C and above. The selectivities for the temperature of 340 °C, however, are higher than the selectivities for the other temperatures. The deviation of the curve at 340 °C was assumed to result from the transient regime of pore transport effects which have to be considered at this temperature. The changes in catalyst body selectivities of IP which were presented in the previous section showed this transient behaviour for temperatures below 400 °C. The simulated curves of the reactor selectivities agree with the experimentally determined curves only for the temperatures of 400 and 420 °C. The simulated curves for temperatures below 400 °C represent the transient regime and depend therefore on the temperature. The changes in the selectivity curves between 340 °C and 360 °C are smaller than the changes in the curves between 360 and 380 °C. The lower temperatures are in the vicinity of the intrinsic regime and the changes represent the temperature dependence of the intrinsic kinetics.

The extrapolation of the experimentally determined reactor selectivities for 340 °C results in a catalyst body selectivity of IP of about 50%. That agrees with the catalyst body selectivity calculated in the simulation. The selectivities calculated in the simulation, however, are higher than the corresponding experimentally determined selectivities.

The reactor selectivities of maleic anhydride are presented in Fig. 5.9(d). The differences between simulation and effective kinetics as described in the previous section are also visible in this figure. The experimentally determined reactor selectivities of maleic anhydride are higher than the corresponding simulated selectivities.

The fraction profiles of maleic anhydride are presented in Fig. 5.9(b). The reasons for the differences between experimentally determined and simulated fraction profiles of maleic anhydride are the same as for the reactor selectivities.

[2]The kinetic parameter set of the VPO-14 was used

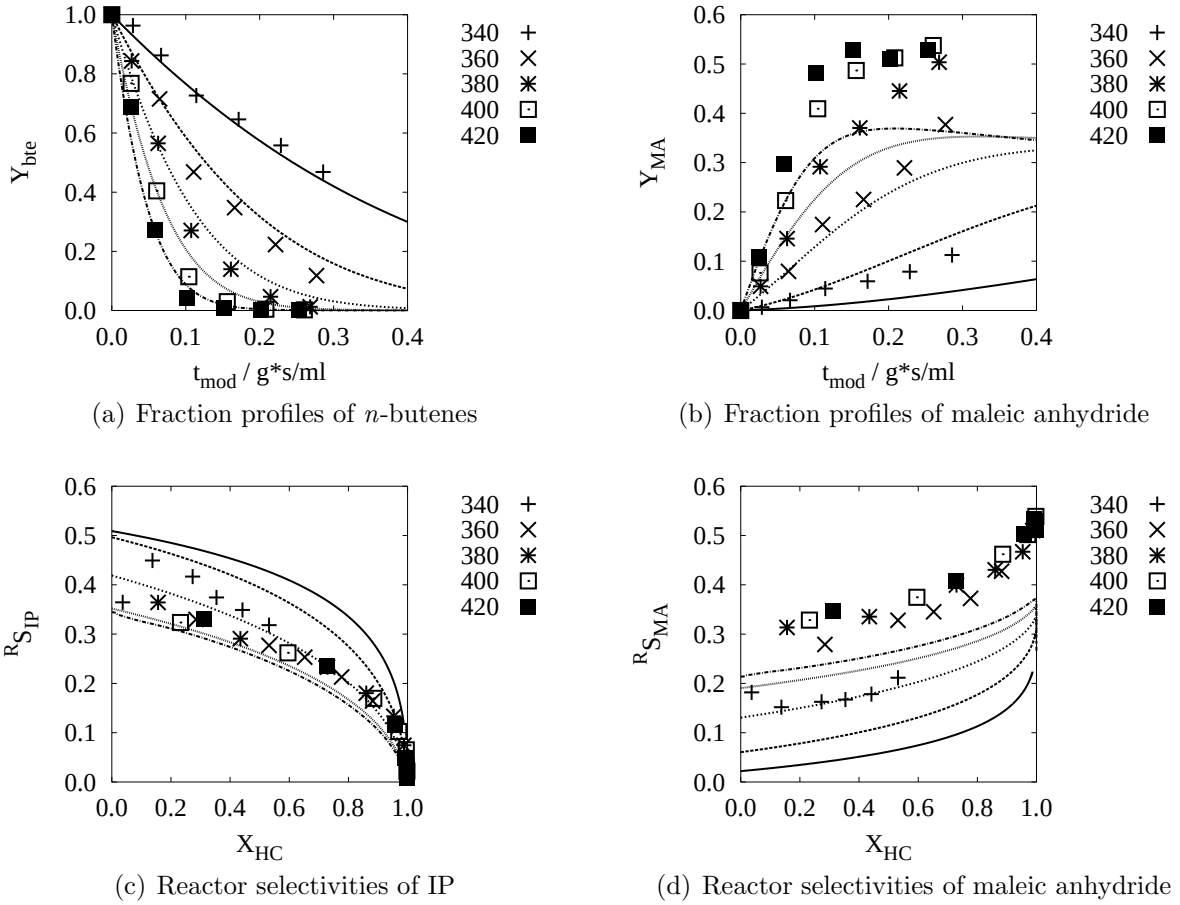

(a) Fraction profiles of *n*-butenes

(b) Fraction profiles of maleic anhydride

(c) Reactor selectivities of IP

(d) Reactor selectivities of maleic anhydride

Fig. 5.9: *Variation of the reaction temperature (values are given in* °C*) in the oxidation of 1% of 1-butene in air over the VPO-50 catalyst. The symbols represent the experimentally determined values, the lines represent the values obtained by the coupled simulations.*

5.3.2 Oxidation of Raffinate II

The coupled simulations were also carried out for the conversion of 1% of synthetic raffinate II over a VPO-50 catalyst for the same reaction temperatures that were used in the experiments presented in section 4.4.2. Fig. 5.10 shows the experimentally determined and simulated fraction profiles and reactor selectivities for a temperature range from 400 °C to 450 °C.

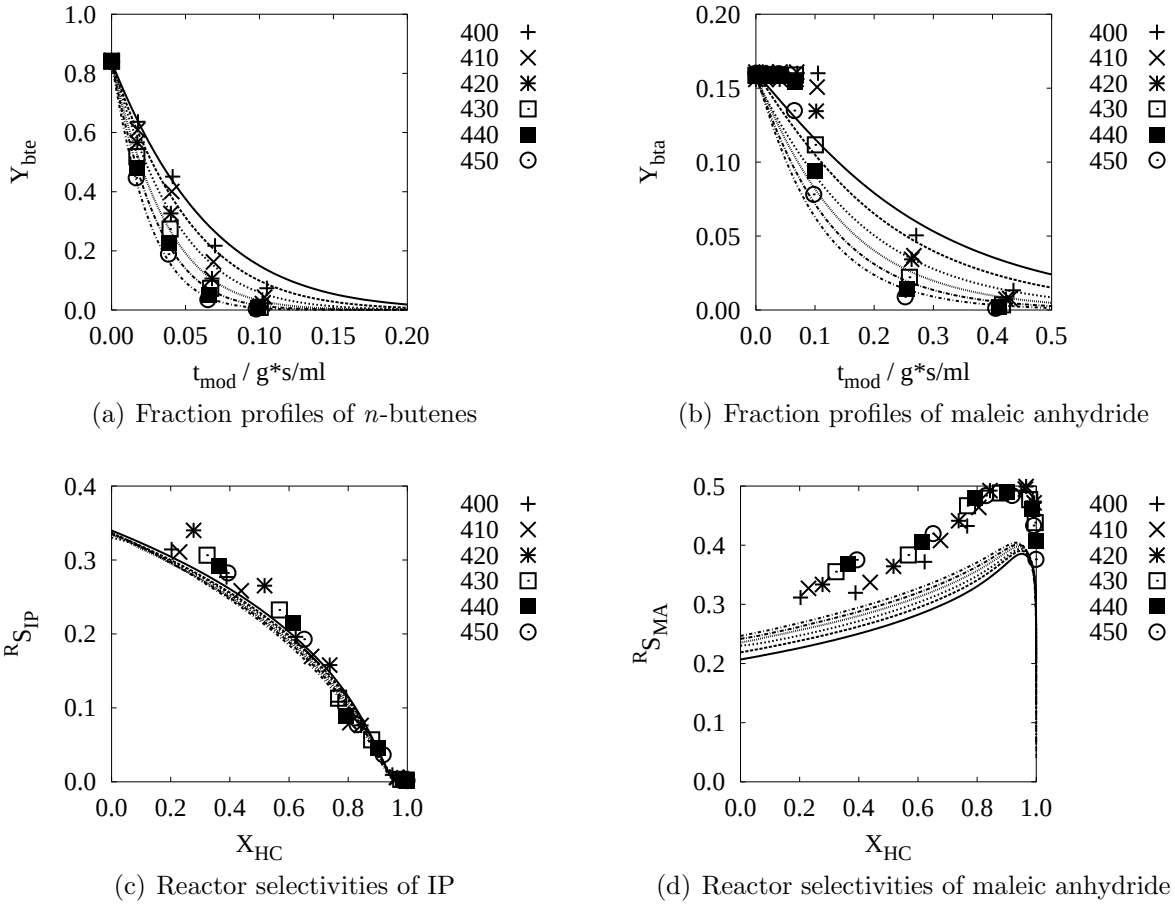

(a) Fraction profiles of *n*-butenes

(b) Fraction profiles of maleic anhydride

(c) Reactor selectivities of IP

(d) Reactor selectivities of maleic anhydride

Fig. 5.10: *Variation of the reaction temperature (in °C) in the oxidation of 1% of synthetic raffinate II in air over the VPO-50 catalyst. The symbols represent the experimentally determined values, the lines represent the values obtained by the coupled simulations.*

Plots 5.10(a) and 5.10(b) display the fraction profiles of *n*-butenes and *n*-butane, respectively. The experimentally determined profiles are represented better by the simulation than by the effective kinetics.

The reactor selectivities of IP are presented in Fig. 5.10(c). The simulated reactor selecitivities differ from the experimentally determined selectivities for smaller conversion levels. The reactor selectivities of maleic anhydride are displayed in Fig. 5.10(d). The simulated values are clearly lower than the experimentally determined reactor selectivities.

5.3.3 Summary of the Coupled Simulations

In section 4.3.2, it was shown that the effective kinetics cannot describe the conversion of n-butenes at lower temperatures. The catalyst is operated in the transient region between the reaction controlled and transfer controlled regions. The transient region is represented better by the coupled simulation. However, the coupled simulations show significant deviations between the simulated and the experimental selectivities. The effective kinetics are better suited to quantify the catalyst behaviour for temperatures above 380 °C. These temperatures are the preferred temperatures for the production of maleic anhydride, since activity and selectivity towards maleic anhydride are higher. The consideration of transport resistances in the catalyst pores gave more insight in the effects of these resistances on catalyst performance. However, the effective kinetics are more accurate in the quantification of reactor performance.

5.4 External Transport Resistances

It was assumed that external transport resistances were negligible in the determination and quantification of the effective kinetics of the conversion of mixtures of n-butenes and n-butane over VPO-50 and VPO-14 catalysts. This section presents the estimation of the influences of external transport resistances on the reactor performance. They are calculated by coupled simulations of the reactor and the local external transport of molecules between the catalyst body surface and the bulk gas phase.

The molar formation rates of the species in a catalyst body have to equal the molar flow of these species from the body surface to the bulk gas phase. This results in the algebraic equation

$$m_{\text{active}}^{\text{body}}\, {}^{\text{B}}R_i(\mathbf{c}^{\text{S}}, T) = A_{\text{geo}}^{\text{body}} \beta_i \left(c_i^{\text{S}} - c_i\right). \tag{5.11}$$

The differential formation rate of each species i equals the catalyst body formation rate of this species for the calculated concentrations at the catalyst body surface $\mathbf{c}^{\text{S}}$:

$${}^{\text{D}}R_i(\mathbf{c}, T) = {}^{\text{B}}R_i(\mathbf{c}^{\text{S}}, T). \tag{5.12}$$

Important for the solution of the algebraic equation is the knowledge of the mass transfer coefficients β_i. They depend on geometrical properties of the catalyst bed, the physical properties of the gas phase and the mean gas velocity in the reactor.

5.4.1 Correlations for External Transfer Coefficients

Mass transfer coefficients β_i depend strongly on the flow field of the gas phase surrounding the catalyst bodies. A number of correlations have been presented in the literature to estimate these coefficients for fixed beds. Most of these correlations have been developed for heat transfer from the gas phase to the solids in the bed. By assuming the analogy of the molecular transport mechanisms of heat and mass, the mass transfer coefficients can be estimated from correlations of the heat transfer coefficients. For more accurate descriptions of the mass transfer, however, it is suggested to use especially developed mass transfer correlations [34]. In [34], correlations of this type are reviewed. In most of the correlations, the dimensionless Sherwood, Reynolds and Schmidt numbers are used to express the relations between the transfer coefficients and the mean velocity, fixed

bed geometry and physical properties of the gas phase. The dimensionless numbers are defined as $Sh_i = \frac{\beta_i \times d_{\mathrm{p,A}}}{D_i^{\mathrm{mol}}}$, $Re_{\mathrm{A}} = \frac{\bar{w} \times d_{\mathrm{p,A}}}{\nu^{\mathrm{F}}}$ and $Sc_i = \frac{\nu^{\mathrm{F}}}{D_i^{\mathrm{mol}}}$. The characteristic diameter $d_{\mathrm{p,A}}$ is typically chosen as the diameter of a sphere with the same geometric surface area as the catalyst body.

From the correlations listed in [34, 46], one was selected which was valid for the conditions in the reactor and also led to the lowest mass transport coefficients for a worst case estimation. The correlation used in the present work was developed by Petrovic and Thodos [47] and is also recommended by Satterfield [48]. It was developed for gas-phase catalytic reactions and also considers axial mixing effects that have an influence on the mass transfer at low gas velocities. Low gas velocities have to be considered in the laboratory reactor [47]. The proposed correlation is expressed as

$$Sh_i = \frac{0.357}{\psi} \times Re_{\mathrm{A}}^{0.641} \times Sc_i^{1/3}, \tag{5.13}$$

$$3 < Re_{\mathrm{A}} < 2000, \tag{5.14}$$

$$1.8 \text{ mm} < d_{\mathrm{p,A}} < 9.3 \text{ mm}. \tag{5.15}$$

5.4.2 External Transport Effects in the Laboratory Reactor

It was assumed for the simulation that the reactor was filled with catalyst bodies and inert material with identical geometries. In reality, the catalyst bodies were bigger than the inert spheres that were used in the experiments. The porosity of the packed bed was assumed to be $\psi = 0.4$. These are worst case assumptions, since the different geometric dimensions of the catalyst bodies and the inert spheres lead to a lower porosity of the bed and to higher gas velocities in the vicinity of the catalyst bodies. It is likely that the mass transfer from the bulk gas phase to the catalyst bodies is higher than assumed with the values mentioned above. The dimensionless numbers resulted in values of about $Re_{\mathrm{A}} \approx 19$, $Sc_i \approx 2$ and $Sh_i \approx 7.4$.

The highest influences of external mass transport can be expected at highest temperatures and highest concentrations of hydrocarbons. VPO-50 has a thicker layer of catalyst than VPO-14. Therefore, the external transport resistances have higher influence on catalyst performance in case of the VPO-50 catalyst. Fig. 5.11 shows the fraction profiles and reactor selectivities obtained in the experiment with the worst influences of transport resistances, namely the conversion of synthetic raffinate II at 450 °C with a hydrocarbon feed fraction of 1.75% n/n in air. The measurement was carried out with a VPO-50 catalyst and a standard volumetric flow rate of 30 ml/s. The fraction profiles are plotted against the axial position in the reactor. The kink at a position of $z = 1$ m results from a higher catalyst density in the upper 0.5 m of the reactor.

At these conditions, the reactor performance can be influenced by external mass transport resistances, since there are significant differences between the calculation of the curves with and without consideration of mass transfer resistances. The effects of external mass transport resistances on reactor performance are similar to those of the pore transport resistances. The transport resistances lead to a lower apparent activity, lower differential selectivities of IP and higher differential selectivities of maleic anhydride. The differential selectivity of IP is decreased from about 35% to about 28%. The differential selectivity of maleic anhydride is increased from about 32% to about 36%. The reactor selectivities of maleic anhydride at higher conversion levels are almost identical.

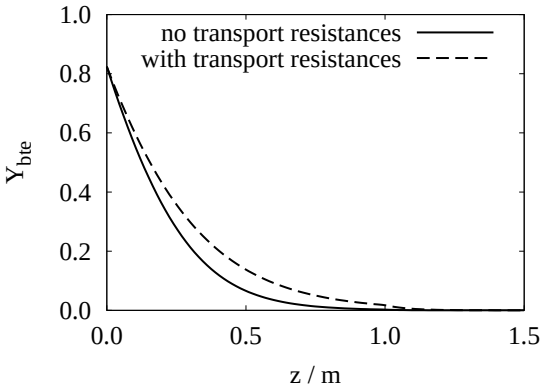

(a) Fraction profiles of *n*-butenes

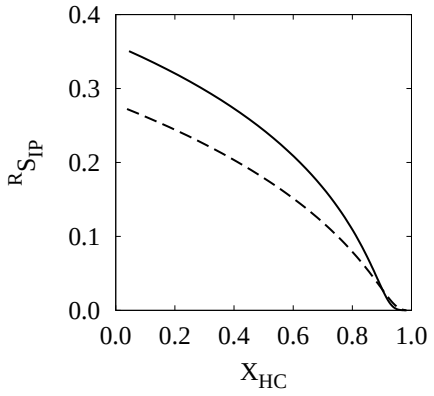

(b) Reactor selectivities of IP

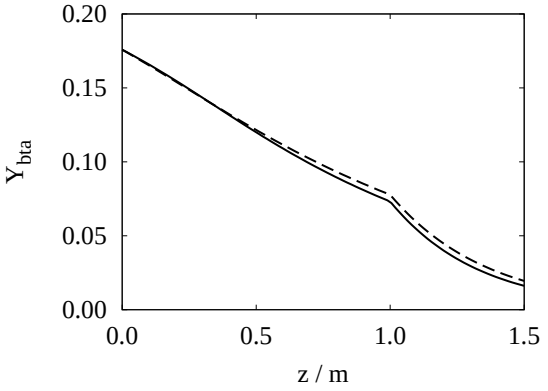

(c) Fraction profiles of *n*-butane

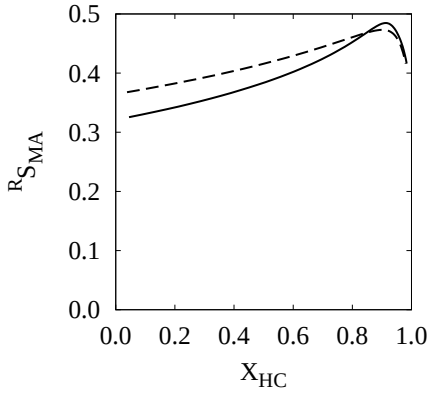

(d) Reactor selectivities of maleic anhydride

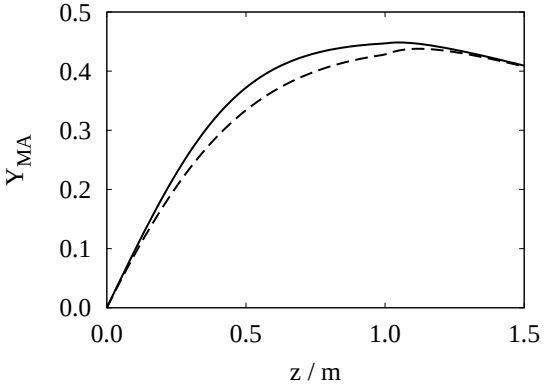

(e) Fraction profiles of maleic anhydride

Fig. 5.11: *Effect of external mass transfer on the performance of the laboratory reactor in the partial oxidation of raffinate II (1.75% n/n in air) at 450 °C over a VPO-50 catalyst and a standard volumetric flow rate of 30 ml/s.*

Two effects have to be considered in interpreting the plots. The transport resistances are probably lower than assumed because of the bimodal body size distribution that is present in the experiments but not considered in the estimation. On the other hand, the catalyst body reaction rates are higher than determined for the effective kinetics if transport resistances are significant. Higher catalyst body reaction rates than assumed for the simulation, however, lead to higher influences of transport resistances on the reactor performance.

Further estimations for different temperatures and for both catalyst types were carried out and are presented in appendix B.

5.4.3 External Transport Effects in a Production-Scale Fixed-Bed Reactor

The estimation of external transport effects was also carried out for a possible production-scale fixed-bed reactor. The simulation of the reactor is described in chapter 6. The reaction conditions chosen in this reactor lead to dimensionless numbers of $Re_{\mathrm{A}} \approx 161$ and $Sh_i \approx 29$. The consideration of external mass transport resistances led to no visible differences in the fraction profiles for the production-scale reactor.

Chapter 6

Reactor Simulation

To determine suitable reaction conditions, the throughput, the yield of maleic anhydride and the amount of active catalyst required to operate the reactor at optimum have to be considered. In the first step of the reactor analysis, only the yield of maleic anhydride is considered, since this property describes how much of the feedstock can be used to produce maleic anhydride. In case of an ideal reactor, the throughput can be increased by increasing the amount of active material in the reactor without loss of yield. In case of a real production-scale reactor, more details have to be considered. Further restrictions which limit reactor performance are the pressure drop along the reactor and the heat removal capabilities.

In this chapter, simulations of a production-scale reactor are presented. The reactor simulations led to the determination of throughput, yield of maleic anhydride and the amount of catalyst required to achieve this yield.

6.1 Effect of Mixing on the Oxidation of Raffinate II

The absence of axial mixing is an assumption that cannot be fulfilled in a real reactor. The effects of axial mixing on the performance of a fixed-bed reactor are typically small.

The model of the ideal stirred tank reactor, on the other hand, represents maximum mixing effects. It is assumed that the content of the reactor vessel is completely mixed and no gradients are present in the vessel. For the oxidation of mixtures of n-butenes and n-butane, the fractions of each species i in an ideal stirred tank reactor can be calculated from the integral balance

$$c_{i,0} - c_i + t_{\mathrm{mod}}{}^{\mathrm{D}}R_i = 0. \tag{6.1}$$

The fractions and the reactor selectivities for the oxidation of a synthetic raffinate II mixture (1% n/n in air) at 410 °C by using a VPO-50 catalyst in an ideal stirred tank reactor are presented in Fig. 6.1. The corresponding plots for the ideal plug flow reactor are shown in Fig. 4.12. The fraction and reactor selectivity curves resemble those of the plug flow reactor. The maximum yields and maximum reactor selectivities that can be obtained with the stirred tank reactor are lower than those achievable with the plug flow reactor. The maximum yields of maleic anhydride amount to about 38% and 47% for the stirred tank reactor and the plug flow reactor, respectively. The residence time required to achieve the maximum yield amounts to about 0.3 (g s)/ml and is higher than the required residence time in the plug flow reactor, being slightly above 0.2 (g s)/ml.

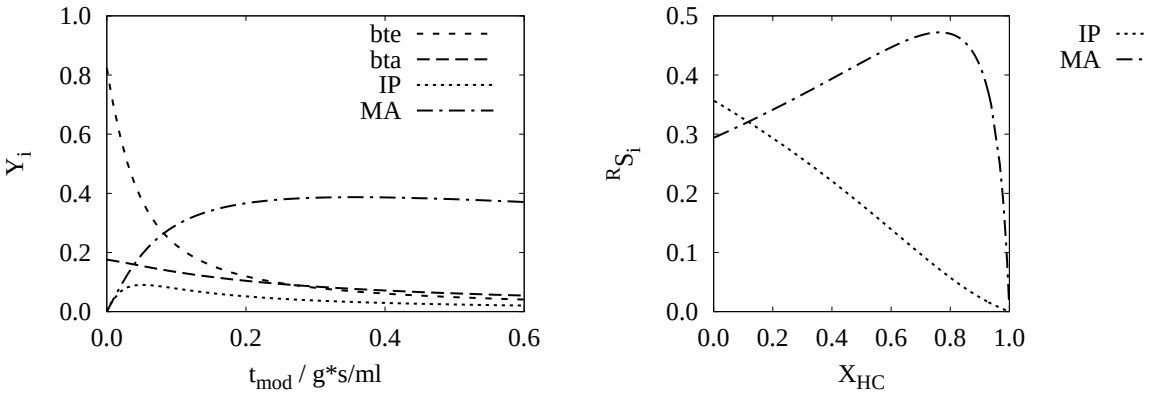

(a) Fraction profiles

(b) Reactor selectivities

Fig. 6.1: *Oxidation of raffinate II (1% n/n in air) at 410 °C over a VPO-50 catalyst in an ideal stirred tank reactor.*

The mixing in real reactor types such as the production-scale multi-tubular fixed-bed reactor, the fluidised-bed reactor and the transport-bed reactor are in-between the mixing patterns of the ideal plug flow and the ideal stirred tank reactor. Among the three real reactor types, the fixed-bed reactor comes closest to the ideal plug flow reactor while the fluidised-bed reactor can be considered as being closest to the stirred tank reactor. If the mixing in the three reactors is considered alone, the fixed-bed reactor is the best choice to maximise the yield.

6.2 The Non-Ideal Fixed-Bed Reactor

The aim to describe non-ideal fixed-bed reactors has led to the development of a multiplicity of reactor models with different grades of complexity. The preferred models for fixed-bed reactors are dispersion models. The basic flow pattern is assumed to be similar to that of the plug flow reactor. The mixing through turbulence and diffusion is lumped together to the macroscopic effect that is named 'dispersion'.

Dispersion models are divided into four categories which differ in two properties: the number of spatial dimensions and the number of phases. In one-dimensional models, it is assumed that there are no gradients in radial direction. The heat transfer resistance is located directly at the reactor wall. Two-dimensional models consider both gradients in radial direction and deviations of the velocity profile from plug flow.

In homogeneous models, the gas phase and the solid catalyst particles are lumped together to a single pseudo-homogeneous phase. The heterogeneous models regard the gas and the solids as two phases. Thermal conductivity is then divided into the conductivity in the solids matrix and the effective conductivity in the gas phase.

The heat transfer and hot spot properties are better represented by a two-dimensional model. Hein gives a comprehensive survey over two-dimensional models [35]. He compared results from homogeneous and heterogeneous two-dimensional models with results obtained in the experiments concerning the total oxidation of hydrocarbons. The maximum differences between the temperature of the catalyst bodies and the surrounding gas

phase were about 8 K under conditions with low gas velocities. The partial oxidation in the present work should lead to lower differences between the two temperatures, since the gas phase velocities in a production scale reactor are much higher and the reaction heats are smaller.

The heterogeneous models are more difficult to apply because of the higher numerical requirements. Another disadvantage is the higher uncertainty in the heat and mass transfer properties and the heat conductivity of the solids matrix. These models are less elaborated than the homogeneous models. There are also more experimental validations for the homogeneous model [49]. It was therefore chosen to use the pseudo-homogeneous two-dimensional model here as presented in [35, 49].

The reactor model used here takes into account a radial porosity profile and a resulting radial velocity profile with higher velocities in the vicinity of walls. Mass and energy are assumed to be transported by the gas flow in axial direction and by dispersion and effective thermal conductivity in axial and radial direction.

6.2.1 Radial Porosity Profile

The higher local porosities in the vicinity of walls are approximated by the empirical equation

$$\psi(r) = \psi_\infty \left[1 + \left(\frac{0.65}{\psi_\infty} - 1\right) \exp\left(-6.0 \frac{R - r}{d_{\mathrm{p,V}}}\right)\right] \tag{6.2}$$

for fixed-beds consisting of cylinders[1] [50]. The porosity of the fixed-bed without wall effects was assumed to be $\psi_\infty = 0.4$ in the present work.

6.2.2 Momentum Balance, Pressure and Velocity Fields

The velocity profile in the reactor is obtained by solving the momentum balance. The momentum balance is weakly coupled to the energy and mass balances because density and viscosity are dependent on temperature and composition. The coupling of the balances leads to a complicated set of axial as well as radial flow components. By neglecting the temperature and concentration dependencies of the physical properties, the momentum balance can be solved independently of the mass and energy balances. Hein compared the results that were obtained by solving the coupled and non-coupled systems [35]. In the total oxidation reaction of propane and ethane, he obtained experimentally a temperature difference between the hot spot and the wall of approximately 120 K at a wall temperature of 600 K. The model with the independently solved momentum balance equation predicted this temperature difference to be 140 K. The more exact coupled system resulted in a hot spot with a temperature difference of 130 K to the wall. Thus, the coupled system described the experiments slightly better. The expected temperature differences in the production scale reactor for the partial oxidation of raffinate II are smaller than those obtained in the work of Hein. Most of the gas phase consists of air and the physical

[1] It was assumed that the small holes of about 1 mm in the catalyst particles are to small to be able to contribute to the flown-through gas phase. Since the porosity profile is used to describe the space where the gas can flow through, the porosity model of cylinders was used instead of the model of hollow cylinders to account for the dead spaces.

properties are therefore almost independent of the gas phase composition. Therefore, the momentum balance was solved independently of the mass and energy balances.

The macroscopic flow in the reactor was assumed to have only components in axial direction. Tube inlet and outlet disturbances of the velocity field were neglected. The momentum balance was based on the well known Ergun equation. The Ergun equation was extended to cope with radial porosity profiles. The consideration of the porosity profile results in the extended Brinkmann equation

$$\frac{\partial p}{\partial z} = -f_1 w - f_2 w^2 + \frac{\eta^{\text{eff}}}{r}\frac{\partial}{\partial r}\left(r\frac{\partial w}{\partial r}\right), \tag{6.3}$$

$$f_1 = 150\frac{(1-\psi)^2}{\psi^3}\frac{\eta^{\text{F}}}{d_{\text{p,V}}^2}, \tag{6.4}$$

$$f_2 = 1.75\frac{1-\psi}{\psi^3}\frac{\rho^{\text{F}}}{d_{\text{p,V}}}, \tag{6.5}$$

$$\eta^{\text{eff}} = 1.6\eta^{\text{F}}. \tag{6.6}$$

The effective viscosity η^{eff} accounts for the effective friction of the fluid in the vicinity of the wall. The relation of the effective viscosity to the gas phase viscosity that is valid for a bed of cylinders (equation 6.6) was given in [50]. The functions f_1 and f_2 account for laminar and turbulent friction in the bed, respectively.

It is assumed that there are no radial pressure gradients and flow components. It is further assumed that the physical properties except for density are independent of pressure. In the literature, incompressibility of the gas phase is assumed for the solution of equation (6.3) [35, 49, 50]. This assumption is not valid in the present work because of the high pressure drops. Therefore, equation (6.3) was solved for a compressible gas phase. Additionally to equation (6.3), the continuity equation has to be considered in this case. The extension for compressible flows yields a slightly more complicated system of differential equations and is therefore described in detail in the present section.

The continuity equation for steady state

$$\text{div}(\rho^{\text{F}}\mathbf{w}) = 0 \tag{6.7}$$

can be simplified to

$$\frac{\partial(\rho^{\text{F}} w)}{\partial z} = 0 \tag{6.8}$$

for velocity fields with axial components only as it is the case in the present work. With the assumption of ideal gas behaviour of the gas phase in the reactor, the density can be expressed as

$$\rho^{\text{F}} = \frac{M^{\text{F}} p}{RT}. \tag{6.9}$$

With equation (6.9), the continuity equation (6.8) results in

$$\frac{\partial(pw)}{\partial z} = 0. \tag{6.10}$$

The multiplication of the Brinkmann equation (6.3) with p and the subsequent differentiation with respect to z results in

$$\frac{\partial}{\partial z}\left(p\frac{\partial p}{\partial z}\right) = 0. \tag{6.11}$$

By solving equation (6.11) with the boundary conditions

$$p(z=0) = p_0, \tag{6.12}$$
$$p(z=L) = p_L, \tag{6.13}$$

the pressure field in the reactor tube

$$p(z) = \sqrt{p_0^2 + 2p_0 p_{z,0} z} \tag{6.14}$$

is obtained with the differential pressure drop at reactor inlet

$$p_{z,0} = \left.\frac{\partial p}{\partial z}\right|_{z=0} = \frac{p_L^2 - p_0^2}{2p_0 L}. \tag{6.15}$$

The radial velocity profile at the tube inlet ($z = 0$) is obtained by solving equation (6.3) with the boundary conditions

$$\left.\frac{\partial p}{\partial z}\right|_{z=0} = p_{z,0}, \tag{6.16}$$
$$\left.\frac{\partial w}{\partial r}\right|_{r=0} = 0, \tag{6.17}$$
$$w(r=R) = 0. \tag{6.18}$$

This two point boundary value problem was solved in Matlab by using a finite differences method coupled with a relaxation method.

Equation (6.10) can be written as

$$\frac{\partial w}{\partial z} = -\frac{w}{p}\frac{\partial p}{\partial z}. \tag{6.19}$$

With equation (6.14) and the radial velocity profile at the tube inlet $w(r, z = 0)$ as a boundary condition, the velocity field in the reactor tubes

$$w(r,z) = \frac{w(r,z=0)}{\sqrt{1 + 2\frac{p_{z,0}}{p_0} z}} \tag{6.20}$$

is obtained. Because of the steadily decreasing pressure along the reactor tubes, the axial velocity is increasing in axial direction.

6.2.3 Mass and Energy Balances

The species and energy balances of the reactor in steady state operation can be expressed as

$$0 = -\mathbf{w}\,\mathrm{grad}\,y_i + \mathrm{div}\left(\mathbf{D_i^{eff}}\,\mathrm{grad}\,y_i\right) + \frac{M_i}{\rho^{\mathrm{F}}}\frac{1-\psi}{1-\psi_\infty}\rho^{\text{active D}}R_i, \tag{6.21}$$

$$0 = -\rho^{\mathrm{F}}c_{\mathrm{p}}^{\mathrm{F}}\mathbf{w}\,\mathrm{grad}\,T + \mathrm{div}\left(\boldsymbol{\lambda}^{\mathrm{eff}}\,\mathrm{grad}\,T\right) + \frac{1-\psi}{1-\psi_\infty}\rho^{\text{active}}\sum_{j=1}^{N_{\text{rcts}}}\Delta_{\mathrm{R}}H_j{}^{\mathrm{D}}r_j, \tag{6.22}$$

respectively. The gas composition is expressed in terms of mass fractions y_i. Because of the simplicity of the velocity field and through the introduction of cylinder coordinates, the equations can be simplified to

$$0 = -w\frac{\partial y_i}{\partial z} + \frac{\partial}{\partial z}\left(D_{\text{ax},i}^{\text{eff}}\frac{\partial y_i}{\partial z}\right) + \frac{1}{r}\frac{\partial}{\partial r}\left(rD_{\text{rad},i}^{\text{eff}}\frac{\partial y_i}{\partial r}\right) + \frac{M_i}{\rho^{\mathrm{F}}}\frac{1-\psi}{1-\psi_\infty}\rho^{\text{active D}}R_i, \tag{6.23}$$

$$\begin{aligned} 0 = &-\rho^{\mathrm{F}}c_{\mathrm{p}}^{\mathrm{F}}w\frac{\partial T}{\partial z} + \frac{\partial}{\partial z}\left(\lambda_{\text{ax}}^{\text{eff}}\frac{\partial T}{\partial z}\right) + \frac{1}{r}\frac{\partial}{\partial r}\left(r\lambda_{\text{rad}}^{\text{eff}}\frac{\partial T}{\partial r}\right) \\ &+ \frac{1-\psi}{1-\psi_\infty}\rho^{\text{active}}\sum_{j=1}^{N_{\text{rcts}}}\Delta_{\mathrm{R}}H_j{}^{\mathrm{D}}r_j. \end{aligned} \tag{6.24}$$

The differential formation and reaction rates equal the corresponding catalyst body formation and reaction rates, since external mass transport resistances do not influence the reaction performance[2]. The mass dispersion and effective thermal conductivity are treated differently for axial and radial direction. These properties are presented in the subsequent section.

The physical properties of the gas phase were assumed to equal the corresponding physical properties of air as given in tables in [51]. The values for temperatures not listed in these tables were interpolated.

The fields of the mass fractions and the temperature field were obtained by solving the mass and energy balances with the following boundary conditions:

$$T(r=R) = T_{\mathrm{w}}, \qquad \left.\frac{\partial \mathbf{y}}{\partial r}\right|_{r=R} = 0, \tag{6.25}$$

$$T(z=0) = T_0, \qquad \mathbf{y}(z=0) = \mathbf{y}_0, \tag{6.26}$$

$$\left.\frac{\partial T}{\partial z}\right|_{z=L} = 0, \qquad \left.\frac{\partial \mathbf{y}}{\partial z}\right|_{z=L} = 0, \tag{6.27}$$

$$\left.\frac{\partial T}{\partial r}\right|_{r=0} = 0, \qquad \left.\frac{\partial \mathbf{y}}{\partial r}\right|_{r=0} = 0. \tag{6.28}$$

In these boundary conditions, it is assumed that the temperature directly at the inner tube wall is constant along the reactor (T_{w}). In reality, the tubes are cooled by a molten salt mixture that circulates through the shell side of the multi-tubular reactor. From entry to exit of the salt flow, the salt is heated up by the heat of reaction. The temperature

[2] See section 5.4.3 for details.

differences between salt entry and salt exit are typically about 2 K to 4 K. The salt entry is on the side of the reactor feed. Thus, the hot-spot region, the most sensitive region to changes in the wall temperature, is cooled with the fresh salt. The salt flows perpendicular to the tubes to optimise the heat transfer from the tubes to the salt bath. The highest heat transfer resistance is found in the catalyst bed. Therefore, the inner wall temperature shows only a small difference to the salt bath temperature. These two effects, the non-isothermal salt bath and the existing temperature difference between salt bath and wall are considered insignificant to the overall accuracy of the simulation.

The equations were solved in Matlab by using the partial differential equations toolbox. A non-linear finite elements solver with mesh refinement was applied.

6.2.4 Mass and Energy Dispersion

The dispersion of mass and energy results from molecular movement (diffusion and thermal conductivity) and from mixing by turbulent vortices.

Molecular Transport Mechanisms

The molecular diffusion of species in the reactor is hindered by the presence of the catalyst particles. Therefore, diffusivities and thermal conductivities of the catalyst bed have to be introduced. According to [52] the transport parameters in the bed can be assumed to be

$$D_i^{\mathrm{bed}} = \left(1-\sqrt{1-\psi}\right) D_i^{\mathrm{mol}}, \tag{6.29}$$

$$\lambda^{\mathrm{bed}} = \left[\left(1-\sqrt{1-\psi}\right)+\left(\sqrt{1-\psi}\times k_{\mathrm{c}}\right)\right]\lambda^{\mathrm{F}}. \tag{6.30}$$

The diffusivities in the bed are reduced by the reduced fluid space since no diffusion takes place through the catalyst bodies[3]. The molecular diffusivities are calculated as presented in section 5.2.1. In contrary to the diffusivities in the bed, the thermal conductivity of the catalyst bodies contributes significantly to the conductivity of the bed. This is represented by the second expression in the brackets in equation (6.30). The factor k_{c} represents the relative thermal conductivity of the core of a virtual unit cell [52] and, for spheres, results in

$$k_{\mathrm{c}} = \frac{2}{N}\times\left(\frac{B}{N^2}\times\frac{k_{\mathrm{p}}-1}{k_{\mathrm{p}}}\times\ln\frac{k_{\mathrm{p}}}{B}-\frac{B+1}{2}-\frac{B-1}{N}\right), \tag{6.31}$$

$$N = 1-(B/k_{\mathrm{p}}), \tag{6.32}$$

$$B = 1.25\times\left(\frac{1-\psi}{\psi}\right)^{10/9}, \tag{6.33}$$

$$k_{\mathrm{p}} = \frac{\lambda^{\mathrm{body}}}{\lambda^{\mathrm{F}}}. \tag{6.34}$$

It was decided to use spheres instead of cylinders or rings in the calculation of the conductivity of the bed since the highest uncertainty lies in the conductivity of the catalyst

[3]The diffusion inside the catalyst bodies can be neglected compared to the diffusion in the gas phase around the bodies.

particles. If Raschig rings had been chosen instead, the conductivity of the bed would increase by a factor of about 1.23. Therefore, choosing the spheres results in a worst case approximation.

The catalyst bodies used in the present work consist of steatite supports and active layers of VPO material. The thermal conductivity of steatite has a value between 3.5 W/(m K) and 4.5 W/(m K) [53]. No statement can be given about the exact values of the thermal conductivity of the porous VPO layer. Even for the same active VPO material, the thermal conductivity of the porous material can vary because of different porosities and pore geometries. Wellauer [28] used a cylindrical VPO catalyst with a thermal conductivity of about 0.585 W/(m K). According to [34,48], smaller values of the thermal conductivity of typical porous catalysts are about 0.1 W/(m K).

For the estimation of the thermal conductivity of the catalyst bodies, a serial connection of transfer resistances resulting from active mass and steatite support was assumed. The resulting catalyst body conductivity is then in a range between 0.5 W/(m K) and 1.7 W/(m K). All simulations in the present work were carried out with a lower cautious value of 0.5 W/(m K) and an optimistic value of 3.5 W/(m K). A thermal conductivity of the catalyst bodies of 0.5 W/(m K) leads to $k_c \approx 4$. The thermal conductivity of the bed is about $\lambda^{bed} \approx 0.2$ W/(m K). The diffusivities in the bed are about 0.07 cm^2/s.

Axial Dispersion

The axial dispersion consists of the molecular transport and the macroscopic transport. The macroscopic transport depends on the gas velocity through the catalyst bed. It is assumed to be

$$D^{eff}_{ax,i} = D^{bed}_i + \frac{Pe^D_i}{2} D^{mol}_i, \tag{6.35}$$

$$\lambda^{eff}_{ax} = \lambda^{bed} + \frac{Pe^{\lambda}}{2} \lambda^F. \tag{6.36}$$

The bed transport parameters depend on the local porosity. On the other hand, the convective part of the axial dispersion is assumed to be independent of the radial position. The gas velocity is considered by the two Péclet numbers $Pe^D_i = \frac{\bar{w} d_{p,V}}{D^{mol}_i}$ and $Pe^{\lambda} = \frac{\bar{w} d_{p,V}}{\kappa^F}$ that are formed with the mean gas velocity $\bar{w}$. The thermal diffusivity is defined as $\kappa^F = \frac{\lambda^F}{\rho^F c^F_p}$. With a gas velocity of about $\bar{w} = 2.6$ m/s which was calculated in the simulations presented below, values of the individual properties result in $Pe^D_i \approx 350$, $Pe^{\lambda} \approx 120$, $D^{eff}_{ax,i} \approx 53$ cm^2/s and $\lambda^{eff}_{ax} \approx 3.2$ W/(m K).

Radial Dispersion

The radial dispersion depends on the radial position. The proposed equations are

$$D^{eff}_{rad,i} = D^{bed}_i + K^D_{1,i} Pe^D_{c,i} D^{mol}_i f(r, K^D_2) \tag{6.37}$$

$$\lambda^{eff}_{rad} = \lambda^{bed} + K^{\lambda}_1 Pe^{\lambda}_c \lambda^F f(r, K^{\lambda}_2). \tag{6.38}$$

The radial dependence of the dispersion is represented by the function

$$f(r, K_2) = \begin{cases} \left(\frac{R-r}{K_2 d_{\mathrm{p,V}}}\right)^2 & \text{if } r > R - K_2 d_{\mathrm{p,V}} \\ \\ 1 & \text{otherwise.} \end{cases} \tag{6.39}$$

For cylinders, the parameters K_i are calculated by means of equations

$$K_1^{\mathrm{D}} = \frac{1}{4.6} \times \frac{1}{1 + \frac{3}{\sqrt{Pe_{\mathrm{c},i}^{\mathrm{D}}}}}, \tag{6.40}$$

$$K_2^{\mathrm{D}} = 0.44, \tag{6.41}$$

$$K_1^{\lambda} = \frac{1}{4.6}, \tag{6.42}$$

$$K_2^{\lambda} = 0.44 + 4 \exp\left(-\frac{Re}{70}\right). \tag{6.43}$$

The Reynolds number is defined as $Re = \frac{\bar{w} d_{\mathrm{p,V}}}{\nu^{\mathrm{F}}}$, the Péclet numbers for the flow in the core are defined as $Pe_{\mathrm{c},i}^{\mathrm{D}} = \frac{w(r=0) d_{\mathrm{p,V}}}{D_i^{\mathrm{mol}}}$ and $Pe_{\mathrm{c}}^{\lambda} = \frac{w(r=0) d_{\mathrm{p,V}}}{\kappa^{\mathrm{F}}}$.

The radial position where the radial effective thermal conductivity begins to decrease is about $K_2 d_{\mathrm{p,V}} \approx 3.4$ mm. With a value of the gas velocity at the reactor axis of $w(r = 0) = 2.3$ m/s, the Péclet numbers equal $Pe_{\mathrm{c},i}^{\mathrm{D}} \approx 310$ and $Pe_{\mathrm{c}}^{\lambda} \approx 100$. The resulting radial dispersion parameters are about $D_{\mathrm{rad},i}^{\mathrm{eff}} \approx 17$ cm^2/s and $\lambda_{\mathrm{rad}}^{\mathrm{eff}} \approx 1.3$ W/(m K) in the bulk of the fixed bed. The radial dispersion parameters are a factor of about 2.4 lower than the corresponding axial dispersion parameters.

6.3 Oxidation of Raffinate II in a Production-Scale Fixed-Bed Reactor

The aim of the simulation was to find the best geometry of a multi-tubular reactor, catalyst bed arrangement and operation conditions to maximise the production capacity and yield of maleic anhydride. Important constraints are given by minimum and maximum values of some of the parameters. These constraints are listed in Tab. 6.1.

parameter	min. value	max. value
length of the tubes	3.5 m	6.0 m
inner diameter of the tubes	21 mm	30 mm
number of tubes	1	36,000
catalyst temperature		460 °C

Tab. 6.1: *Parameter constraints for the reactor geometry and maximum catalyst temperature. The reactor geometry constraints are given by the manufacturer of the reactors; the maximum catalyst temperature avoids the rapid catalyst ageing.*

The reactor model presented in the previous section is a rigorous simulation of a fixed-bed reactor. In such a rigorous simulation, the reactor geometry, the data about the

catalyst bed and the operation conditions are input parameters. The simulation then returns the reactor performance as the result. In the task of designing a reactor, however, the input parameters of the simulation are unknown. They have to be determined and optimised during the design process. The desired performance is specified and the design process results in the reactor geometry, catalyst bed structure and operation conditions required. There are many examples, especially in the distillation technology, where short-cut models (also called design models) were developed. These models use the design parameters as the input parameters. The output parameters are then the nature, the specification and the operation conditions of the apparatus. There are no such design models known in the open literature for highly exothermic reactions in multi-tubular fixed-bed reactors. Therefore, the input parameters for the rigorous simulation were found by repeated simulation and continuous improvement of the input parameters (reactor geometry, catalyst bed and operation conditions). Each run presented new insights and quantified the dependences of, for example, the inner tube diameter on the hot spot temperature. Several runs were necessary to find the reactor geometry, catalyst bed parameters and operation parameters that are listed below. Only the final set of parameters is presented in this section.

6.3.1 Finding Suitable Operation Conditions

The production rate of maleic anhydride depends on the throughput of hydrocarbons ($\dot{m}_{\mathrm{RII},0}$) and the yield of maleic anhydride (Y_{MA}). The production rate of maleic anhydride can be expressed as

$$\dot{m}_{\mathrm{MA}} = \frac{M_{\mathrm{MA}}}{M_{\mathrm{RII}}} \times Y_{\mathrm{MA}} \times \dot{m}_{\mathrm{RII},0}. \tag{6.44}$$

Both, increases in throughput and in yield, lead to a proportional increase in the production rate of maleic anhydride. However, the fraction of hydrocarbons affects the maximum yield inversely. The increase in the total flow rate increases the pressure drop along the reactor. Therefore, a compromise must be found for both parameters, the flow rate and the fraction of hydrocarbons in the feed.

The yields of maleic anhydride achieved with the VPO-50 catalyst are clearly higher than the yields achieved with the VPO-14 catalyst. The yields are about 48% and 38%, respectively. Therefore, the VPO-50 catalyst was chosen for the production-scale reactor. Additionally, the VPO-50 catalyst exhibits lower activation energies leading to lower temperature sensitivities and enabling higher stability in reactor operation.

There are different sizes of multi-tubular reactors available. The scale-up parameter that can best be varied without making changes to reaction conditions necessary is the number of reactor tubes. The production capacity is directly proportional to the number of tubes. The number of tubes that can be incorporated in a single vessel can typically be varied between a few 1,000 and about 36,000 tubes. In the simulation, the maximum number of 36,000 tubes was chosen to obtain the production capacity for the largest possible reactor.

Higher pressure drop in the reactor leads to higher energy costs for the air compressor. Additionally, the investment cost increases with increasing operational pressure. It was chosen to allow a pressure drop of 1 bar which is typical for reactors converting n-butane to maleic anhydride. The inlet pressure was then chosen to be 2.2 bar; thus the

product stream leaves the reactor with a pressure of 1.2 bar and can be fed directly to the purification section without the need for a new compression of the stream. By fixing the pressure drop, the total flow rate through the reactor tubes is also determined.

Multi-tubular fixed-bed reactors consist of reaction tubes that have a length of typically between 3.5 and 6 m. Since the reaction rates are high in the case of the *n*-butenes conversions, the minimum length of tubes of 3.5 m is sufficient to achieve the maximum yield at the chosen pressure drop.

At first, a non-diluted catalyst bed was simulated where the inlet temperature equalled the wall temperature. Under these conditions, the amount of raffinate II in the feed, the wall temperature and the inner diameter were varied to achieve high yield as well as high throughput at limited hot spot temperature. The wall temperature was minimised to minimise the subsequent oxidation of maleic anhydride to carbon oxides while the conversion level at the reactor outlet was still high enough to achieve the residence time at which the yield has its highest value. The molar fraction of raffinate II in the feed was chosen to be low to achieve higher yields[4]. At the same time, the inner diameter was maximised to maximise throughput. The limiting factor for the inner diameter was the heat removal capability. Higher diameters result in higher throughput at the same pressure drop but also increases the distance for heat transfer from the reactor axis to the cooling salt bath.

According to section 4.3.2, the selectivities of maleic anhydride can be increased by increasing the temperature during the conversion of the *n*-butenes. Therefore, a second optimisation procedure was carried out which aimed at achieving high temperatures during the conversion of the *n*-butenes. The inlet temperature was raised above the wall temperature. At the same time, the catalyst bed was diluted with inert material at the reactor inlet to limit the hot-spot temperature. The axial position at which the gas temperature begins to decrease again was chosen as the position where the non-diluted second reactor zone begins. Thus, the decrease in temperature was slowed down and the hot-spot profile was broadened to achieve temperatures around 415 °C. During the second optimisation procedure, the inner diameter of the tubes, the wall temperature and the amount of raffinate II in the feed were further adjusted.

The fixed-beds in the individual tubes were divided into a diluted zone (the first 0.5 m with 60% m/m VPO) and a subsequent non-diluted zone. To fill the reactor, an amount of 30.7 t of active material is required.

The second optimisation led to the choice of an inner wall temperature of 360 °C and an inlet temperature of the feed stream of 390 °C. For the reactor tubes, an inner diameter of 28 mm was found to be suitable.

The molar fraction of raffinate II in the feed was chosen to be 0.6%. In contrast to the synthetic raffinate II mixture used in the determination of reaction kinetics, the raffinate II mixture for the reactor simulation was assumed to consist of 75% of *n*-butenes and 25% of *n*-butane. The nitrogen amount that represented isobutane in the laboratory reactor was replaced by *n*-butane to represent a probable inhibition effect of isobutane and to better approximate the heat production in the reactor.

The annual production time was assumed to equal the typical value of 8000 h/year for chemical plants. The reactor geometry and the reaction conditions for the base case are summarised in Tab. 6.2.

[4]See section 4.4.3 for details.

reactor geometry	
length of the tubes	3.5 m
inner diameter of the tubes	28 mm
number of tubes	36,000
catalyst bed	
bed dilution at reactor inlet	60% m/m of catalyst bodies 40% m/m of inert steatite bodies
length of diluted zone	0.5 m
active mass density in non-diluted zone	420 kg/m^3
total amount of active mass	30.7 t
operation conditions	
amount of raffinate II in the feed	0.6% n/n
remaining gas: air	
wall temperature	360 °C
inlet temperature	390 °C
inlet pressure	2.2 bar
pressure drop along the tubes	1 bar
annual production time	8000 h/year

Tab. 6.2: *Reactor geometry and reaction conditions used as the input parameters for the simulation run presented in section 6.3.2 (base case).*

6.3.2 Results of the Base Case Simulation

The radial porosity profile in the particle bed is displayed in Fig. 6.2(a). The porosity has a value of 40% in the bulk of the fixed-bed. The porosity is increasing sharply in the vicinity of the wall for dimensionless radial positions of $r/R > 0.8$ and achieves a value of about 65% directly at the reactor wall. The radial velocity profile at reactor inlet is displayed in Fig. 6.2(b). The velocity in the bulk of the fixed bed has a value of about 2.0 m/s. Directly at the wall, the velocity equals 0 because of the no-slip condition of Newtonian fluids. For dimensionless radial positions of $r/R > 0.8$, the velocity profile has a maximum with a value of about 4.3 m/s. The resulting mean velocity has a value of about 2.3 m/s. The pressure drop along the reactor was set to a value of $\Delta p = 1$ bar and leads to the axial pressure profile as displayed in Fig. 6.2(c). Because of the compressibility of the gas phase, the axial pressure does not decrease linearly with the axial position. The mean velocity is increasing with increasing axial position because of the decreasing density of the gas phase. The mean velocity increases from 2.3 m/s at reactor inlet to 4.2 m/s at reactor outlet. This is shown in Fig. 6.2(d). Since the simulation was calculated with the shapes of the inert material and the catalyst particles being the same, no kink is visible in the plots at an axial position of 0.5 m.

The temperature and fraction profiles calculated in the simulation are displayed in Fig. 6.3. Fig. 6.3(a) shows the axial temperature profile on the tube axis and the axial temperature profile of the mean temperatures. As it was expected, the temperature depends strongly on the radial position. The mean temperatures were calculated by averaging the temperatures in the cross section of a specific axial position. The temperature

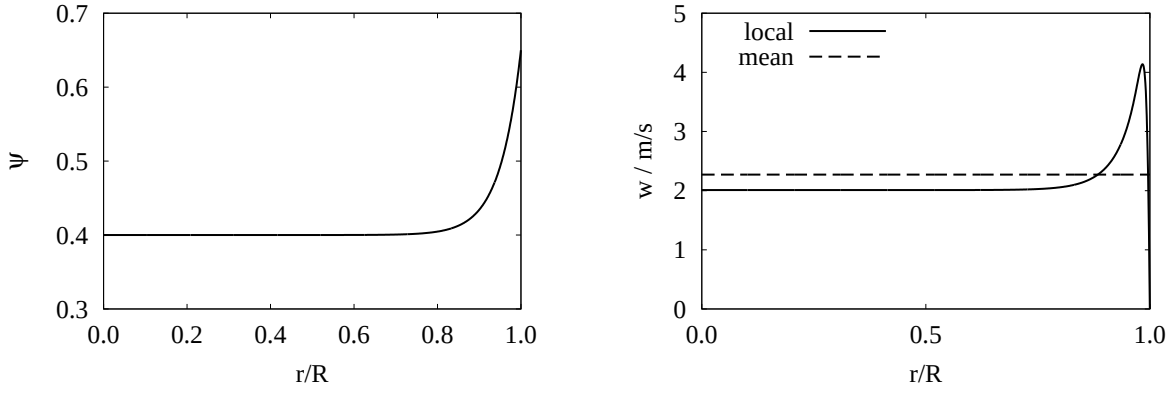

(a) Radial porosity profile

(b) Radial velocity profile at reactor inlet

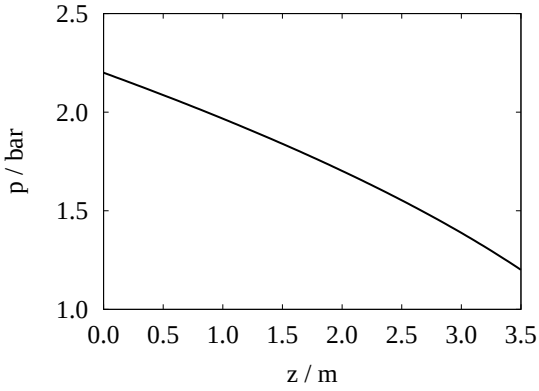

(c) Axial pressure profile

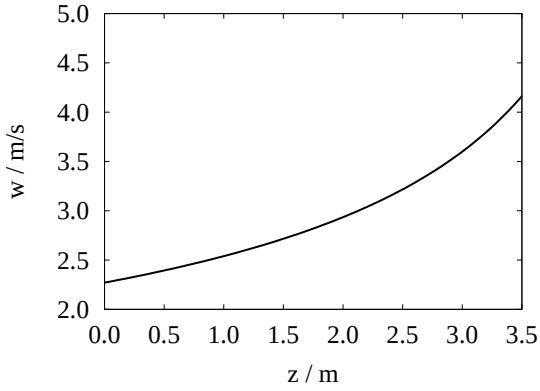

(d) Axial profile of mean velocity

Fig. 6.2: *Radial profiles of porosity and velocity at the reactor inlet, axial profiles of pressure and mean velocity obtained by the simulation with the simulation conditions listed in Tab. 6.2. The horizontal line in the plot (b) of the radial velocity profile shows the value of the mean velocity.*

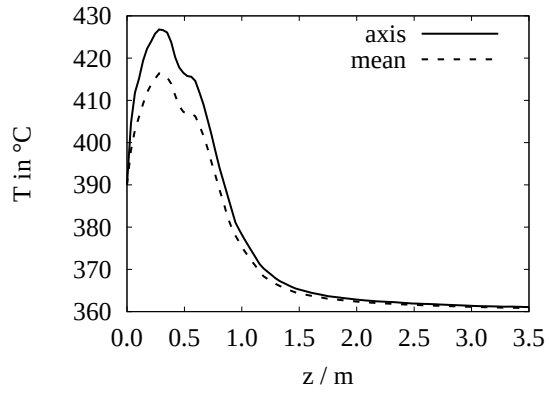

(a) Axial temperature profiles

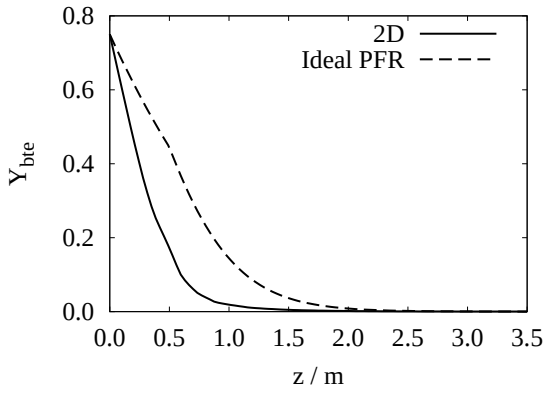

(b) Fraction profiles of *n*-butenes

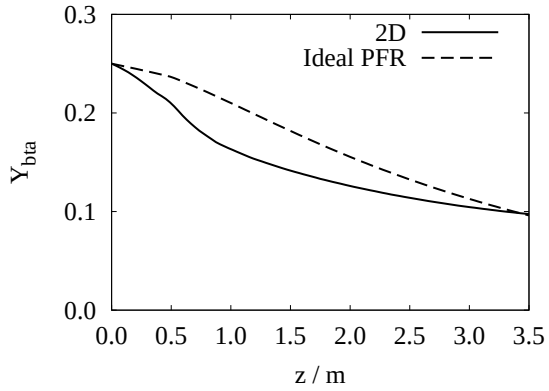

(c) Fraction profiles of *n*-butane

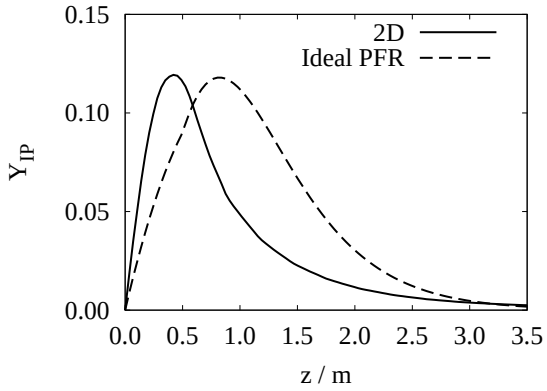

(d) Fraction profiles of IP

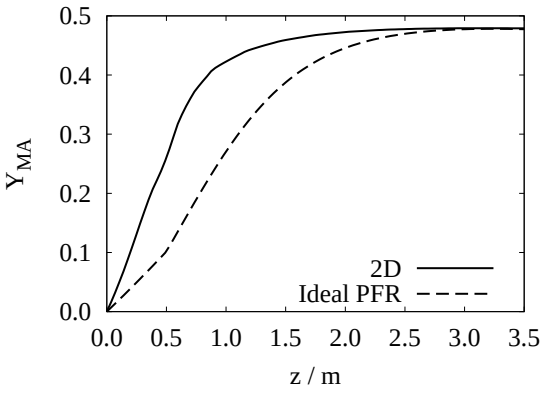

(e) Fraction profiles of maleic anhydride

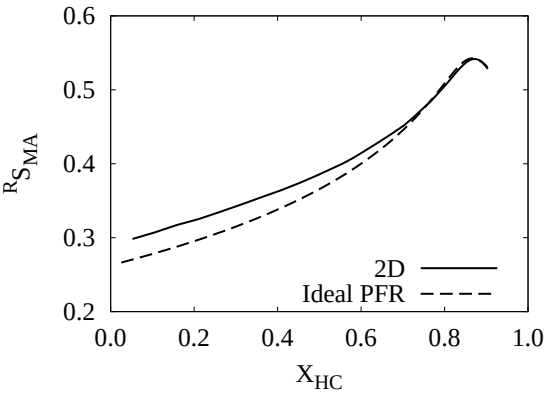

(f) Reactor selectivities of maleic anhydride

Fig. 6.3: *Simulation of the production-scale reactor with the parameters listed in Tab. 6.2. The temperature profiles on the tube axis, the mean temperature and the fraction profiles of the individual species and the reactor selectivity of maleic anhydride resulting from the rigorous simulation (2D) are compared to the corresponding results obtained with the ideal plug flow reactor model using a uniform reactor temperature of 360 °C (Ideal PFR). The fraction profiles calculated in the rigorous simulation were independent of the radial position.*

at the reactor wall had a fixed value of 360 °C, since this was a boundary condition for the simulation. The simulation shows a hot spot of about 410 °C at about $z < 1.5$ m. The maximum value is about 427 °C on the tube axis at an axial position of about $z = 0.3$ m. The transition of the diluted zone and the non-diluted zone at $z = 0.5$ m is visible as sharp bends in the decreasing temperature profiles. For $z \approx 1$ m, the temperature is decreasing sharply and remains slightly above the cooling temperature of 360 °C in the remaining part of the tubes.

Figures 6.3(b) to 6.3(e) show the fraction profiles of *n*-butenes, *n*-butane, IP and maleic anhydride as functions of the axial position in the reactor tubes. Additionally to the fraction profiles obtained by the rigorous simulation, the corresponding fraction profiles obtained by an ideal plug flow reactor that was assumed to be operated isothermally at 360 °C and isobaric at a pressure of 2.2 bar are presented. The fractions obtained by the rigorous simulation were found to be independent of the radial position. The radial mass dispersion evens out fraction gradients.

Fig. 6.3(b) displays the fraction profiles of *n*-butenes. The *n*-butenes are fully converted at an axial position of about 1.5 m. At this position, the temperature has decreased to about 365 °C. The location of the hot spot is directly coupled to the conversion of the *n*-butenes. The conversion rate of *n*-butenes is much higher than the conversion rate of *n*-butane and is therefore the main cause for the formation of the hot spot. The fraction profile that is obtained for an ideal plug flow reactor shows a lower decreasing rate, because of the constant reaction temperature of 360 °C. The total conversion of the *n*-butenes is achieved at an axial position of above 2 m in this case.

The fraction profiles of *n*-butane are presented in Fig. 6.3(c). At $z = 1.5$ m, the fraction of *n*-butane has decreased to a value of about 15%. This corresponds to an amount of 40% of the *n*-butane that has been converted in the hot spot. At reactor outlet, *n*-butane is still present with a fraction of about 10%. That corresponds to a conversion level of *n*-butane of about 60%. The conversion level of the raffinate II mixture amounts to 90%. The conversion rate[5] of *n*-butane in the 2D reactor simulation is higher for axial positions smaller than about 1 m because of the higher temperature in the hot spot zone. At reactor outlet, however, the same conversion level is achieved, since the pressure drop considered in the 2D reactor simulation leads to lower pressures and thus lower conversion rates at axial positions above 1 m.

Fig. 6.3(d) displays the fraction profiles of IP. The maximum yield of IP amounts to about 12% in both reactor models. Because of the higher conversion rate in the hot spot, the maximum yield of IP is achieved at $z = 0.5$ m in the rigorous simulation and at a higher position of $z = 0.9$ m in the plug flow simulation. The fraction decreases to below 1% at reactor outlet. A low fraction is beneficial for the recovery section.

The fraction profiles of maleic anhydride are displayed in Fig. 6.3(e). The fraction of maleic anhydride is increasing steadily and approximates 48% at reactor outlet. The reaction conditions were chosen to achieve the maximum yield of maleic anhydride at the reactor outlet. The fraction profile of maleic anhydride resulting from the plug flow reactor model shows lower yields of maleic anhydride in the first part of the reactor but reaches the same yield as calculated in the rigorous simulation at the reactor outlet.

Fig. 6.3(f) shows the reactor selectivities of maleic anhydride as functions of the conversion level. In case of the two-dimensional simulation, the reactor selectivity is slightly

[5]The conversion rate corresponds to the slope of the curve of the conversion level.

higher during the conversion of the *n*-butenes. This behaviour can be attributed to the higher temperature in the hot spot in which most of the *n*-butenes are converted. The reactor selectivities for the conversion level of 90% at reactor outlet, however, are identical in both simulations.

The main results of the rigorous simulation are summarised in Tab. 6.3. The simulation results in a production capacity of maleic anhydride of 17,100 t/a. The heats of reaction lead to a heat removal of 17.5 MW from the reactor that can be used for high pressure steam generation. If a new plant is being designed, lower production capacities can easily be accomplished by decreasing the number of reactor tubes in the reactor vessel.

reaction	
conversion level of raffinate II	90%
conversion level of *n*-butenes	100%
conversion level of *n*-butane	60%
yield of maleic anhydride	48%
yield of IP	0.2%
production	
production capacity of maleic anhydride	17,100 t/a
heat removal for steam generation	17.5 MW

Tab. 6.3: *Main results of the simulation with the simulation parameters listed in Tab. 6.2.*

The feedstock in the simulation consisted solely of linear hydrocarbons. A real raffinate II mixture also contains isobutane that is converted at the same rate as *n*-butane but yields mainly carbon oxides. The yield of maleic anhydride for a real raffinate II mixture can, therefore, be assumed to be lower than the yield calculated in the simulation. The yield obtained with a real raffinate II mixture can be estimated by considering a superposition of virtual yields for the conversion of the individual hydrocarbons:

$$Y_{\mathrm{MA}} = \sum_i (x_i^{\mathrm{HC}} \times {}_iY_{\mathrm{MA}}). \tag{6.45}$$

Several assumptions can be made: Since the reaction rates of *n*-butane and isobutane are the same[6], the conversion levels of the two saturated hydrocarbons can be assumed to be the same. Then, these conversion levels equal the conversion level of *n*-butane in the simulation of 60%. The virtual yield of maleic anhydride from *n*-butane is assumed to remain constant, and the virtual yield of maleic anhydride from isobutane is assumed to equal 0. Then the yield that results from an isobutane containing raffinate II stream results in

$$Y_{\mathrm{MA}}^{\mathrm{r2}} = Y_{\mathrm{MA}}^{\mathrm{sim}} - \left(x_{\mathrm{bta}}^{\mathrm{HC,sim}} - x_{\mathrm{bta}}^{\mathrm{HC,r2}}\right) \times {}_{\mathrm{bta}}Y_{\mathrm{MA}}. \tag{6.46}$$

The values $Y_{\mathrm{MA}}^{\mathrm{sim}}$ and $x_{\mathrm{bta}}^{\mathrm{HC,sim}}$ are calculated in the simulation and are therefore known as well as the amount of *n*-butane in raffinate II ($x_{\mathrm{bta}}^{\mathrm{HC,r2}}$). It is assumed that the virtual yield of maleic anhydride equals the yield of maleic anhydride for the conversion of pure *n*-butane with a value of about 55%. The estimation results in a value of

$$Y_{\mathrm{MA}}^{\mathrm{r2}} \approx Y_{\mathrm{MA}}^{\mathrm{sim}} - 5\% = 43\%. \tag{6.47}$$

[6]See section 4.6 for details.

6.3.3 Dependence of Reactor Performance on the Thermal Conductivity of the Catalyst Bodies

The thermal conductivity of the catalyst bodies is the most uncertain input parameter. In the simulation above, a cautious value of the thermal conductivity of 0.5 W/(m K) was assumed. This section presents an additional simulation with the same parameters as above except for the thermal conductivity of the catalyst bodies. The second simulation was carried out with a conductivity of 3.5 W/(m K). The first simulation can be regarded as the worst case approximation for bulk catalyst bodies that consist solely of the active VPO material. The thermal conductivity in the second simulation can be regarded as a value that is valid for a diluted fixed-bed where also pure steatite bodies with a higher thermal conductivity of 3.5 to 4.5 W/(m K) are used.

Fig. 6.4 shows the plots of the temperature and fraction profiles calculated in the two simulations. Fig. 6.4(a) displays the temperature profiles on the tube axis as functions of the axial position in the reactor tubes. It is clearly seen that the maximum value of the temperature is decreasing with increasing conductivity. The maximum temperatures in the reactor are 427 and 406 °C for conductivities of 0.5 W/(m K) and 3.5 W/(m K), respectively.

The fraction profiles of *n*-butenes, *n*-butane and IP are presented in plots 6.4(b) to 6.4(d). The higher hot spot temperatures for lower conductivities result in higher conversion rates of *n*-butenes. Total conversion of *n*-butenes is achieved in both cases. The resulting conversion levels of *n*-butane are 60% and 54% for conductivities of 0.5 and 3.5 W/(m K), respectively. The yield of IP is similar in both cases, and reduces to ¡1% at the reactor exit.

Fig. 6.4(e) displays the fraction profiles of maleic anhydride. The same maximum yield of 48% is achieved at the reactor outlet. The profile for 3.5 W/(m K) is slightly shifted to higher axial positions because of the lower hot spot temperatures. The reactor selectivities of maleic anhydride are almost unchanged, as it is displayed in Fig. 6.4(f).

6.3.4 Variation of Feed Stream Temperature and Wall Temperature

The simulation presented above in section 6.3.2 was carried out with a feed stream temperature of 390 °C and a tube wall temperature of 360 °C. A second simulation was carried out with temperatures that were both 10 K higher than the corresponding temperatures of the above presented simulation. A third simulation was carried out with a value of 360 °C for both temperatures.

Fig. 6.5 shows the temperature and fraction profiles resulting from the three simulation variants. Fig. 6.5(a) shows the axial temperature profiles on the tube axis. The temperature profile with identical temperatures of the feed stream and the tube wall of 360 °C is labelled '360/360'. Other than for the case of the 360/390 reaction conditions, the maximum hot spot temperature is located in the non-diluted zone. Since the reaction temperature is lower at reactor inlet, the reaction rates are lower in the diluted zone. More unreacted hydrocarbons enter the non-diluted zone, and the temperature increases to its maximum of about 422 °C there. Such an operation condition might occur during reactor start-up and during a failure of the pre-heating equipment of the feed stream. We

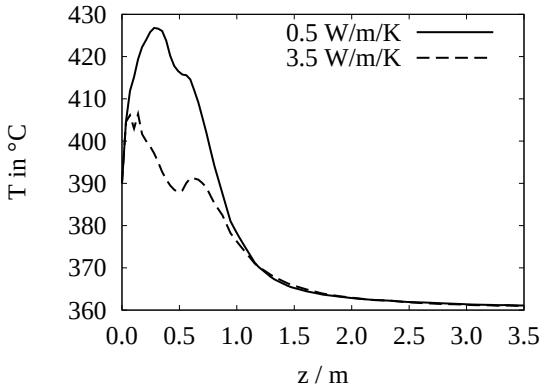

(a) Temperature profiles on the tube axis

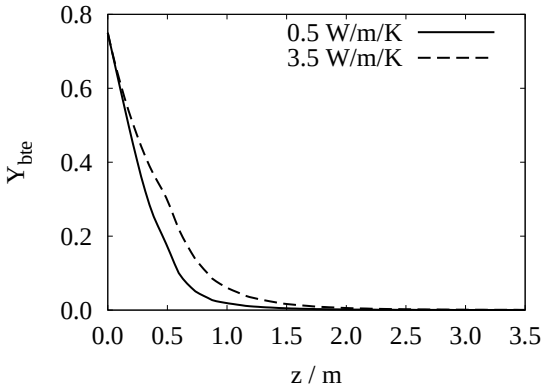

(b) Fraction profiles of *n*-butenes

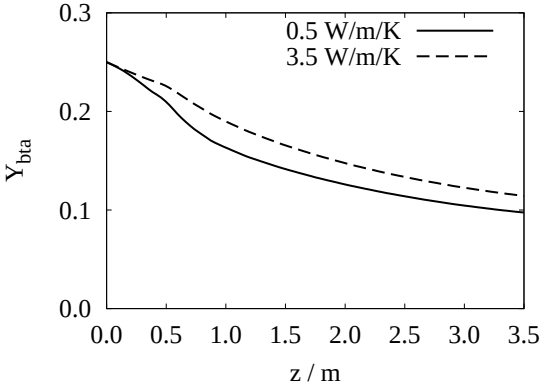

(c) Fraction profiles of *n*-butane

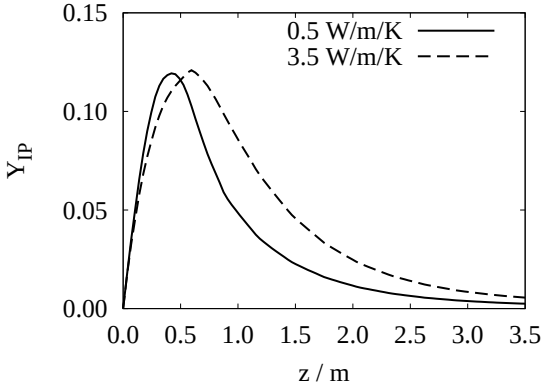

(d) Fraction profiles of IP

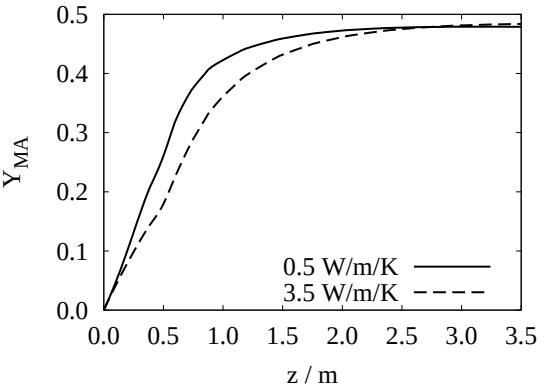

(e) Fraction profiles of maleic anhydride

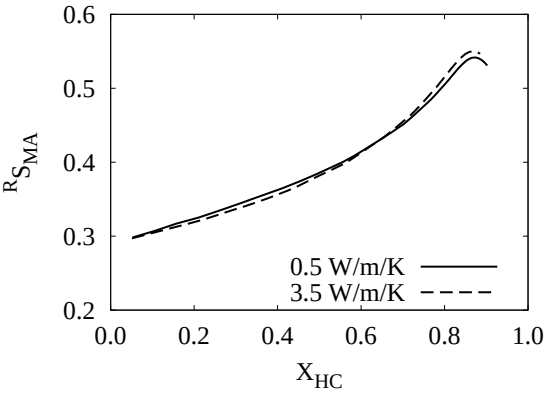

(f) Reactor selectivities of maleic anhydride

Fig. 6.4: *Dependence of the reactor performance on the thermal conductivity of the catalyst bodies of 0.5 and 3.5 W/(m K). The thermal conductivity was the sole parameter that was altered.*

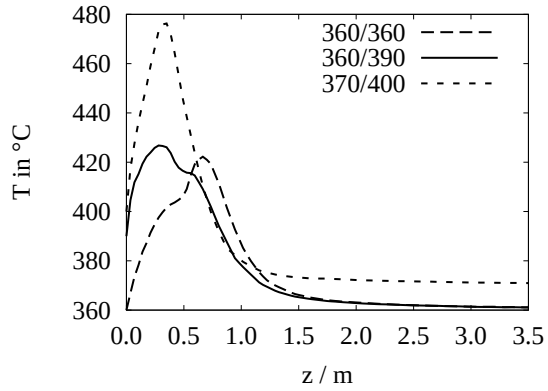

(a) Temperature profiles on the tube axis

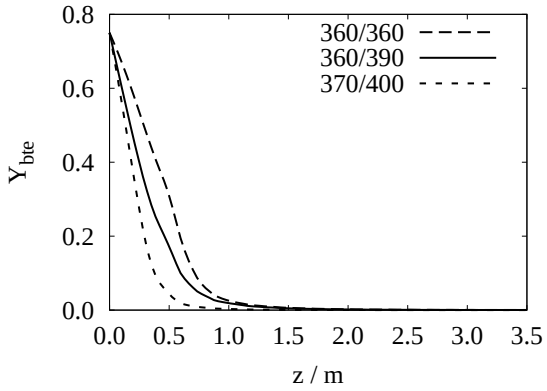

(b) Fraction profiles of *n*-butenes

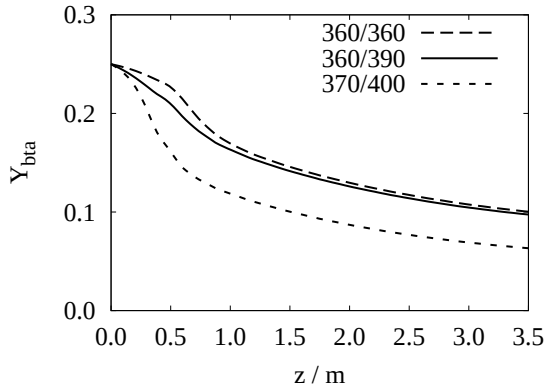

(c) Fraction profiles of *n*-butane

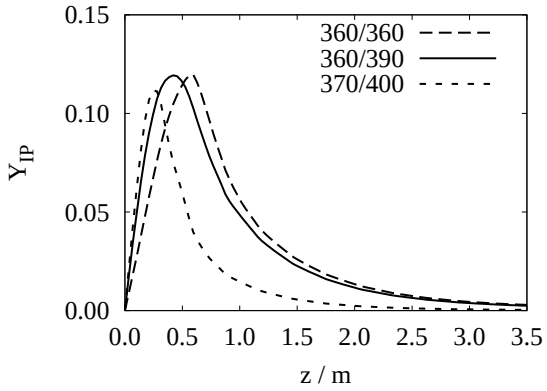

(d) Fraction profiles of IP

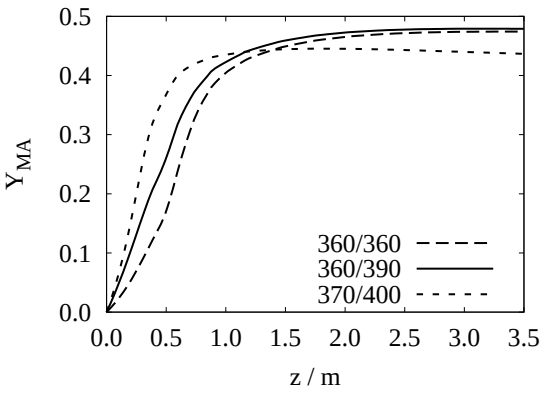

(e) Fraction profiles of maleic anhydride

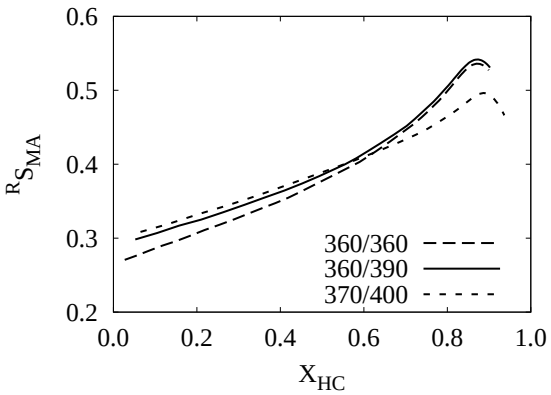

(f) Reactor selectivities of maleic anhydride

Fig. 6.5: *Variation of feed stream temperature and wall temperature. The labels of the curves consist of two temperature values: the first is the wall temperature, the second is the feed stream temperature.*

see that these conditions do not lead to intolerable temperatures in the catalyst bed.

The simulated profiles obtained for the tube wall and feed stream temperatures of 370 and 400 °C, respectively, are labelled '370/400'. The higher reaction rates in the dilution zone result in a higher hot spot temperature in this zone of about 476 °C. The temperature reaches an almost constant value of slightly above 370 °C for axial positions of $z > 1.5$ m. The undesired increase in tube wall and feed stream temperatures may result, for example, from simultaneous failure of the cooling system of the reactor and of the pre-heating system of the feed stream.

The fraction profiles are in accordance with the hot spot temperatures. At higher hot spot temperatures, the gradients in the fraction profiles are higher. The conversion levels of *n*-butane as well as the yields of maleic anhydride are identical for lower feed stream temperature and normal operation conditions. The conversion level of *n*-butane for higher tube wall and feed stream temperatures, however, is about 75%. The corresponding maximum yield has a value of about 45% and is achieved at an axial position of about $z = 2$ m.

The results presented above were obtained with a value of the thermal conductivity of the bodies of 0.5 W/(m K). For a thermal conductivity of 3.5 W/(m K), the axial temperature profiles and the fraction profiles of maleic anhydride are presented in Fig. 6.6. The maximum temperatures in the hot spots are below 424 °C in all cases. This is much lower than the value of 476 °C determined for a thermal conductivity of 0.5 W/(m K). The yield of maleic anhydride has a value of 48% in all cases.

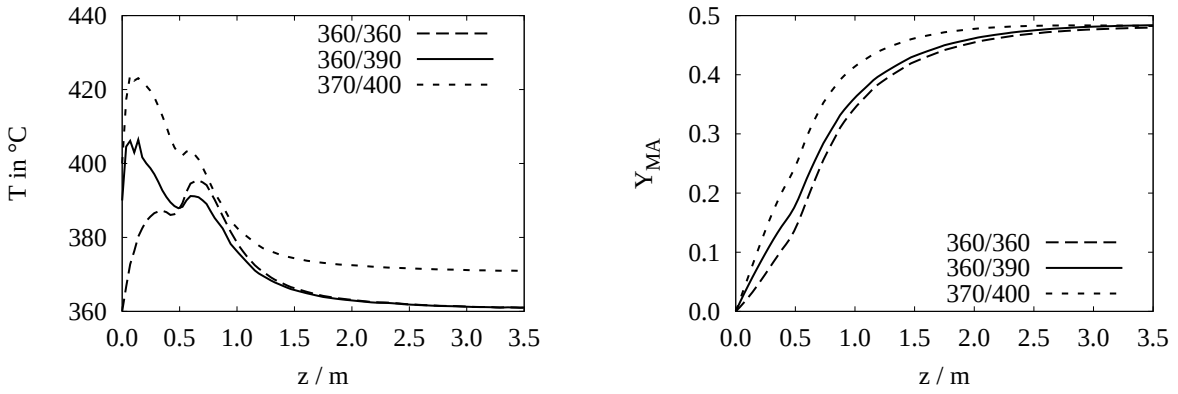

(a) Temperature profiles on the tube axis

(b) Fraction profiles of maleic anhydride

Fig. 6.6: *Variation of temperature with the assumption of a thermal conductivity of the catalyst bodies of 3.5* W/(m K).

6.3.5 Variation of Throughput

The simulations presented so far were carried out with a feed stream pressure of 2.2 bar and a pressure drop along the reactor of 1 bar. A process should be flexible concerning the throughput to be able to respond to variations of the demand. Higher throughputs are typically more critical for the reactor operation. Therefore, an additional simulation with an inlet pressure of 2.7 bar and a pressure drop of 1.5 bar was carried out.

Fig. 6.7 shows the radial and axial profiles of porosity, pressure and velocity for both throughputs. The porosity profile is independent of throughput. Hence, one curve is plotted, only. The radial velocity profiles are displayed in Fig. 6.7(b) and show only small differences between the simulations with pressure drops of 1.0 bar and 1.5 bar. The mean velocities at the reactor inlet are about 2.3 m/s and 2.5 m/s at a pressure drop of 1.0 bar and 1.5 bar, respectively. The change in velocity in axial direction is higher at higher pressure drops. At the reactor outlet, the mean velocities have values of 4.2 m/s and 5.6 m/s, respectively.

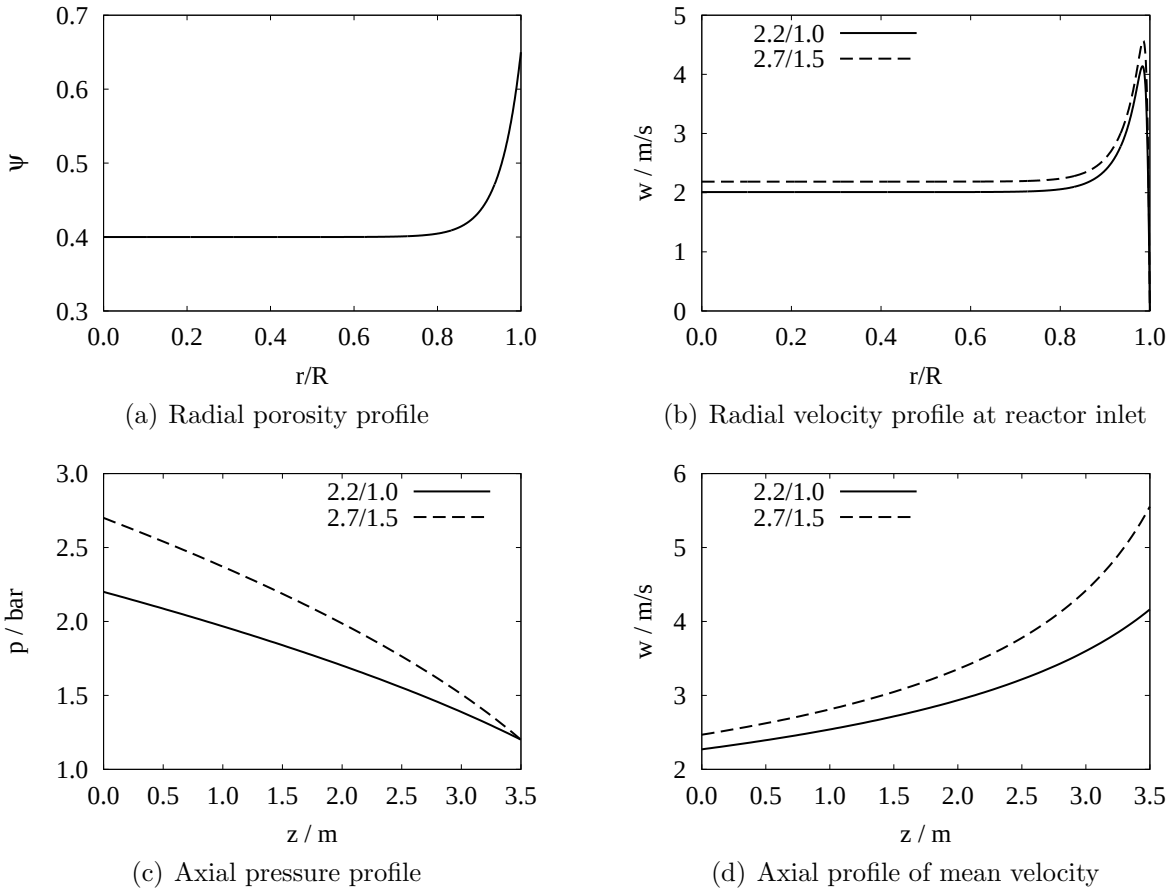

(a) Radial porosity profile

(b) Radial velocity profile at reactor inlet

(c) Axial pressure profile

(d) Axial profile of mean velocity

Fig. 6.7: *Radial profiles of porosity and velocity at the reactor inlet, axial profiles of pressure and mean velocity obtained for simulation conditions with a pressure drop of 1.0 bar and 1.5 bar.*

The resulting temperature and fraction profiles are presented in Fig. 6.8. The fraction profiles can be regarded as identical. Also the temperature profiles displayed in Fig. 6.8(a) are very similar. The higher throughput leads to a second maximum in the non-diluted zone, since more hydrocarbons enter this zone and lead to a higher local conversion rate. The maximum temperature is about 428 °C and can also be regarded as identical to the maximum temperature that is achieved at the lower throughput.

The production capacity, however, is increased strongly at a higher throughput. The resulting production capacity of maleic anhydride amounts to 22,500 t/year. This is a factor of about 1.3 higher than the production capacity of 17,100 t/year with the lower

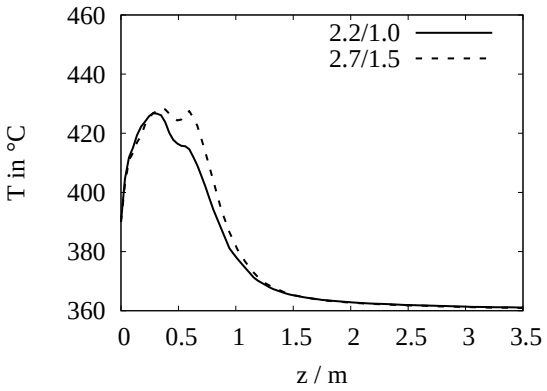

(a) Temperature profiles on the tube axis

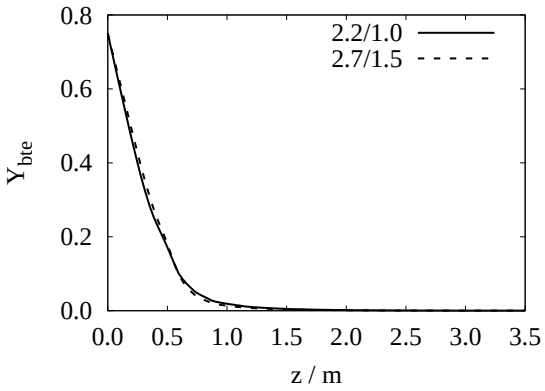

(b) Fraction profiles of *n*-butenes

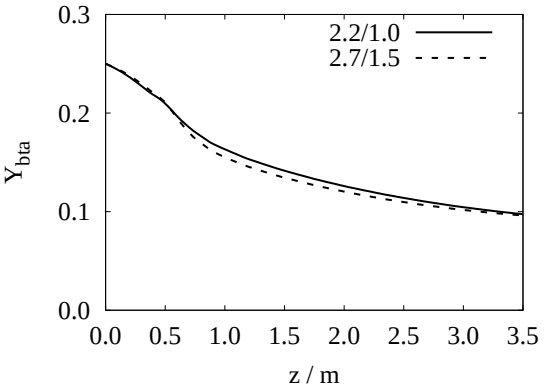

(c) Fraction profiles of *n*-butane

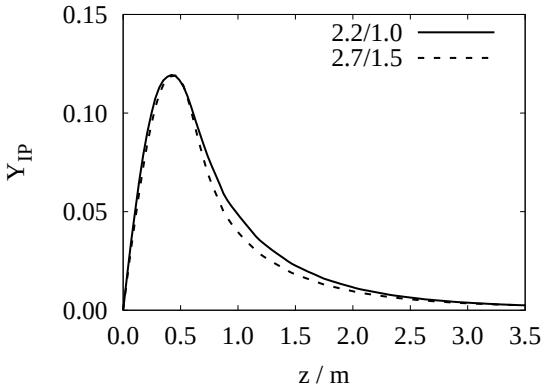

(d) Fraction profiles of IP

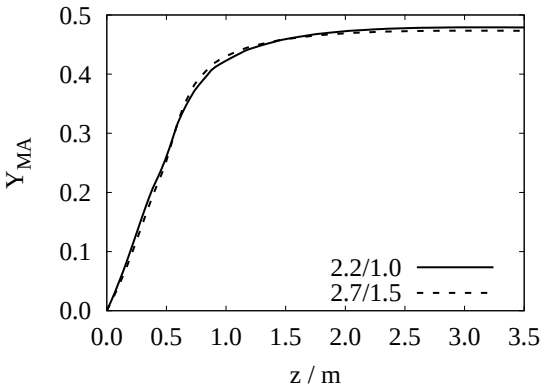

(e) Fraction profiles of maleic anhydride

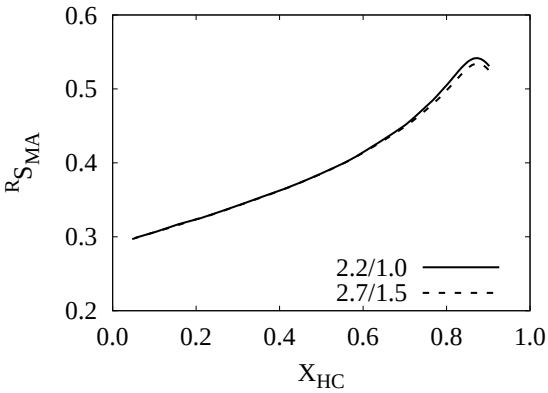

(f) Reactor selectivities of maleic anhydride

Fig. 6.8: *Variation of throughput by variation of the feed stream pressure and the pressure drop along the reactor. Compared are simulations with a feed stream pressure of 2.2 bar and a pressure drop of 1 bar (labelled '2.2/1.0') with those using a feed stream pressure of 2.7 bar and a pressure drop of 1.5 bar (labelled '2.7/2.5').*

throughput. The heat for steam generation is increased from a value of 17.5 MW to a value of 23.4 MW, correspondingly.

Therefore, the increase in throughput is possible by increasing the inlet pressure and the allowed pressure drop along the reactor. In the pressure range investigated in the present section, the yield of maleic anhydride remains constant.

6.3.6 Further Simulation Results

Further simulations were carried out and the results are summarised in Tab. 6.4. The conversion levels, the yields of maleic anhydride, the yields of IP, the maximum temperatures in the reactor and the production capacities (Ω) are presented for each of the pressure and temperature combinations. Each column contains two values: the left and right values were calculated with thermal conductivities of the catalyst bodies of 0.5 W/(m K) and 3.5 W/(m K). Except for the values that were obtained with a wall temperature of 370 °C and a conductivity of 0.5 W/(m K), the production capacities for pressure drops of 1.0 bar and 1.5 bar show a variation of below 1% and 2%, respectively. For a wall temperature of 370 °C and a conductivity of 0.5 W/(m K), the production capacities decrease by a relative amount of about 10% and 13% for pressure drops of 1.0 bar and 1.5 bar, respectively. The resulting maximum temperatures are 476 °C and 489 °C in these cases, which is unacceptable for operation because the catalyst is being irreversibly damaged at these high temperatures.

Δp in bar	T_w in °C	T_0 in °C	X_{HC}		Y_{MA}		Y_{IP}		T_{max} in °C		Ω in t/a	
1.0	360	360	90%	88%	47%	48%	0.3%	0.6%	422	395	16,900	17,100
	360	390	90%	89%	48%	48%	0.2%	0.6%	427	406	17,100	17,200
	370	400	94%	91%	44%	48%	0.0%	0.2%	!476!	424	15,400	17,000
1.5	360	360	90%	88%	47%	48%	0.3%	0.8%	430	401	22,300	22,700
	360	390	90%	88%	47%	48%	0.2%	0.7%	428	405	22,500	22,900
	370	400	95%	91%	42%	48%	0.0%	0.2%	!489!	428	19,500	22,600

Tab. 6.4: *Summary of all reactor simulations. Two values are listed in each column: the left and right values are calculated for catalyst body conductivities of 0.5* W/(m K) *and 3.5* W/(m K)*, respectively. The exclamation marks show temperature values that irreversibly damage the catalyst.*

Chapter 7

Process Overview

The following chapter gives an overview of the process for the production of maleic anhydride from raffinate II. A simplified flow scheme of the reactor section and the absorption column is presented in Fig. 7.1. Air from the atmosphere is compressed to the reactor inlet

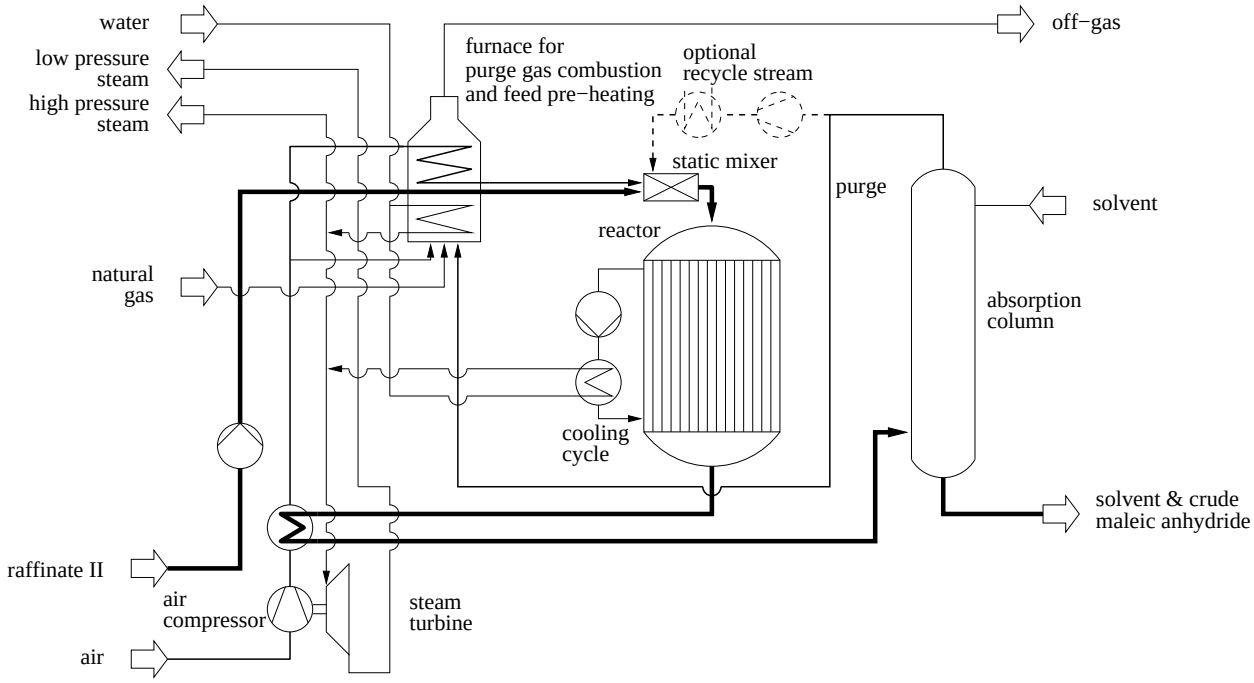

Fig. 7.1: *Simplified flow scheme of the reactor section and the subsequent absorption column for the partial oxidation of raffinate II to maleic anhydride.*

pressure. In an internal heat exchanger, the compressed air is heated to a temperature of about 340 °C by cooling the product stream of the reactor. In the pre-heater and combustion unit, the air is further heated to the reactor inlet temperature by combustion of the purge gas and additional natural gas. The pre-heating is necessary to achieve higher selectivities in the conversion of *n*-butenes. In the static mixer, the heated air is mixed with the raffinate II stream. The feed mixture enters the reactor from the top. The product

stream leaves the reactor at the bottom. It is cooled in the internal heat exchanger and subsequently enters the absorption column at the bottom. Water can be used to separate maleic anhydride from the product stream. The gas stream leaving the absorber at the top contains nitrogen, oxygen, unreacted *n*-butane, and carbon oxides. *n*-Butane as well as carbon monoxide are burnt in the pre-heater to heat the feed stream and to generate high pressure steam. Most of the high pressure steam is generated by cooling the reactor. Part of the steam is used in the steam turbine to drive the air compressor. The excess high pressure steam is exported and can be used in the recovery and purification section or in other units on the site.

The stream specifications are summarised in Tab. 7.1. Two alternatives are displayed with different production capacities of maleic anhydride.

			feed stream		product stream		
p_0	Δp	Ω	$\dot{m}_{\mathrm{RII},0}$	$\dot{V}_{\mathrm{N,air},0}$	$\dot{n}_{\mathrm{MA}}$	$\dot{n}_{\mathrm{bta}}$	$\dot{n}_{\mathrm{CO}}$
bar	bar	t/year	kg/h	m^3/h	mol/h	mol/h	mol/h
2.2	1.0	17,100	2,570	168,900	21,800	4,460	40,600
2.7	1.5	22,500	3,430	225,500	28,700	5,830	55,900

Tab. 7.1: *Stream specifications for the reactor section of the process. Two alternatives with different production capacities are displayed. The production capacity Ω is calculated for an annual production time of 8000 h/year. Only the carbon containing components that can be further oxidised are specified in the product stream.*

7.1 Energy Balance

Energy balances give information about the excess steam generation and can be used as a first estimation of the design parameters for the compressor and the internal heat exchanger. The control volume of the reactor section and some individual sub-control volumes are displayed in Fig. 7.2. The energy streams are drawn as bold lines. The thin lines represent mass streams. The change in enthalpy during steam generation is represented by the heat stream $\dot{Q}_{\mathrm{s}}$.

Air is sucked in from the atmosphere with a temperature of $T_{\mathrm{a}} = 25\ ^{\circ}\mathrm{C}$ and a pressure of $p_{\mathrm{a}} = 1.013$ bar. For a first estimation of the compressor power that is needed to compress the air stream to the reactor inlet pressure p_0, an adiabatic behaviour of the compressor is assumed. The mechanical power which is necessary for the compression equals

$$P = \int_{p_{\mathrm{a}}}^{p_0} \dot{V}\,\mathrm{d}p = \frac{p_{\mathrm{a}}\dot{V}_{\mathrm{a}}}{\alpha - 1}\left[\left(\frac{p_0}{p_{\mathrm{a}}}\right)^{\frac{\alpha-1}{\alpha}} - 1\right] \tag{7.1}$$

with a ratio of heat capacities of $\alpha = 1.4$ of air [54]. The temperature of the gas stream after compression T_{cpr} can be expressed as

$$T_{\mathrm{cpr}} = T_{\mathrm{a}}\left(\frac{p_0}{p_{\mathrm{a}}}\right)^{\frac{\alpha-1}{\alpha}}. \tag{7.2}$$

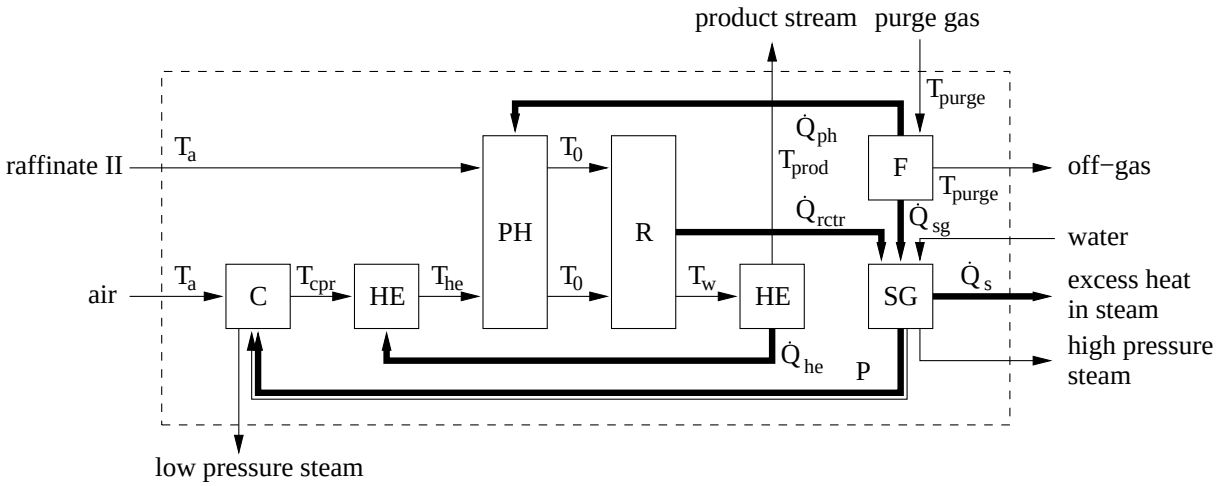

Fig. 7.2: *Energy and mass streams around the reactor. The sub-control volumes belong to the compressor C, the heat exchanger HE, the pre-heating section of the furnace PH, the reactor R, the furnace F and the steam generation section of the furnace SG.*

The mechanical power for the compressor and the temperature of the gas stream after compression are listed in Tab. 7.2 for both alternatives.

Ω	P	T_a	T_cpr
t/year	MW	°C	°C
17,100	4.5	25	100
22,500	7.8	25	123

Tab. 7.2: *Mechanical energy input of the compressor and temperature specifications of the air stream.*

The internal heat exchanger uses the temperature difference between the air and the product streams to heat the air and to cool the product streams. It is assumed that a typical temperature difference of 20 K is necessary for the operation of the heat exchanger. The molar flows of the two streams are assumed to be identical since the amount of total moles is not changed much during the reaction. The addition of raffinate II is negligible. The heat capacity of the product stream is assumed to equal the value of air. The heat flow that is transferred between the two streams equals

$$\dot{Q}_\mathrm{he} = \dot{n}_\mathrm{air} C_\mathrm{p,air} (T_\mathrm{he} - T_\mathrm{compr}) = \dot{n}_\mathrm{air} C_\mathrm{p,air} (T_\mathrm{w} - T_\mathrm{prod}). \tag{7.3}$$

The heat flow and temperature specifications of the streams are presented in Tab. 7.3. The product stream is assumed to leave the reactor with the cooling temperature of the reactor, $T_\mathrm{w} = 360$ °C. The air feed stream is heated to $T_\mathrm{he} = 340$ °C.

The air has to be heated to the reactor inlet temperature of $T_0 = 390$ °C. This is carried out in the pre-heating section of the furnace. Additionally, the raffinate II stream

Ω	feed air		product stream		$\dot{Q}_{\mathrm{he}}$
	T_{cpr}	T_{he}	T_{w}	T_{prod}	
t/year	°C	°C	°C	°C	MW
17,100	100	340	360	120	14.8
22,500	123	340	360	143	17.9

Tab. 7.3: *Heat flow and temperatures in the internal heat exchanger.*

is vapourised and heated from ambient temperature to reactor inlet temperature. The necessary heat flows equal

$$\dot{Q}_{\mathrm{ph,air}} = \dot{n}_{\mathrm{air}} C_{\mathrm{p,air}} (T_0 - T_{\mathrm{he}}), \tag{7.4}$$

$$\dot{Q}_{\mathrm{ph,RII}} = \dot{n}_{\mathrm{rII}} \left[\Delta_{\mathrm{v}} H_{\mathrm{RII}} + C_{\mathrm{p,rII}} (T_0 - T_{\mathrm{a}}) \right]. \tag{7.5}$$

Ω	$\dot{Q}_{\mathrm{ph,air}}$	$\dot{Q}_{\mathrm{ph,RII}}$	$\dot{Q}_{\mathrm{ph}}$
t/year	MW	MW	MW
17,100	3.1	0.8	3.9
22,500	4.1	1.1	5.2

Tab. 7.4: *Heat specifications of the pre-heater.*

The air and raffinate II streams are mixed and enter the reactor. The energy balance for the reactor can be split in two parts: the cooling of the inlet gas stream from reactor inlet temperature to the cooling temperature of the reactor

$$\dot{Q}_{\mathrm{rctr,c}} = (\dot{n}_{\mathrm{air}} C_{\mathrm{p,air}} + \dot{n}_{\mathrm{rII}} C_{\mathrm{p,rII}}) \times (T_0 - T_{\mathrm{w}}) \tag{7.6}$$

and the heat of reaction

$$\dot{Q}_{\mathrm{rctr,r}} = -\dot{n} \left(x_{\mathrm{bte},0} \Delta_{\mathrm{S}} H_{\mathrm{bte}} - x_{\mathrm{RII},0} \sum_{i=1}^{N_{\mathrm{species}}} Y_i \Delta_{\mathrm{S}} H_i \right). \tag{7.7}$$

Tab. 7.5 shows the corresponding values as well as the total amount of heat that has to be removed by steam generation.

Ω	$\dot{Q}_{\mathrm{rctr,r}}$	$\dot{Q}_{\mathrm{rctr,c}}$	$\dot{Q}_{\mathrm{rctr}}$
t/year	MW	MW	MW
17,100	17.6	1.9	19.5
22,500	23.5	2.5	26.0

Tab. 7.5: *Heat specifications of the reactor.*

The purge gas consists of n-butane and carbon monoxide as species that can be further oxidised. Since the oxygen content and the amount of n-butane and carbon monoxide are

too low to operate the furnace, additional air and natural gas have to be fed to the furnace. The heat stream that results from the combustion of natural gas is not considered in the energy balance. Only the heat stream that results from the combustion of the purge gas is considered. The heat flow equals

$$\dot{Q}_{\mathrm{T}} = \dot{n} \times x_{\mathrm{RII,0}} \times \sum_{i=1}^{N_{\mathrm{species}}} Y_i(\Delta_{\mathrm{S}} H_i - \Delta_{\mathrm{S}} H_{\mathrm{CO2}}). \tag{7.8}$$

The heat flows of the furnace are listed in Tab. 7.6.

Ω	$\dot{Q}_{\mathrm{T}}$	$\dot{Q}_{\mathrm{ph}}$	$\dot{Q}_{\mathrm{sg}}$
t/year	MW	MW	MW
17,100	6.5	3.9	2.6
22,500	8.7	5.2	3.5

Tab. 7.6: *Heat stream specifications of the furnace.*

The heat streams of the reactor and the residual heat stream of the furnace are used to generate high pressure steam. The cooling of the reactor is carried out at a temperature of 360 °C. With a temperature difference between the steam generator and the salt in the cooling cycle of 10 K, saturated steam with a temperature of $T_{\mathrm{s}} = 350$ °C and with the corresponding pressure of $p_{\mathrm{s}} = 165$ bar is obtained [55]. The mass flow of generated steam results in

$$\dot{m}_{\mathrm{steam}} = \frac{\dot{Q}_{\mathrm{sg}}}{c_{\mathrm{p,H2O}}(T_{\mathrm{s}}(p_{\mathrm{s}}) - T_{\mathrm{cw}}) + \Delta_{\mathrm{v}} h_{\mathrm{H2O}}}. \tag{7.9}$$

The temperature of the water stream that is vapourised is assumed to be $T_{\mathrm{cw}} = 25$ °C. Tab. 7.7 shows the amount of heat that is used for the production of excess steam. Some high pressure steam is used in the turbine to drive the compressor, resulting in a stream of low pressure steam. The specifications for low pressure steam differ from site to site [56]. Additionally, the amount of high pressure steam that is needed for the turbine depends on the specifications of the low pressure steam. Therefore, the amount of excess steam is calculated for high pressure conditions as a reference.

Ω	$\dot{Q}_{\mathrm{rctr}}$	$\dot{Q}_{\mathrm{sg}}$	$\dot{Q}_{\mathrm{cpr}}$	$\dot{Q}_{\mathrm{s}}$	$\dot{m}_{\mathrm{HP-steam,max}}$
t/year	MW	MW	MW	MW	kg/h
17,100	19.4	2.6	-4.5	17.5	27,800
22,500	26.0	3.5	-7.8	21.6	34,500

Tab. 7.7: *Steam generation by using the heat of the reactor and of the furnace.*

The heat capacities of air and raffinate II were assumed to be independent of temperature. They were calculated by using correlations given in [40] for a temperature of 200 °C. The heat of vaporisation of raffinate II was also taken from [40] for a temperature of 25 °C. A steam table is given in [55]. The physical properties that were used in the energy balances are presented in Tab. 7.8.

$C_{\mathrm{p,air}}$ kJ/(mol K)	$C_{\mathrm{p,rII}}$ kJ/(mol K)	$c_{\mathrm{p,H2O}}$ kJ/(kg K)	$\Delta_{\mathrm{v}}H_{\mathrm{rII}}$ kJ/mol	$\Delta_{\mathrm{v}}h_{\mathrm{H2O}}$ kJ/kg
0.03	0.12	4,2	21	896

Tab. 7.8: *Physical properties required for the process energy balances.*

7.2 Effects of a Recycle Stream on Process Performance

In the present section, a recycle stream is considered that transports part of the unreacted *n*-butane back to the reactor feed. The corresponding streams are presented in Fig. 7.3. The reactor products are separated into a product stream and a residual stream. By considering an aqueous absorption column, the product stream consists of maleic acid solved in water. The residual stream consists of all other species. This stream is split into a purge gas stream and a recycle stream. A purge gas stream is necessary to regulate the concentrations of the inert species in the recycle stream. The components contained in the pseudo-species IP are not present in significant amounts. Tab. 7.9 shows which

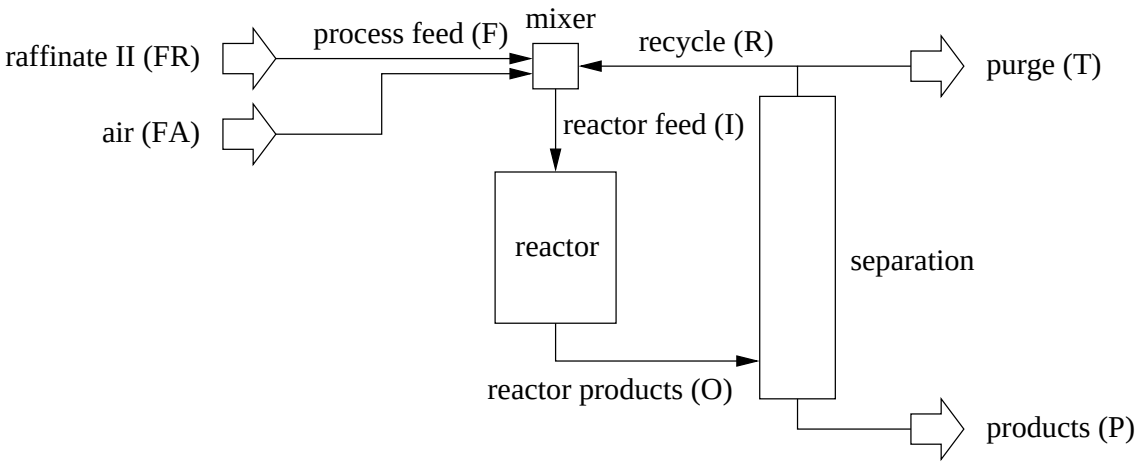

Fig. 7.3: *Streams in a process with recycle. The letters in parentheses represent the indices of the individual streams for the molar flow rates and molar fractions that are used in the equations.*

components are present in each single stream. The recycle ratio R is defined as the fraction of the residual stream that is recycled to the reactor. The ratio can be expressed as

$$R = \frac{\dot{n}_{\mathrm{R}}}{\dot{n}_{\mathrm{R}} + \dot{n}_{\mathrm{T}}}. \tag{7.10}$$

Fig. 7.4 shows the reactor selectivity and yield of maleic anhydride as functions of the conversion level. The curves are calculated in the reactor simulation for a production capacity of 17,100 t/year. The simulation results are described in detail in section 6.3.2. If no hydrocarbons are recycled, the reactor is best operated at maximum reactor yield. The maximum possible amount of maleic anhydride is then obtained. If non-converted

	Nitrogen	Oxygen	*n*-Butane	*n*-Butenes	MA	CO	CO_2	Water
F	X	X	X	X				
FA	X	X						
FR			X	X				
I	X	X	X	X		X	X	
O	X	X	X		X	X	X	X
P					X			X
R	X	X	X			X	X	
T	X	X	X			X	X	

Tab. 7.9: *The presence of components in each single stream of Fig. 7.3.*

hydrocarbons are recycled, the reactor is best operated by maximising the reactor selectivity. The conversion level of the hydrocarbons and the yield of maleic anhydride related to the reactor are lower in this case, but the converted hydrocarbons are used best for the production of maleic anhydride. Overall conversion level and yield are optimised. The

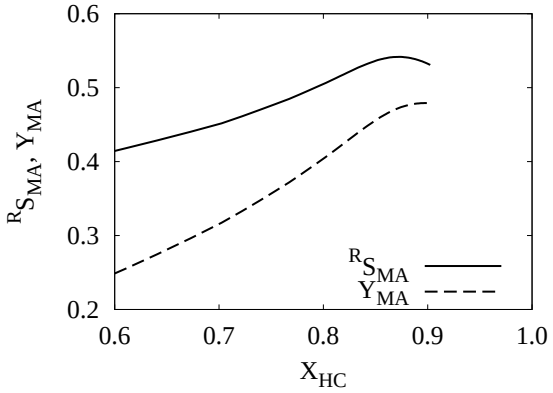

Fig. 7.4: *Reactor selectivity of maleic anhydride and yield of maleic anhydride as functions of the conversion level. The curves are calculated in the reactor simulation described in section 6.3.2.*

Y_{bte}	Y_{bta}	Y_{IP}	Y_{MA}	Y_{CO}	Y_{CO2}	X_{HC}	$^{R}S_{MA}$
00%	13%	00%	47%	20%	20%	87%	54%

Tab. 7.10: *Normalised carbon related fractions of the individual species in the reactor product stream in the case that the reactor is operated for maximised reactor selectivity.*

fractions of the individual species that are calculated for maximised reactor selectivity are listed in Tab. 7.10. In contrast to the operation conditions with a conversion level of 90% and a maximum yield of 48%, the conversion level of raffinate II and the yield of maleic anhydride amount to 87% and 47% for a maximised reactor selectivity, respectively. The effect of a recycling stream on the overall performance is investigated with the conditions

of fixed reactor throughput and a fixed fraction of hydrocarbons in the reactor feed. The mass balances were solved for the conditions that the gas stream through the reactor for a production capacity of maleic anhydride of 18,700 t/year was chosen. The hydrocarbon fraction was kept at a fixed value of 0.6% n/n of hydrocarbons. The reactor simulation for a non-existent recycling stream leads to the fractions displayed in Tab. 7.10. The reactor behaviour is assumed to be independent of small changes in the composition of the reactor feed. Since the reactor is operated at fixed operation conditions, the production capacity is also fixed despite the variation of the recycling ratio. The performance of the reactor section can be expressed in terms of 6 parameters: the relative feed flow rate of raffinate II ($F_{\mathrm{raffinateII}}$); the relative feed flow rate of air (F_{air}); the molar fraction of *n*-butenes in the hydrocarbon feed of the reactor ($x^{\mathrm{HC}}_{\mathrm{bte,I}}$); the molar fraction of oxygen in the reactor feed ($x_{\mathrm{O2,I}}$); the overall conversion level ($X_{\mathrm{HC,recycle}}$); and the overall yield of maleic anhydride ($Y_{\mathrm{MA,recycle}}$). The relative feed flow rate of raffinate II is defined as the ratio of the molar feed flow rate of raffinate II for the recycle ratio R and the molar feed flow rate of raffinate II that is necessary without recycling:

$$F_{\mathrm{raffinateII}} = \frac{\dot{n}_{\mathrm{FR}}(R)}{\dot{n}_{\mathrm{FR}}(R=0)}. \tag{7.11}$$

The relative feed flow rate of air is defined in the same way:

$$F_{\mathrm{air}} = \frac{\dot{n}_{\mathrm{FA}}(R)}{\dot{n}_{\mathrm{FA}}(R=0)}. \tag{7.12}$$

The overall conversion level is related to the feed (FR) and the purge gas stream (T):

$$X_{\mathrm{HC,recycle}} = 1 - \frac{\dot{n}_{\mathrm{HC,T}}}{\dot{n}_{\mathrm{FR}}} \tag{7.13}$$

The overall yield of maleic anhydride is obtained by relating the molar flow rate of maleic anhydride in the product stream (P) to the molar flow rate of raffinate II in the feed (FR):

$$Y_{\mathrm{MA,recycle}} = \frac{\dot{n}_{\mathrm{MA,P}}}{\dot{n}_{\mathrm{FR}}} \tag{7.14}$$

The six parameters are calculated for recycle ratios between $R = 0$ and $R = 1$ by solving the mass balances of the system. The results are presented in Fig. 7.5. For a non-existent recycle stream ($R = 0$), the relative feed streams equal 1 by definition. The *n*-butenes fraction in the hydrocarbons at reactor inlet has a value of 75% and therefore equals the fraction in the synthetic raffinate II mixture. The fraction of oxygen at reactor inlet corresponds to that of air. Overall conversion level and overall yield equal the corresponding reactor values. Plots 7.5(a) and 7.5(b) show the relative molar flow rate of raffinate II and air in the feed, respectively. The flow rates decrease with increasing recycle ratio. The recycling of non-converted hydrocarbons leads to a lower amount of fresh raffinate II that is needed to achieve the same hydrocarbon throughput through the reactor. Since the carrier air stream is partly recycled, the relative molar flow rate of feed air is reduced.

The fraction of *n*-butenes in the hydrocarbon feed of the reactor is displayed in Fig. 7.5(c). The *n*-butenes are completely converted in the reactor. The reactor feed

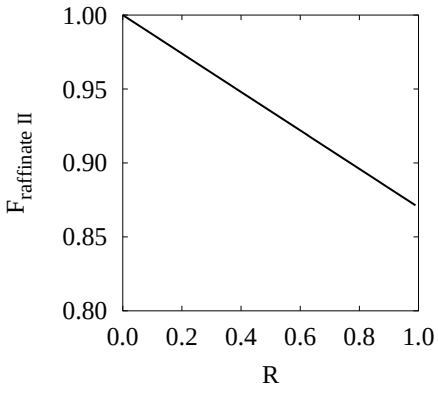

(a) Raffinate II feed stream reduction

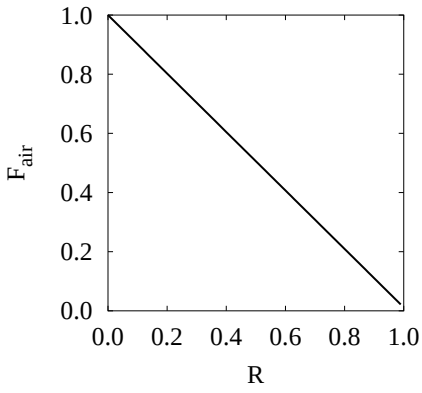

(b) Air feed stream reduction

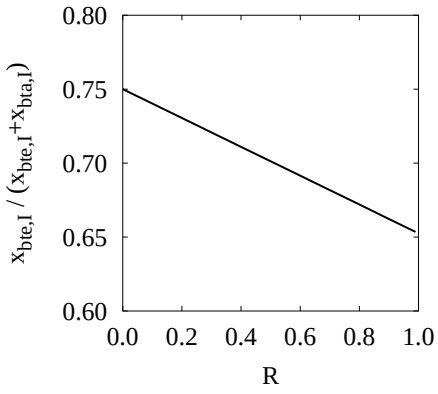

(c) Butene fraction of hydrocarbons in reactor feed stream

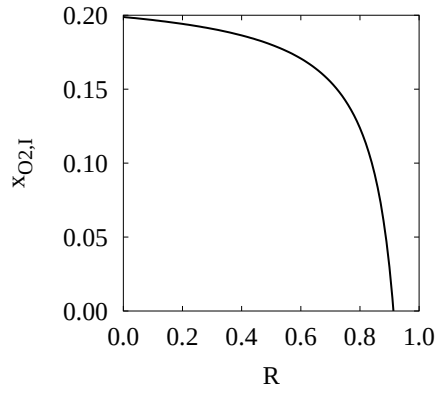

(d) Oxygen fraction in reactor feed

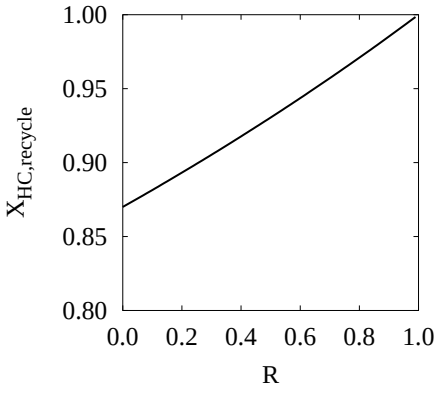

(e) Overall conversion level of raffinate II

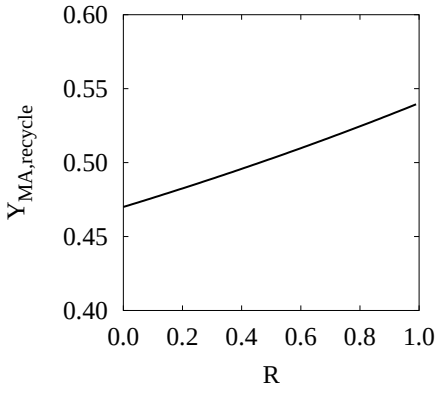

(f) Overall yield of maleic anhydride

Fig. 7.5: *Performance of the reactor section for varying recycling ratios. A ratio of $R = 0$ denotes reactor operation without recycling.*

is therefore enriched with *n*-butane by the recycle stream. The relative amount of *n*-butenes is decreasing with increasing recycle ratio. The fraction of oxygen in the reactor feed is presented in Fig. 7.5(d). The recycle stream has a lower oxygen fraction than air, since part of it has been converted in the reactor. An increasing recycle ratio therefore leads to lower oxygen fractions in the reactor feed.

Plots 7.5(e) and 7.5(f) show the overall conversion levels and overall yields of maleic anhydride. By increasing the recycle ratio, a higher amount of non-converted *n*-butane is recycled and leads to increased conversion levels. The molar flow rate of maleic anhydride remains constant and leads to increased overall yields, since a smaller amount of fresh raffinate II is needed to achieve the same molar flow rate of maleic anhydride.

The deviation of the reactor feed composition from that of reactor operation without recycling is increased with an increasing recycle ratio. A higher recycle ratio leads to a lower *n*-butenes content and a lower oxygen content. The reactor behaviour therefore deviates more and more from the assumed behaviour with increasing recycle rate. The oxygen fraction decreases sharply for recycle ratios of over 70%. The performance parameters for reactor operation without a recycle stream and for reactor operation with a recycle ratio of $R = 70\%$ are listed in Tab. 7.11. The hydrocarbon composition in the

R	$F_{\text{raffinateII}}$	F_{air}	$x^{\text{HC}}_{\text{bte,I}}$	$x_{\text{O2,I}}$	$X_{\text{HC,recylce}}$	$Y_{\text{MA,recycle}}$
00%	100%	100%	75%	20%	87%	47%
70%	91%	31%	68%	16%	96%	52%

Tab. 7.11: *Comparison of the overall performance of a plant with and without a recycle stream.*

reactor feed is changed to about 68% of *n*-butenes and 32% of *n*-butane. The oxygen fraction is decreased to 16%. If the reactor performance is not influenced by this change in the reactor feed stream, the production capacity of maleic anhydride remains the same. The advantage of the recycling stream is the lower demand of fresh raffinate II. A relative hydrocarbon feed rate of about 91% is sufficient for operation with a recycle stream. The overall conversion level and the overall yield are increased from 87% to 96% and from 47% to 52%, respectively. The lower demand of fresh air has no positive effect, since the recycle stream has also to be compressed. The necessary power for compression remains about the same. The realisation of a recycle stream, however, necessitates a second compressor and a second heating unit for the recycle stream. The investment costs are therefore higher for the realisation of a recycle stream. The advantage is the lower demand of fresh raffinate II for the production of the same amount of maleic anhydride.

Chapter 8

Summary and Conclusions

The motivation of the present work was the improvement of the utilisation of the C_4 streams of steamcrackers by converting raffinate II to maleic anhydride in one step. Thus, this thesis' goal was to determine the performance of the raffinate II conversion to maleic anhydride. The main tasks were the experimental determination of the reaction kinetics and the rigorous simulation of a production-scale reactor.

The measurements were carried out with a synthetic raffinate II mixture in the feed. The mixture consisted of 75% of 1-butene, 16% of *n*-butane and 9% of nitrogen. The nitrogen represented the isobutane fraction in a real raffinate II mixture. The synthetic mixture allowed for the variation of the relative amounts of *n*-butenes and *n*-butane in the reactor feed. The oxidations of pure 1-butene and pure *n*-butane were investigated as well.

Two kinds of catalysts named 'VPO-50' and 'VPO-14' were used. The catalysts consisted of the same VPO active material that was brought onto the same inert, non-porous support. The catalyst types differed in the thickness of the active shell. Therefore, it was possible to investigate the influence of pore transport resistances on catalyst performance. The weight fractions of active material per catalyst particle of the VPO-50 and the VPO-14 catalyst types were 50% and 14%, respectively.

The oxidation reactions were investigated in an isothermally operated laboratory fixed-bed reactor that was equipped with seven axially distributed sampling ports. The reaction temperature was varied in the range from 340 °C to 450 °C. The pressure was 1.3 bar in each experiment. The feed stream consisted of the hydrocarbon mixture and air. The hydrocarbon fraction was varied from 0.75% to 2.5% n/n.

Most experiments were carried out with the VPO-50 catalyst. The oxidation of pure *n*-butane leads to yields of maleic anhydride of above 60%. The yield increases with decreasing reaction temperature. The yield achieved with pure 1-butene amounts to more than 50% and is less sensitive to changes in the temperature than upon the oxidation of pure *n*-butane. The selectivity of maleic anhydride for low conversion levels is increased by increasing the temperature. The reaction rates of the *n*-butenes are significantly higher than the reaction rates of *n*-butane. The oxidation of synthetic raffinate II leads to a yield of maleic anhydride of 48% related to the linear hydrocarbons in the feed. Thus, the conversion of mixtures of *n*-butane and 1-butene leads to lower yields than the conversion of the pure components. A real raffinate II mixture with an isobutane content of 9% would yield maleic anhydride in an amount of 43%.

The experimental results were used to propose reaction kinetics for the conversion of

the pure components and the mixtures. The kinetic and stoichiometric parameters of the kinetic models were determined by means of a non-linear regression analysis of the experimental results. The models show a sufficiently good agreement with the experimental results.

The performance of the VPO-50 catalyst is clearly influenced by pore diffusional resistances. Experiments concerning the conversion of synthetic raffinate II with the VPO-14 catalyst lead to significantly lower yields with differences of about $\Delta Y_{\mathrm{MA}} \approx 0.1$. These differences were investigated and explained by simulations of the simultaneous transport and reaction processes in the pores of the catalyst bodies. The catalyst with the thicker active shell (VPO-50) is better suited for the production of maleic anhydride from raffinate II because a higher yield can be achieved. Another advantage of this catalyst type refers to the lower apparent activation energies. This results in lower sensitivities of the reaction rates towards changes in temperature. Thus, the VPO-50 catalyst was chosen for the simulation of a potential production-scale multi-tubular fixed-bed reactor.

The main difficulty in the operation of a production-scale reactor is the high exotherm of the oxidation reactions. A hot spot evolves in the vicinity of the reactor inlet. Temperatures higher than about 460 °C might damage or destroy the catalyst. On the other hand, it was found that higher temperatures in the first part of the reactor, where mostly *n*-butenes are converted, lead to higher yields of maleic anhydride. The hydrocarbon feed fraction was assumed to consist of 75% of *n*-butenes and 25% of *n*-butane. A two-dimensional pseudo-homogeneous reactor model was used since the heat removal and the representation of a hot spot are considered most realistically in this type of model. Simulations were carried out with two different hydrocarbon throughputs which result in production capacities of 17,100 t/a and 22,500 t/a. Lower production capacities can easily be accomplished by decreasing the number of tubes in the multi-tubular fixed-bed reactor. The catalyst bed has to be diluted in the first part of the reactor to avoid intolerably high hot spot temperatures. The pressure drops along the reactor are 1.0 bar and 1.5 bar for production capacities of 17,100 t/a and 22,500 t/a, respectively. The feed was assumed to be preheated to 390 °C before it enters the reactor. The temperature of the tube walls in the reactor was assumed to be 360 °C. The higher reactor inlet temperature was chosen to exploit the higher selectivities of maleic anhydride during the conversion of *n*-butenes in the first part of the reactor.

The simulations resulted in a conversion level of 90% and a yield of maleic anhydride of 48%. A typical raffinate II mixture which also contains isobutane would result in a yield of maleic anhydride of about 43%.

In the reactor simulation, the VPO-50 catalyst was chosen. The reactor performance could be optimised by optimising the shape of the catalyst bodies as well as the thickness of the layer of active material. Furthermore, the active material could be tailored to the conversion of *n*-butenes by adjusting the redox properties (optimisation of the amount of vanadium species in the oxidation state of +4 and +5).

A simplified flow scheme of the reactor section is proposed. Accordingly, the feed stream is first pre-heated in a heat exchanger by simultaneous cooling of the product stream. A furnace is used to further heat the feed stream to reactor inlet temperature. Maleic anhydride is recovered from the product stream by absorption. The purge gas that leaves the absorption column is burnt in the furnace. Excess heat from reactor and furnace is used to generate high pressure steam. The rate of steam production is clearly

sufficient to drive the feed stream compressor by a steam turbine.

It is shown in a simplified calculation that a recycle stream can lead to a lower demand for fresh raffinate II at the same production capacity of maleic anhydride. The overall conversion level of raffinate II and the overall yield of maleic anhydride related to linear hydrocarbons can be increased from 90% to 96% and from 48% to 52%, respectively, by recycling 70% of the gas stream that leaves the absorption column.

In the present work, a yield of maleic anhydride of about 60% was achieved in the conversion of pure *n*-butane. Raffinate II can be converted in a single stage process with a yield of maleic anhydride of about 43%. Bayer produced maleic anhydride from raffinate II around 1970 and achieved a yield of maleic anhydride of 34% [9]. The yield of maleic anhydride achieved in the present work is significantly higher. The overall yield can be increased by recycling part of the non-converted hydrocarbons back to the reactor.

Two further process alternatives for the production of maleic anhydride from raffinate II are conceivable. The alternatives consist of two process stages, each. For the first alternative, a dehydrogenation unit is proposed that produces butadiene which is subsequently oxidised to maleic anhydride. Both process stages can be incorporated into a single fixed-bed reactor. The yield of maleic anhydride may be in the range of 47% to 56% for this process option. The second alternative comprises of two separate reactors. In the first reactor, raffinate II is hydrogenated resulting in *n*-butane as the sole linear hydrocarbon. This hydrocarbon is then converted to maleic anhydride with an overall yield of about 55%. For this alternative, hydrogen must be continuously supplied.

There is no single best economic alternative to produce maleic anhydride. The choice depends strongly on the location of the site since the prices of *n*-butane, raffinate II and hydrogen depend strongly on the location.

Appendix A

Details of Gas Chromatography

The organic species in the gas samples taken from the reactor were detected and the corresponding concentrations were quantified by means of gas chromatography. The contents of the sampling loop were injected into a chromatography column of the type Chrompack CP-SIL 8 CB 50 m $\times$ 0.53 mm ($d = 5$ μm). The individual species left the column at specific retention times and were detected by a flame ionisation detector.

The peak area of a species i in a chromatogramme F_i depends on the amount of injected species i, on the sensitivity of the detector for this species and on operation conditions as well as construction details of the hardware. The peak area of the signal of the flame ionisation detector shows a linear dependence on the amount of the corresponding injected species. Therefore, the peak area of a species i can be expressed as

$$F_i = C \times q_i \times n_{i,\mathrm{loop}}. \tag{A.1}$$

The proportionality factor C represents the construction and operational details and remains constant during the measurements. The sensitivity of the flame ionisation detector for the species i is represented by q_i.

The amount of species i is directly proportional to the molar fraction of species i in the sample and can be expressed as

$$n_{i,\mathrm{loop}} = \frac{p_{\mathrm{loop}} V_{\mathrm{loop}}}{R T_{\mathrm{loop}}} \times x_i. \tag{A.2}$$

With the definition of the normalised dimensionless fraction Y_i, one obtains the relation

$$Y_i = \frac{\epsilon_{\mathrm{C},i}}{4} \times \frac{F_i/q_i}{\sum_j F_{j,0}/q_j}. \tag{A.3}$$

The dimensionless fractions are independent of the constant C and the conditions in the loop. The absolute values of the sensitivities q_i are irrelevant. It is sufficient to use relative values. Except for maleic anhydride, the sensitivities of the individual species were calculated as described in [57] and verified by injection of liquid samples in well defined amounts. The sensitivity of maleic anhydride was experimentally determined. Tab. A.1 lists all substances that could be detected together with their retention times and their sensitivities.

For the conversion of mixtures of n-butenes and n-butane, the peak areas of the species n-butane and 1,3-butadiene could not be determined individually because of the identical

Substance	Retention time / min	Sensitivity
isobutane	3.6	400
acetaldehyde	3.8	120
1-butene	4.0	400
n-butane	4.1	400
1,3-butadiene	4.1	391
trans-2-butene	4.3	400
cis-2-butene	4.6	400
acrolein	6.2	200
furan	6.6	300
methacrolein	8.3	300
crotonaldehyde	8.5	300
acetic acid	8.7	120
methylvinylketone	10.7	335
acrylic acid	10.8	210
maleic anhydride	16.3	230

Tab. A.1: *Retention times and sensitivities of all substances that were detected in the present work.*

retention times. For the oxidation of these mixtures, an assumption was made concerning the fractions of *n*-butane and 1,3-butadiene. The assumption was based on the experimental observation of the conversion of the pure components and the conversion of the mixture. The conversion of *n*-butane was strongly inhibited by the presence of *n*-butenes and 1,3-butadiene. It was therefore assumed that the *n*-butane conversion does not set in until the gas stream is free of 1,3-butadiene. If the measured sum concentration of both species was greater than the concentration of *n*-butane in the feed, the concentration of *n*-butane was assumed to be the same as in the feed and the difference to the sum concentration was ascribed to 1,3-butadiene. Sum concentrations lower than the feed concentration of *n*-butane were fully ascribed to *n*-butane and no 1,3-butadiene was expected to be in the gas phase. This assumption is justified by comparison of the concentration profiles that were obtained for the conversion of raffinate II and for the conversion of pure *n*-butenes with identical amounts of *n*-butenes in the feed. Both experiments were carried out with a molar fraction of 0.75% of 1-butene in the feed at 410 °C on a VPO-14 catalyst. No *n*-butane was present in the feed that was used in the first experiment. The second experiment was carried out with 0.16% of *n*-butane in the feed.

The conversion levels of *n*-butenes and the concentration profiles of IP and *n*-butane obtained in both experiments are presented in Fig. A.1. The conversion levels of *n*-butenes are displayed in Fig. A.1(a). The experimentally determined conversion levels as well as the conversion levels resulting from calculations are identical. Fig. A.1(b) presents the fraction profiles of IP and *n*-butane. Since the identical conversion levels of *n*-butenes were achieved in the experiments, it can be expected, that the real fraction profiles of IP are also identical for both experiments. The dimensionless fractions are related to the amount of hydrocarbons in the feed. Therefore, the dimensionless fractions of IP for the conversion of pure *n*-butenes are expected to be higher. The calculated fraction profiles show the expected behaviour. The fractions of IP could be determined exactly in case of

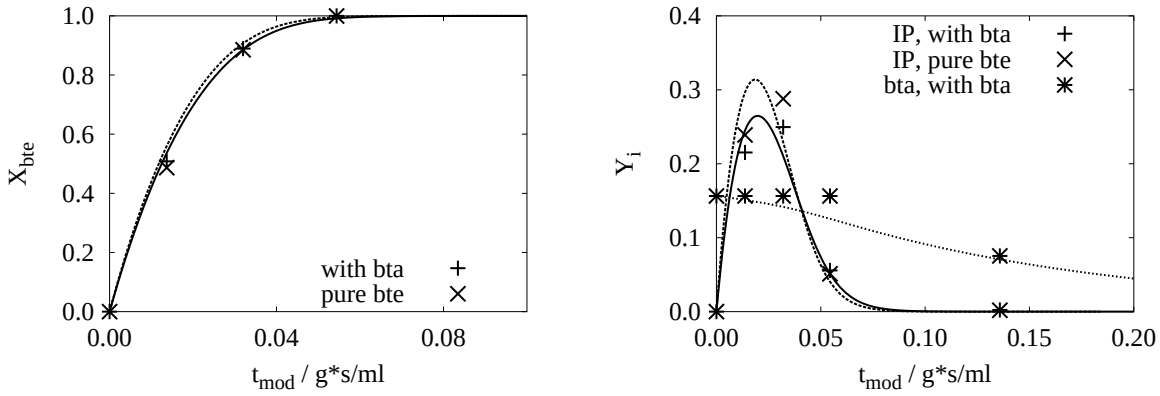

(a) Conversion levels of *n*-butenes

(b) Fraction profiles of IP and *n*-butane

Fig. A.1: *Comparison of the conversion levels of n-butenes and the fraction profiles of IP and n-butane obtained in two experiments. Both experiments were carried out with a molar fraction of 0.75% of 1-butene in the feed at 410 °C over a VPO-14 catalyst. No n-butane was present in the feed in the first experiment. The second experiment was carried out with 0.16% of n-butane in the feed.*

the conversion of pure *n*-butenes. With *n*-butane present in the gas phase, however, the above mentioned assumption had to be made. Nevertheless, both of the experimentally determined fraction profiles of IP show the same level of agreement with the calculation. The approximations for the fractions of *n*-butane and 1,3-butadiene are therefore justified.

The experimentally determined fractions of *n*-butane at low residence times (below 0.05 (g s)/ml) are assumed to be identical because of the approximation. In reality, however, it can be expected that the fraction of *n*-butane has already decreased slightly for residence times below 0.05 (g s)/ml. For higher residence times, however, it can be expected that the measured fraction represents the real fraction, since no more 1,3-butadiene is present in the gas phase. The real fraction profile can therefore be expected to be identical to the calculated fraction profile.

Appendix B

Further Estimations Concerning External Transport Resistances

In section 5.4.2, the effects of external transport resistances on the determination of the reaction kinetics in the laboratory reactor are discussed. In the present section, the results of further calculations are presented. Fig. B.1 shows the estimated deviations with the VPO-50 catalyst for a hydrocarbon fraction of 1.75% and a temperature of 420 °C. The deviations are much smaller than those that were estimated for a temperature of 450 °C as presented in section 5.4.2. The subsequent plots B.2 and B.3 show the estimated deviations for the measurements with the VPO-14 catalyst with the highest effects of transport resistances. It can be seen that the estimated deviations are small for the measurement at 410 °C.

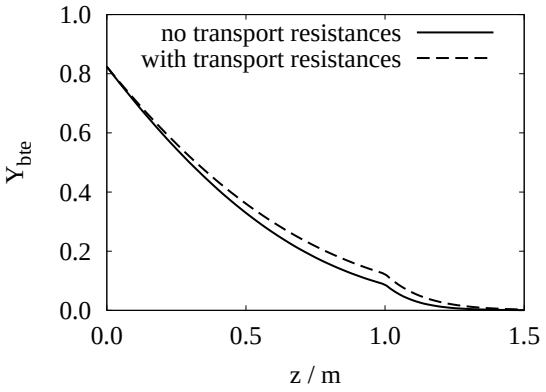

(a) Fraction profiles of *n*-butenes

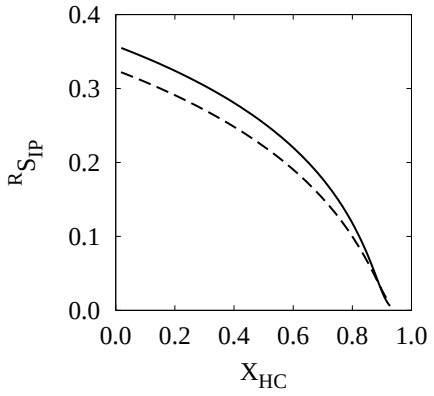

(b) Reactor selectivities of IP

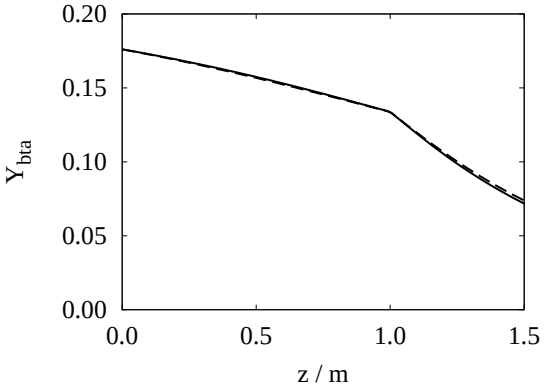

(c) Fraction profiles of *n*-butane

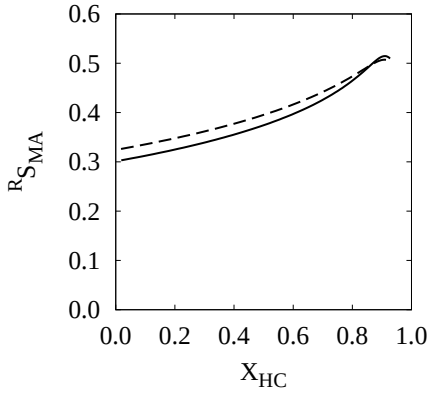

(d) Reactor selectivities of maleic anhydride

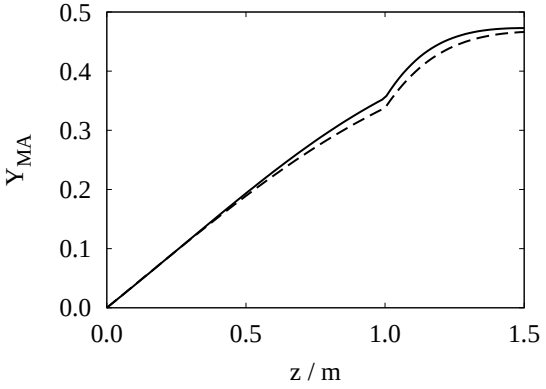

(e) Fraction profiles of maleic anhydride

Fig. B.1: *Effect of external mass transfer on the performance of the laboratory reactor for the partial oxidation of raffinate II (1.75% n/n in air) at 420* °C *over a VPO-50 catalyst and a standard volumetric flow rate of 30 ml/s.*

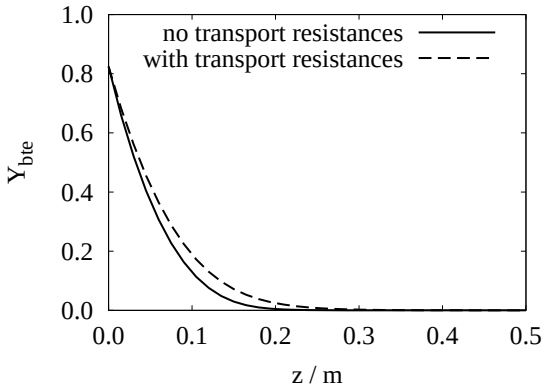

(a) Fraction profiles of *n*-butenes

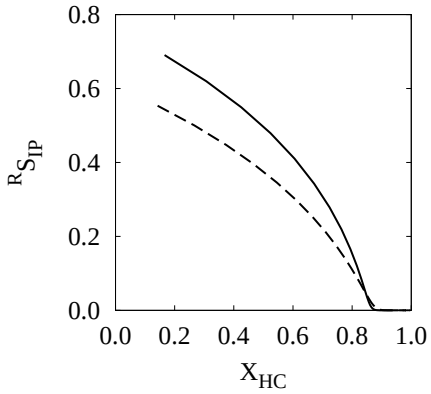

(b) Reactor selectivities of IP

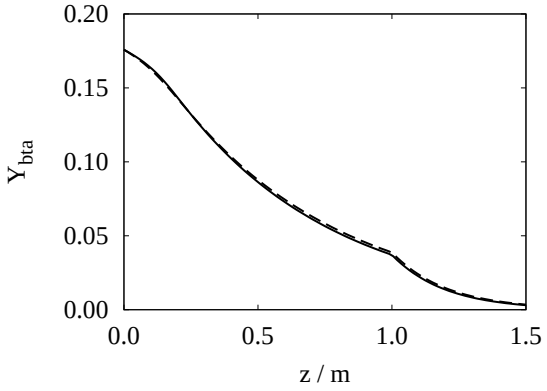

(c) Fraction profiles of *n*-butane

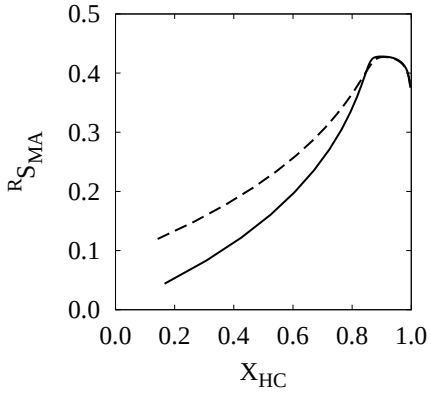

(d) Reactor selectivities of maleic anhydride

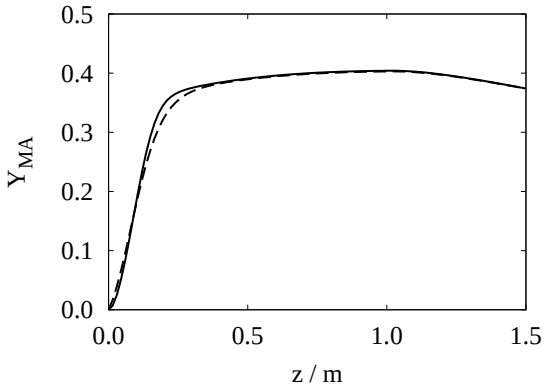

(e) Fraction profiles of maleic anhydride

Fig. B.2: *Effect of external mass transfer on the performance of the laboratory reactor for the partial oxidation of raffinate II (1% n/n in air) at 430* °C *over a VPO-14 catalyst and a standard volumetric flow rate of 20 ml/s.*

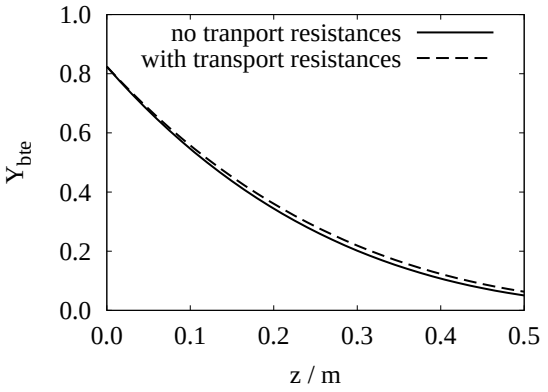

(a) Fraction profiles of *n*-butenes

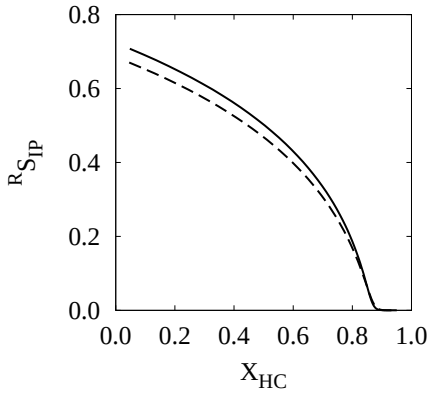

(b) Reactor selectivities of IP

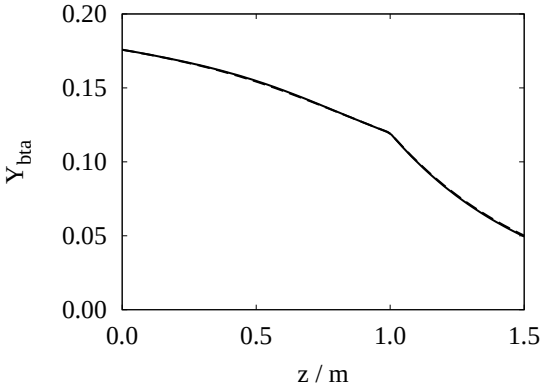

(c) Fraction profiles of *n*-butane

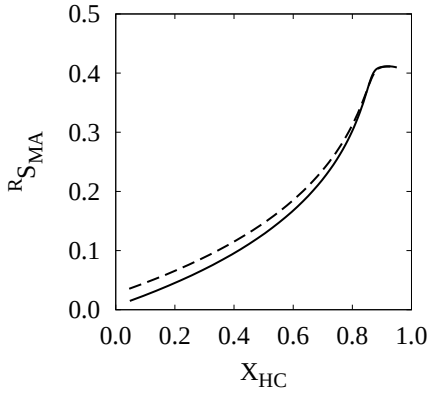

(d) Reactor selectivities of maleic anhydride

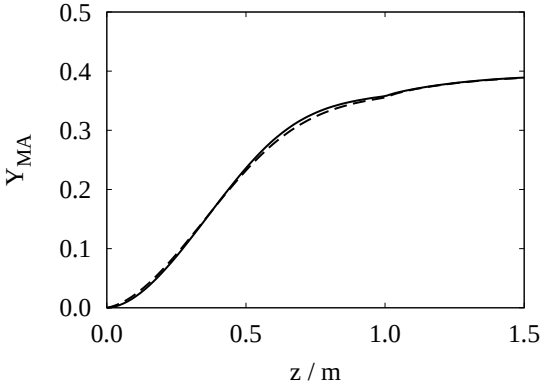

(e) Fraction profiles of maleic anhydride

Fig. B.3: *Effect of external mass transfer on the performance of the laboratory reactor for the partial oxidation of raffinate II (2% n/n in air) at 410* °C *over a VPO-14 catalyst and a standard volumetric flow rate of 20 ml/s.*

Appendix C

Numerical Details

C.1 Parameter Transformations in the Determination of the Kinetic and Stoichiometric Parameters

The Arrhenius equation is highly non-linear and often results in high cross correlations between the pre-exponential factor and the activation energy when these parameters are estimated. Therefore, the parameters were transformed by following the suggestion made in [39]. The Arrhenius equation

$$k_{i,j} = k_{i,j}^{\infty} \exp\left[-\frac{E_{\mathrm{A},i,j}}{RT}\right] \tag{C.1}$$

was transformed by substituting

$$k_{i,j}^{\infty} = k^{+} \exp\left[A_{i,j} + B_{i,j}\right], \tag{C.2}$$

$$E_{\mathrm{A},i,j} = RT^{+} B_{i,j}, \tag{C.3}$$

with $k^{+} = 10^{3} \frac{\mathrm{mol}}{\mathrm{s\,kg\,MPa}}$ and $T^{+} = 693.15$ K. The resulting equation

$$k_{i,j} = k^{+} \exp\left[A_{i,j} - B_{i,j}\left(\frac{T^{+}}{T} - 1\right)\right] \tag{C.4}$$

yields better results in the parameter determination. The inhibition constants were found to be independent of reaction temperature and are transformed into a single A-value:

$$b_i = b^{+} \exp\left[A_i^{b}\right], \tag{C.5}$$

with $b^{+} = 10^{6}\,\mathrm{MPa}^{-1}$. The stoichiometric parameters were confined to values between 0 and 1 by using the transformation

$$s_i = \frac{1}{1 + \exp\left[A_i^{s}\right]}. \tag{C.6}$$

At first, the stoichiometric parameters were assumed to depend on temperature, but no such dependence was found.

The standard deviations and therefore confidence limits for a probability of about 68.3% were transformed back by the relation between the variances

$$(\sigma_{i,j}^k)^2 = \left(\frac{\partial k_{i,j}}{\partial A_{i,j}}\right)^2 \times (\sigma_{i,j}^A)^2 + \left(\frac{\partial k_{i,j}}{\partial B_{i,j}}\right)^2 \times (\sigma_{i,j}^B)^2. \tag{C.7}$$

The back-transformed confidence limits were adopted to a probability of 95%.

The transformed parameters and the confidence limits which resulted directly from the parameter estimations are listed in Tab. C.1, Tab. C.2 and Tab. C.3.

parameter	A-value		B-value		parameter	A-value	
$k_{\mathrm{bta,MA}}$	-6.962	±0.030	14.66	±0.28	b_{bta}	-7.660	±0.053
$k_{\mathrm{bta,COx}}$	-7.771	±0.032	19.77	±0.36	b_{H2O}	-11.99	±0.51
$k_{\mathrm{MA,COx}}$	-9.289	±0.050	23.6	±1.4	s_{bta}	-0.596	±0.019
					s_{MA}	0.224	±0.053

Tab. C.1: *Transformed parameter set for the n-butane oxidation over a VPO-50 catalyst.*

parameter	A-value		B-value		parameter	A-value	
$k_{\mathrm{bta,MA}}$	-7.276	±0.024	10.79	±0.40	b_{bta}	-8.456	±0.091
$k_{\mathrm{bta,COx}}$	-8.207	±0.035	28.41	±0.80	b_{bte}	-6.816	±0.055
$k_{\mathrm{bte,IP}}$	-5.846	±0.036	12.31	±0.60	b_{IP}	-33.297	±4.58e10
$k_{\mathrm{bte,MA}}$	-6.081	±0.044	14.01	±0.79	b_{H2O}	-38.361	±1.97e11
$k_{\mathrm{bte,COx}}$	-5.915	±0.034	10.18	±0.26	s_{bta}	-0.512	±0.033
$k_{\mathrm{IP,MA}}$	-5.646	±0.054	9.7	±1.2	s_{bte}	0.073	±0.023
$k_{\mathrm{IP,COx}}$	-6.578	±0.096	25.4	±1.8	s_{IP}	-1.56	±0.26
$k_{\mathrm{MA,COx}}$	-8.771	±0.052	9.3	±1.1	s_{MA}	0.114	±0.081

Tab. C.2: *Transformed parameter set for the oxidation of mixtures of n-butenes and n-butane over a VPO-50 catalyst.*

C.2 Jacobian Matrices for Integration and Parameter Estimation

The integration of the differential balances is carried out by a semi-implicit algorithm in Matlab. The system of differential equations

$$\frac{\mathrm{d}\mathbf{Y}}{\mathrm{d}z} = \mathbf{r}(z, \mathbf{Y}, \mathbf{a}) \tag{C.8}$$

is solved with the initial condition

$$\mathbf{Y}(z = 0) = \mathbf{Y}_0. \tag{C.9}$$

parameter	A-value		B-value		parameter	A-value	
$k_{\mathrm{bta,MA}}$	-6.098	±0.063	15.28	±0.79	b_{bta}	-6.95	±0.10
$k_{\mathrm{bta,COx}}$	-6.694	±0.064	20.60	±0.89	b_{bte}	-5.20	±0.11
$k_{\mathrm{bte,IP}}$	-2.780	±0.097	24.51	±0.51	b_{IP}	-5.58	±0.22
					b_{H2O}	-8.44	±0.11
$k_{\mathrm{bte,COx}}$	-3.88	±0.11	17.68	±0.51	s_{bta}	-0.408	±0.029
$k_{\mathrm{IP,MA}}$	-3.447	±0.094	28.72	±0.66	s_{bte}	0.680	±0.052
$k_{\mathrm{IP,COx}}$	-3.64	±0.10	28.17	±0.87	s_{IP}	-0.331	±0.068
$k_{\mathrm{MA,COx}}$	-8.62	±0.11	17.5	±3.9	s_{MA}	-0.14	±0.18

Tab. C.3: *Transformed parameter set for the oxidation of mixtures of n-butenes and n-butane over a VPO-14 catalyst.*

The optimiser used in the parameter estimation requires the Jacobian matrix with respect to the parameters $\mathbf{a}$

$$\mathbf{J_a} = \frac{\partial \mathbf{Y}}{\partial \mathbf{a}}. \tag{C.10}$$

Since numerical derivations are very inaccurate, it is necessary to supply analytical derivatives for a successful optimisation process [39]. The Jacobian matrix is then obtained by numerical integration of

$$\mathbf{s} := \frac{\mathrm{d}\mathbf{J_a}}{\mathrm{d}z} = \left(\frac{\partial \mathbf{r}}{\partial \mathbf{Y}} \mathbf{J_a} + \frac{\partial \mathbf{r}}{\partial \mathbf{a}} \right) \tag{C.11}$$

with the initial condition

$$\mathbf{J_a}(z = 0) = \mathbf{0}. \tag{C.12}$$

The Jacobian matrix equals 0 for $z = 0$, because $\mathbf{Y}(z = 0)$ will always equal $\mathbf{Y}_0$, regardless of the chosen parameters.

Because of the semi-implicitness of the integrator, the integrator also depends on the Jacobian matrices $\mathbf{J_Y} := \partial \mathbf{r} / \partial \mathbf{Y}$. The derivations which are necessary for the integration of $\mathbf{s}$ are more complicated. By splitting $\mathbf{J_a}$ and $\mathbf{s}$ into the vectors

$$(\mathbf{J_a}_i)_j := (\mathbf{J_a})_{i,j}, \tag{C.13}$$

$$(\mathbf{s}_i)_j := (\mathbf{s})_{i,j}, \tag{C.14}$$

the Jacobian matrices for the individual vectors can be expressed as

$$\frac{\partial \mathbf{s}_i}{\partial \mathbf{Y}} = \left(\frac{\partial^2 r_i}{\partial \mathbf{Y}^2} \mathbf{J_a} + \frac{\partial^2 r_i}{\partial \mathbf{Y} \partial \mathbf{a}} \right)^{\mathrm{T}}, \tag{C.15}$$

$$\frac{\partial \mathbf{s}_i}{\partial \mathbf{J_a}_k} = \frac{\partial r_i}{\partial Y_k} \mathbf{1}. \tag{C.16}$$

List of Used Symbols

Latin Letters

symbol	*unit*	*description*
a_i	$\frac{\mathrm{m}^2}{\mathrm{m}^3}$	Surface area of catalytically active mass per volume of catalyst
a_i		Relative reaction rate of species i
$\mathbf{a}$		Vector of all kinetic and stoichiometric parameters that have to be determined
$A_{i,j}$		Transformed rate constant of the conversion of species i to species j
A_i^b		Transformed inhibition constant related to species i
A_i^s		Transformed stoichiometric coefficient for the conversion of species i to carbon oxides
$A_\mathrm{geo}^\mathrm{body}$	m^2	Geometrical surface area of a catalyst body
b_i	MPa^{-1}	Inhibition constant related to species i
$B_{i,j}$		Transformed activation energy of the reaction of species i to species j
c_i	$\frac{\mathrm{mol}}{\mathrm{m}^3}$	Concentration of species i
$c_{i,0}$	$\frac{\mathrm{mol}}{\mathrm{m}^3}$	Concentration of species i at reactor inlet
$c_{\mathrm{p},i}$	$\frac{\mathrm{kJ}}{\mathrm{kg\,K}}$	Specific heat capacity of species i for constant pressure
c_i^S	$\frac{\mathrm{mol}}{\mathrm{m}^3}$	Concentration of species i in the gas phase directly surrounding the catalyst body
$\mathbf{c}_0$	$\frac{\mathrm{mol}}{\mathrm{m}^3}$	Vector of concentrations of all species at reactor inlet
$\mathbf{c}^\mathrm{bulk}$	$\frac{\mathrm{mol}}{\mathrm{m}^3}$	Vector of concentrations of all species in the bulk gas phase
$\mathbf{c}^\mathrm{S}$	$\frac{\mathrm{mol}}{\mathrm{m}^3}$	Vector of concentrations of all species in the gas phase directly surrounding the catalyst body
C	mol^{-1}	Proportionality factor which represents construction and operational details of the gas chromatograph

symbol	*unit*	*description*
$C_{\mathrm{p},i}$	$\frac{\mathrm{kJ}}{\mathrm{mol\,K}}$	Molar heat capacity of species i for constant pressure
$c_{\mathrm{p}}^{\mathrm{F}}$	$\frac{\mathrm{kJ}}{\mathrm{kg\,K}}$	Specific heat capacity of the gas phase for constant pressure
$d_{\mathrm{p,A}}$	mm	Surface equivalent diameter
$d_{\mathrm{p,V}}$	mm	Volume equivalent diameter
D_i^{bed}	$\frac{\mathrm{cm}^2}{\mathrm{s}}$	Effective diffusivity of species i in the fixed bed
D^{body}	$\frac{\mathrm{cm}^2}{\mathrm{s}}$	Effective diffusivity in the catalyst body
D_i^{body}	$\frac{\mathrm{cm}^2}{\mathrm{s}}$	Effective diffusivity of species i in the catalyst body
$D_{\mathrm{ax},i}^{\mathrm{eff}}$	$\frac{\mathrm{cm}^2}{\mathrm{s}}$	Mass dispersion of species i in axial direction
$D_{\mathrm{rad},i}^{\mathrm{eff}}$	$\frac{\mathrm{cm}^2}{\mathrm{s}}$	Mass dispersion of species i in radial direction
D_i^{kn}	$\frac{\mathrm{cm}^2}{\mathrm{s}}$	Knudsen diffusivity of species i
D_i^{mol}	$\frac{\mathrm{cm}^2}{\mathrm{s}}$	Molecular diffusivity of species i
D_i^{pore}	$\frac{\mathrm{cm}^2}{\mathrm{s}}$	Effective diffusivity of species i in a cylindrical pore
$\mathbf{D}_i^{\mathrm{eff}}$	$\frac{\mathrm{cm}^2}{\mathrm{s}}$	Mass dispersion tensor of species i in the reactor
$E_{\mathrm{A},i,j}$	$\frac{\mathrm{kJ}}{\mathrm{mol}}$	Activation energy of the reaction of species i to species j
F_i		Relative feed flow of species i,
		Peak area of species i
$F_{i,0}$		Peak area of species i in the reactor feed
$\Delta_{\mathrm{F}}G_i$	$\frac{\mathrm{kJ}}{\mathrm{mol}}$	Molar Gibbs energy of formation of species i
$\Delta_{\mathrm{R}}G_j$	$\frac{\mathrm{kJ}}{\mathrm{mol}}$	Molar Gibbs energy of reaction j
$\Delta_{\mathrm{v}}h_i$	$\frac{\mathrm{kJ}}{\mathrm{mol}}$	Specific enthalpy of vaporisation of species i
$\Delta_{\mathrm{F}}H_i$	$\frac{\mathrm{kJ}}{\mathrm{mol}}$	Molar enthalpy of formation of species i
$\Delta_{\mathrm{R}}H_j$	$\frac{\mathrm{kJ}}{\mathrm{mol}}$	Molar enthalpy of reaction of j
$\Delta_{\mathrm{R}}H_{i,j}$	$\frac{\mathrm{kJ}}{\mathrm{mol}}$	Molar enthalpy of reaction of the conversion of species i to species j
$\Delta_{\mathrm{S}}H_i$	$\frac{\mathrm{kJ}}{\mathrm{mol}}$	Molar enthalpy of state of species i
$\Delta_{\mathrm{v}}H_i$	$\frac{\mathrm{kJ}}{\mathrm{mol}}$	Molar enthalpy of vaporisation of species i
j_i	$\frac{\mathrm{mol}}{\mathrm{s\,m}^2}$	Molar flux of species i caused by diffusion
$\mathbf{J_a}$		Jacobian matrix with respect to the parameters $\mathbf{a}$
$\mathbf{J_Y}$		Jacobian matrix with respect to the properties $\mathbf{Y}$

symbol	*unit*	*description*
k_c		Relative thermal conductivity of the core of a virtual unit cell in the fixed bed
k_p		Relative thermal conductivity of catalyst bodies
${}^\mathrm{B}k_\mathrm{a}$	$\frac{\mathrm{mol}}{\mathrm{s\,kg\,MPa}}$	Catalyst body activity parameter related to the mass of active material
${}^\mathrm{B}k_{\mathrm{a},i}$	$\frac{\mathrm{mol}}{\mathrm{s\,kg\,MPa}}$	Partial catalyst body activity parameter of species i related to the mass of active material
${}^\mathrm{I}\hat{k}_\mathrm{a}$	$\frac{\mathrm{mol}}{\mathrm{s\,m^2\,MPa}}$	Intrinsic activity parameter related to the surface area of active material
$k_{i,j}$	$\frac{\mathrm{mol}}{\mathrm{s\,kg\,MPa}}$	Rate constant for the conversion of i to j related to the mass of active material
$k_{i,j}^\infty$	$\frac{\mathrm{mol}}{\mathrm{s\,kg\,MPa}}$	Pre-exponential factor in Arrhenius' law for the reaction of species i to species j related to the mass of active material
${}^\mathrm{I}\hat{k}_{i,j}$	$\frac{\mathrm{mol}}{\mathrm{s\,m^2\,MPa}}$	Intrinsic rate constant for the conversion of i to j related to the surface area of active material
$K_{\mathrm{x},j}$		Equilibrium constant of reaction j related to molar fractions
L	m	Length or Height of reactor tube,
	mm	Thickness of the active layer
m_active	kg	Mass of catalytically active material
$m_\mathrm{active}^\mathrm{body}$	kg	Mass of catalytically active material of a catalyst body
$\dot{m}_i$	$\frac{\mathrm{kg}}{\mathrm{h}}$	Mass flow of species i
$\dot{m}_{i,0}$	$\frac{\mathrm{kg}}{\mathrm{h}}$	Mass flow of species i at reactor inlet
M_i	$\frac{\mathrm{g}}{\mathrm{mol}}$	Molar mass of species i
M^F	$\frac{\mathrm{g}}{\mathrm{mol}}$	Molar mass of the gas phase
n_i	mol	Number of moles of species i
$n_{i,\mathrm{loop}}$	mol	Number of moles of species i in the sampling loop
$\dot{n}$	$\frac{\mathrm{mol}}{\mathrm{s}}$	Molar flow rate through the reactor
$\dot{n}_i$	$\frac{\mathrm{mol}}{\mathrm{s}}$	Molar flow rate of species i
$\dot{n}_{i,j}$	$\frac{\mathrm{mol}}{\mathrm{s}}$	Molar flow rate of species i in stream j
$\dot{n}_{i,0}$	$\frac{\mathrm{mol}}{\mathrm{s}}$	Molar flow rate of species i at reactor inlet
N_rcts		Total number of reactions
N_samples		Total number of samples

symbol	*unit*	*description*
N_{species}		Total number of species
p	MPa	Pressure
p_0	MPa	Pressure at reactor inlet
p_{a}	MPa	Ambient pressure
p_i	MPa	Partial pressure of species i
$p_{i,0}$	MPa	Partial pressure of species i at reactor inlet
p_L	MPa	Pressure at reactor outlet
p_{loop}	MPa	Pressure in the sampling loop
$p_{z,0}$	$\frac{\text{MPa}}{\text{m}}$	Differential pressure drop at reactor inlet
$p^{\ominus}$	bar	Standard pressure, $p^{\ominus} = 1.013$ bar
Δp	bar	Pressure drop along the reactor
P	MW	Power for gas compression
$\mathbf{p}_0$	MPa	Vector of partial pressures of all species at reactor inlet
q_i		Sensitivity of the detector for species i
$\dot{Q}$	MW	Heat flow
$\dot{Q}_{\text{he}}$	MW	Heat flow in internal heat exchanger
$\dot{Q}_{\text{ph}}$	MW	Heat flow for feed stream pre-heating
$\dot{Q}_{\text{ph,air}}$	MW	Heat flow for feed air stream pre-heating
$\dot{Q}_{\text{ph,rII}}$	MW	Heat flow for feed raffinate II stream pre-heating
$\dot{Q}_{\text{rctr}}$	MW	Heat flow from reactor
$\dot{Q}_{\text{rctr,c}}$	MW	Heat flow from reactor resulting from feed stream cooling from reactor inlet temperature to tube wall temperature
$\dot{Q}_{\text{rctr,r}}$	MW	Heat flow from reactor resulting from reaction
$\dot{Q}_{\text{s}}$	MW	Heat flow that is used for excess steam generation (not used for compression)
$\dot{Q}_{\text{sg}}$	MW	Heat flow that is used for steam generation
$\dot{Q}_{\text{T}}$	MW	Heat flow resulting from total combustion of n-butane
r	mm	Radial position in the reactor tube
$\bar{r}_{\text{pore}}$	nm	Mean pore radius

symbol	*unit*	*description*
r_j	$\frac{\text{mol}}{\text{s kg}}$	Reaction rate for reaction j per mass of active material
${}^{\text{D}}r_j$	$\frac{\text{mol}}{\text{s kg}}$	Differential reaction rate for reaction j per mass of active material
${}^{\text{I}}\hat{r}_j$	$\frac{\text{mol}}{\text{s m}^2}$	Intrinsic reaction rate for reaction j per surface area of active material
$r_{i,j}$	$\frac{\text{mol}}{\text{s kg}}$	Reaction rate for the conversion of i to j per mass of active material
$\mathbf{r}$		Vector function that has to be integrated
R	$\frac{\text{J}}{\text{mol K}}$	Ideal gas constant, $R = 8.314\frac{\text{J}}{\text{mol K}}$,
	mm	Inner radius of the reactor tube,
		Recycle ratio
R_i	$\frac{\text{mol}}{\text{s kg}}$	Formation rate of species i per mass of active material
${}^{\text{B}}R_i$	$\frac{\text{mol}}{\text{s kg}}$	Catalyst body formation rate of species i per mass of active material
${}^{\text{B}}R_{i,0}$	$\frac{\text{mol}}{\text{s kg}}$	Catalyst body formation rate of species i per mass of active material at reactor inlet
${}^{\text{D}}R_i$	$\frac{\text{mol}}{\text{s kg}}$	Differential formation rate of species i per mass of active material
${}^{\text{I}}\hat{R}_i$	$\frac{\text{mol}}{\text{s m}^2}$	Intrinsic formation rate of species i per surface area of active material
${}^{\text{I}}R_i$	$\frac{\text{mol}}{\text{s kg}}$	Intrinsic formation rate of species i per mass of active material
s_i		Stoichiometric parameter for the conversion of species i to carbon oxides
$\mathbf{s}$		Derivation of the Jacobian matrix $\mathbf{J_a}$ with respect to the axial reactor position
${}^{i}\mathbf{s}$	div.	Vector of all reaction conditions for which sample i was taken
S	m^2	Cross sectional area of reactor tube
${}^{\text{B}}S_i$		Catalyst body selectivity of species i related to carbon
${}^{\text{B}}_{j}S_i$		Partial catalyst body selectivity of species i for the conversion of species j
${}^{\text{D}}S_i$		Differential selectivity of species i related to carbon
${}^{\text{I}}S_i$		Intrinsic selectivity of species i related to carbon
${}^{\text{R}}S_i$		Reactor selectivity of species i related to carbon
${}^{\text{R}}S_i^{\text{O}}$		Reactor selectivity of species i related to oxygen
$\Delta_{\text{F}}S_i$	$\frac{\text{J}}{\text{mol K}}$	Entropy of formation of species i

symbol	*unit*	*description*
t	s	Time
t_{layer}		Dimensionless thickness of the active layer
t_{mod}	$\frac{\text{g s}}{\text{ml}}$	Modified residence time referring to the mass of active VPO material.
${}^{\max}t_{\text{mod}}$	$\frac{\text{g s}}{\text{ml}}$	Modified residence time at which the maximum yield of maleic anhydride is achieved
T	K	Temperature
T_0	K	Temperature at reactor inlet
T_{a}	K	Ambient temperature
T_{cpr}	K	Temperature of gas stream after compression
T_{cw}	K	Temperature of cold water that is used for steam generation
T_{hc}	K	Temperature of feed stream of air after internal heat exchange
T_{loop}	K	Temperature in the sampling loop
$T_{\max}$	K	Maximum temperature in the hot spot
T_{prod}	K	Temperature of product stream after internal heat exchange
$T_{\text{s}}(p_{\text{s}})$	K	Boiling point for pressure p_{s}
T_{w}	K	Temperature of inner reactor tube wall
T^{bulk}	K	Temperature in the bulk gas phase
$T^{\ominus}$	K	Standard temperature, $T^{\ominus} = 25\ ^{\circ}\text{C}$
V_{loop}	m^3	Volume of the sampling loop
$\dot{V}$	$\frac{\text{m}^3}{\text{h}}$	Volumetric flow rate
$\dot{V}_{\text{a}}$	$\frac{\text{m}^3}{\text{h}}$	Volumetric flow rate of feed air at ambient conditions
$\dot{V}_{\text{N,i,0}}$	$\frac{\text{m}^3}{\text{h}}$	Volumetric flow rate of species i at reactor inlet related to a temperature of $T = 0\ ^{\circ}\text{C}$ and $p = 1.013$ bar
w	$\frac{\text{m}}{\text{s}}$	Axial velocity in the reactor
$\bar{w}$	$\frac{\text{m}}{\text{s}}$	Mean axial velocity in the reactor
$\mathbf{w}$	$\frac{\text{m}}{\text{s}}$	Velocity vector
x	mm	Position in the catalytically active layer
x_i		Molar fraction of species i
$x_{i,j}$		Molar fraction of species i in stream j
$x_{i,0}$		Molar fraction of species i at reactor inlet

symbol	*unit*	*description*
$x_{\mathrm{bte},i}$		Molar fraction of the n-butene isomer i related to the molar fraction of all n-butenes
x_j^{calc}		Calculated molar fraction of species j
${}^{i}x_j^{\mathrm{exp}}$		In sample i experimentally determined molar fraction of species j
x_i^{HC}		Molar fraction of species i in the hydrocarbon feedstock
$x_{i,j}^{\mathrm{HC}}$		Molar fraction of species i of all hydrocarbons in stream j
X		Conversion level
X_i		Conversion level of species i
$X_{i,\mathrm{recycle}}$		Conversion level of species i related to a process with recycle stream
y_i		Mass fraction of species i
$\mathbf{y}$		Vector of all mass fractions
$\mathbf{y}_0$		Vector of all mass fractions at reactor inlet
Y_i		Normalised dimensionless molar fraction and yield of species i related to carbon
$Y_{i,0}$		Normalised dimensionless molar fraction of species i related to carbon at reactor inlet
$Y_{i,\mathrm{recycle}}$		Yield of species i related to a process with recycle stream
${}^{\max}Y_i$		Maximum achievable yield of species i
${}_{j}Y_i$		Yield of species i from the conversion of j
$\mathbf{Y}$		Vector of all properties that have to be obtained by integration
$\mathbf{Y}_0$		Vector of all properties at reactor inlet
z	m	Axial position in reactor
${}^{i}z$	m	Position of sampling port where sample i was taken from
Z_i		Normalised dimensionless molar fraction and yield of species i related to oxygen
$\mathbf{1}$		Unity matrix

Greek Letters

symbol	*unit*	*description*
α		Ratio of heat capacities
β_i	$\frac{\mathrm{m}}{\mathrm{s}}$	Mass transfer coefficient of species i
$\gamma_{i,j}$		Cross correlation coefficient for parameters i and j
ϵ		Porosity of the active material of a catalyst body
$\epsilon_{\mathrm{C},i}$		Number of carbon atoms in a molecule of species i
$\epsilon_{\mathrm{O},i}$		Number of oxygen atoms in a molecule of species i
ζ_j	mol	Extent of reaction j
${}^{\mathrm{B}}\eta_i$		Catalyst body effectiveness factor related to species i
${}^{\mathrm{D}}\eta_i$		Differential effectiveness factor related to species i
η^{eff}	Pa s	Effective dynamic viscosity in the vicinity of the reactor wall
η^{F}	Pa s	Dynamic viscosity of the gas phase
κ^{F}	$\frac{\mathrm{cm}^2}{\mathrm{s}}$	Thermal diffusivity of the gas phase
${}^{\mathrm{B}}\lambda_i$		Catalyst body stability of species i
${}^{\mathrm{B}}_{j}\lambda_i$		Partial catalyst body stability of species i related to its formation by conversion of species j
${}^{\mathrm{I}}\lambda_i$		Intrinsic stability of species i
λ^{bed}	$\frac{\mathrm{W}}{\mathrm{m\,K}}$	Effective thermal conductivity in the fixed bed
$\lambda^{\mathrm{eff}}_{\mathrm{rad}}$	$\frac{\mathrm{W}}{\mathrm{m\,K}}$	Effective thermal conductivity in radial direction
$\lambda^{\mathrm{eff}}_{\mathrm{ax}}$	$\frac{\mathrm{W}}{\mathrm{m\,K}}$	Effective thermal conductivity in axial direction
λ^{body}	$\frac{\mathrm{W}}{\mathrm{m\,K}}$	Thermal conductivity of the catalyst bodies
λ^{F}	$\frac{\mathrm{W}}{\mathrm{m\,K}}$	Thermal conductivity of the gas phase
$\boldsymbol{\lambda}^{\mathrm{eff}}$	$\frac{\mathrm{W}}{\mathrm{m\,K}}$	Tensor of the effective thermal conductivity in the reactor
$\nu_{i,j}$		Stoichiometric coefficient of species i in reaction j
ν^{F}	$\frac{\mathrm{cm}^2}{\mathrm{s}}$	Kinematic viscosity of the gas phase
$\Delta\nu_j$		Change in number of moles in reaction j
ρ^{active}	$\frac{\mathrm{kg}}{\mathrm{m}^3}$	Density of catalytically active mass per reactor volume
ρ^{body}	$\frac{\mathrm{kg}}{\mathrm{m}^3}$	Density of catalytically active mass per volume of active mass
ρ^{F}	$\frac{\mathrm{kg}}{\mathrm{m}^3}$	Mass density of the gas phase

symbol	*unit*	*description*
σ_{abs}		Detection limit
σ_{rel}		Relative error
${}^{i}\sigma_{j}$		Standard deviation of the molar fraction of species j in sample i
$\sigma_{i,j}^{A}$		Standard deviation of the transformed rate constant of the reaction of species i to species j
$\sigma_{i,j}^{B}$		Standard deviation of the transformed activation energy of the reaction of species i to species j
$\sigma_{i,j}^{k}$	$\frac{\mathrm{mol}}{\mathrm{s\,kg\,MPa}}$	Standard deviation of the rate constant of the reaction of species i to species j
τ		Tortuosity factor
χ^2		Chi square for parameter estimation
ψ		Porosity of the fixed bed
ψ_{∞}		Porosity of the fixed bed without wall effects
Ω	$\frac{\mathrm{t}}{\mathrm{a}}$	Production capacity of maleic anhydride

A-dimensional Numbers

symbol	*definition*	*description*
Pe_{i}^{D}	$= \frac{\bar{w} d_{\mathrm{p,V}}}{D_{i}^{\mathrm{mol}}}$	Molecular Péclet number of species i
$Pe_{\mathrm{c},i}^{\mathrm{D}}$	$= \frac{w(r=0) d_{\mathrm{p,V}}}{D_{i}^{\mathrm{mol}}}$	Molecular Péclet number of species i in the core
Pe^{λ}	$= \frac{\bar{w} d_{\mathrm{p,V}}}{\kappa^{\mathrm{F}}}$	Péclet number
$Pe_{\mathrm{c}}^{\lambda}$	$= \frac{w(r=0) d_{\mathrm{p,V}}}{\kappa^{\mathrm{F}}}$	Péclet number in the core
Re	$= \frac{\bar{w} d_{\mathrm{p,V}}}{\nu^{\mathrm{F}}}$	Reynolds number with volume equivalent diameter
Re_{A}	$= \frac{\bar{w} d_{\mathrm{p,A}}}{\nu^{\mathrm{F}}}$	Reynolds number with surface equivalent diameter
Sc_{i}	$= \frac{\nu^{\mathrm{F}}}{D_{i}^{\mathrm{mol}}}$	Schmidt number of species i
Sh_{i}	$= \frac{\beta_{i} d_{\mathrm{p,A}}}{D_{i}^{\mathrm{mol}}}$	Sherwood number of species i
ϕ	$= L \times \sqrt{\frac{RT a_{\mathrm{i}} \times {}^{\mathrm{I}}\hat{k}_{\mathrm{a}}}{D^{\mathrm{body}}}}$	Thiele number

Indices

Species

symbol	*description*
bta	*n*-butane
bte	*n*-butenes
CO	carbon monoxide
COx	carbon oxides
CO2	carbon dioxide
HC	sum of *n*-butenes and *n*-butane
H2O	water
ibt	isobutane
IP	lumped together organic intermediates
MA	maleic anhydride
O2	oxygen
RII	raffinate II

Process Streams

symbol	*description*
F	Process feed stream
FA	Process air feed stream
FR	Process raffinate II feed stream
I	Reactor feed stream
O	Reactor product stream
P	Product stream after absorption column
R	Recycle stream
T	Purge gas stream

Other Indices

symbol	*description*
+	reference value

Bibliography

[1] Arpentinier, P.; Cavani, F.; Trifirò, F. *The Technology of Catalytic Oxidations. 1. Chemical, catalytic & engineering aspects;* Editions Technip: Paris, France, 2001.

[2] Hibst, H.; Noe, R.; Exner, K. M.; Duda, M. *Verfahren zur Herstellung von Maleinsäureanhydrid.* German patent application (to BASF AG), 2001. DE 101 37 534.

[3] Weissermel, K.; Arpe, H.-J. *Industrielle Organische Chemie*, 5th ed.; Wiley-VCH: Weinheim, Germany, 1998

[4] Kaufmann, D. Valorization of Raffinate II. In *C_4 Chemistry – Manufacture and Use of C_4 Hydrocarbons*, Proceedings of the DGMK Conference, Aachen, Germany, Oct 6 – 8, 1997; Keim, W., Ed.; DGMK Tagungsbericht 9705.

[5] Lohbeck, K.; Haferkorn, H.; Fuhrmann, W.; Fedtke, N. *Industrial organic chemicals: starting materials and intermediates; an Ullmann's encyclopedia*; Wiley-VCH: Weinheim, Germany 1999; Chapter Maelic and Fumaric Acids.

[6] *Maleic anhydride.* Europ. Chem. News 2 – 8 October 2000,

[7] *Butanediol.* Europ. Chem. News 15 – 21 October 2001.

[8] Becker, C. Katalytische Wandreaktorkonzepte für MSA-Synthese und Methanol-Dampfreformierung. *Dissertation, Universität Stuttgart*, 2002.

[9] Heller, H.; Lenz, G.; Thiel, R. The Bayer Process for the Manufacture of Maleic Anhydride from Butenes and as a By-Product of the Phthalic Anhydride Production. In *Advances in Petrochemical Technology*; Chemical Engineering Symposium; London, U.K., May 11 – 12, 1977; Vol 50.

[10] Kirk, R. E.; Othmer, D. F. *Encyclopedia of Chemical Technology*, chapter Maleic Anhydride, Maleic Acid and Fumaric Acid; John Wiley & Sons: New York, 1995.

[11] Frame, R. F.; Stine, L. O.; Hammershaimb, H. U.; Muldoon, B. S. High octane gasoline from field butanes by the UOP indirect alkylation (Inalk) process. In *C_4 Chemistry – Manufacture and Use of C_4 Hydrocarbons*, Proceedings of the DGMK Conference, Aachen, Germany, Oct 6 – 8, 1997; Keim, W., Ed.; DGMK Tagungsbericht 9705.

[12] van den Bosch, A. V. P. Manufacture of C_4s by refining processes and their future use in gasoline. In *C_4 Chemistry – Manufacture and Use of C_4 Hydrocarbons*, Proceedings of the DGMK Conference, Aachen, Germany, Oct 6 – 8, 1997; Keim, W., Ed.; DGMK Tagungsbericht 9705.

[13] Onken, U.; Behr, A. *Chemische Prozesskunde, Lehrbuch der Technischen Chemie, Band 3*; Georg Thieme Verlag: Stuttgart, New-York, 1996.

[14] Beyer, H.; Walter, W. *Lehrbuch der Organischen Chemie*, 23rd ed.; S. Hirzel Verlag: Stuttgart, Leipzig, Germany, 1998.

[15] Morgan, M. L. The C_4 chain – maximising value. In *C_4 Chemistry – Manufacture and Use of C_4 Hydrocarbons*, Proceedings of the DGMK Conference, Aachen, Germany, Oct 6 – 8, 1997; Keim, W., Ed.; DGMK Tagungsbericht 9705.

[16] Quast, A. Partielle Oxidation von C_4-Kohlenwasserstoffen zur Darstellung von Maleinsäureanhydrid und Furan. *Dissertation, Universität Karlsruhe*, 1999.

[17] Dente, M.; Pierucci, S.; Tronconi, E.; Cecchini, M.; Ghelfi, F. Selective oxidation of *n*-butane to maleic anhydride in fluid bed reactors: detailed kinetic investigation and reactor modelling. *Chem. Eng. Sci.*, 2003, 58, 643–648.

[18] Lerou, J. J.; Mills, P. L. Du Pont butane oxidation process. *Prec. Proc. Tech.*, 1993, 175–195.

[19] May, A. Das Reaktor-Regenerator-System als neues Konzept für die getrennte Reaktionsführung bei der selektiven Oxidation von n-Butan zu Maleinsäureanhydrid. *Dissertation, Universität Erlangen-Nürnberg*, 2002.

[20] Duda, M.; Machhammer, O.; Weck, A. *Verfahren zur Herstellung von Maleinsäureanhydrid*. PCT patent application (BASF AG), 2005. WO 05/019148.

[21] Hodnett, B. K. *Heterogeneous Catalytic Oxidation*. John Wiley & Sons: New-York, 2000.

[22] Centi, G.; Trifirò, F. Mechanistic aspects of maleic anhydride synthesis from C_4 hydrocarbons over phosphorus vanadium oxide. *Chem. Rev.*, 1988, 88, 55–80.

[23] Xue, Z.-Y.; Schrader, G. L. Transient FTIR studies of the reaction pathway for *n*-butane selective oxidation over vanadyl pyrophosphate. *J. Catal.*, 1999, 184, 87–104.

[24] Bej, S. K.; Rao, M. S. Selective oxidation of *n*-butane to maleic anhydride. 3. Modeling studies. *Ind. Eng. Chem. Res.*, 1991, 30, 1829–1832.

[25] Mallada, R.; Menéndez, M.; Santamaría, J. On the favourable effect of CO_2 addition in the oxidation of butane to maleic anhydride using membrane reactors. *Appl. Catal. A: General*, 2002, 231, 109–116.

[26] Brandstädter, W. M.; Kraushaar-Czarnetzki, B. Pilot plant processing of *n*-butane to maleic anhydride above the explosion limit. In *Creating Value from Light Olefins – Production and Conversion*, Proceedings of the DGMK Conference, Hamburg, Germany, Oct 10-11, 2001; Emig, G., Ed.; DGMK-Tagungsbericht 2001-4.

[27] Sharma, R. K.; Cresswell, D. L. Kinetics and fixed-bed reactor modeling of butane oxidation to maleic anhydride. *AIChE J.*, 1991, 37, 39–47.

[28] Wellauer, T. P. Optimal Policies in Maleic Anhydride Production through Detailed Reactor Modelling. *Dissertation, Eidgenössische Technische Hochschule Zürich*, 1985.

[29] Uihlein, K. Butanoxidation an VPO-Wirbelschichtkatalysatoren. *Dissertation, Universität Karlsruhe*, 1993.

[30] Bej, S. K.; Rao, M. S. Selective oxidation of *n*-butane to maleic anhydride. 2. Identification of rate expression for the reaction. *Ind. Eng. Chem. Res.*, 1991, 30, 1824–1828.

[31] Varma, R. L.; Saraf, D. N. Selective oxidation of C_4 hydrocarbons to maleic anhydride. *Ind. Eng. Chem. Prod. Res. Dev.*, 1979, 18, 7–13.

[32] Kotter, M.; Riekert, L. Beeinflussung der Aktivität und Selektivität von Tränkkatalysatoren durch die topographische Verteilung der Aktivkomponente. Teil I: Aktivität und Selektivität in Abhängigkeit von der Zugänglichkeit der Aktivkomponente. *vt verfahrenstechnik*, 1983, 17, 639–649.

[33] Riekert, L. Observation and quantification of activity and selectivity of solid catalysts. *Appl. Catal.*, 1985, 15, 89–102.

[34] Baerns, M.; Hofmann, H.; Renken, A. *Chemische Reaktionstechnik, Lehrbuch der Technischen Chemie, Band 1*, 3rd ed.; Georg Thieme Verlag: Stuttgart, New-York, 1999.

[35] Hein, S. Modellierung wandgekühlter katalytischer Festbettreaktoren mit Ein- und Zweiphasenmodellen. *Dissertation, Technische Universität München*, 1999.

[36] Brandstädter, W. M.; Casaretto, P.; Kraushaar-Czarnetzki, B. Maleic anhydride from mixtures of *n*-butane and *n*-butenes. In *Chances for Innovative Processes at the Interface between Refining and Petrochemistry*, Proceedings of the DGMK Conference, Berlin, Germany, Oct 2002; DGMK-Tagungsbericht 2002-4.

[37] Press, W. H.; Teukolsky, S. A.; Vetterling, W. T.; Fannery B. P. *Numerical Recipes in C: The Art of Scientific Computing*, 2nd ed.; Cambridge University Press: New York, 1992.

[38] Bates, D. M.; Watts, D. G. *Nonlinear Regression Analysis and Its Applications.* John Wiley & Sons: New York, 1988.

[39] Zander, H.-J. Dynamische Modellierung reaktionskinetischer Systeme mit Neuronalen Netzen und hybriden Modellen. *Dissertation, Universität Erlangen-Nürnberg*, 1999.

[40] Liley, P. E.; Thomson, G. H.; Friend, D. G.; Daubert, T. E.; Buck, E. *Perry's Chemical Engineers' Handbook*, 7th ed.; McGraw–Hill International Editions: New York, 1998; Chapter 2: Physical and Chemical Data.

[41] Database of the Design Institute for Physical Properties (DIPPR), see www.aiche.org.

[42] Lucas, K.; Luckas, M. *VDI-Wärmeatlas*, 9th ed.; VDI-Verlag: Düsseldorf, Germany, 2002; Chapter Da: Berechnungsmethoden für Stoffeigenschaften.

[43] Centi, G. Vanadyl pyrophosphate – a critical overview. *Catal. Today*, 1993, 16, 5–26.

[44] Cavani, F.; Trifirò, F. Catalyzing butane oxidation to make maleic anhydride. *Chemtech*, 1994, 24, 18–25.

[45] Thomas, J. M.; Thomas, W. J. *Principles and Practice of Heterogeneous Catalysis.* VCH: Weinheim, Germany, 1997.

[46] Doraiswamy, L. K.; Sharma, M. M. Gas–solid and solid–solid reactions. In *Heterogeneous Reactions: Analysis, Examples and Reactor Design*, volume 1. John Wiley & Sons: New York, 1984.

[47] Petrovic, L. J.; Thodos, G. Mass transfer in the flow of gases through packed beds. Low reynolds number region. *Ind. Eng. Chem. Fundamentals*, 1968, 7, 274–280.

[48] Satterfield, C. N. *Heterogeneous Catalysis in Practice.* McGraw–Hill: New-York, 1980.

[49] Tsotsas, E. *VDI-Wärmeatlas*, 9th ed.; VDI-Verlag: Düsseldorf, Germany, 2002; Chapter Mh: Wärmeleitung und Dispersion in durchströmten Schüttungen.

[50] Tsotsas, E. Entwicklungsstand und Perspektiven der Modellierung von Transportvorgängen in durchströmten Festbetten. *Chem. Ing. Tech.*, 2000, 72, 313–321.

[51] Krauss, R. *VDI-Wärmeatlas*, 7th ed.; VDI-Verlag: Düsseldorf, Germany, 1994; Chapter Db 16: Stoffwerte von Luft.

[52] Tsotsas, E. *VDI-Wärmeatlas*, 9th ed.; VDI-Verlag: Düsseldorf, Germany, 2002; Chapter Dee: Wärmeleitfähigkeit von Schüttschichten.

[53] Krause, E.; Berger, I.; Nehlert, J.; Wiegmann, J. *Technologie der Keramik, Band 1: Verfahren – Rohstoffe – Erzeugnisse*, 2nd ed.; Verlag für Bauwesen: Berlin, German Democratic Republic, 1985.

[54] Stephan, K.; Mayinger, F. *Thermodynamik 1: Einstoffsysteme.* Springer-Verlag: Berlin, Heidelberg, Germany, 1992.

[55] Stephan, K. *Dubbel Taschenbuch für den Maschinenbau, Kapitel D: Thermodynamik*, 17th ed.; Springer-Verlag: Berlin, Heidelberg, New-York, 1990.

[56] Bernecker, G. *Planung und Bau verfahrenstechnischer Anlagen*, 4th ed.; Springer-Verlag: Berlin, Heidelberg, Germany, 2001.

[57] Ackman, R. G. Fundamental groups in the response of flame ionization detectors to oxygenated aliphatic hydrocarbons. *Journal of Gas Chromatography*, 1964, 6, 173–179.

Universität Karlsruhe (TH)
Institut für Chemische Verfahrenstechnik

More and more steamcracker capacity is added to meet the increasing global demand for propylene. Formation of C4 by-product is inevitable during the propylene production process. Value added products based on C4 streams become more and more important since the demand for C4 hydrocarbons is not growing as fast. In the present work, the improvement of the utilisation of the C4 streams by converting raffinate II to maleic anhydride in one step was studied. Measurements were carried out with different mixtures of 1-butene and n-butane. The oxidation reactions were investigated in an isothermally operated laboratory-scale fixed-bed reactor which was equipped with seven axially distributed sampling ports. Reaction kinetics was proposed based on the experimental results. The effects of pore diffusional resistance were investigated and explained. A two-dimensional pseudo-homogeneous reactor model was used for the simulation of a production-scale fixed-bed reactor. Reaction conditions and reactor configurations were optimized according to the model. A simplified flow scheme of the reactor section was proposed. The rate of steam production is clearly sufficient to drive the feed stream compressor by a steam turbine. It can also be concluded that a recycle stream reduces the demand for fresh raffinate II at the same production capacity of maleic anhydride.

ISBN: 978-3-86644-199-6

www.uvka.de